

AD-A157 226

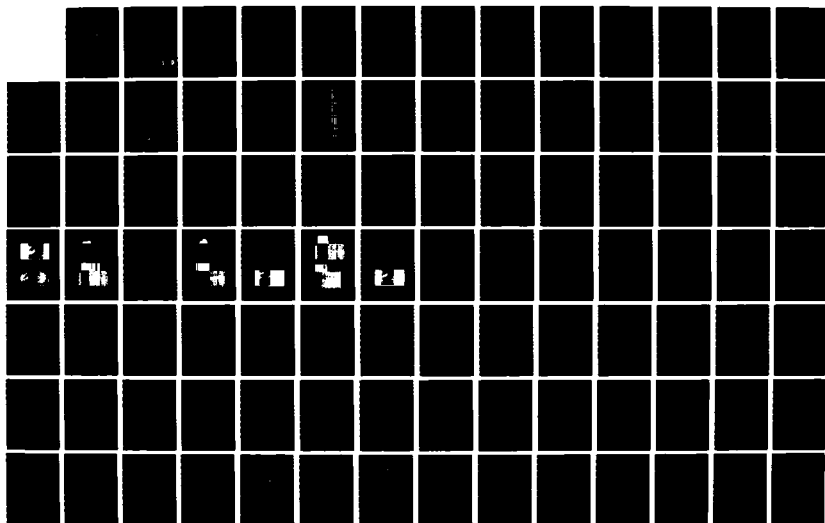
SINGLE SITE LOCATION WITH IONOSPHERIC SPECIFICATION  
FROM OBLIQUE-INCIDENCE SOUNDERS(U) NAVAL RESEARCH LAB  
WASHINGTON DC M H REILLY ET AL. 24 JUN 85 NRL-MR-5586

1/3

UNCLASSIFIED

F/G 20/14

NL





MICROCOPY RESOLUTION TEST CHART  
NATIONAL BUREAU OF STANDARDS-1963-A

7

NRL Memorandum Report 5586

# Single Site Location with Ionospheric Specification from Oblique-Incidence Sounders

M. H. REILLY

*Ionospheric Effects Branch  
Space Science Division  
E. O. Hulburt Center for Space Research*

June 24, 1985

AD-A157 226

DTIC FILE COPY



NAVAL RESEARCH LABORATORY  
Washington, D.C.

DTIC  
ELECTE  
JUL 17 1985  
S D

Approved for public release; distribution unlimited.

85 06 27 030

AD-A157226

SECURITY CLASSIFICATION OF THIS PAGE

REPORT DOCUMENTATION PAGE				
1a. REPORT SECURITY CLASSIFICATION <b>UNCLASSIFIED</b>			1b. RESTRICTIVE MARKINGS	
2a. SECURITY CLASSIFICATION AUTHORITY			3. DISTRIBUTION / AVAILABILITY OF REPORT  <b>Approved for public release; distribution unlimited.</b>	
2b. DECLASSIFICATION / DOWNGRADING SCHEDULE				
4. PERFORMING ORGANIZATION REPORT NUMBER(S) <b>NRL Memorandum Report 5586</b>			5. MONITORING ORGANIZATION REPORT NUMBER(S)	
6a. NAME OF PERFORMING ORGANIZATION <b>Naval Research Laboratory</b>	6b. OFFICE SYMBOL (If applicable) <b>Code 4182</b>	7a. NAME OF MONITORING ORGANIZATION <b>U.S. Army Signal Warfare Laboratory</b>		
6c. ADDRESS (City, State, and ZIP Code) <b>Washington, DC 20375-5000</b>		7b. ADDRESS (City, State, and ZIP Code) <b>Vint Hill Farm Station Warrenton, VA 22186</b>		
8a. NAME OF FUNDING / SPONSORING ORGANIZATION	8b. OFFICE SYMBOL (If applicable)	9. PROCUREMENT INSTRUMENT IDENTIFICATION NUMBER		
8c. ADDRESS (City, State, and ZIP Code)		10. SOURCE OF FUNDING NUMBERS PROGRAM ELEMENT NO. PROJECT NO. TASK NO. WORK UNIT ACCESSION NO. <b>DN280-477</b>		
11. TITLE (Include Security Classification) <b>Single Site Location with Ionospheric Specification from Oblique-Incidence Sounders</b>				
12. PERSONAL AUTHOR(S) <b>Reilly, M.H.</b>				
13a. TYPE OF REPORT <b>Interim</b>	13b. TIME COVERED FROM TO	14. DATE OF REPORT (Year, Month, Day) <b>1985 June 24</b>	15. PAGE COUNT <b>222</b>	
16. SUPPLEMENTARY NOTATION  <b>High Frequency</b>				
17. COSATI CODES FIELD GROUP SUB-GROUP			18. SUBJECT TERMS (Continue on reverse if necessary and identify by block number) <b>Single site location ; HF propagation assessment ; Ionospheric specification ; Transmitter location</b>	
19. ABSTRACT (Continue on reverse if necessary and identify by block number) <p>A twelve-hour December 6 segment of oblique-incidence sounder data from the 1982 SSL-BCT experiments is analyzed, in order to develop techniques for accurate incorporation of ionospheric properties into the single site location algorithm. It is shown from SSL-BCT prototype calculations, and by comparison with vertical-incidence sounder data, that true height profiles can be accurately obtained from the oblique ionograms, and that they characterize the ionosphere at the sounder midpath locations. The time development of the ionosphere at these control points is found to be accurately characterized by the variation of a set of nine or eleven parameters from the true height profile calculations. By a strategic choice of the independent variable as cosine of an effective or the actual solar zenith angle, it is found that the background daytime ionosphere variation is described by trend lines for the ionospheric parameters, which are convenient for predictions. It is shown how the trend line information at sounder control points can be spatially interpolated to unsounded raypaths, and how this can be used. Modifications of present SSL techniques to incorporate the more accurate ionospheric specification are discussed, and future research and development is indicated. <i>Keywords:</i></p>				
20. DISTRIBUTION / AVAILABILITY OF ABSTRACT <input checked="" type="checkbox"/> UNCLASSIFIED/UNLIMITED <input type="checkbox"/> SAME AS RPT <input type="checkbox"/> DTIC USERS			21. ABSTRACT SECURITY CLASSIFICATION <b>UNCLASSIFIED</b>	
22a. NAME OF RESPONSIBLE INDIVIDUAL <b>M. H. Reilly</b>			22b. TELEPHONE (Include Area Code) <b>(202) 767-2891</b>	22c. OFFICE SYMBOL <b>Code 4182</b>

DD FORM 1473, 84 MAR

83 APR edition may be used until exhausted.  
All other editions are obsolete

SECURITY CLASSIFICATION OF THIS PAGE

# CONTENTS

1. INTRODUCTION.....	1
2. FROM OBLIQUE IONOGRAMS TO TRUE HEIGHT PROFILES.....	5
2A. Basic Method.....	5
2B. Idealized True Height Profile Fit.....	7
2C. SSL-BCT Prototype Calculations.....	13
2D. Path 4 True Height Profiles and Midpath Ionospheres....	33
3. SSL-BCT CALCULATIONS FOR DECEMBER 6-7.....	35
3A. Ionograms.....	35
3B. True Height Profiles.....	40
3C. Solar Zenith Angle Dependence and Trend Lines.....	40
3D. Trend Lines Compared.....	69
4. INTERPOLATION OF SOUNDER RESULTS TO UNSOUNDED PATHS.....	70
5. MODIFICATION OF SSL TECHNIQUES.....	73
6. DISCUSSION.....	73
7. REFERENCES.....	76
APPENDICES A-K	
Appendix A - Comparison Between Calculated and Experimental Vertical Ionograms.....	77
Appendix B - Plots of $foF_2^2$ vs. $\cos \chi_{eff}$ .....	105
Appendix C - Plots of $hmF_2$ vs. $\cos \chi_{eff}$ .....	115
Appendix D - Plots of $foF_1^2$ vs. $\cos \chi_{eff}$ .....	122
Appendix E - Plots of $hmF_1$ vs. $\cos \chi_{eff}$ .....	129
Appendix F - Plots of $fbF^2$ vs. $\cos \chi$ .....	136
Appendix G - Plots of $hbF$ vs. $\cos \chi$ .....	143
Appendix H - Plots of $foE^2$ vs. $\cos \chi$ .....	150
Appendix I - Plots of $hmE$ vs. $\cos \chi$ .....	157
Appendix J - Comparison of Trend Lines.....	164
Appendix K - Comparison of Calculated and Exact Profiles in the SSL-BCT Prototype Calculations.....	179

Dist K/	Avail and/or Special	Availability Codes	By Distribution/	NTIS GRA&I DTIC TAB Unannounced Justification	Accession For
					<input type="checkbox"/> <input type="checkbox"/> <input checked="" type="checkbox"/>



SINGLE SITE LOCATION WITH IONOSPHERIC SPECIFICATION  
FROM OBLIQUE-INCIDENCE SOUNDERS

## 1. INTRODUCTION

The location of a remote HF transmitter, starting with the measured wave frequency and the azimuth and elevation angles of an incoming wave front at a single site, is typically based on an oversimplified characterization of the ionospheric propagation medium. This report is concerned with improvement of single site location (SSL) accuracy through improved ionospheric characterization by means of sounders, which probe the ionosphere along a relatively small set of paths, either at vertical incidence or at oblique incidence. The challenge is to convert these measurements to a complete characterization of the ionosphere along all raypaths of interest.

At present, SSL techniques are typically based on Figure 1, which results from the Breit-Tuве and Martyn Equivalent Path theorems in radio wave propagation theory [e.g., Budden, 1965 or Davies, 1969]. The raypath in Figure 1 is shown by the arrowed line from the transmitter to the receiver. The measurement determines the wave frequency  $f$ , the elevation angle  $\theta_0$ , and the azimuth angle, which determines the plane of propagation. Each side of the constructed isosceles triangle in Figure 1 is half the group path length  $P'$  for ray propagation at frequency  $f$ , and  $h'$  is the virtual height measured by a vertical-incidence sounder at the equivalent vertical frequency

$$f_v = (f \cos i)/k, \quad (1)$$

where  $i$  is half the apex angle, as shown in Figure 1. The validity of this figure depends on the approximation that the ionosphere is horizontally stratified for the portion of the raypath in the ionosphere, i.e., the ionosphere is flat and without tilts for this raypath portion. Magnetic field effects are also ignored. The factor  $k$  in (1), which was introduced by [Smith, 1939] as a rough correction for ionospheric curvature, varies from 1 to about 1.18 as range  $D$  increases from 0 to 4000 km. The central angle  $X$  and distance  $\Delta$  are very simply related to  $D$  by the geometry of Figure 1:

$$X = D/(2R_0) \quad (2)$$

$$\Delta = R_0 (1 - \cos X) \quad (3)$$

Determination of the HF transmitter location typically proceeds from Figure 1 and measurements on the incoming wave front as follows. Virtual height  $h'$  versus frequency is determined at some point, e.g., at the receiver, by a vertical-incidence sounder. Actually, an oblique-incidence sounder can also be used in conjunction with Figure 1 to obtain this information. It is assumed that this virtual height profile is the same throughout the ionospheric portion of the raypath in question. The range  $D$  may then be obtained by means of an alteration of the customary [e.g., Davies, 1969] transmission curve technique, based on Figure 1. The transmitter location is thus achieved, since the receiver location and orientation of the plane of propagation are known. Alternatively, the SSL process can be completely and simply computer-automated [Reilly, 1983a]. First, a digital file consisting of a finite number of points (e.g.,  $\geq 20$ ) along the virtual height profile is stored in computer memory. Some arbitrary guess is then made for the range  $D$ ,

Manuscript approved March 29, 1985.

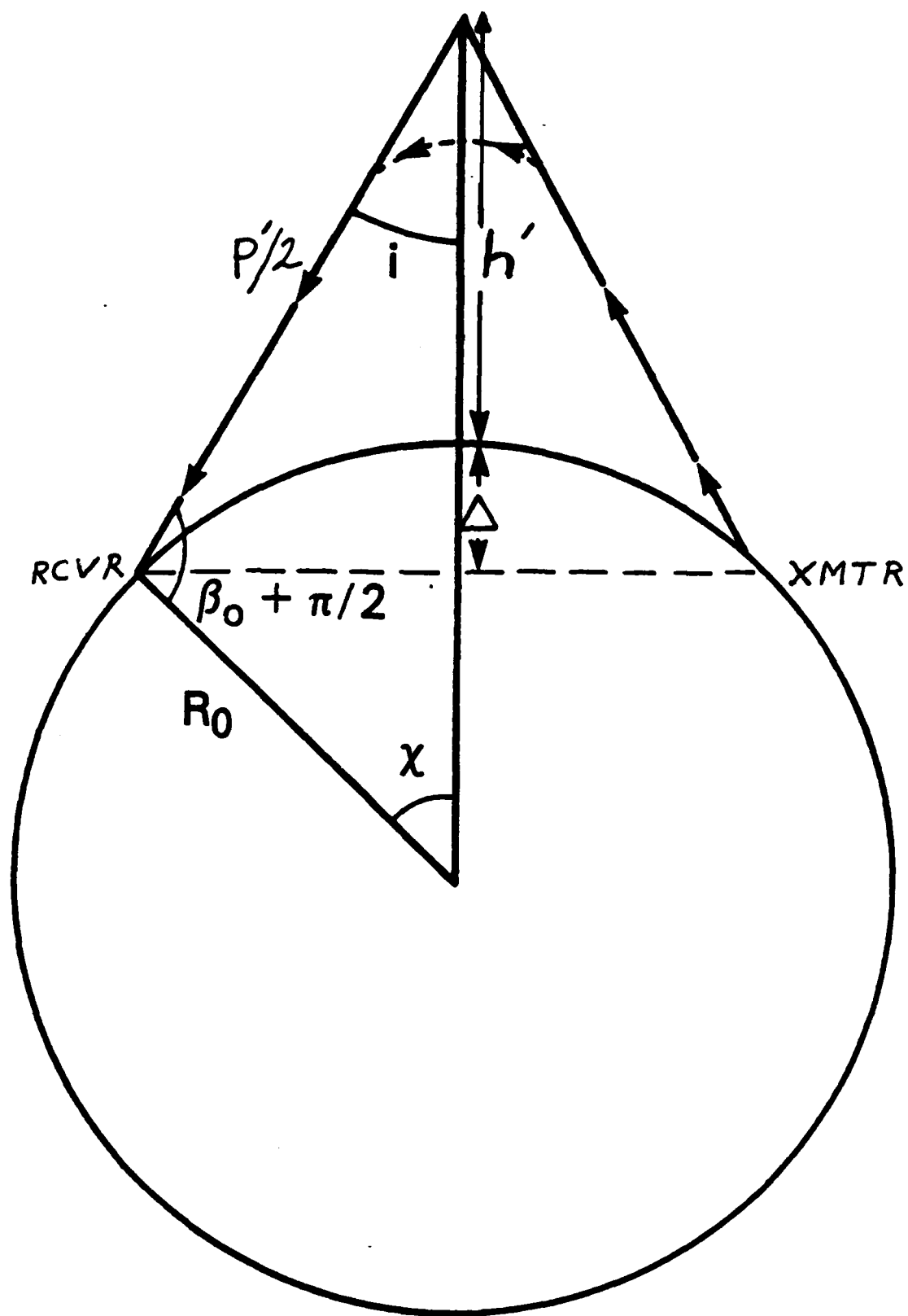


Fig. 1 — Geometrical model for group-path delay parameters

and this initiates computer iteration with the following algorithm, which is based on Figure 1 and Equations (1)-(3):

- (a) Calculate  $f_v$  from (1) and  $h'(f_v)$  from linear interpolation of the  $h'$  data file.

- (b) Determine  $P'/2$  from  

$$P'/2 = (h'(f_v) + \Delta) / \cos i$$

- (c) Obtain a new range from

$$X = \tan^{-1} \left[ \frac{(P'/2) \cos \beta_0}{R_0 + (P'/2) \sin \beta_0} \right]$$

- (d) Test for convergence on D. If the convergence criterion is satisfied, output the transmitter location. If not, go back to (a) and repeat.

It was found [Reilly, 1983a] that convergence was rapid and dependable, even in cases where the initial guess for D was grossly inaccurate.

By far, the most serious approximation of the preceding paragraph is the way that ionospheric assessment is handled. The ionosphere changes along the raypath, and the largest improvement in SSL will come from taking this into account properly. An opportunity for analysis of this problem comes from the SSL-BCT (Single Site Location Baseline Certification Test) sounder data in December, 1982. A network of oblique sounders was deployed, principally for purposes of frequency management; it is shown in Figure 2. Six oblique sounder paths (or "zones") are shown, associated with the receiver R at Fort Ord and the six transmitter positions T1-T6. An oblique ionogram can be converted into an ionospheric true height profile. Of course, the oblique sounder probes the ionosphere all along the sounder path, but it will be confirmed that the true height profile obtained characterizes the ionosphere near midpath. The midpath points X1-X6 for each sounder path are shown in Figure 2. It will also be shown how each true height profile solution can be accurately characterized by only a few parameters, nine in most cases. This enables economical bookkeeping of ionospheric density profile solutions throughout the day.

An oblique ionogram is obtained for each sounder path at fifteen minute intervals. This report processes all available oblique ionograms during an arbitrarily chosen time period which spans 1600 (UT) on December 6 to 0400 on December 7 (days 340 and 341). No oblique ionograms are available between 0400 and 1600 on either day. The period chosen includes most of the daylight hours (local time is eight hours earlier) and a few nighttime hours, during which ionospheric variation at points X1-X6 is thus obtained. Also available for comparison during this period is the data from four vertical incidence sounders, one at R in Figure 2 and three others at the positions given by the solid triangles in Figure 2. Details of the sounder positions are given in [Daehler, 1983]. It will be noticed, for example, that the DRS (Desert Research Station) vertical-incidence sounder position is very close to the midpath position for Path 4, and this is used to demonstrate that the true height profile solutions obtained from the oblique ionograms for Path 4 correspond to the ionosphere near the midpath, even when ionospheric tilts are observed.



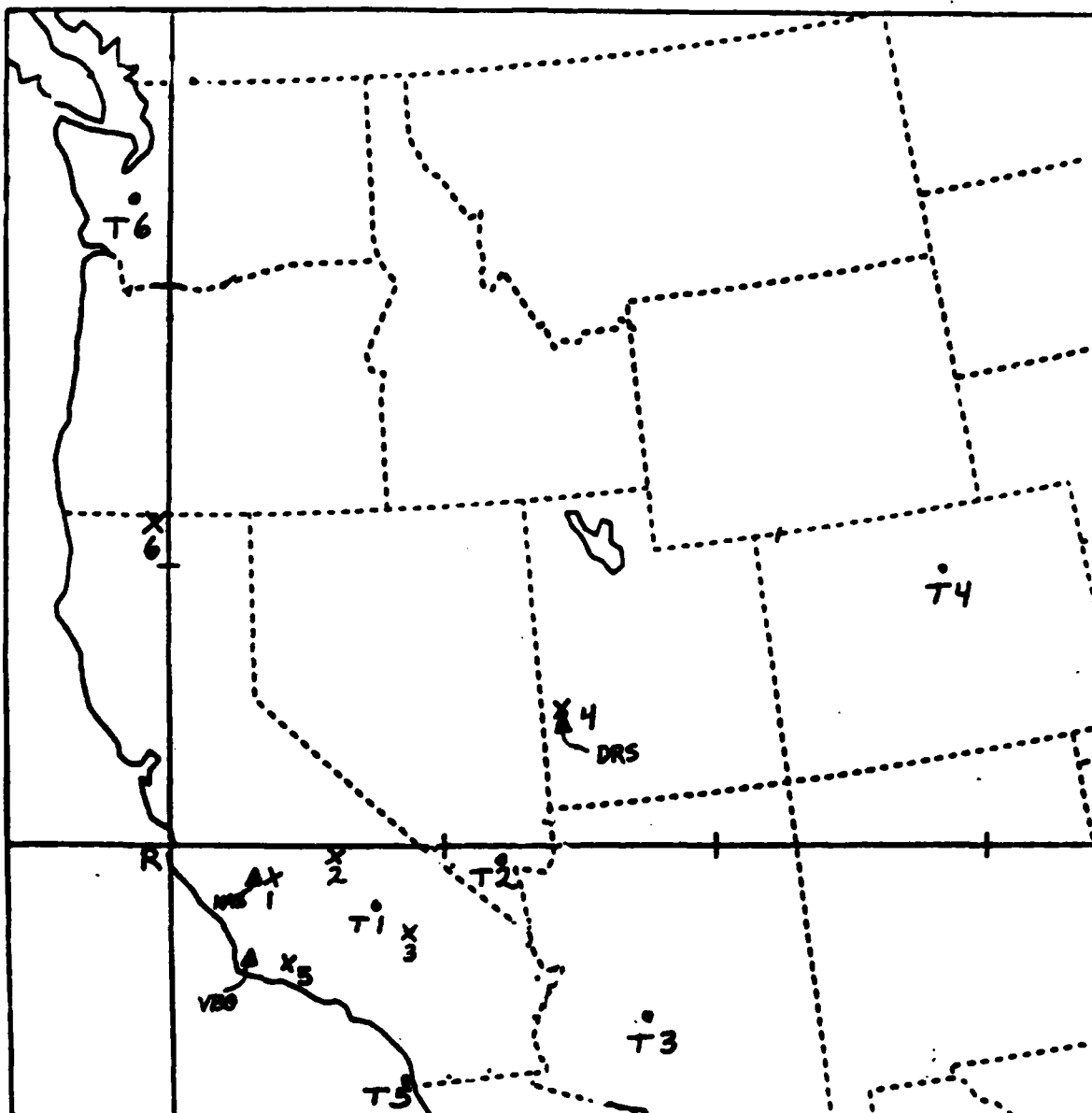


Fig. 2 — SSL-BCT Sounder network (December 1982)

The ionospheric density variation at each of the control points X1-X6 will be seen to be noisy, mainly due to the presence of travelling ionospheric disturbances, but the background variation with time will be seen to be reasonably smooth and predictable. Indeed, the variation of the ionospheric parameters, when plotted against the variation of the cosine of the solar zenith angle, will be seen to show a noisy variation about well-defined trend lines, which can be used to predict background ionospheric properties hours ahead at each of the points X1-X6. This will be useful for SSL if the information at these points can be interpolated to provide ionospheric information along unsounded paths. It will be seen that this is possible through straightforward manipulation of the trend line coefficients for each ionospheric parameter. The role of other ionospheric models will also be discussed in this context. Once the methodology for obtaining ionospheric properties along unsounded paths is developed, modifications for improved SSL techniques follow, and these are discussed. The results are discussed and future directions are indicated in the final section.

## 2. FROM OBLIQUE IONOGRAMS TO TRUE HEIGHT PROFILES

### 2A. The Basic Method

The method developed [Reilly, 1984a] to convert an oblique ionogram, which shows pulse time of transit between transmitter and receiver vs. wave frequency, to a true height profile, which is height vs. plasma frequency squared (proportional to electron density), is partially based on a generalization of the Breit-Tuве theorem. It compares favorably with all other known methods for obtaining true height profiles from oblique ionograms. It employs the usual simplifications, which are common to all these methods:

- (a) absolute values of group path delay times are known, or can be found,
- (b) the ionosphere is spherically symmetric (no tilts), and (c) magnetic field effects are negligible.

Figure 3 shows a typical oblique ionogram and a sketch of a few raypaths by which a pulse can propagate from transmitter to receiver. One-hop (i.e., involving one ionospheric reflection) low- and high-ray modes are shown, as well as a two-hop mode. The ionogram is a plot of relative time delay vs. frequency, since time synchronization between receiver and transmitter is typically, as here, not sufficiently accurate to obtain absolute time delays. The ionogram in Figure 3 shows a weak one-hop E layer mode in the portion of the trace just below 2 msec time delay, a one-hop F mode just above 2 msec, and a two-hop F mode which starts near 3 msec. In order to convert relative time delays to absolute time delays, an assumption is made about the height of the bottom of the E layer, which is associated with the zero-frequency time delay of the one-hop E mode. In most cases this height is assumed to be at 90 km, although in the nighttime case, with sporadic E evident, this value is frequently changed to 100 km. It will be seen that simplification (a) above can thus be sufficiently well justified.

The simplification (b) above can be regarded as the first step of an iterative process in which ionospheric density profiles are inferred at the various sounder control points, ionospheric tilts are inferred from this information, and then ionograms are reduced from this tilt information in a hypothetical second iteration. It will, however, be argued that the ionograms really represent the effect of the ionospheres near the midpath points in the presence of actual tilts, and that simplification (b) is therefore sufficiently justified for our purposes. In other words, the ionogram wouldn't change very much if the midpath ionosphere replaced the actual one throughout the sounder path.

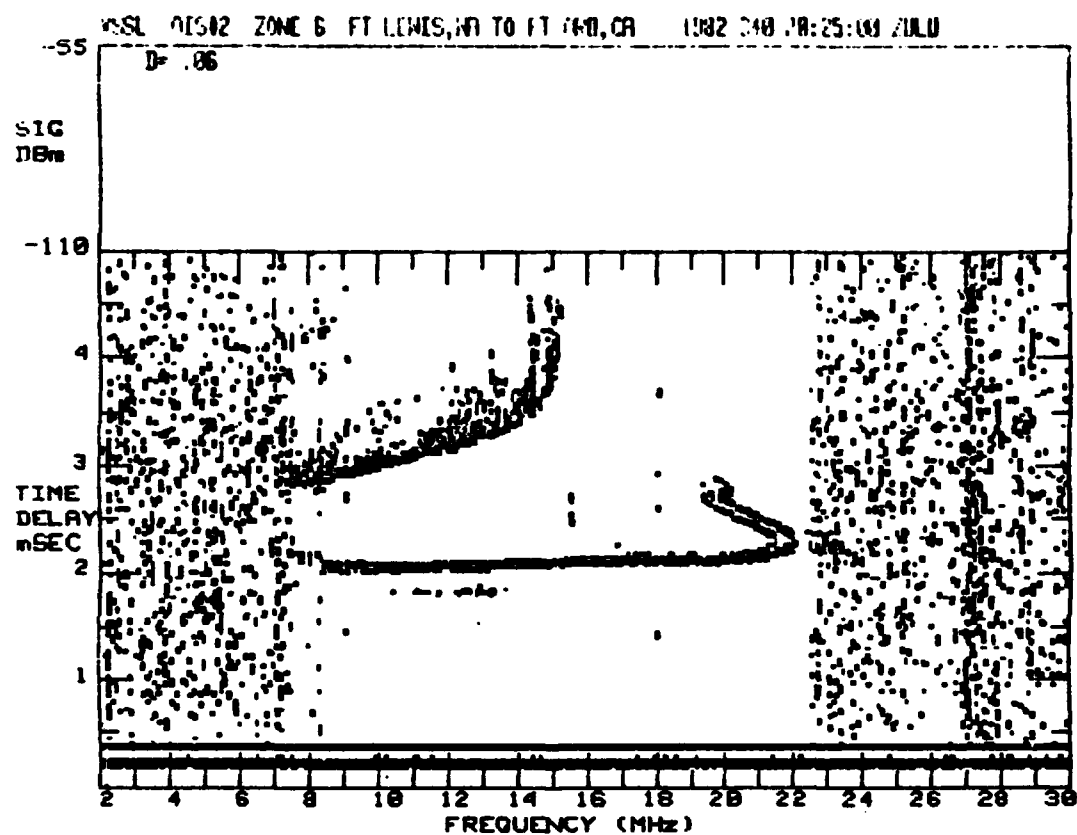
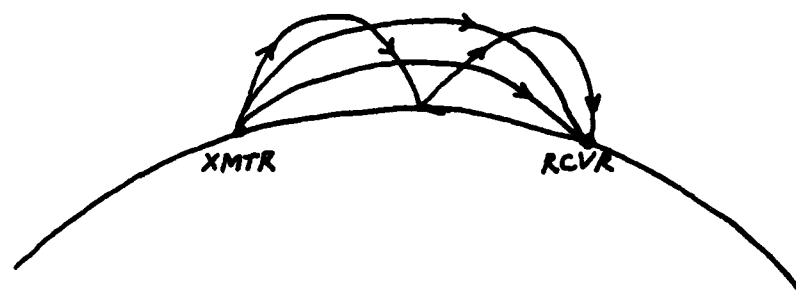


Fig. 3 — Sketch of some raypaths and an actual ionogram

Simplification (c) is justified for oblique ionograms, where magnetic field effects only amount to a relatively small splitting of the trace in the vicinity of the MUF and up into the high-ray portion of the trace. This is seen in Figure 3. It is satisfactory to estimate the no-field trace values by choosing points about halfway between the split ordinary mode and extraordinary mode traces [Kopka and Moller, 1968].

The procedure adopted to process ionograms, such as the one in Figure 3 from the SSL-BCT [Daehler, 1983], is to first identify the one-hop modes, and then enter coordinates sequentially from the one-hop trace into a BASIC language computer program, written for the Tektronix 4052 microcomputer. The interface between the ionogram and the program is a Tektronix 4956 Graphics Tablet Digitizer. The one-hop trace starts at the bottom of the E layer (estimated at  $f=0$ ) and advances up in reflection height to the topmost observed portion of the F layer. As in Figure 3, the trace is typically discontinuous, showing a portion of the E layer low-ray trace (e.g., below the E MUF), a portion of the F layer low-ray trace, and ending after a relatively small portion of the F layer high-ray trace (e.g., above the F MUF). As points are entered from the one-hop trace, the program automatically obtains true height profile solutions. The ionospheric density profile is thus built up from the bottom. Details of the method are contained in [Reilly, 1984a]. Examples will be shown below.

## 2B. Idealized True Height Profile Fit

It is convenient to define a model density profile, as shown in Figure 4. It is composed of a series of segments, in each of which  $R^2 f_N^2$  varies either linearly or quadratically with  $R$ , where  $R$  is the radial distance from the center of the earth. The height  $h$  is found by subtracting the radius of the earth from  $R$ . A dependence of this form, i.e.,

$$R^2 f_N^2 = AR^2 + BR + C \quad , \quad (4)$$

where  $A$ ,  $B$ , and  $C$  are constants, enables the integrals for group path delay and range to be evaluated in closed form [Reilly, 1983a], and this has been found convenient for, e.g., the computation of vertical and oblique ionograms. The idealized profile in Figure 4 consists of a linear segment for the E region, a linear segment for the E-F transition region, a linear segment for the lower part of the F region, and a parabolic segment for the upper part of the F region up to the F layer maximum. Note that the segments of  $R^2 f_N^2$  are linear or parabolic, but the segments of  $f_N^2$  also appear linear or parabolic, as in Figure 4, because  $R$  is nearly constant in the altitude range shown. The profile is specified by nine parameters, the five height parameters  $h_bE$ ,  $h_mE$ ,  $h_bF$ ,  $h_mF1$ , and  $h_mF2$ , and four density parameters  $f_oE^2$ ,  $f_bF^2$ ,  $f_oF1^2$ , and  $f_oF2^2$ . The semi-thickness parameter  $Y2$  for the parabolic layer is redundant. These are suggestive labels only, not necessarily having their usual ionospheric significance. For example, the E layer maximum is not to be found at  $(f_oE^2, h_mE)$ , nor does  $(f_oF1^2, h_mF1)$  necessarily give the coordinates of the F1 layer maximum. Instead, these parameters are manipulated by the computer program to give the best least-squares fit of the idealized profile in Figure 4 to the computed true height profile. The latter is defined by the set of calculated solution points, which are interpolated by segments in each of which the dependence of  $R^2 f_N^2$  on  $R^2$  is linear [Reilly, 1984a]. Indeed, the fit of the idealized profile is so good that the calculated true height profile is well specified by these nine parameters.

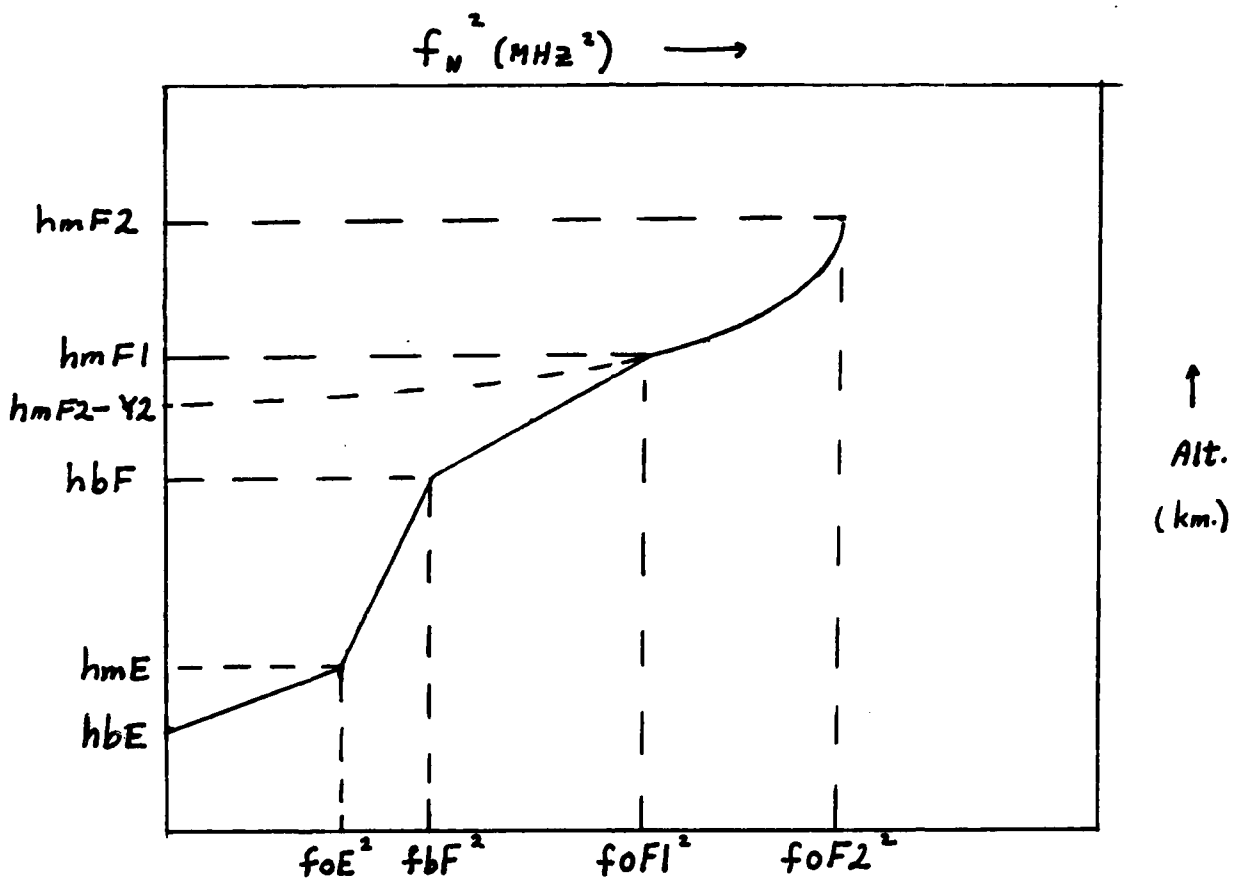


Fig. 4 — Idealized 9-parameter true height profile

The variation of  $g = R^2 f_N^2$  in each of the linear segments of the idealized profile, in which  $g$  varies from  $g_1$  to  $g_2$  as  $h$  varies from  $h_1$  to  $h_2$ , is

$$g = g_1 + \frac{g_2 - g_1}{h_2 - h_1} (h - h_1) \quad (\text{linear}) \quad (5)$$

The variation in the parabolic segment, in which  $g$  varies from  $g_{OF1}$  to  $g_{OF2}$  as  $h$  varies from  $h_{mF1}$  to  $h_{mF2}$ , is

$$g = g_{OF2} \left[ 1 - \left( \frac{h_{mF2} - h}{h_{mF2} - h_{mF1}} \right)^2 \left( 1 - \frac{g_{OF1}}{g_{OF2}} \right) \right] \quad (\text{parabolic}) \quad (6)$$

An example of the computer solution process is shown in Figures 5-7. One-hop trace points are fed into the computer program from the ionogram of Figure 3, and the resulting true height profile solution points are shown by the pluses in Figure 5, connected by solid lines. The program would generate a monotonically increasing profile ( $f_N^2$  increasing uniformly with altitude), except for the presence of a reentrant procedure [Reilly, 1984a], which may be summarized as follows. Whenever (except in the E layer) three adjacent monotonic solution points,  $n-1$ ,  $n$ , and  $n+1$ , are such that the segment between  $n$  and  $n+1$  solution points has a slope  $d(R^2 f_N^2)/dR^2$  twenty percent greater than that for the segment between points  $n-1$  and  $n$ , the reentrant procedure is initiated. A new reentrant point is inserted after point  $n-1$ , placed on the line upward from  $n-1$  with slope  $dh/df_N^2 = -12.5 \text{ km/MHz}^2$  at an altitude such that the segment from this reentrant point to the recomputed solution point  $n$  has the same slope as the segment from  $n$  to the recomputed solution point  $n+1$ . If and when this condition is satisfied, the new point and the latter two points are redefined as points  $n$ ,  $n+1$ , and  $n+2$  in the solution set. The solution procedure then continues on to the next point of the one-hop trace. Evidently, the reentrant procedure was carried out several times in Figure 5 between the E and F layers.

After the last point on the one-hop trace has been converted to a true height profile solution point, the program finds the best parabolic least-squares fit of the last five solution points and determines the F2 peak parameters ( $f_{OF2}^2$ ,  $h_{mF2}$ ) from this parabola. The extrapolation of the parabola upward and backward from the last solution point is shown by the dotted line in Figure 5.

The program next accepts user input for the designation of ( $h_{mE}$ ,  $f_{OE}^2$ ) as one of the solution points (J) and an initial guess for the parameters  $h_bF$  and  $h_{mF1}$  ( $H1$  and  $H2$ ). The parameters  $h_bF$ ,  $h_{mF1}$ ,  $f_{bF}^2$ , and  $f_{OF1}^2$  are then determined by the program in an iterative procedure which finds the best least-squares fit, consistent with continuity requirements, of the calculated true height profile by the idealized profile between the ( $h_{mE}$ ,  $f_{OE}^2$ ) solution point and the fifth to last solution point. Beyond this latter point the idealized solution is the aforementioned parabolic fit. The resulting best idealized fit is shown by the dotted line in Figure 6. It is good enough to characterize the calculated true height profile, which is thus equivalent to the nine parameters given in Figure 7 ( $Y2$  is redundant). This is a great bookkeeping simplification.

ENTER J FOR F0E12: 2  
 MAKE INITIAL GUESS FOR H1 AND H2: 210,220

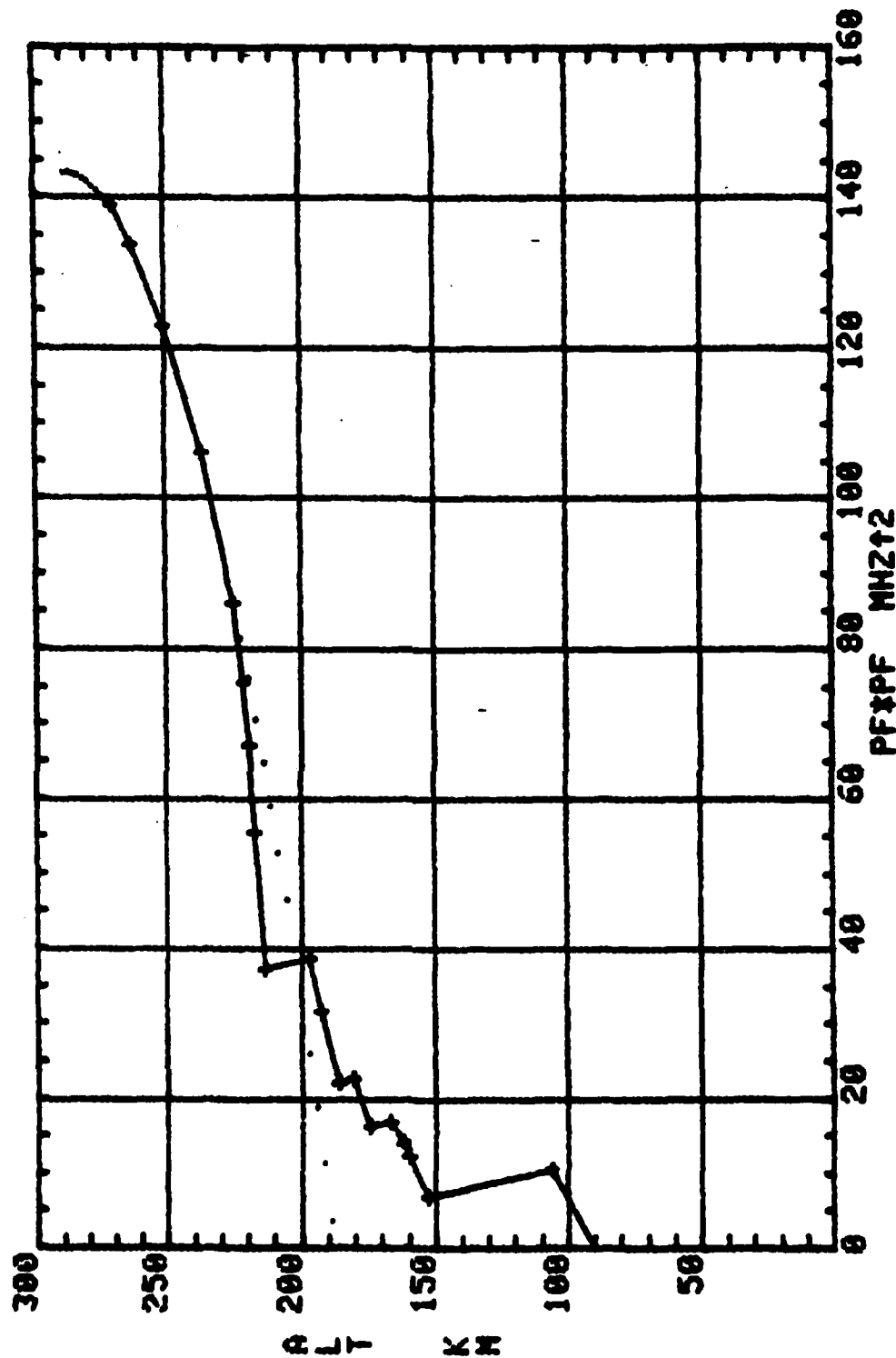


Fig. 5 — Calculated true height profile points (pulses) and best quadratic least squares fit to last five points (dotted)

# TRUE HEIGHT US. DENSITY

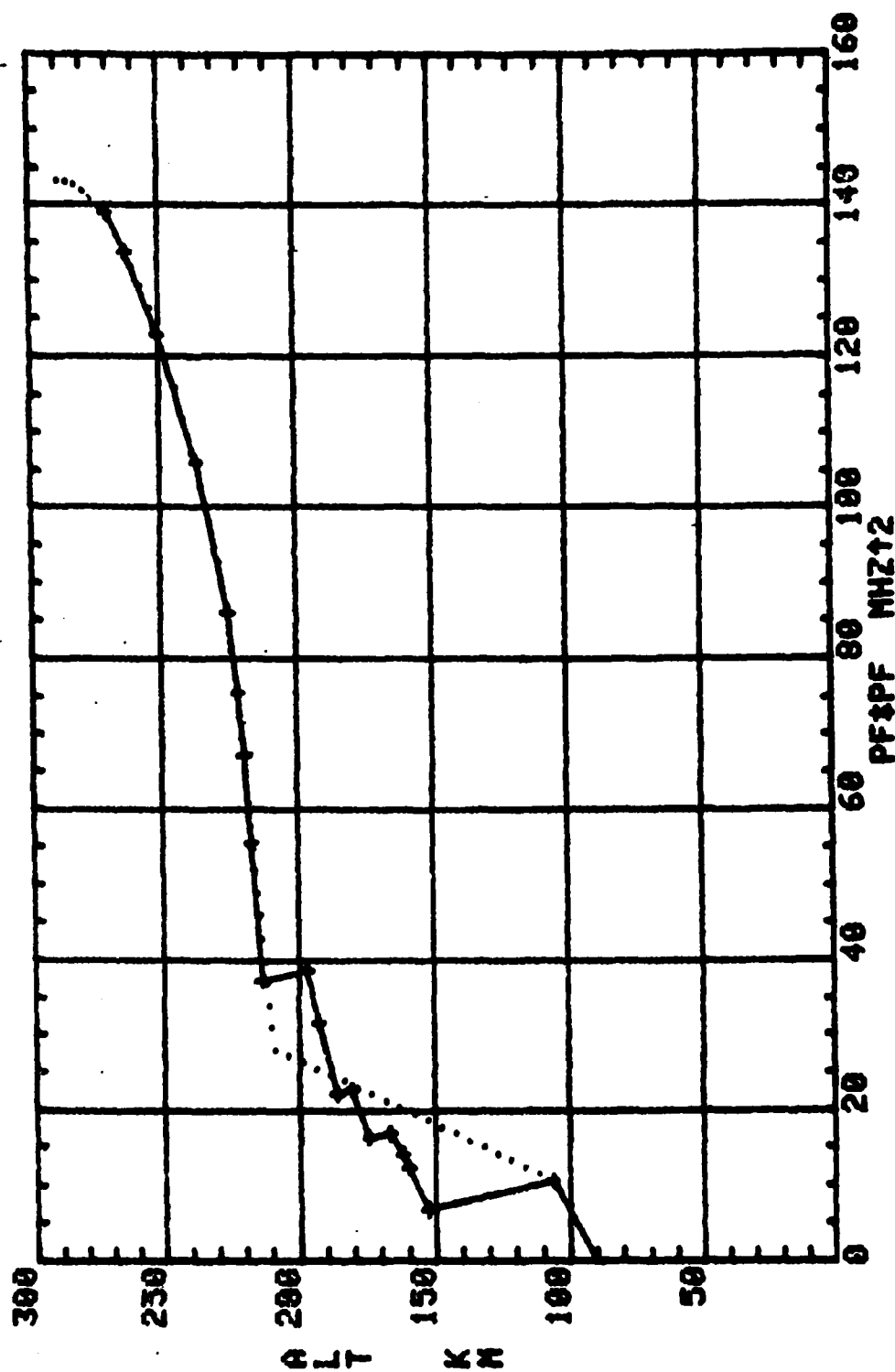


Fig. 6 — Calculated profile and best least squares fit of idealized profile (dotted)



# NINE-PARAMETER DESIGNATION

HME = 106.210862414 F0E12 = 10.5650837647  
HBF = 209.265239234 FBF12 = 27.994811256  
HMF1 = 225.308856277 F0F112 = 87.1362447645  
HMF2 = 288.392689049 F0F212 = 143.335125249 Y2 = 100.746636254  
HBE = 90

Fig. 7 -- Output of 9 parameters for idealized profile fit

It appears that the user can almost entirely be eliminated from the solution process, as follows. The one-hop trace can be downloaded to the computer program from the sounder as a digital file. This would make it unnecessary for a user to march up the one-hop trace of the ionogram with his digitizing device. The solution point (J) for  $(h_m E, f_o E^2)$  in Figure 5 could be determined by the computer as the point just before the first reentrant point or the last point below  $h=130$  km, whichever comes first (recall that the reentrant procedure is not permitted until one-hop trace points in the F layer are processed). The initial guess for  $h_b F$  and  $h_m F_1$  in Figure 5 could be made by the computer as the last reentrant point height and a value 10 km less than the fifth to last solution point height, respectively. These and other steps make the prospects bright for complete computer automation for the vast majority of ionograms encountered.

A condition can occur, especially at nighttime, when eleven parameters are suitable to describe the true height profile solution. In this case, the trial altitude of the first reentrant point advances so far up the line with slope  $-1/2.5 \text{ km/MHz}^2$  that it reaches the  $f_y^2=0$  axis before the reentrant condition is satisfied. This point of intersection with the axis becomes the definition of  $(f_o E^2, h_m E)$ . From here, the trial reentrant point advances up the axis to a point such that the computed slopes of the next two segments are equal, which is the reentrant condition. The fit of idealized profile to the calculated true height profile proceeds as before. An example of this is shown in the true height profile solution of Figure 8. Two new parameters are defined to characterize the true height profile, i.e.,  $h_s E$  and  $f_s E^2$ . These and the other parameters are indicated in Figure 8. Although eleven are shown, there are really ten independent parameters in our present procedure, since, for example,  $h_s E$  is determined from  $f_s E^2$ ,  $h_m E$ ,  $f_o E^2$ , and the fixed slope value  $-1/2.5$  for the reentrant segments. The value of this slope for the first reentrant point might at some future time be made flexible. The best fit in Figure 8 was obtained by the computer for  $f_b F^2=0$ , although this is not always the case.

The procedure for nighttime ionograms, such as the one which yielded Figure 8, which shows a sporadic E layer, will be to input a point on the one-hop E layer trace a small distance out from the  $f_y^2=0$  axis, and then proceed up to the F layer part of the one-hop trace. This defines a small, token E layer, as in Figure 8, which has no significant effect on the calculated F layer solutions.

There will be a few instances in which the first reentrant point in Figure 8 will occur close to, but not on the  $f_y^2=0$  axis. Then the eleven-parameter fit of the type of Figure 8, except that  $f_o E^2$  is not zero, is appropriate to describe the calculated true height profile.

## 2C. SSL-BCT Prototype Calculations

The purpose of this section is to test the solution procedure for obtaining true height profiles on known cases, which resemble the conditions of the SSL-BCT. From the known sounder geometry in Figure 2 [Daehler, 1983] it is found that the transmitter-receiver separation ranges for Paths 1,2,--,6 are 385.3, 601.0, 918.3, 1501.9, 600.5, and 1168.3 km., respectively. Known-case, one-hop oblique ionograms are calculated from the prototype daytime profile in Figures 9 and 10 for the five distinct ranges from the preceding list. In these figures the variation of  $R^2 f_y^2$  with radius  $R$  is parabolic in the E layer from  $h=h_b E$ , past its maximum at  $(f_o E^2, h_m E)$ , to the point  $h$  where  $R^2 f_y^2 = R_m E^2 f_o E^2 X_v^2$ . The linear E-F transition region starts here and ends at  $(f_b F^2, h_b F)$ . The next linear segment for the lower part of the F layer proceeds from here to  $(f_o F_1^2,$

# TRUE HEIGHT VS. DENSITY

Path (Zone) 6, Day 341, 03:10:12 Zulu

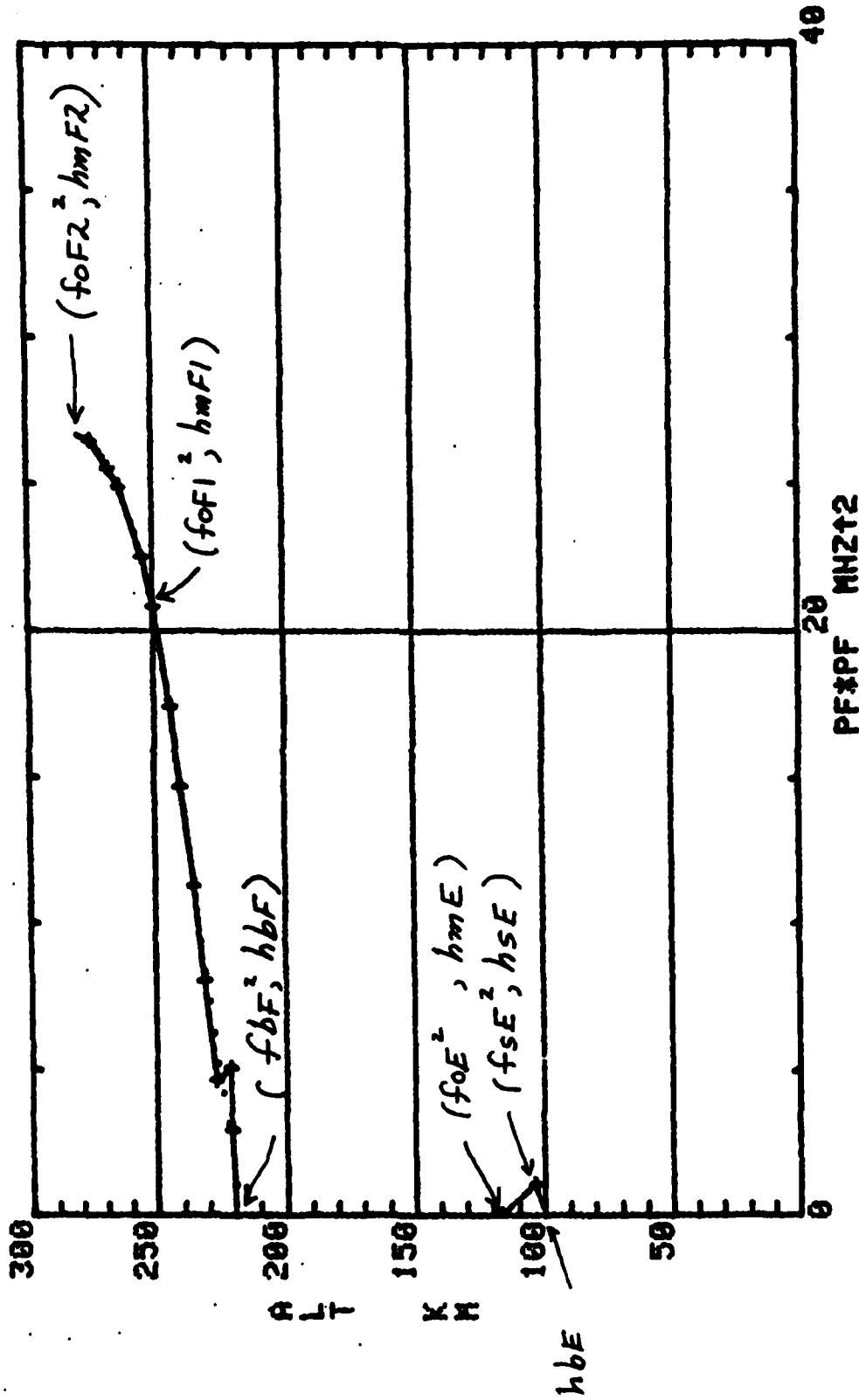


Fig. 8 — Example of the 11-parameter idealized profile fit (dotted) to the calculated true height profile

```

RUN
LIST OF IONOSPHERIC PARAMETERS - H IN KM., Ft2 IN MHZt2
H8E,HYE,F0Et2: 90,110,12.5
H8F,FBFt2: 190,20
HMF1,F0F1t2: 210,80
HMF2,F0F2t2: 290,155
ENTER 1-9PE, 2-9PC, 3-9PPE, 4-11PE, 5-11PC: 3
INPUT TRANSITION PARAMETER XV: .98

```

```

COEFF. IN (R*FN)t2=A*Rt2+B*R+C
HL(KM) HU A(Ft2) B(Ft2*L) C((F*L)t2)
0.0000 90.0000 0.00000000E+000 0.00000000E+000 0.00000000E+000
90.0000 114.0549-1.30458454E+006 1.691070874E+010-5.480084273E+013
114.0549 190.0000 0.00000000E+000 4.696883726E+006-2.905620659E+010
190.0000 210.0000 0.00000000E+000 1.301994283E+008-8.534035022E+011
210.0000 292.0000-5.332219169E+005 7.103795665E+009-2.365302425E+013

```

Fig. 9 - List of profile parameters, coefficients, and associated altitude interval end points for the model profile in Figure 10

# IONOSPHERIC TRUE HEIGHT PROFILE

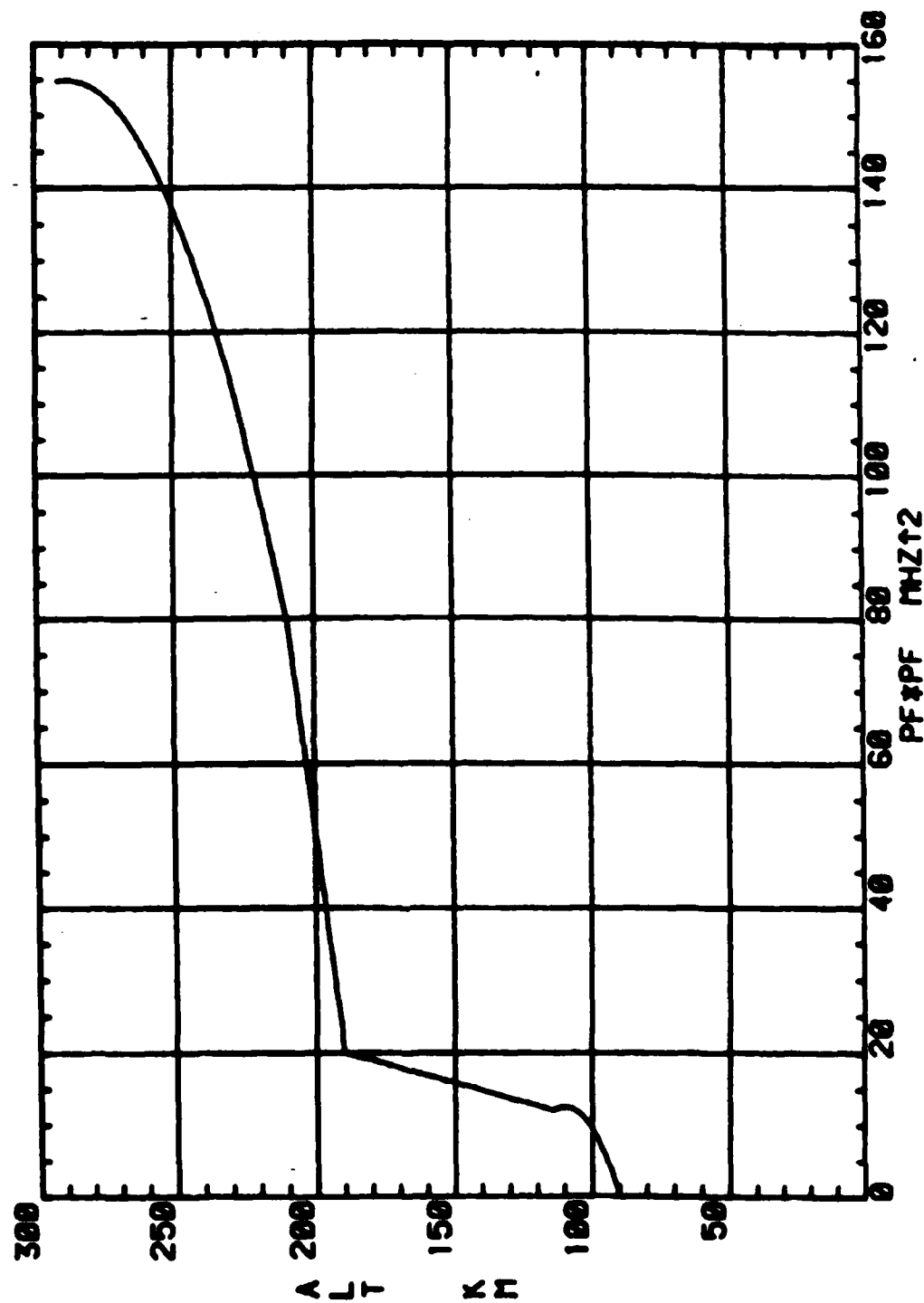


Fig. 10 — Model profile for the SSL-BCT prototype calculations

hmF1), and the parabolic F2 region extends from here to just past its maximum at ( $f_oF2^2$ , hmF2). These parameters for the profile in Figure 10 are given in Figure 9, as are the coefficients in Eq. (4) for the associated five segments, starting with the ground up to the bottom of the E-layer.  $R$  is in units of km, with the earth's radius being 6371.2 km. This profile is similar to that defined in Figure 4 for the idealized profile fit, except that the E layer is linear there.

Figure 11 depicts the vertical ionogram associated with the given density profile, and the next ten figures (12-21) show the calculated one-hop oblique ionograms for five distinct ranges from the above SSL-BCT list. These ionograms can be regarded as exact, since they are based on an exact evaluation of the associated group path and range integrals, made possible by the form of Eq. (4). Each range value is associated with a pair of figures, the first of which gives the reflection heights and elevation angles for a set of points on the one-hop trace. The second one shows circled points which one might at random attempt to digitize on an actual ionogram for input to the computer program which finds the true height profile solution. The only part of the one-hop trace that shows up in a typical ionogram is a portion of the low-ray E layer (below the E MUF), most of the low-ray F layer, and a fairly small portion of the high-ray F layer (above the F MUF). The circled points shown are located on these portions of the trace.

The true height profile solution program has been tested on the oblique ionograms in Figures 13,15,17,19, and 21. Two methods are employed. In one method the calculated values of absolute time delay vs. frequency for the circled ionogram points are stored in a data file. These one-hop trace values are read sequentially by the program, which generates the corresponding true height profile solution values. The other method, which is used for a measured ionogram, requires an initial specification of  $h_bE$ , which is used to convert the observed relative time delays to absolute time delays. The ionogram is interfaced with the computer program through a magnetic wire grid tablet device, on which the ionogram is laid. A cross-hairs device is advanced up the one-hop trace, and values of relative time delay vs. frequency are thus digitized for input to the computer program, which converts relative time delays to absolute time delays and generates the true height profile solution. The technique for carrying out the second method has been varied and compared with the first method, and the results of this experimentation are given in Table 1. It is seen that the solution process has been carried out independently forty times on the five ionograms. Each solution is characterized by nine parameters, as discussed in Section 2B. Of course, it is difficult to visualize the results from Table 1, and so each of the forty cases is also plotted in Appendix K, where the calculated 9-parameter true height profile of Table 1 is depicted by the x-marks, and the exact model profile of Figure 10 is shown by the solid line for comparison.

Each nine-parameter result in Table 1 is followed by a short description of the points included for processing from the one-hop ionogram trace. In most cases the circled points in Figures 13,15,17,19, and 21 are the ones processed. These involve only the low-ray portion of the E layer, in keeping with typical data. Inspection of Appendix K shows that the E layer is thus clipped near its peak. Inclusion of high-ray E layer points improves the E layer peak description somewhat (cf. Nos. 8,10,11,25, and 33 in Table 1), but the F layer solution is fortunately insensitive to this. In the tablet mode of operation,  $h_bE$  is an input parameter. In practice it is usually estimated to be 90 km for daytime ionograms and 100 km for nighttime ionograms, when sporadic E conditions are evident. The effect of varying  $h_bE$  in Nos.

# VERTICAL IONOGRAM

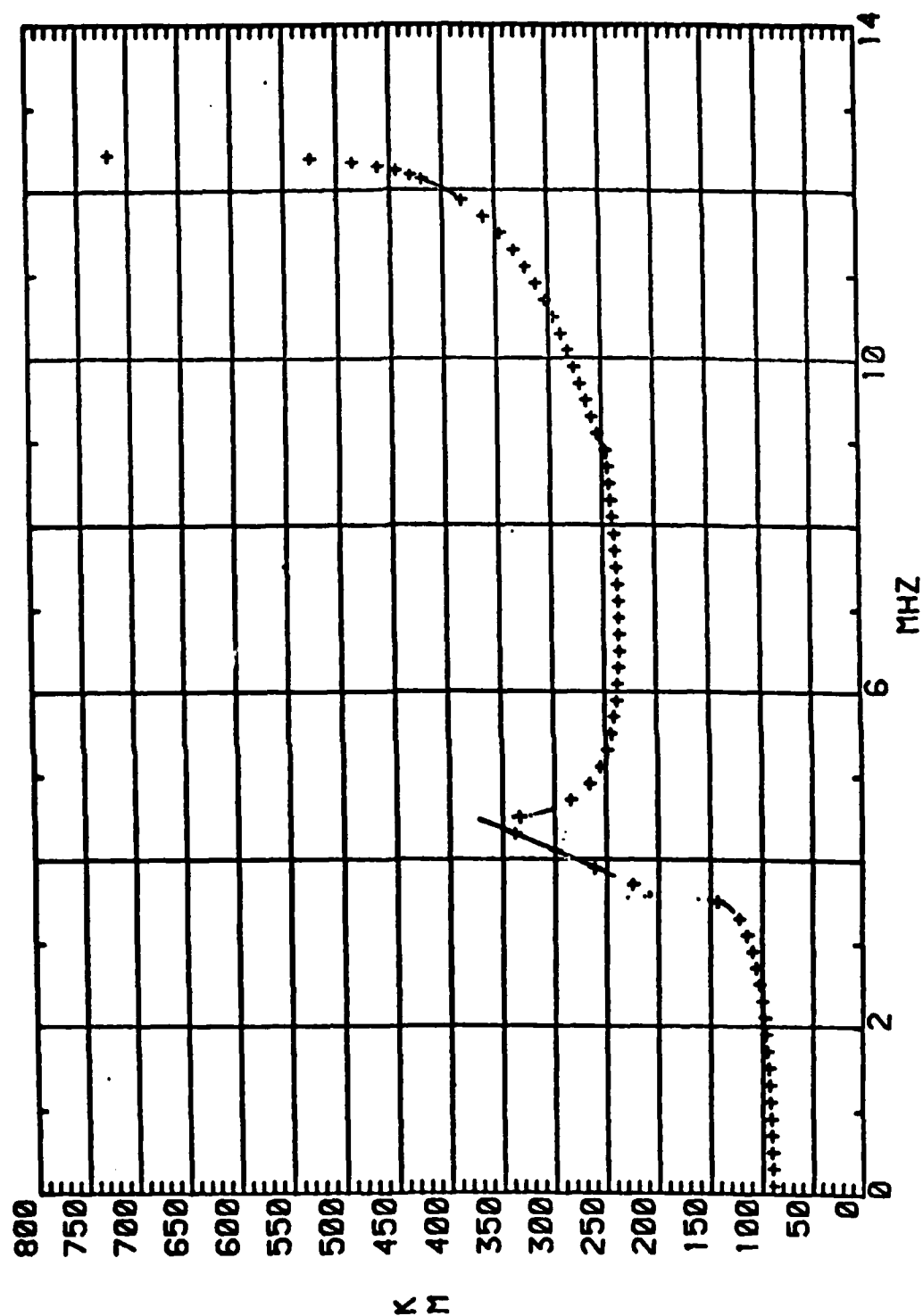


Fig. 11 - SSL-BCT prototype one-hop ionogram

OBLIQUE IONOGRAM  
RANGE = 385.3 KM

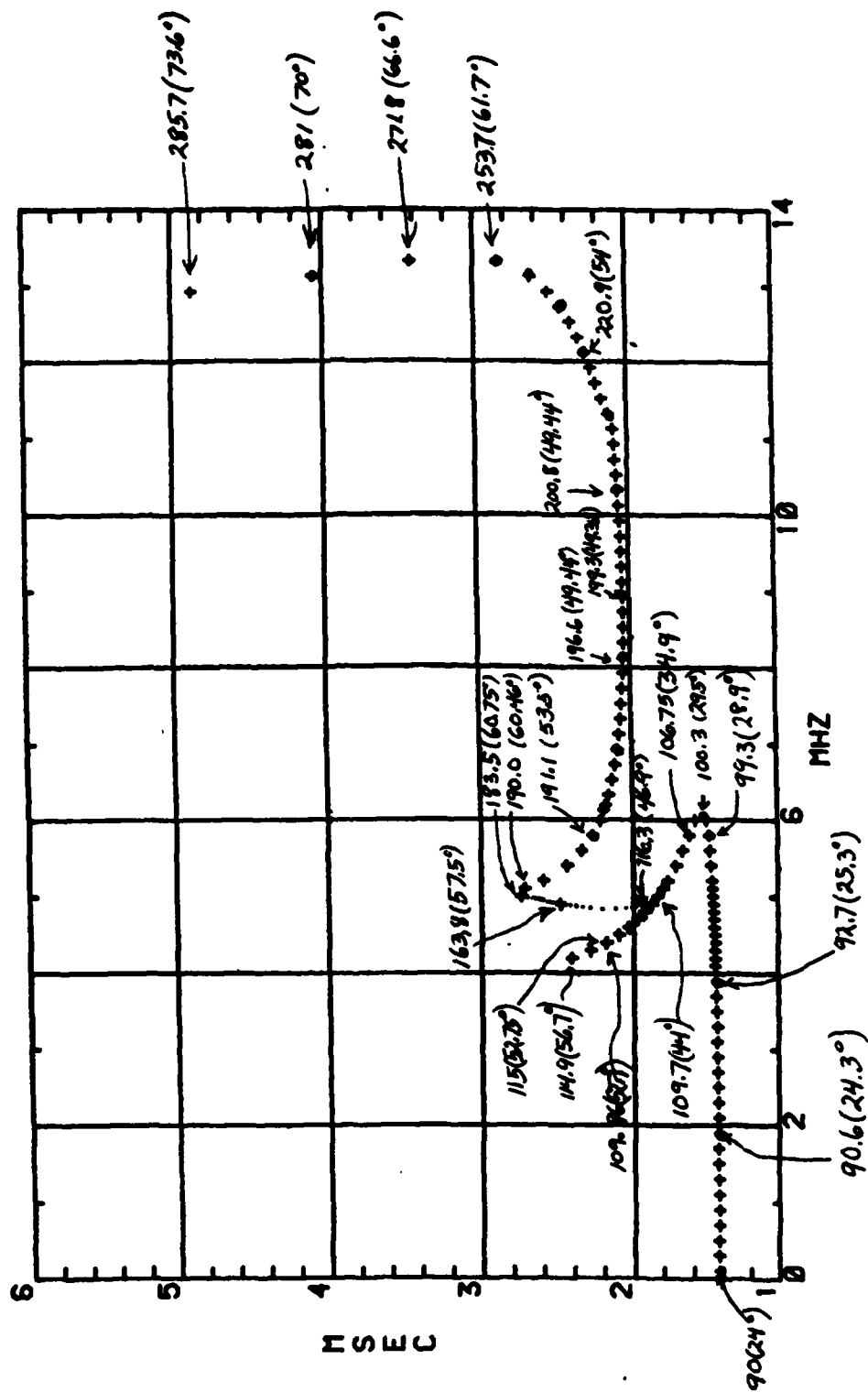


Fig. 12 - SSL-BCT prototype one-hop ionogram



One-hop trace  
 OBLIQUE IONOGRAM  
 RANGE = 385.3 KM  
 (Zone 1)

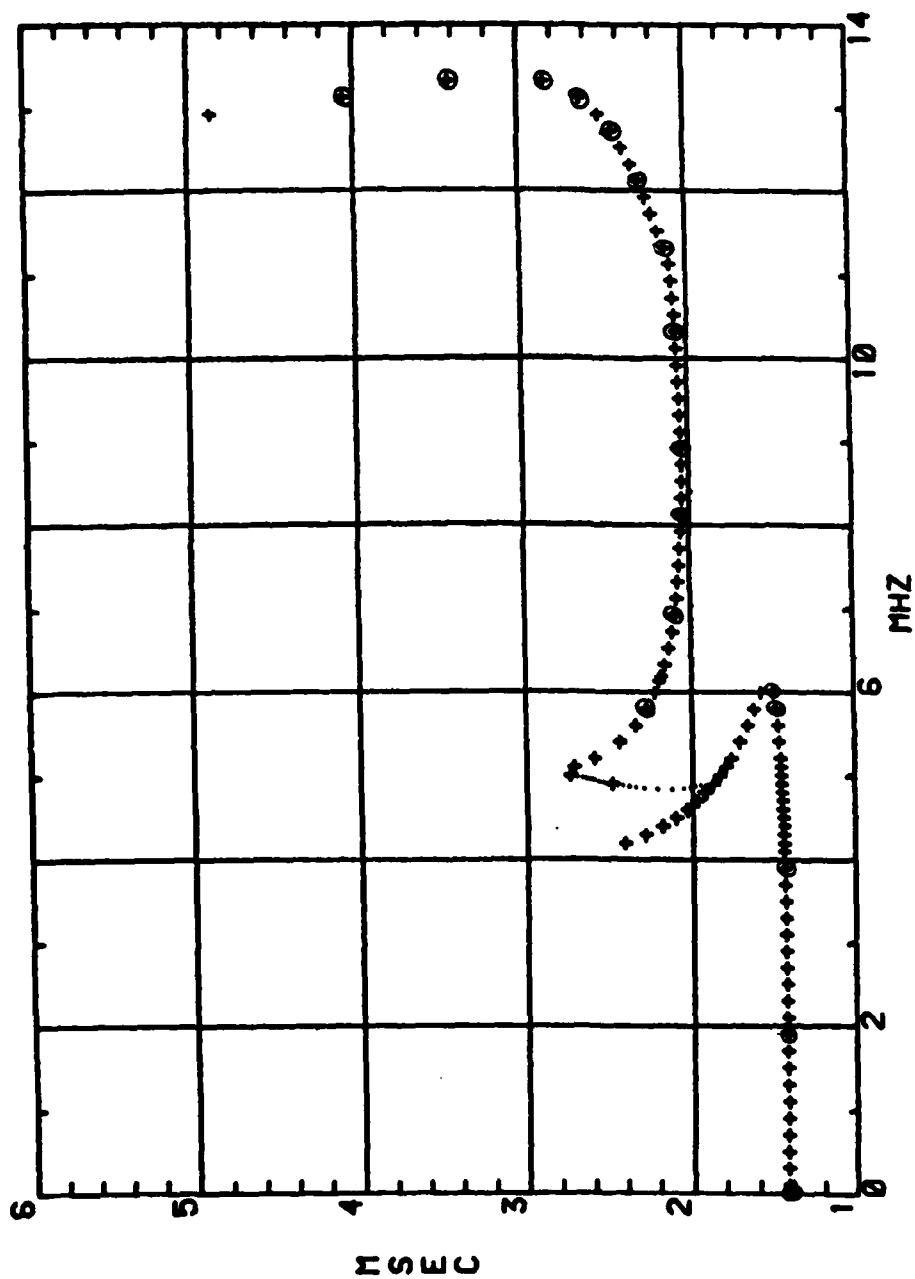


Fig. 13 - SSL-BCT prototype one-hop ionogram

One-hop trace  
OBLIQUE IONOGRAM  
RANGE = 601 KM

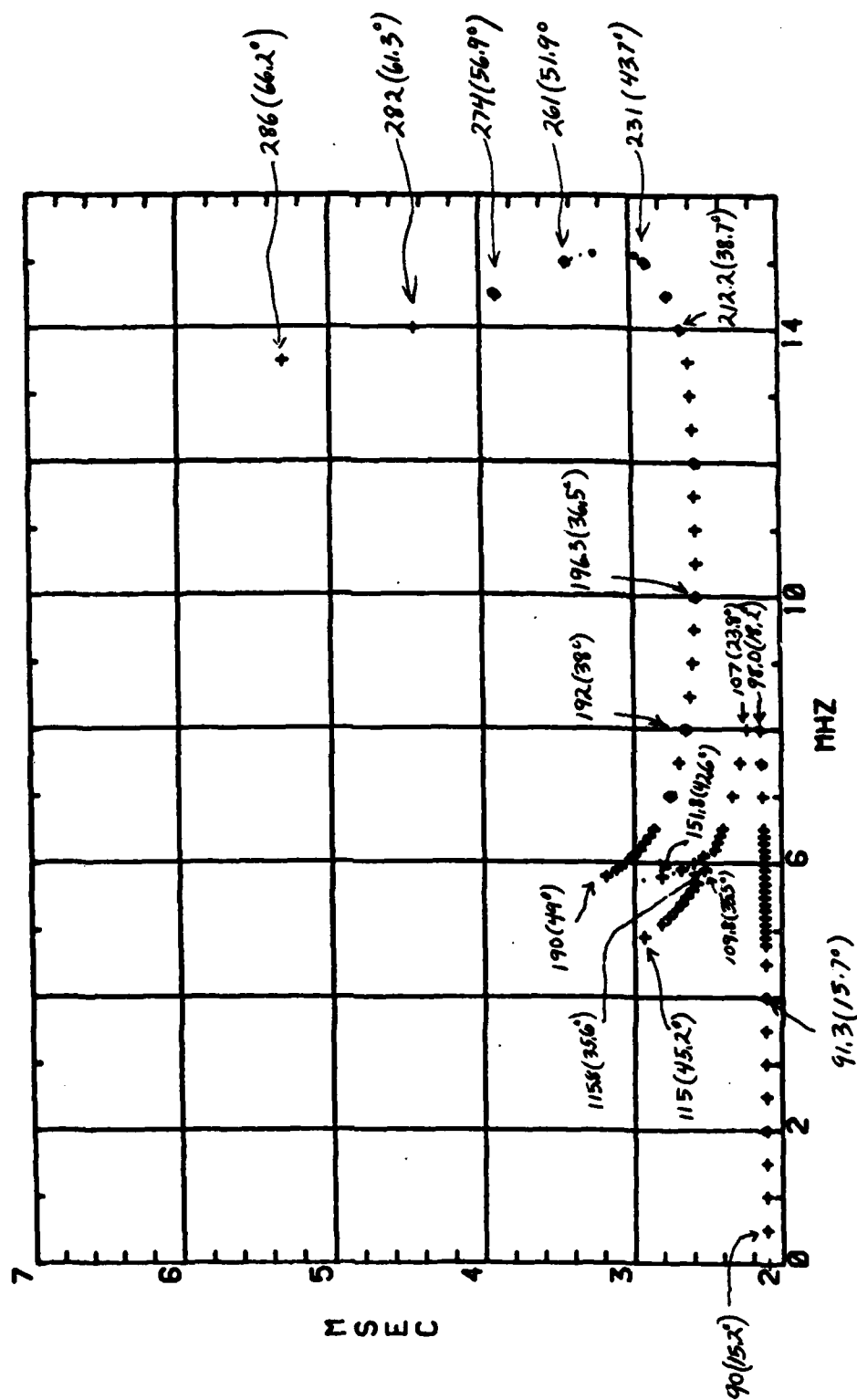
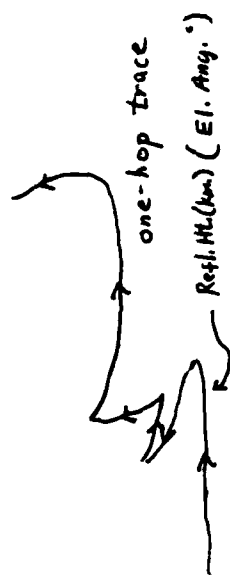


Fig. 14 — SSL-BCT prototype one-hop ionogram

One-hop trace  
 OBLIQUE IONOGRAM  
 RANGE = 601 KM  
 (Zones 2,5)

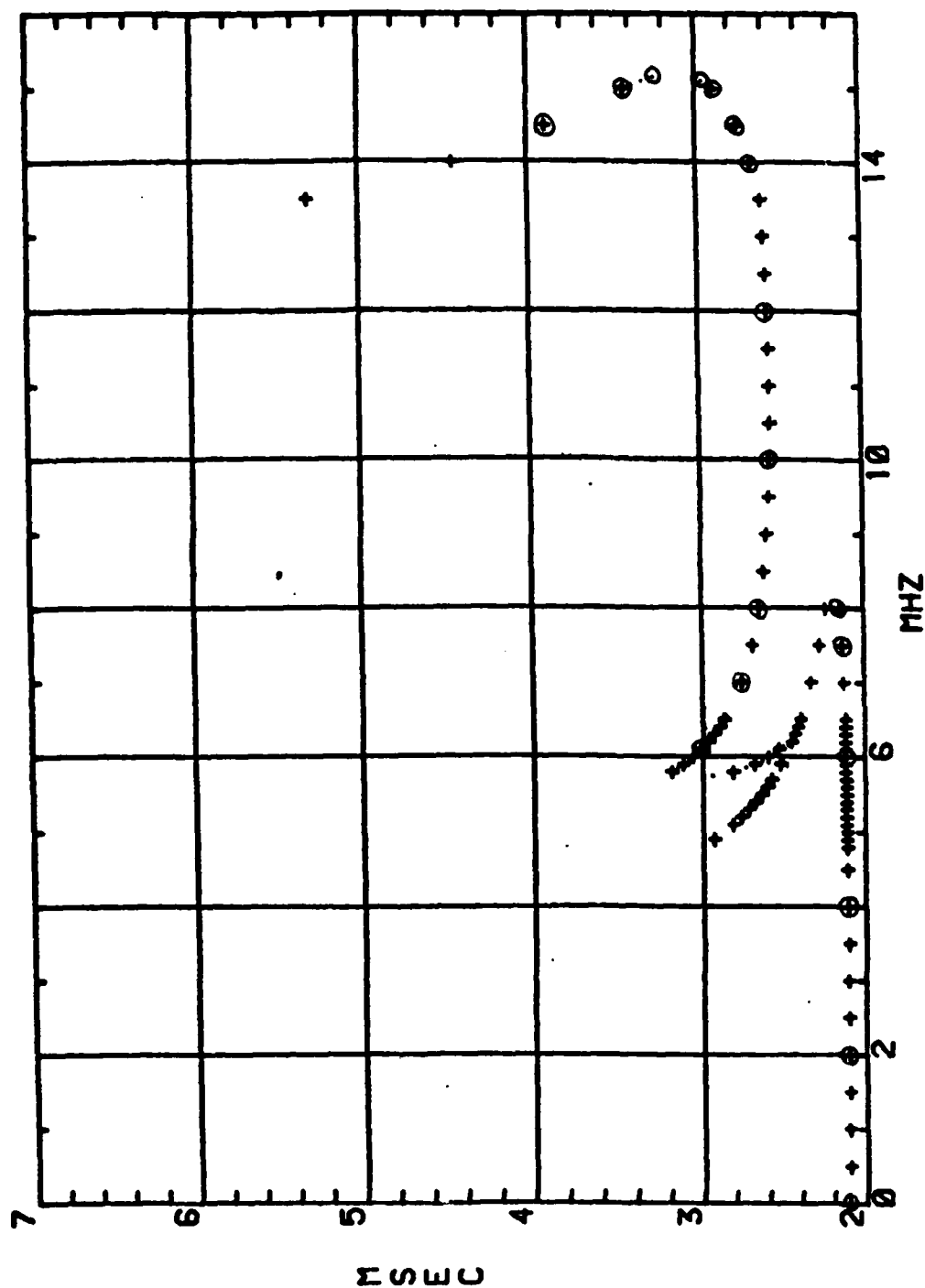
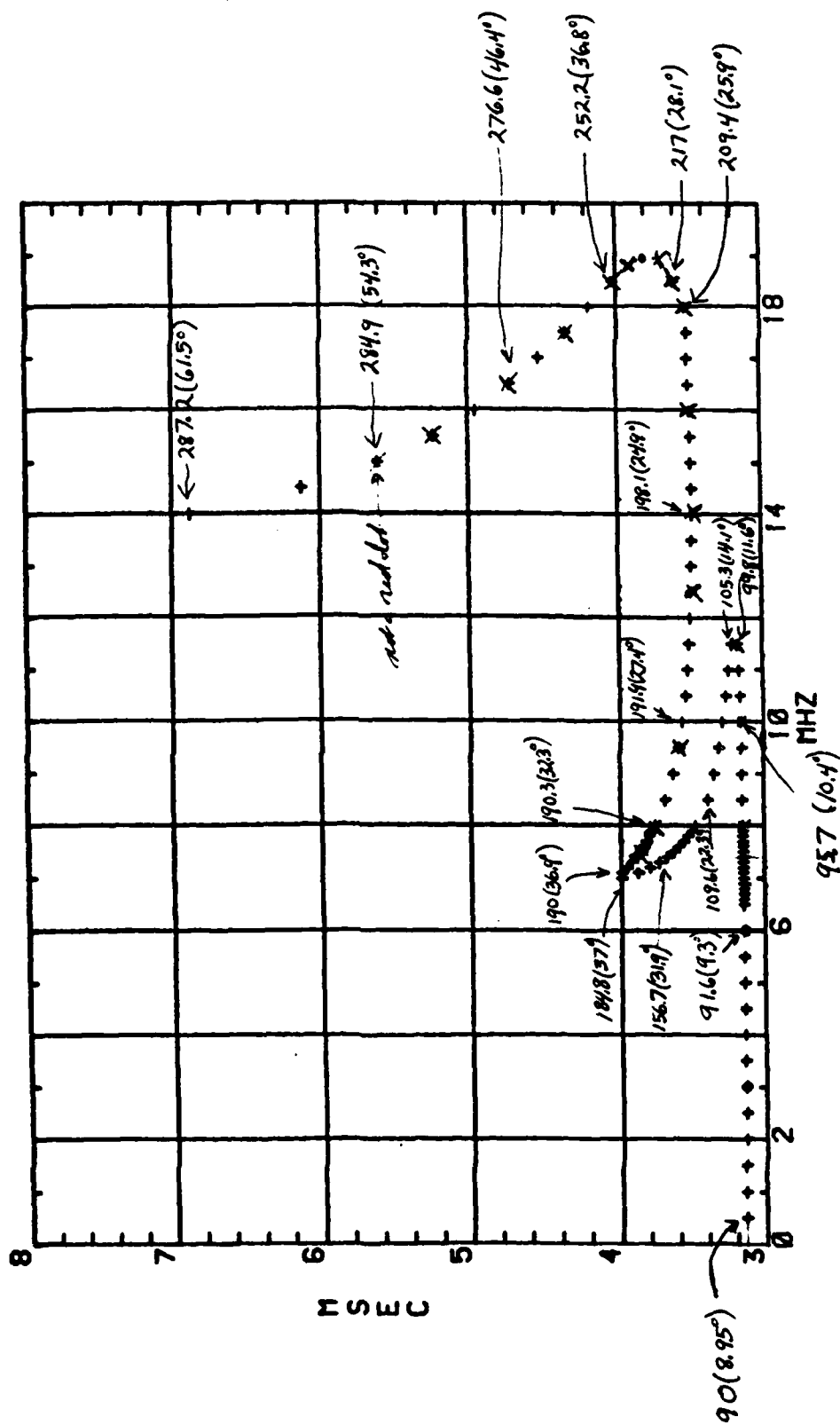
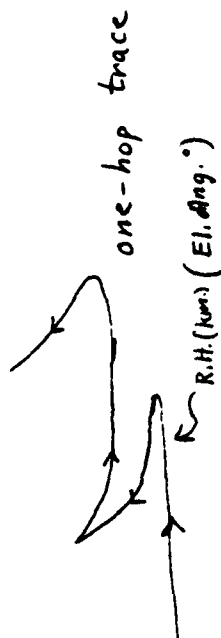


Fig. 15 — SSL-BCT prototype one-hop ionogram

OBLIQUE IONOGRAM  
RANGE = 918.3 KM



One-hop trace  
 OBLIQUE IONOGRAM  
 RANGE = 918.3 KM  
 (Zone 3)

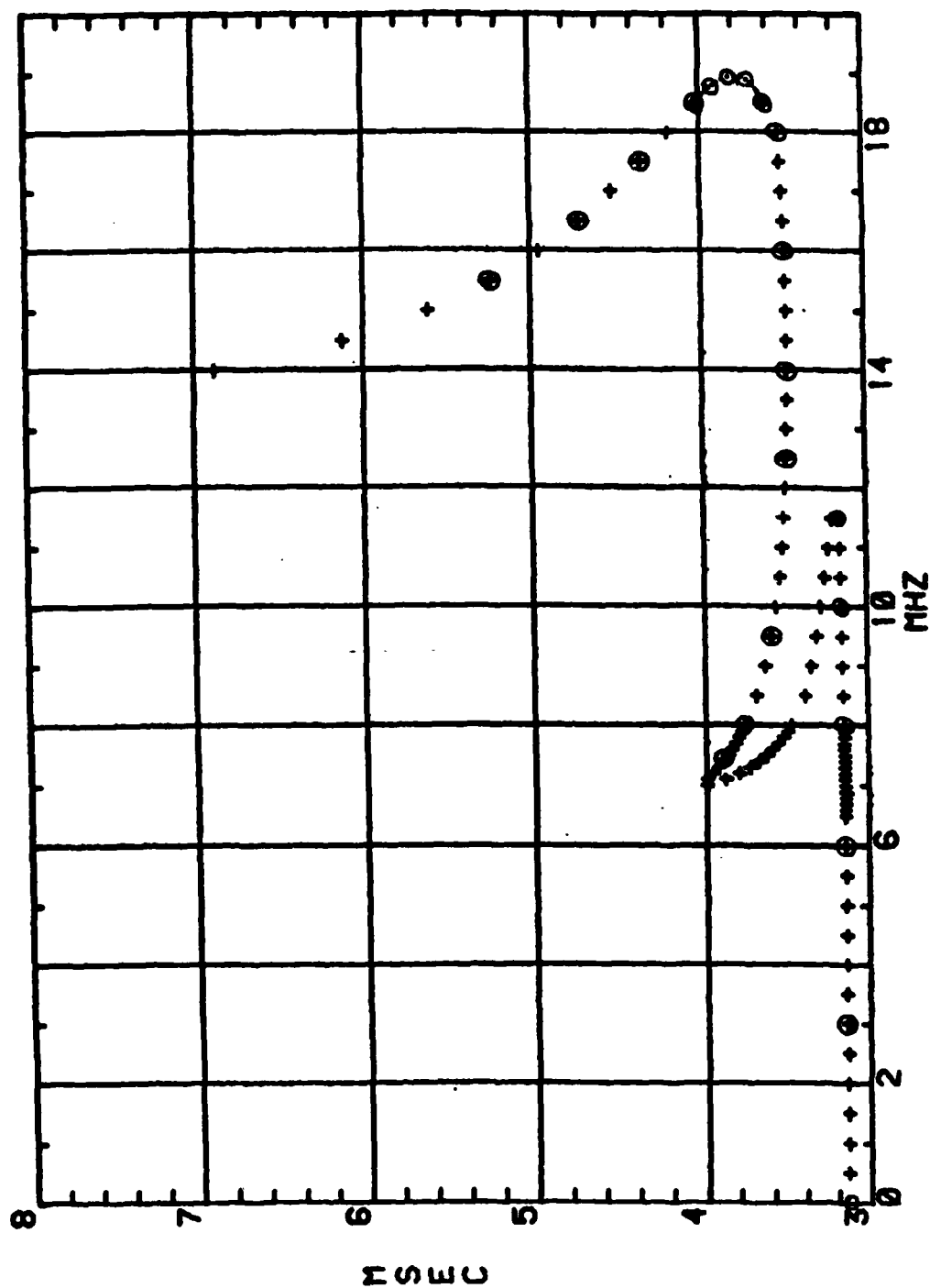
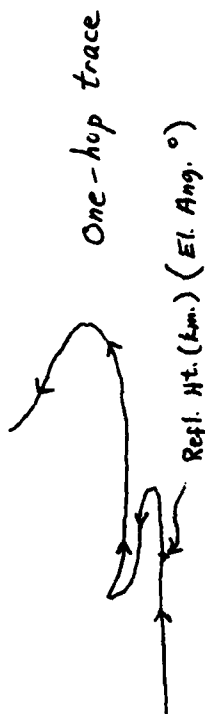


Fig. 17 - SSL-BCT prototype one-hop ionogram

OBLIQUE IONOGRAM  
RANGE = 1168.3 KM



Ref. Ht. (km.) (El. Ang. °)

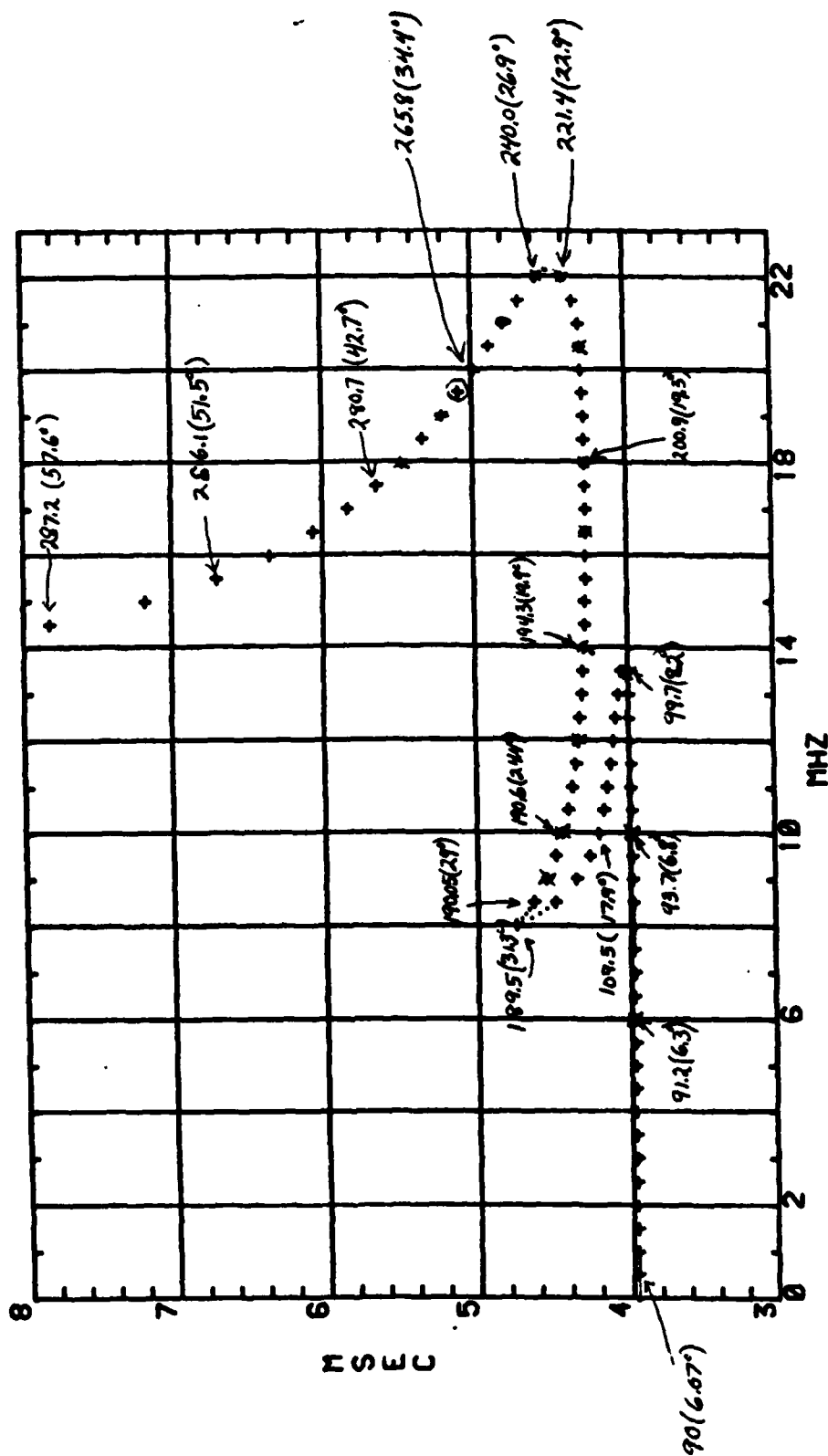


Fig. 18 - SSL-BCT prototype one-hop ionogram

One-hop trace  
**OBLIQUE IONOGRAM**  
**RANGE = 1168.3 KM**  
 (Zone 6)

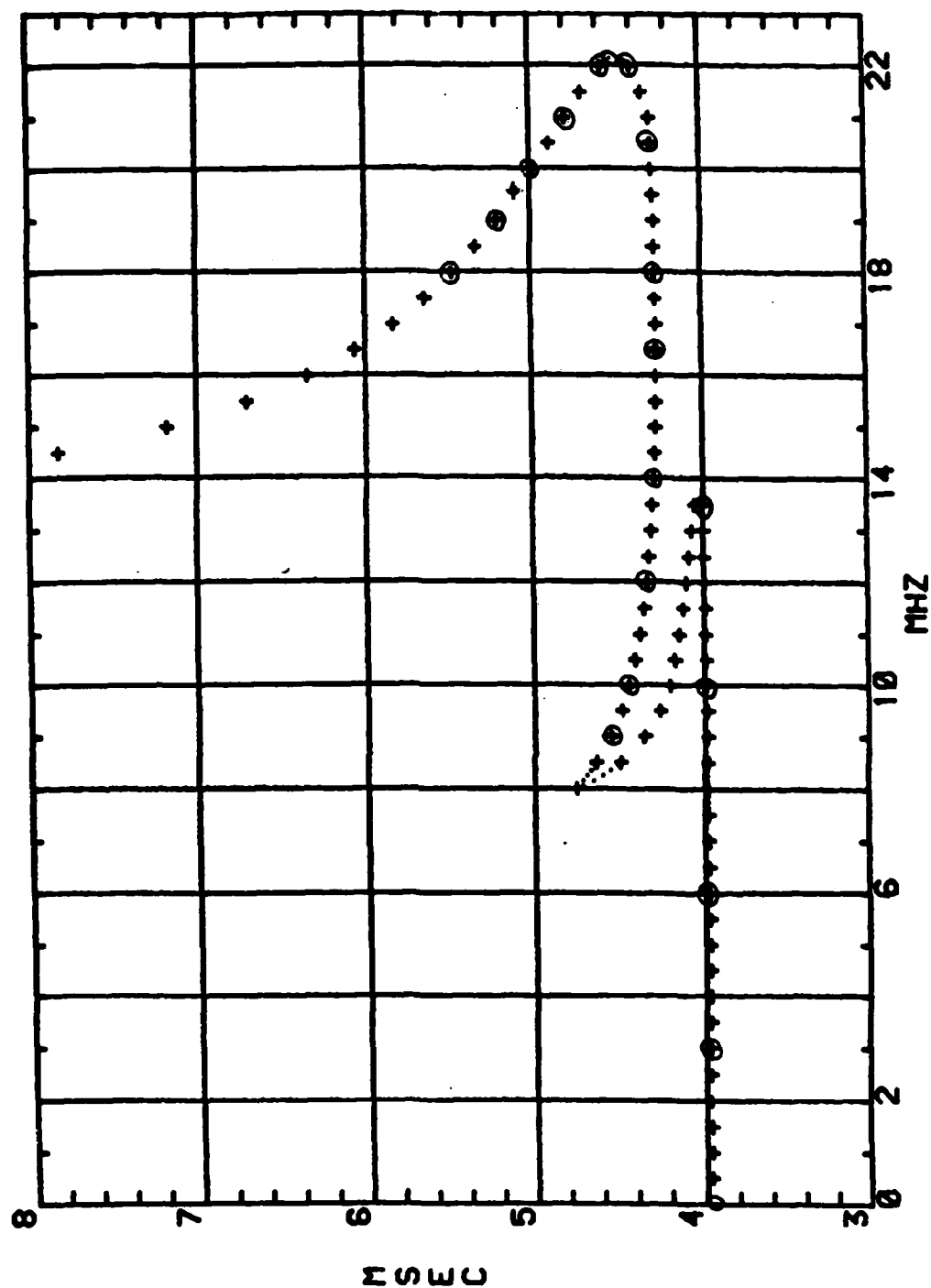


Fig. 19 — SSL-BCT prototype one-hop ionogram

# OBLIQUE IONOGRAM RANGE = 1501.9 KM

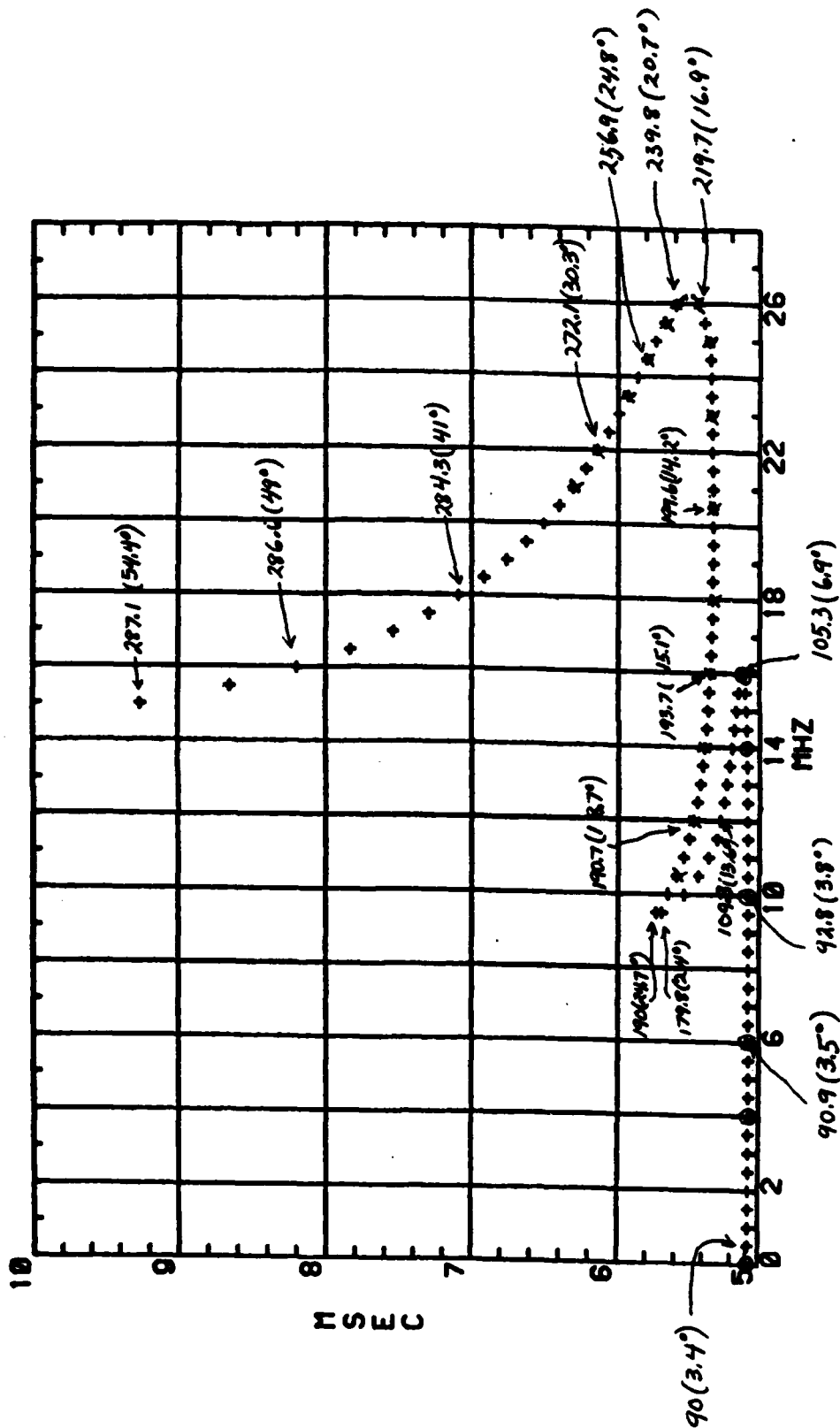
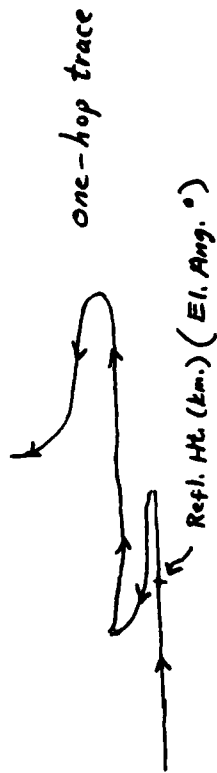


Fig. 20 — SSL-BCT prototype one-hop ionogram



One-hop trace  
OBLIQUE IONOGRAM  
RANGE = 1501.9 KM  
(Zone 4)

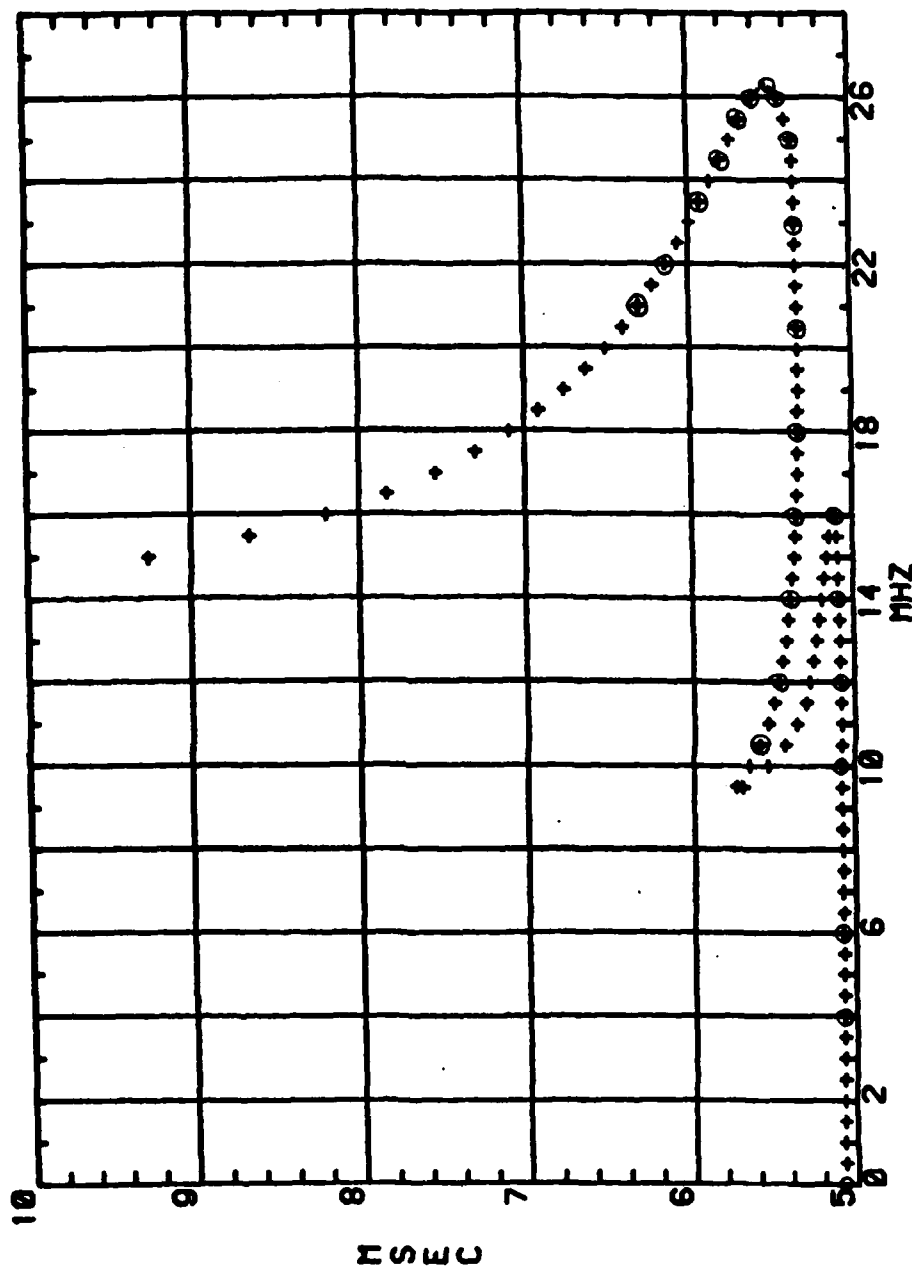


Fig. 21 — SSL-BCT prototype one-hop ionogram

Table 1 - True height profiles calculated from the SSL-BCT prototype one-hop ionograms

No.	D	h <sub>min</sub> E	f <sub>o</sub> E <sup>2</sup>	h <sub>h</sub> F	f <sub>h</sub> F <sup>2</sup>	h <sub>min</sub> F <sub>1</sub>	f <sub>o</sub> F <sub>1</sub> <sup>2</sup>	h <sub>min</sub> F <sub>2</sub>	f <sub>o</sub> F <sub>2</sub> <sup>2</sup>
1	385.3	90	100.7	9.56	191.4	24.65	207.8	84.48	286.4
	data file in -circled pts. in Fig. 13 - with RE procedure								
2	385.3	90	100.1	9.90	174.3	25.63	208.9	92.89	287.0
	Tablet digitizer in -circled pts. in Fig. 13 - no RE procedure								
3	385.3	90	102.1	10.25	175.5	25.95	206.3	87.29	287.4
	Tablet digitizer in -circled pts. in Fig. 13 - no RE procedure								
4	385.3	90	102.1	10.21	180.1	25.17	209.9	89.91	289.2
	Tablet - - circled pts. in Fig. 13 - with RE procedure								
5	385.3	90	104.3	10.94	181.2	25.35	208.2	85.6	290.5
	Tablet - - circled pts. minus 4 <sup>th</sup> to last one - with RE								
6	385.3	100	112.9	12.02	189.7	24.90	217.4	91.21	297.3
	Tablet - same as No. 5; plus a pt. before pt. 6 at f=5.7 MHz, plus a pt. before 2 <sup>nd</sup> to last circled pt.								
7	385.3	90	100.9	10.38	177.1	24.35	211.6	95.89	292.9
	Tablet - circled pts. plus pts. inserted before circled pts 3, 8, 10 and 16 in Fig. 13 - no RE								
8	385.3	90	105.9	11.52	184.4	25.03	209.7	84.50	292.8
	Tablet - similar selection to circled pts plus one on E-highway near E-MUF - with RE								
9	385.3	90	102.1	9.46	184.3	23.78	215.1	94.78	292.9
	Tablet - similar selection to circled pts. plus one beyond the last circled pt. - with RE								
10	385.3	90	113.4	12.98	190.7	20.80	218.2	89.70	301.9
	Tablet - attempt to process points along the continuous one-hop trace in Fig. 13 - with RE								
11	601	90	110.1	12.22	184.9	21.28	211.3	85.28	287.3
	data file in -circled pts. in Fig. 15 plus the next pt. after the 6 <sup>th</sup> circled pt. (near E-MUF on E-highway) - with RE								
12	601	80	86.94	6.46	183.6	20.32	208.8	87.02	290.3
	Tablet - circled pts. in Fig. 15 - no RE								
13	601	100	102.3	8.53	191.4	21.10	215.3	88.77	292.9
	Tablet - circled pts. - with RE								
									156.0

**Table 1 (Cont'd) -- True height profiles calculated from the SSL-BCT prototype one-hop ionograms**

No.	D	bhE	bmE	fOE <sup>2</sup>	hbF	fbF <sup>2</sup>	hmF1	fOE1 <sup>2</sup>	hmF2	fOE2 <sup>2</sup>
14	601	90	96.90	7.90	186.7	20.68	212.9	89.89	291.4	155.7
	Tablet - circled pts. - no RE									
15	601	90	97.63	7.81	178.8	24.39	209.2	90.11	288.6	156.0
	Tablet - circled pts. minus pt. 7 - with RE									
16	601	90	99.56	8.20	189.1	21.06	215.4	89.81	291.2	155.4
	Tablet - circled pts. - with RE									
17	601	90	-	-	-	-	-	-	-	-
	lost results for 7 parameters - - - - - 288.7 154.1									
	Tablet - - attempt to process points all along the continuous one-hop trace in Fig. 15 - no RE									
18	918.3	90	103.8	10.52	187.2	20.47	213.9	91.72	290.3	154.4
	data file in - circled pts. in Fig. 17 - with RE									
19	918.3	80	98.03	8.91	188.2	20.83	212.2	87.22	291.2	156.3
	Tablet - circled pts minus last pt. - with RE									
20	918.3	100	110.5	10.71	191.5	21.12	216.4	88.89	292.8	156.7
	Tablet - circled pts. minus last pt. - with RE									
21	918.3	90	104.2	10.43	187.0	20.96	216.9	98.42	296.5	157.8
	Tablet - circled pts. - with RE									
22	918.3	90	105.5	10.24	187.5	20.90	211.0	85.57	291.8	156.2
	Tablet - circled pts. minus last pt. - no RE									
23	918.3	90	101.1	9.31	181.8	21.58	217.1	102.9	296.9	157.8
	Tablet - circled pts minus pt. 7 - with RE									
24	918.3	90	102.8	10.05	186.7	20.93	211.1	86.44	290.5	155.6
	Tablet - circled pts. minus last pt. - with RE									
25	918.3	90	113.0	12.74	183.6	19.68	218.4	103.9	296.5	158.0
	Tablet - points all along continuous one-hop trace in Fig. 17, attempted - with RE									
26	1168.3	90	100.2	9.19	185.7	20.98	214.8	92.32	291.1	154.4
	data file in - circled pts. in Fig. 19 - with RE									

Table 1 (Cont'd) - True height profiles calculated from the SSL-BCT prototype one-hop ionograms

No.	<u>D</u>	<u>h<sub>1</sub>E</u>	<u>h<sub>3</sub>E</u>	<u>f<sub>o</sub>E<sup>2</sup></u>	<u>h<sub>1</sub>F</u>	<u>f<sub>1</sub>E<sup>2</sup></u>	<u>h<sub>m</sub>F<sub>1</sub></u>	<u>f<sub>o</sub>F<sub>1</sub><sup>2</sup></u>	<u>h<sub>m</sub>F<sub>2</sub></u>	<u>f<sub>o</sub>F<sub>2</sub><sup>2</sup></u>
27	148.3	90	102.2	9.24	183.6	21.31	212.5	91.48	294.4	152.6
	table - circled pts minus last pt. - no RE									
28	148.3	80	96.13	9.21	179.8	21.52	206.1	85.20	290.7	156.3
	table - circled pts. minus last pt. - with RE									
29	148.3	100	112.0	10.97	190.1	22.17	210.2	80.61	294.1	158.1
	table - circled pts. minus last pt. - with RE									
30	148.3	90	103.2	9.74	184.8	21.91	213.5	93.17	295.3	158.3
	table - circled pts. - with RE									
31	148.3	90	100.3	9.23	185.6	21.87	210.2	86.56	294.0	156.8
	table - circled pts. minus last pt. - with RE									
32	148.3	90	100.3	9.55	184.1	21.57	202.2	71.41	287.2	154.4
	table - circled pts. minus last two pts. - with RE									
33	148.3	90	108.4	12.04	180.6	19.27	250.7	148.6	321.4	159.7
	table - points all along cont. one-hop trace in Fig. 19, attempted - with RE									
34	150.9	90	116.6	12.65	183.4	20.93	209.2	83.66	286.0	152.9
	data file in - circled pts in Fig. 21 minus 3rd to last pt. plus a pt near F-MUF - with RE									
	- pts 2-7 could be processed - pt. 7 was redispersed with a larger time delay value									
35	150.9	80	112.0	12.96	182.0	22.09	213.9	91.46	290.6	156.2
	table - circled pts in Fig. 21, except same trouble with E-layer seen in No. 34 - with RE									
36	150.9	80	110.2	12.68	175.8	23.56	218.2	104.5	291.4	156.3
	table - circled pts. minus pt. 8 (f <sub>10.5</sub> ) - same trouble with E-layer - with RE									
37	150.9	80	110.4	12.21	175.7	20.55	214.8	100.05	288.7	154.5
	table - circled pts - same E-layer trouble - no RE									
38	150.9	70	100.4	8.83	164.0	17.48	191.7	79.03	289.1	151.4
	table - circled pts. - same E-layer trouble - with RE									
39	150.9	100	124.4	14.53	189.4	22.63	221.3	94.32	290.5	157.2
	table - circled pts. - same E-layer trouble - with RE									
40	150.9	85	115.1	13.70	185.6	20.82	255.9	149.4	321.2	159.6
	table - points all along cont. one-hop trace in Fig. 21, attempted - same E-layer trouble - with RE									

6,12,13,19,20,28, 29, and 35-40 can be seen by comparing these results with the hbE=90 km results and with each other. The E-layer solution shows about the expected variation with hbE. Some additional variability in the E layer solution, especially at large ranges, derives from human error in tablet digitization of the flat low-ray E layer part of the ionogram trace. The effect of the variability of the E layer solution on the F layer solution is found to be relatively small. Most SSL measurements are associated with F layer reflections, so that this insensitivity of the F layer solution to the errors made for the E layer is fortunate for HF transmitter location. It is also fortunate that the true height profile calculations are reproducible and capable of high accuracy, as seen in Appendix K, and that the tablet digitization method is almost as accurate as the data file method (compare Nos. 1 and 4, 11 and 16, 18 and 21, and 26 and 30). The tablet digitization tends to give  $fOF2^2$  values slightly too large, a result of misalignment of wires in the grid, but the effect is insignificant (and largely correctible).

The cases for range 1501.9 in Table 1 show a processing difficulty for the E layer trace that seems characteristic of large ranges. It was found that circled points 2-7 in Figure 21 could not be processed by the computer algorithm, for reasons presently not clear. The procedure adopted in the tablet operation was to (1) lay the cross-hairs on and digitize the estimated  $f=0$  position for the bottom of the one-hop trace, (2) input the associated value of hbE (usually estimated to be 90 km), which was used to convert observed relative time delays to absolute time delays, (3) attempt to digitize the observed point at the E MUF, and, failing a solution here, (4) advance the cross-hairs up the high-ray portion of the E layer one-hop trace until the second solution point is found. This is the procedure also followed for an actual ionogram at this range, except that the high-ray portion of the E layer trace has to be imagined, using Figure 20 or 21 as a guide. From here, the points in the F layer part of the trace are processed, as per usual. Despite inaccuracy in the E layer solution, the F layer solution is again quite accurate, as seen in Nos. 34-39 in Table 1 and Appendix K.

Most cases in Table 1 employ the reentrant (RE) procedure (cf. Section 2B), but some do not. There is little difference in this case, since the starting profile in Figures 9 and 10 is not essentially reentrant, i.e., it is almost a monotonically increasing function. For profiles which have a significant reentrant portion, the RE procedure usually gives much greater accuracy [Reilly, 1984a]. Nevertheless, the RE procedure gives small improvement in this case too. The solutions of Table 1 tend to underestimate the value of hbF, partially because of the discontinuous slope at the boundary of the E-F transition segment and the F layer segment in Figure 10. The RE procedure tends to improve the solution somewhat in the vicinity of this boundary [Reilly, 1984a].

The preceding boundary point is associated with the cusp at the low frequency end of the F layer low-ray portion of the ionogram trace. It is important, at least for this model profile, to select a point near the cusp for the true height profile calculation. In most of the range 385.3 entries of Table 1, the sixth circled point of Figure 13 was selected for processing. This is apparently not near enough to the cusp. The effect of this in Nos. 1-5 and 7-9 is seen in Appendix K to place the calculated solution points too low in altitude for the lower part of the F layer. Inspection of No. 10 in Appendix K shows the improvement from selecting a point closer to the cusp. The entries for larger ranges in Table 1 use points closer to the cusps on the ionogram traces, and better accuracy is thus achieved. This point is further illustrated by comparison with Nos. 15,23,25,33, and 40. In practice, however, difficulty in getting a solution is sometimes found by trying to

select a point too near the cusp. In these cases, the digitization cross-hairs are gradually moved away from the cusp until a solution can be obtained.

One further problem with the computer algorithm should be noted. If points too far up in the high-ray portions of the E and F layer portions of the ionogram trace are processed, the associated true height solutions are found to be too high [Reilly, 1984a]. This leads to an inaccurate determination of  $h_m F_2$  and, to a lesser extent, of  $f_o F_2^2$ . In practice, the computer algorithm has difficulty generating a solution in some of these cases. Normally, this is not a problem for typical ionograms, where enough of the high-ray trace is visible to find the peak parameters with sufficient accuracy, but not so much that inaccurate heights are calculated. By using a little sophistication in signal processing, it is often possible to generate ionograms that show "too much" of the high-ray F layer trace. It is not difficult, however, to stop processing the high-ray points at some point. This is one of the values of prototype calculations of this type, which serve as a guide for the real thing. It is found that stopping the calculations at or slightly below the last circled points in Figures 13, 15, 17, 19, and 21 yields sufficient accuracy for the peak parameters of the F2 layer. In Nos. 10, 17, 25, 33, and 40 in Table 1, an attempt was made to digitize points well beyond the last circled points of the aforementioned figures. It is found that there are gross errors made in  $h_m F_2$  for the two largest ranges; apparently the errors incurred are not serious for the smaller ranges. It will also be seen that the values for  $h_m F_1$  and  $f_o F_1^2$  are anomalously high for the two largest range cases. This does not mean that the middle part of the F layer solution is also very inaccurate. Inspection of Nos. 33 and 40 in Appendix K shows this. The significance of  $h_m F_1$  and  $f_o F_1^2$  as parameters in a least-squares fitting scheme should be remembered.

## 2D. Path 4 True Height Profiles and Midpath Ionospheres

An oblique-incidence sounder senses the ionosphere all along the raypaths, which brings into question the significance of the true height profiles calculated from the oblique ionograms. Does such a true height profile represent some weighted average of ionospheres all along the sounder path? It is reasonable to suppose that this is the case, and it may also be argued that the weighting factor for the ionosphere near midpath is particularly large, since this is where most of the refraction of the rays occurs for one-hop modes, at least for the relatively small ionospheric tilts ( $< 5^\circ$ ) actually found. Rephrased, the true height profile is the solution of an inverse scattering problem, where most of the scattering takes place near the midpath latitude and longitude coordinates. This notion is supported by analysis of oblique-backscatter records [Basler and Scott, 1973], where the oblique-backscatter ionograms are converted to equivalent vertical ionograms, using approximations similar to those discussed for Figure 1, and these are found to correspond quite closely to vertical ionograms measured at midpath.

The sounder configuration for Path 4 in Figure 2 allows a further examination of the correspondence between the true height profile solutions and the associated midpath ionosphere. The approach is to identify cases where ionogram data from the vertical-incidence sounders at Fort Ord (R in Figure 2) and Desert Research Station (DRS in Figure 2) can be compared with equivalent data obtained from the true height profile solutions calculated from Path 4 oblique ionograms. This will also provide another check on the accuracy of the calculated true height profiles. It would be nice to also have vertical ionogram data from Boulder, CO, (i.e., near T4 in Figure 2), but it seems that this data is unreliable during the time periods of interest in

the SSL-BCT data base. Hence, during time periods in which there are oblique ionograms for Path 4 and vertical ionograms from Fort Ord and Desert Research Station, true height profiles are calculated, and then used to calculate vertical ionograms, as in Figure 11, for comparison with the measured vertical ionograms. The comparison is properly made with the ordinary-mode traces of these measured vertical ionograms, since the reflection conditions are identical between the ordinary-mode and no-field cases. If the calculated true height profiles are to correspond closely to the midpath ionosphere, then the calculated vertical ionogram should be much closer to the Desert Research Station data than to the Fort Ord data in cases where these data differ from each other.

The time periods chosen for the above comparison were December 14 (Day 348) between 1600 and 1915 (UT), December 16 (Day 350) between 0100 and 0245, and December 18 (Day 352) between 1530 and 1545 (two oblique ionograms). Surprisingly, this represents a significant fraction of the cases which were available for this comparison. During the above three time periods, the ionospheres at DRS and Fort Ord are expected to differ. The first and third time periods include early morning hours near sunrise, and the second time period includes dusk and early nighttime hours (subtract eight hours from UT to get local time).

The aforementioned comparison is shown in Appendix A for seventeen different times during the three time periods. At each time a copy is shown of the oblique ionogram from which the true height profile was calculated. This is followed by the comparison between the equivalent no-field vertical ionogram (pluses and dots), which was calculated from the true height profile solution, and the ordinary-mode traces from the corresponding vertical ionograms at Desert Research Station (x-marks) and Fort Ord (little black rectangles). In some cases only one of the two oblique ionograms shown on a page is processed; the other one is not, because of an incomplete set of data for comparison at that time. In some cases a line will be seen to be drawn through the E layer portion of the one-hop trace. This was used to help estimate the position of the bottom of the trace at  $f=0$ . In many cases this E layer portion was weak and indistinct, thus making it even more difficult to process the E layer portion of the one-hop trace for Path 4, as discussed in Section 2C. In some cases, it was difficult to identify the ordinary mode on the Fort Ord and DRS vertical ionograms, particularly in the jumble of points near the E layer critical frequency. Several points of the jumble were typically plotted, as were some sporadic E-layer points (e.g., see Day 352, 1545).

It is generally seen in the vertical ionogram comparisons that, in cases where the DRS and Fort Ord data differ, the calculated equivalent vertical ionogram points for Path 4 agree much more closely with the DRS data. This is in keeping with the notion that the calculated true height profile solution characterizes the midpath ionosphere. An interesting exception is the comparison shown for Day 350, 0200, where the agreement with the Fort Ord data seems better near the F2 critical frequency. Still, it must be noticed that the DRS and Fort Ord data don't differ very much from each other. Further, the OI calculations are based on a relatively incomplete ionogram. Hence, this apparent exception does not seem at all significant.

In a few cases, the true height profile solution must be somewhat inaccurate. Examples of this are shown for Day 348 at times 1615 and 1830. Evidently, the calculated E layer and F2 layer critical frequencies are too high in each of these cases. This is not surprising for the E layer critical frequency, because of the highly approximate way that the E layer has to be treated for Path 4, as previously discussed. The fact that the calculation of

the vertical ionogram near the F2 critical frequency differs from the DRS data in some cases may be a reflection of the uncertainty in the extrapolation procedure used to infer F2 peak parameters in the true height profile calculation. Overall, however, the agreement between the DRS data and the calculated equivalent vertical ionogram is striking, especially in the F layer, and this lends confidence in the calculations. Greater accuracy should be obtained by repeating the calculations on ionograms which are replotted for lower threshold values. All signals are excluded from the ionogram plots for intensities below this threshold, and, if it is lowered, greater detail in the E layer and on the high-ray F layer portion of the ionogram trace will be visible.

### 3. SSL-BCT CALCULATIONS FOR DECEMBER 6-7:

#### 3A. Ionograms

The method developed for obtaining true height profiles from oblique ionograms has been applied to the ionograms of SSL-BCT for December 6-7 (Days 340 and 341). From the discussion of Section 2D, these profiles will specify the ionosphere at the midpath points X1-X6 in Figure 2 during this time period. Later, these results will be compared with available vertical ionogram data [Daehler, 1983] associated with the stations denoted by the solid triangles and R in Figure 2. The locations of all these points are given in Table 2.

The time period covered is between 1600 UT on December 6 (Day 340) and 0400 UT on December 7 (Day 341), 1982, a period of twelve hours which spans 0800 to 2000, Pacific Standard Time. The six oblique-incidence sounders were active during this time, recording ionograms every fifteen minutes. A digital file of each oblique ionogram was processed, by which signals in excess of a threshold value  $D=0.15$  were plotted in oblique ionogram form, and sets of all these plots for the SSL-BCT have already been distributed to participants. These plots were processed to obtain true height profiles for Paths (or Zones) 1, 2, 3, and 5 during 1600-2200 UT on December 6. It was inconvenient to use these plots for Paths 4 and 6 since they frequently did not show an E layer, which the calculation procedure uses to convert relative time delays to absolute time delays. A peak-processing method was developed by F. Rhoads of NRL to overcome this difficulty. An example of the problem and this solution to it are shown in Figure 22. The top part shows the oblique ionogram for Path 4 at 1800 which resulted from the  $D=0.15$  threshold. The E layer is invisible, and there is not much high-ray F layer in the trace. The result of the peak-processing method on the digital file is shown in the bottom part of Figure 22. Some E layer is visible, typically somewhat more than seen here, and the high-ray F layer trace is much more visible. Ionograms of this type were processed during 1600-1800 UT for Paths 4 and 6. The E layer parts of the calculated true height profiles are not expected to be accurate during this time for Paths 4 and 6, particularly since they show up weakly, but the important F layer parts are expected to be reasonably accurate (cf. Sections 2C and 2D).

After 1800, the ionograms processed for Paths 4 and 6, provided by M. Daehler of NRL, were of the thresholded type, but the threshold value was much lower. The 1800 UT ionogram for Path 4, thresholded at  $D=0.02$ , is shown in the top part of Figure 23. The E layer trace is strong now, for our purposes (cf. Section 2D), and the high-ray F layer is evident. The ionogram processed at a later time is shown in the bottom part of Figure 23. Note the appearance of sporadic E. The regular E layer is essentially non-existent at this time, since the solar influence is practically nil. Note also the nose extension



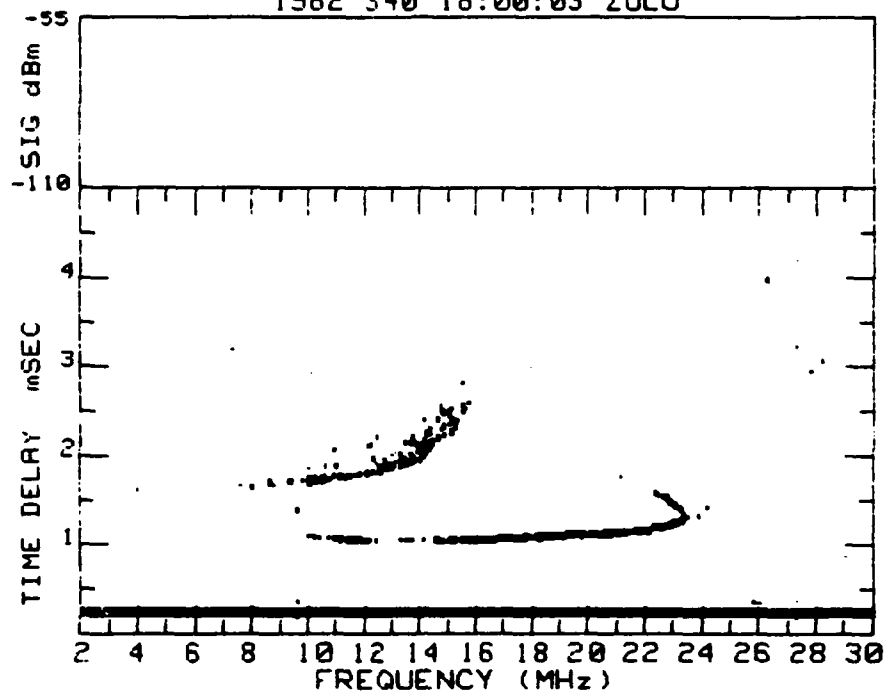
near the F MUF. It is important to ignore the nose extension in the true height profile calculation.

The appearance of the ionograms for the paths other than Path 4 is now discussed. For the most part, the D=0.15 ionograms for Paths 1,2,3 and 5 are adequate for processing, although the lower threshold ionograms were processed after 2200 UT for improved accuracy. Path 1 examples are shown in Figure 24. The top part shows a D=0.15 ionogram, and D=0.06 for the bottom part. The E MUF region is just visible here, but often it isn't.

Table 2 — Location of midpath and vertical ionosonde points in Figure 2

<u>IDENTIFICATION</u>	<u>LAT. (°N)</u>	<u>LOH. (°W)</u>
Midpath X1	36.174	119.67
Midpath X2	36.498	118.38
Midpath X3	35.183	116.97
Midpath X4	38.673	113.59
Midpath X5	34.701	119.44
Midpath X6	41.896	122.13
Ft. Ord (R)	36.652	121.74
LeMoore (NAS)	36.25	119.95
Pt. Arguello Vandenberg AFB (VBG)	34.600	120.600
Desert Range Station (DRS)	38.667	113.75

SSL OIS#2 ZONE 4 ERIE,CO TO FT ORD,CA  
1982 340 18:00:03 ZULU



SSL OIS#2 ZONE 4 ERIE,CO TO FT ORD,CA  
1982 340 18:00:03 ZULU

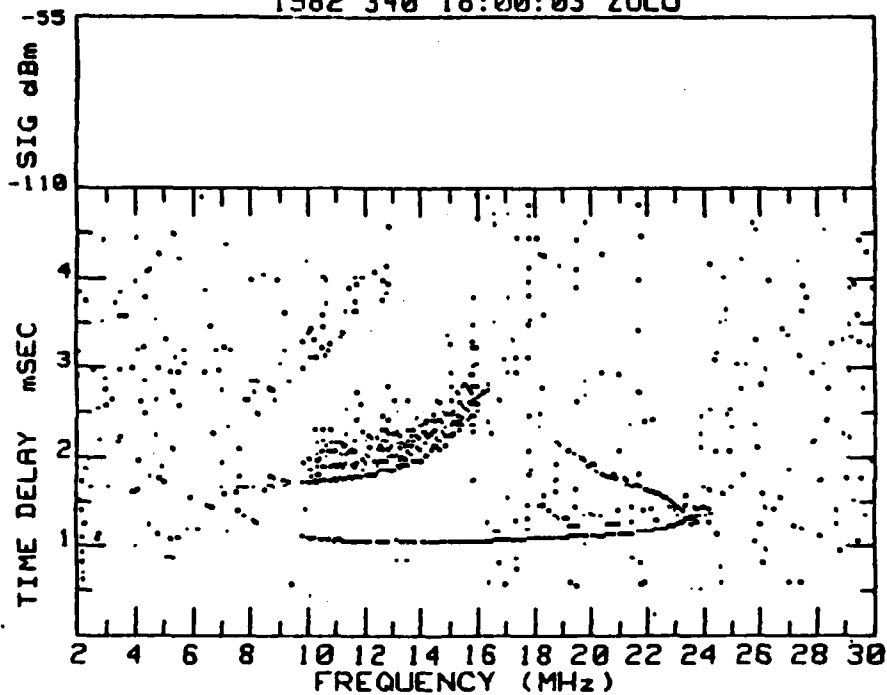


Fig. 22 — Oblique ionograms: thresholded at  $D=0.15$  (top) and peak-processed (bottom)

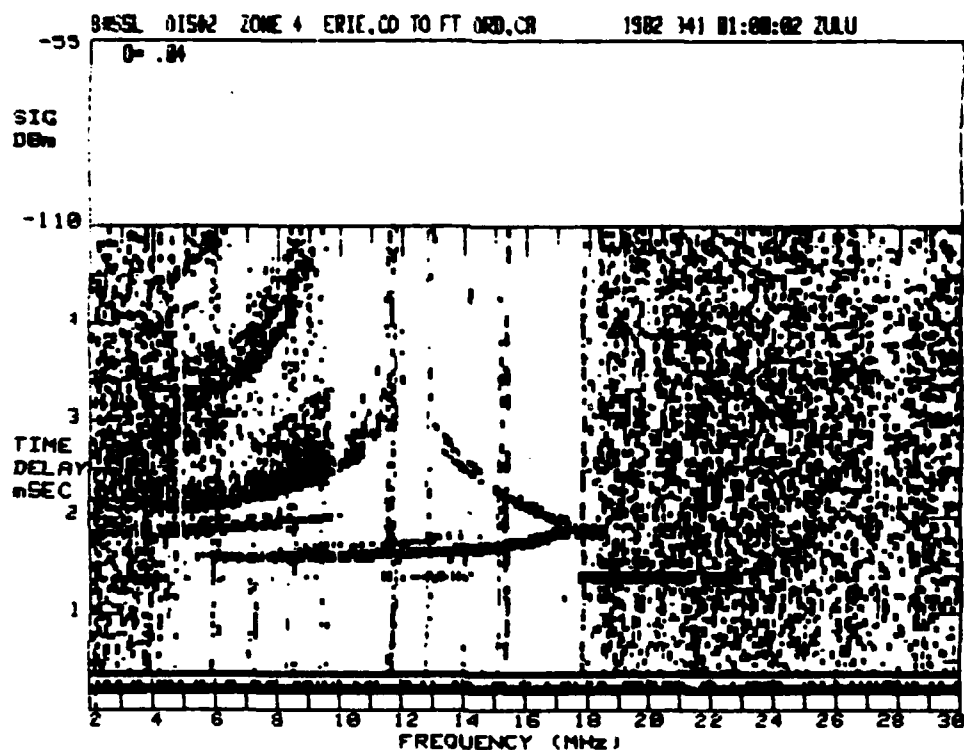
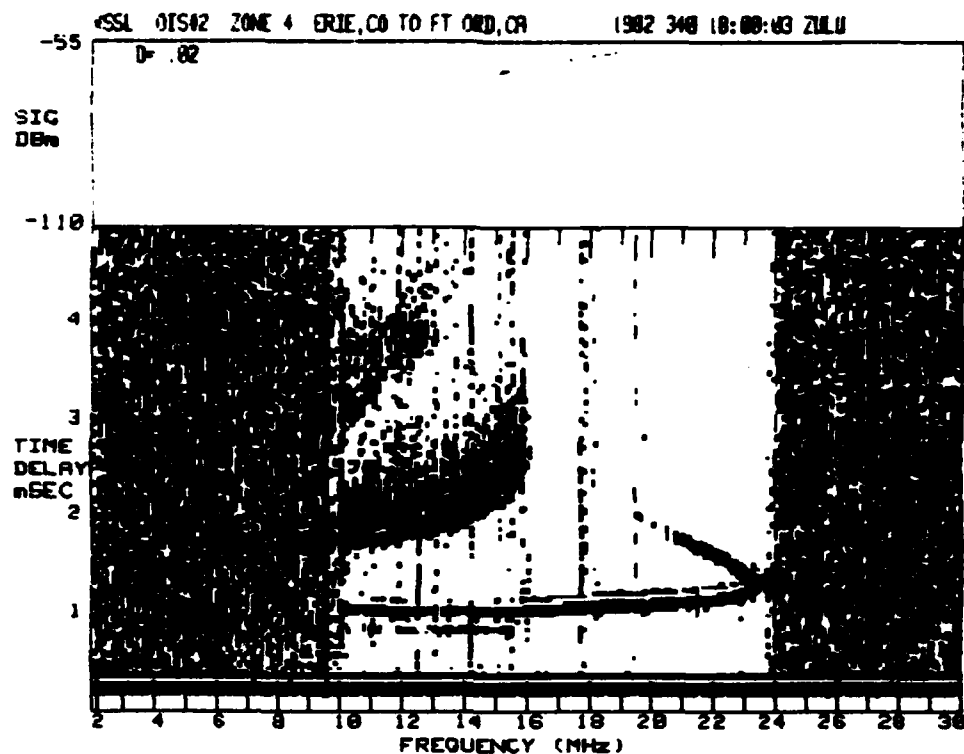


Fig. 23 — Threshold oblique ionograms

SSL OIS#1 ZONE 1 CHINA LAKE, CA TO FT ORD, C  
1982 340 20:10:00 ZULU

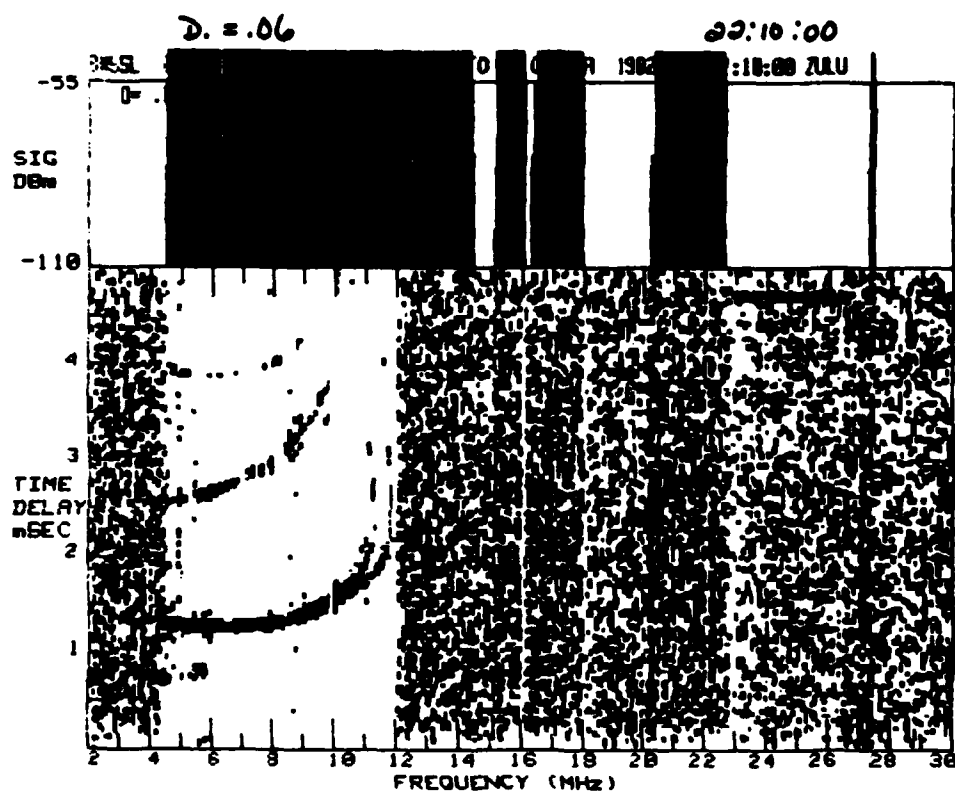
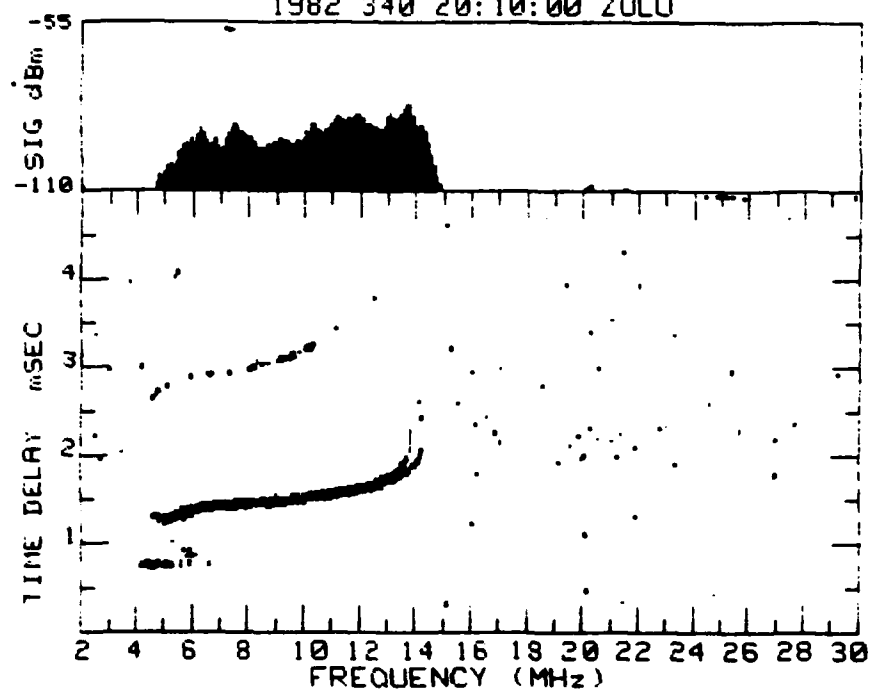


Fig. 24 — Thresholded oblique ionograms:  $D=0.15$  (top) and  $D=0.06$  (bottom)

A similar pair of examples for Path 2 is shown in Figure 25. Both examples seem to show a sporadic E contribution at high frequencies, in addition to the regular E layer. Figure 25 illustrates an apparent problem with the Path 2 data. There seems to be an upward equipment drift in time delay, superimposed upon the natural one. A straight-edge laid along the sporadic E part will show an upward tilt, instead of the expected flatness. This drift will cause some inaccuracy in the true height profile calculation. For example, the calculated values of  $hmE$  and  $hmF2$  are expected to be too high from this effect, but the results are, nevertheless, expected to be qualitatively accurate.

Some Path 3 ionogram examples are shown in Figure 26. The upper part is a  $D=0.15$  ionogram, and  $D=0.02$  in the lower part. Note that the E layer is faint and incomplete, and not very much of the high-ray F layer is seen in the upper ionogram. This compromises the accuracy of the true height profile calculations for Path 3 before 2200 UT, although the trends of the results for the whole group of ionograms should be reliable. After 2200 UT the results are obtained from ionograms like the bottom one in Figure 26, and relatively good accuracy is expected.

Path 5 ionograms are similar to Path 2 ionograms, as expected, since the sounder range is close to 600 km for both. Some examples are shown in Figure 27. The top ionogram was measured not long before sunset. The bottom ionogram was measured about 3.5 hours later; it shows pronounced sporadic E conditions. Generally, these conditions apply toward nighttime. Relatively good accuracy is expected from Path 5 ionograms.

Ionograms from Path 6 are shown in Figure 28. The peak-processing method gives the upper ionogram, and a low threshold gives the lower ionogram a short time later. Both methods result in ionograms which should yield relatively good accuracy for Path 6, although the E layer is somewhat better defined in the lower ionogram. The question arises, in connection with ionograms like this, about which part of the thick, low-ray F layer trace it is proper to digitize. It is presently not clear whether to digitize the leading edge, middle, or trailing edge of the trace. As a practical matter, however, it doesn't make much difference in our scheme, where the observed ionogram time delays are relative values. We choose to digitize the middle portion; the potential loss of accuracy is relatively insignificant. As stated previously, the magnetically split portion of the high-ray F layer portion of the trace is approximately bisected in the digitization for the no-field trace.

### 3B. True Height Profiles

The calculated true height profile results for Paths 1-6 in Figure 2 in the time period 1600, December 6 (Day 340) to 0400, December 7 (Day 341) are given in Tables 3-8. Each table gives a time, an ionogram number, and either nine parameters when ( $f_oE^2$ ,  $hmE$ ) is chosen to correspond to the maximum plasma frequency calculated in the E layer (cf. Figure 4), or eleven parameters when ( $f_oE^2$ ,  $hmE$ ) is chosen to correspond to the first reentrant point (cf. Figure 8). In the eleven-parameter case, which is found to be prevalent toward nighttime, the additional values of the parameters  $hsE$  and  $fsE^2$  are listed directly underneath the values of  $hmE$  and  $f_oE^2$ .

### 3C. Solar Zenith Angle Dependence and Trend Lines

If the ionospheric parameters of the preceding section are plotted vs. the time, a noisy variation about a background diurnal dependence is obtained. This background dependence is wave-like. For example, the background dependence for  $f_oF2^2$  is seen to grow during the morning hours until about local noon, after which the dependence falls off into the

SSL OIS#1 ZONE 2 NELLIS AFB, NV TO FT ORD, C  
1982 340 17:00:15 ZULU

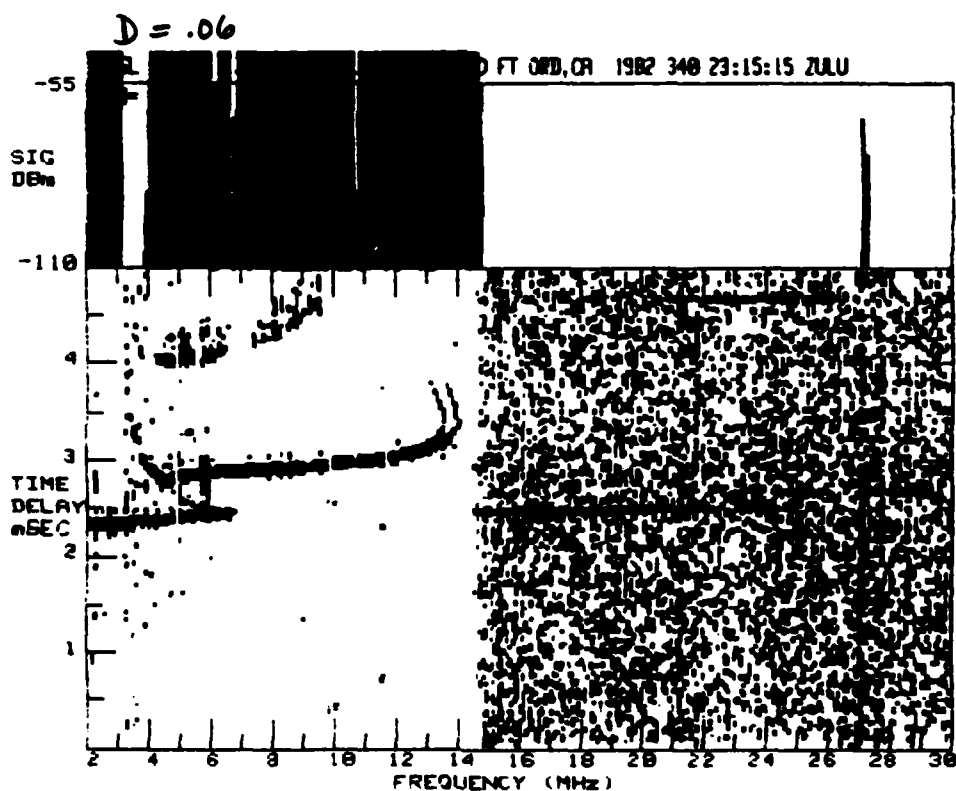
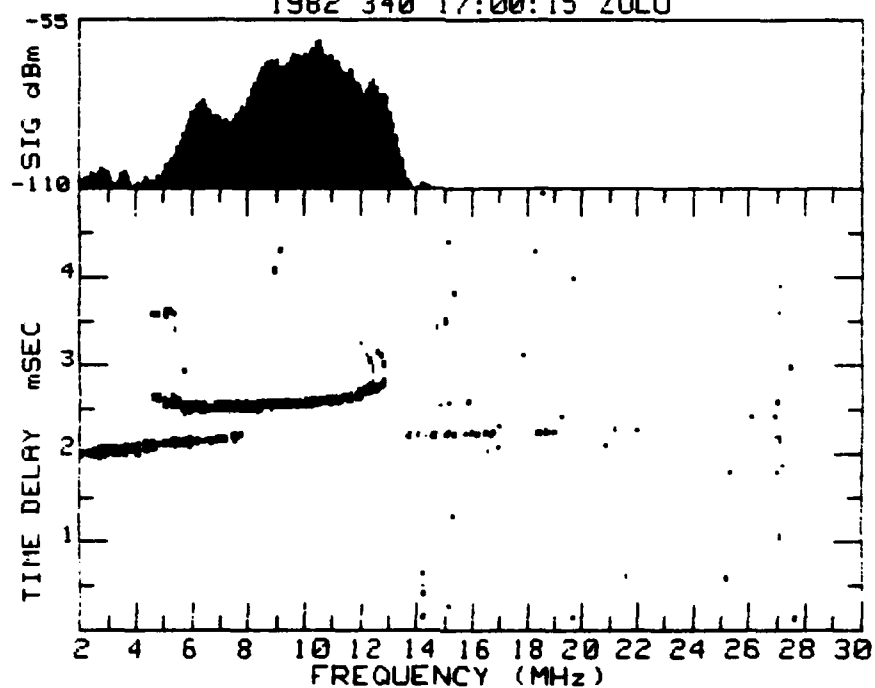


Fig. 25 — Thresholded oblique ionograms:  $D=0.15$  (top) and  $D=0.06$  (bottom)

SSL OIS#2 ZONE 3 LUKE AFB, AZ TO FT ORD, CA  
1982 340 20:50:00 ZULU

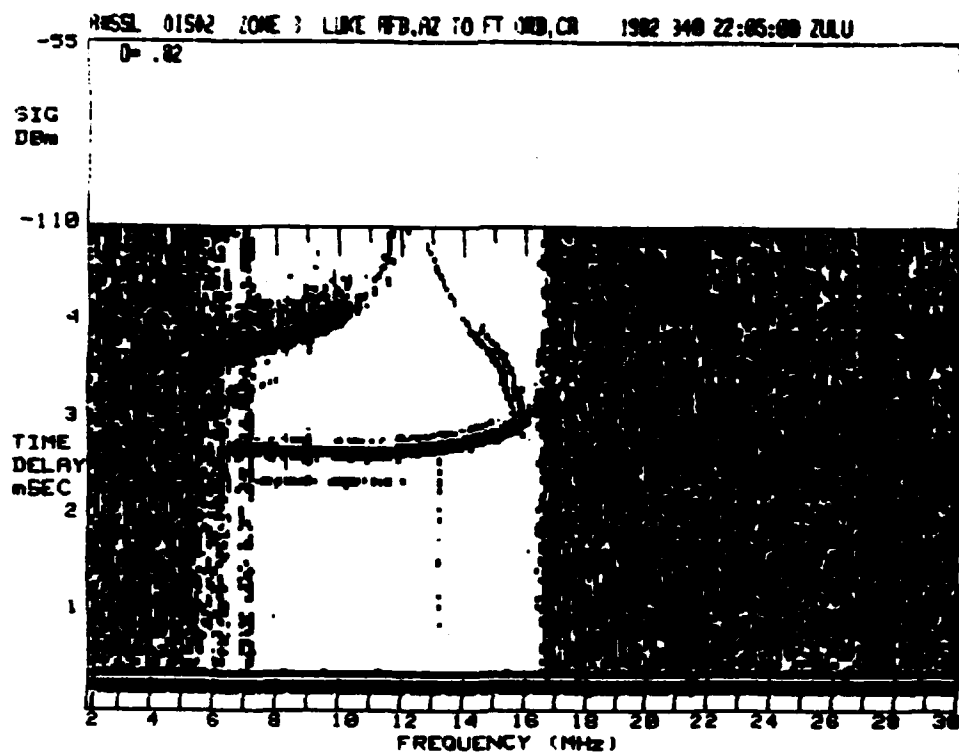
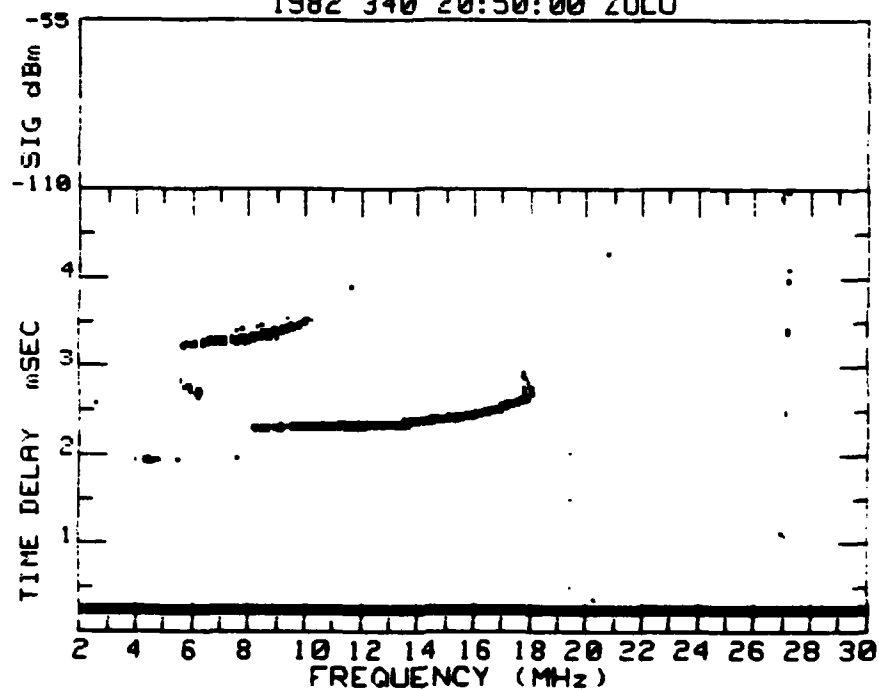


Fig. 26 — Thresholded oblique ionograms:  $D=0.15$  (top) and  $D=0.02$  (bottom)

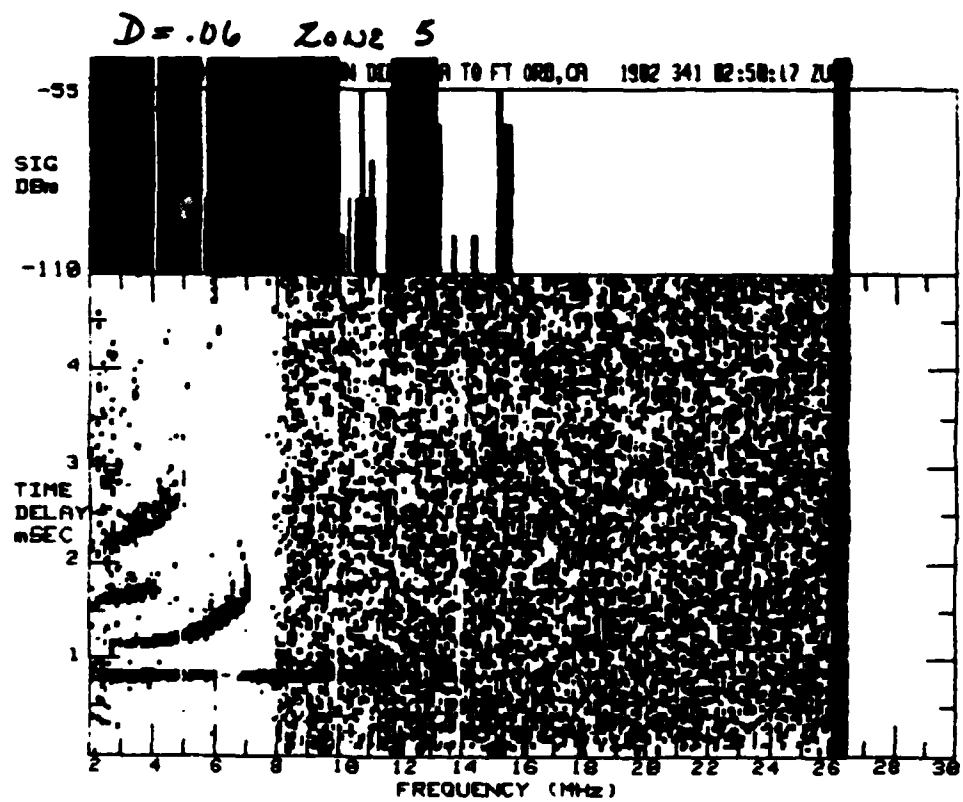
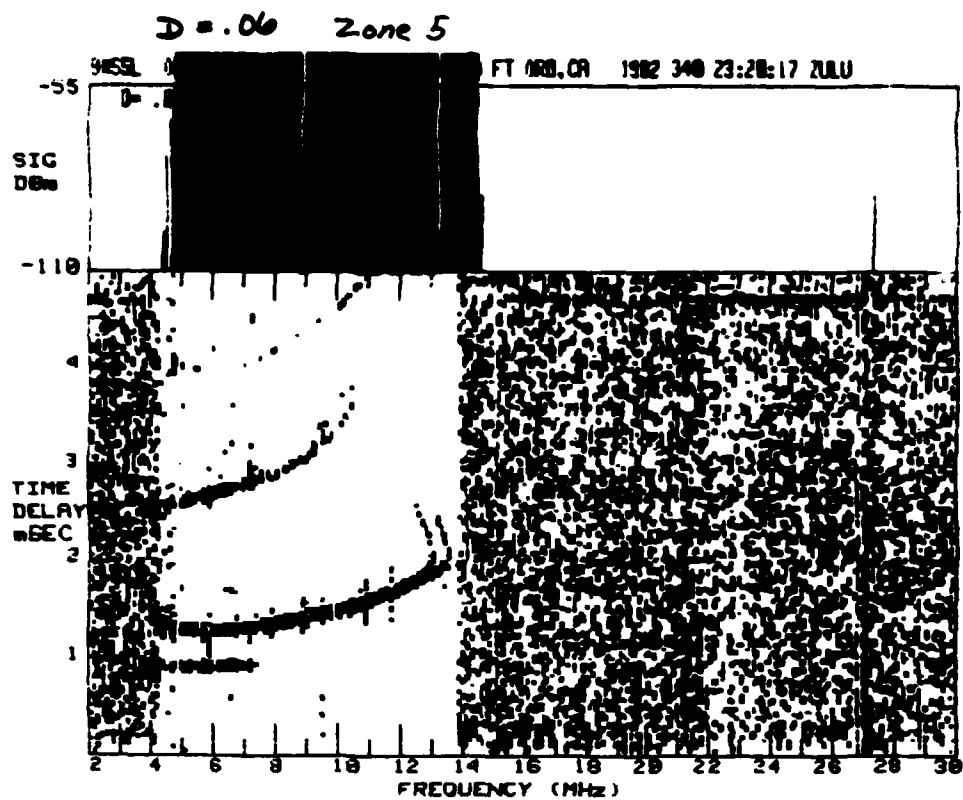
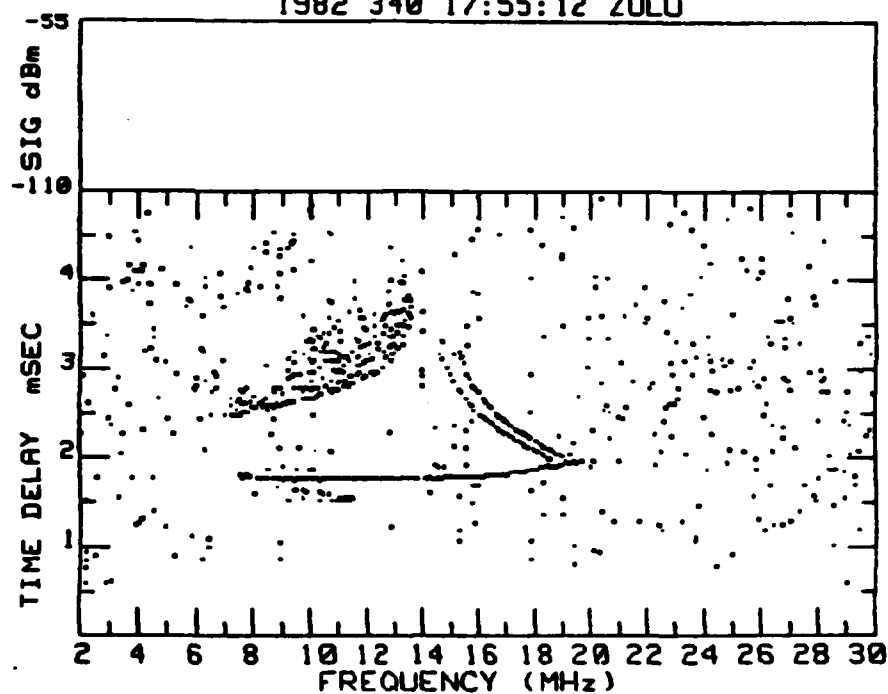


Fig. 27 — Thresholded oblique ionograms



SSL OIS#2 ZONE 6 FT LEWIS, WA TO FT ORD, CA  
1982 340 17:55:12 ZULU



SSL OIS#2 ZONE 6 FT LEWIS, WA TO FT ORD, CA 1982 340 18:10:12 ZULU

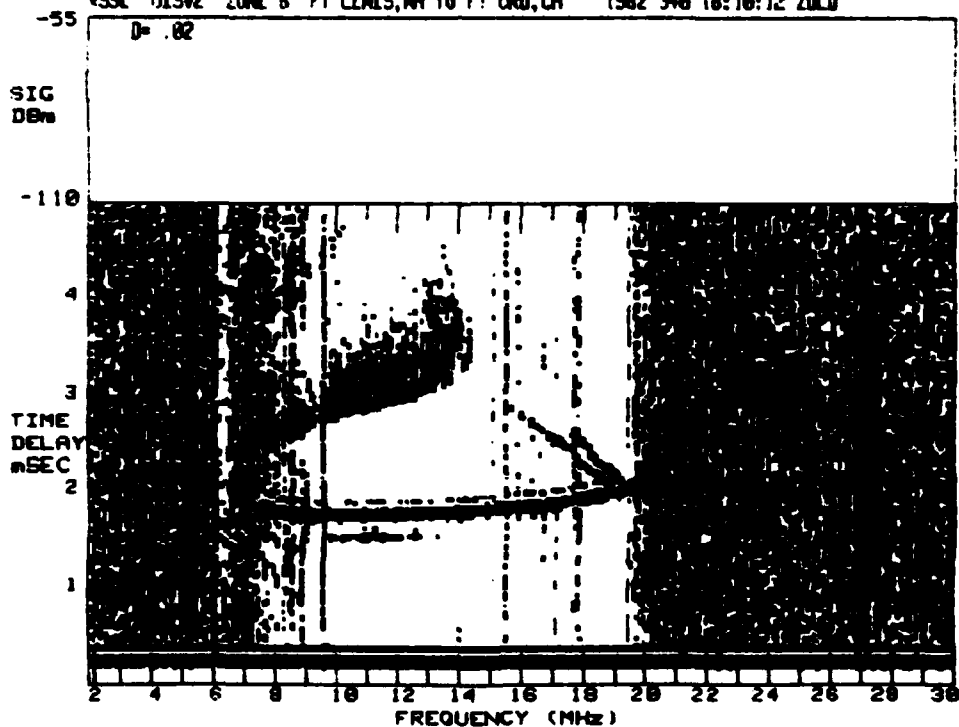


Fig. 28 — Oblique ionograms: peak-processed (top) and thresholded at  $D=0.02$  (bottom)

Table 3 — True height profile calculations — Zone 1

$h_bE = 90 \text{ km. (this page)}$

Time (HMS)	No.	$h_mE$	$f_oE^2$	$h_bF$	$f_oF^2$	$h_mF1$	$f_oF1^2$	$h_mF2$	$f_oF2^2$
Day 340 155519	1	104.05	5.3411	175.95	7.6989	190.98	32.565	244.73	76.801
161019	2	108.03	6.1097	178.27	3.7455	207.37	42.766	262.36	80.282
162519	3	102.26	6.5645	172.80	10.427	213.89	68.733	255.13	85.939
164019	4	104.97	8.4658	171.41	10.260	220.81	77.921	273.73	99.475
165519	5	105.91	8.9893	164.76	10.424	208.41	73.603	266.64	100.41
171019	6	99.729	8.4322	168.19	3.6476	235.35	86.746	272.53	109.28
172519	7	111.054	11.088	150.82	10.839	193.28	40.479	264.74	120.64
174019	8	106.302	10.327	159.39	10.422	193.58	46.734	262.25	129.04
175519	9	101.91	10.212	175.76	11.036	215.59	80.819	274.48	131.78
181019	10	102.47	11.012	160.10	10.863	179.11	26.004	285.64	124.57
182519	11	101.42	9.6771	176.51	15.335	201.69	47.043	293.60	128.85
184000	12	105.90	11.193	195.77	21.846	249.73	124.61	285.82	143.82
1855	13	107.30	12.627	168.38	18.305	229.47	108.01	274.29	140.30
1910	14	102.00	10.097	177.00	24.166	193.26	60.27	267.97	142.81
192519	15	111.22	12.960	172.30	14.940	235.47	95.005	292.00	144.125
1940	16	104.22	10.740	180.36	11.013	232.47	94.016	299.82	146.81
1955	17	100.69	9.1659	168.75	19.837	224.56	77.462	295.61	157.80
2010	18	109.65	12.414	179.24	17.717	219.38	64.681	288.25	165.34
202519	19	103.83	11.550	189.12	22.427	209.72	73.395	272.85	150.98
2040	20	104.72	9.8261	165.72	4.9563	188.87	21.539	293.78	143.66
2055	21	102.33	10.563	163.36	9.3471	230.04	94.165	296.46	135.56
2111	22	93.936	7.3461	147.78	13.965	209.32	71.095	289.48	136.82
2125	23	100.32	9.5192	184.18	10.910	229.85	86.842	289.40	135.67
2140	24	103.71	10.051	184.69	3.5876	215.92	37.829	283.19	126.18
2155	25	107.51	9.8651	182.59	4.2006	227.92	63.885	289.82	122.77
2210	26	114.45	10.128	172.76	7.7255	231.53	77.987	294.72	115.09

Table 3 (Cont'd) - True height profile calculations - Zone 1

Time	No.	h <sub>BE</sub>	h <sub>ME</sub> h <sub>SE</sub>	f <sub>0E</sub> <sup>2</sup> f <sub>SE</sub> <sup>2</sup>	h <sub>BF</sub>	f <sub>0F</sub> <sup>2</sup> f <sub>BF</sub> <sup>2</sup>	h <sub>MF1</sub>	f <sub>0F1</sub> <sup>2</sup>	h <sub>MF2</sub>	f <sub>0F2</sub> <sup>2</sup>
Reg 340										
22:25	27	90	101.57	8.6507	178.73	3.1610	237.32	75.817	301.28	110.41
225519	28		102.15	7.6243	174.23	13.407	245.73	80.629	315.29	121.96
231019	29		101.18	6.9592	197.46	10.215	227.02	58.711	304.38	121.59
232519	30		99.712	5.7949	188.56	14.267	214.18	61.195	280.79	121.74
234019	31		103.72	4.8521	181.70	13.189	221.32	70.811	285.08	116.62
235519	32		102.12	3.8408	185.81	9.0978	233.13	79.337	292.77	107.59
Reg 341										
001019	33		96.377	2.8967	189.55	10.554	228.95	62.599	290.60	102.83
002519	34		95.074	2.9802	185.92	9.4477	239.96	77.227	291.06	96.491
004019	35	90	155.16	0	201.84	2.8443	221.06	35.669	285.36	90.238
			98.266	4.5514						
002:14	36	100	140.00	0	214.02	1.1885	245.45	54.504	293.60	82.555
			100.17	3.1857						
011019	37	100	144.72	0	185.62	0.22046	229.16	46.026	282.49	73.709
			102.93	3.3428						
012519	38	100	155.69	1.540	193.58	10.063	229.08	43.069	286.80	62.394
			101.24	4.5103						
014019	39	100	156.97	1.817	189.43	7.2082	222.08	38.212	291.34	56.561
			106.21	4.2430						
015519	40	100	170.99	0	204.36	8.6210	237.02	38.361	283.77	51.933
			107.12	5.1098						
021019	41	100	160.61	0	205.86	0	233.30	32.575	271.35	48.228
			103.30	4.5850						
022519	42	100	157.95	.98662	177.94	9.3411	207.42	26.598	271.16	38.907
			107.97	4.9855						
024019	43	100	141.60	0	199.40	.00919	239.85	24.031	285.34	33.461
			105.13	2.9173						
031018	44	100	134.69	0	190.52	.40863	243.21	20.356	295.65	26.371
			100.95	2.6997						
032519	45	100	137.53	0	182.94	0	211.03	12.849	259.41	18.439
			100.93	2.9280						
034019	46	100	127.49	0	186.96	0	222.14	10.814	255.72	15.918
			103.03	1.9569						
035519	47	100	134.93	0	165.35	0	206.10	8.3815	258.26	14.380
			104.29	2.4516						
041019	48	100	129.46	0	187.43	0	210.53	5.3150	243.83	9.1849
			100.97	2.2739						

DATA PAPER (11 COLUMN) NWD-GEN-3900/215-441

GPO 938-172

Table 4 — True height profile calculations — Zone 2

		h <sub>b</sub> E = 90 km. (this page)								
Time (HMS)		No.	h <sub>m</sub> E	f <sub>o</sub> E <sup>2</sup>	h <sub>b</sub> F	f <sub>b</sub> F <sup>2</sup>	h <sub>m</sub> F1	f <sub>o</sub> F1 <sup>2</sup>	h <sub>m</sub> F2	f <sub>o</sub> F2 <sup>2</sup>
Dav 340	034515		101.34	2.1552	160.71	2.4935	204.54	16.042	235.69	19.228
	160015	1	114.48	5.6836	197.17	8.1026	208.73	24.449	286.56	79.274
	161515 :	2	121.45	9.4421	174.29	7.4326	235.23	73.714	269.10	87.527
	163615.	3	116.98	9.9632	182.61	13.470	225.12	69.010	257.47	89.876
	164515	4	111.76	9.2502	191.81	12.665	233.89	78.342	272.28	107.91
	170015	5	131.19	13.581	188.04	15.363	207.29	48.307	263.91	96.464
	171515.	6	116.98	10.634	175.49	5.9579	237.51	58.254	281.61	120.03
	173015.	7	114.62	11.437	152.22	10.997	201.93	33.751	262.80	116.39
	174515	8	112.46	10.406	189.91	10.327	233.43	77.239	277.47	135.35
	180015 =	9	120.35	13.309	187.14	16.599	220.48	61.126	276.33	128.11
	181515 =	10	120.48	12.011	186.52	12.507	246.22	89.639	311.64	131.14
	183015 :									
	184515 =	11	109.37	11.297	148.23	8.1970	219.77	46.106	280.39	141.98
	190015	12	114.36	13.179	181.93	15.427	217.31	56.488	327.04	164.38
	191500 :	13	119.20	13.197	201.00	22.071	240.60	84.912	303.27	154.85
	193000	14	111.56	12.521	183.25	16.291	226.14	73.013	319.18	163.07
	194500 =	15	113.90	10.869	212.35	18.398	261.00	111.11	304.51	151.96
	200000	16	116.34	13.371	189.29	20.967	237.92	94.517	298.88	171.04
	201515 -	17	112.45	13.780	186.95	18.312	208.29	58.351	285.19	157.76
	203000	18	113.05	13.289	169.66	15.512	213.31	53.463	301.58	150.08
	204500 =	19	119.62	14.634	189.63	16.271	235.42	85.928	309.07	141.18
	210000	20	122.25	13.357	184.45	15.086	241.40	83.542	314.47	138.72
	211500 -									
213001	21	112.20	8.4267	205.43	5.4870	249.27	76.758	302.24	135.47	
214500.	22	109.21	11.763	172.83	13.104	221.76	72.902	298.50	131.31	
220000	23	114.11	10.725	183.99	12.511	231.92	69.379	289.63	118.44	

Table 4 (Cont'd) - True height profile calculations - Zone 2

Time	No.	h <sub>DE</sub>	h <sub>ME</sub>	f <sub>OE</sub> <sup>2</sup>	h <sub>DF</sub>	f <sub>DF</sub> <sup>2</sup>	h <sub>ME1</sub>	f <sub>OE1</sub> <sup>2</sup>	h <sub>ME2</sub>	f <sub>OE2</sub> <sup>2</sup>
			h <sub>SE</sub>	f <sub>SE</sub> <sup>2</sup>						
221500	24	90	111.81	4.7762	177.25	8.6305	257.34	92.093	302.86	115.24
223000	25		110.865	9.4894	178.46	11.516	235.05	59.202	305.47	115.85
230015	26		105.14	7.5336	179.64	11.958	241.59	54.019	307.49	122.18
231515	27		109.19	7.6399	200.11	14.858	227.47	45.599	291.18	122.89
233015	28		111.57	5.9721	191.47	15.389	238.91	82.684	289.59	118.12
234515	29		109.08	5.0783	189.93	11.299	247.07	85.907	288.98	112.80
000015	30		103.60	4.3453	190.18	9.0436	247.85	79.171	292.46	103.35
001516	31		178.42	0.05894	204.22	17.488	250.39	73.744	292.71	99.170
			108.97	5.6156						
003015	32		104.10	4.3114	183.51	8.3795	229.64	59.383	290.42	92.519
004515	33		153.96	0	205.70	32.663	241.41	36.028	302.10	88.374
			99.153	4.3842						
010015	34		162	0	189.34	0	252.11	65.404	294.68	78.882
			100.70	5.0225						
011516	35		97.805	5.1430	174.08	3.6794	226.54	36.280	295.04	67.776
013015	36		106.45	6.7375	176.45	5.5652	211.59	21.852	295.53	58.746
014515	37		102.36	4.7609	189.67	3.3366	230.28	31.066	291.64	53.994
020015	38		107.63	5.5706	175.16	1.7699	215.77	23.125	279.60	51.944
021515	39		104.65	4.6765	193.36	3.3499	226.41	27.766	269.92	43.680
023015	40	100	139.57	0	195.82	0	227.69	19.904	280.32	36.431
			104.95	2.7709						
024515	41	100	114.95	0	199.51	0	223.12	17.039	274.07	29.622
			102.88	.9650						
030015	42	100	130.02	0	190.54	0	227.76	16.864	267.01	25.655
			102.98	2.1631						
031515	43	100	126.52	0	201.19	.00083	216.62	7.6498	272.65	21.977
			103.23	1.8626						
033015	44	100	117.79	0	204.24	0	216.37	6.9191	275.37	17.300
			101.52	1.3013						
034516	45	100	117.78	0	210.82	.00351	227.64	5.3270	285.36	14.417
			102.26	1.2417						
040015	46	100	119.90	0	181.98	1.4566	223.93	7.5103	292.66	12.005
			102.97	1.3548						
041515	47	100	116.93	0	189.26	0	241.55	5.7584	347.30	11.489
			101.12	1.2647						

DATA PAPER (11 COLUMN) NDS-GEN-3900/23-441

GPO 536-178

Table 5 — True height profile calculations — Zone 3

$h b E = 90 \text{ km. (this page)}$

Time (HMS)	No.	$h m E$	$f o E^2$	$h b F$	$f b F^2$	$h m F1$	$f o F1$	$h m F2$	$f o F2^2$
Day 340	1	112.13	5.6655	184.84	13.666	212.51	46.337	257.30	85.306
160507	2	121.77	8.4913	170.54	4.5986	205.60	23.731	264.92	96.793
162007 =	3	121.47	8.9031	185.58	16.698	203.40	36.582	273.37	101.06
163507 =	4	119.38	5.8144	194.00	19.966	225.92	56.813	276.14	119.63
165007 =	5	115.88	3.8830	192.31	10.762	213.17	36.357	285.70	117.39
170507 =	6	107.04	9.9565	169.88	12.599	212.76	70.565	292.66	123.87
172007 :	7	111.54	7.5790	197.95	24.690	245.70	108.771	288.55	139.71
173507 =	8	114.44	11.738	180.33	14.648	226.10	82.717	265.64	141.84
175007 :	9	118.20	12.092	179.56	15.047	205.93	49.630	296.56	146.07
180507 =	10	112.80	11.128	180.73	13.845	210.82	47.094	285.89	140.39
182007 :	11	111.55	13.013	175.74	13.299	233.46	72.968	351.19	191.27
185000	12	109.49	8.4040	173.09	19.030	224.81	56.644	288.02	153.24
190500	13	108.40	11.055	178.73	21.860	219.73	63.468	319.64	176.59
192000	14	104.89	10.456	164.96	5.6562	216.67	40.997	297.50	157.29
193500	15	111.38	9.7610	187.69	9.1489	237.58	81.001	301.53	162.81
195000 =	16	107.29	11.782	175.47	16.529	232.11	93.350	291.21	164.58
200500 =	17	107.88	8.8204	191.56	26.263	200.91	45.591	325.47	173.98
202000 =	18	110.13	12.733	167.97	14.674	214.90	63.686	290.95	149.28
203500	19	105.87	10.859	158.46	6.9471	213.63	38.115	307.75	150.98
205000 :	20	114.50	13.354	193.91	22.022	208.94	47.312	323.15	142.92
210500	21	112.41	13.204	168.31	13.517	229.19	81.587	340.11	142.44
212000	22	104.61	11.018	154.23	8.7726	223.44	60.313	287.24	132.06
213500 =	23	117.57	13.319	170.56	13.172	215.84	44.201	317.50	133.74
215000 =									

Table 5 (Cont'd) — True height profile calculations — Zone 3

Time	No.	h <sub>bE</sub>	h <sub>mE</sub>	f <sub>oE</sub> <sup>2</sup>	h <sub>bF</sub>	f <sub>oF</sub> <sup>2</sup>	h <sub>mF1</sub>	f <sub>oF1</sub> <sup>2</sup>	h <sub>mF2</sub>	f <sub>oF2</sub> <sup>2</sup>
			h <sub>sE</sub>	f <sub>sE</sub> <sup>2</sup>						
July 3410 220500	24	90	100.49	9.4374	174.96	10.199	234.08	79.841	317.88	121.73
225007	25		103.14	7.9861	171.11	8.2429	229.74	58.384	302.34	113.81
230507	26		105.55	8.9590	189.89	13.059	255.58	95.355	314.50	121.83
232007	27		104.21	8.1359	192.16	13.232	248.12	86.381	306.57	123.94
233507	28		98.583	7.7294	185.85	11.183	229.78	74.297	288.61	115.99
235007	29		100.22	4.9586	206.74	11.187	236.95	61.917	298.26	112.92
July 3410 000507	30		107.29	2.9741	204.06	9.5405	243.16	71.957	302.33	105.23
002007	31	100	100.09	4.5911	181.60	1.1916	250.30	74.641	307.91	98.363
003507	32	90	98.046	4.6670	199.01	1.9745	255.47	75.951	291.81	91.097
005007	33		106.41	6.5866	190.21	7.7399	238.80	53.154	299.39	86.003
010507	34		97.849	3.4595	189.80	3.2321	239.86	57.090	290.17	77.707
012007	35		103.86	5.0675	190.51	4.1293	246.89	47.705	296.15	62.397
013507	36	90	95.523	2.8793	193.01	0	247.63	35.643	295.40	54.455
015007	37	90	125.56	0	212.80	3.3818	262.41	43.528	302.75	53.779
			97.133	2.2746						
020507	38		98.495	1.9411	188.74	6.0762	210.18	22.810	278.39	49.257
022007	39		122.36	0	201.17	8.3775	225.19	21.057	269.86	43.759
			97.285	2.0057						
023507	40	100	136.37	0	209.97	0.0145	238.10	24.031	275.26	32.423
			110.88	2.0386						
030507	41	100	114.79	0	205.12	0	247.16	16.302	288.75	24.263
			101.54	1.0594						
032007	42	100	120.94	0	200.94	8.0920	216.38	10.032	259.26	18.333
			102.04	1.5117						
033507	43	100	111.62	0	203.46	0	226.98	9.2963	301.65	16.279
			101.94	1.7147						
035007	44	100	105.47	0	213.18	0	244.72	9.0277	290.27	13.419
			100.0	1.4683						
040507	45	100	104.83	0	193.90	0	213.10	3.4726	323.05	12.235
			100.0	1.4446						

DATA PAPER (11 COLUMN) HDW-GEN-3900/2(544)

GPO 936-172

Table 6 — True height profile calculations — Zone 4

$h_b E = 90 \text{ km. (this page)}$

Time(HMS)	No	$h_m E$	$f_o E^2$	$h_o E$	$f_b E^2$	$h_m F1$	$f_o F1$	$h_m F2$	$f_b F2$
Day 340									
160003	1	114.11	8.0534	168.47	7.0512	203.85	32.605	265.54	90.202
161502	2	118.20	6.7743	188.25	1.1744	223.16	57.392	294.32	92.489
163041	3	106.88	6.7048	164.98	8.1587	240.84	90.162	293.77	104.48
164502	4	117.87	5.3748	201.02	6.7993	238.08	82.620	293.87	116.05
170002	5	117.83	4.2194	172.57	10.923	215.87	64.220	274.63	121.50
171502	6	119.58	5.2666	215.34	24.658	240.04	81.415	294.25	143.23
173002	7	117.69	5.1700	208.01	23.224	248.18	122.97	317.89	144.55
174502	8	119.91	6.5244	194.68	16.677	242.14	105.87	333.13	139.91
180003	9	117.07	5.0657	187.64	16.902	248.37	105.60	305.26	133.20
181503	10	116.98	12.688	154.18	14.133	215.37	61.288	292.70	142.01
184500	11	118.40	11.068	183.00	12.860	230.08	106.62	283.63	159.18
190000	12	118.76	11.517	180.26	22.378	226.98	118.57	283.73	159.12
191500	13	118.51	13.343	196.10	25.739	231.83	103.25	292.13	167.96
193000	14	117.96	10.794	178.19	20.651	225.05	102.40	283.97	170.98
194500	15	120.45	11.084	181.54	23.735	220.76	105.39	297.53	166.82
200000	16	107.67	10.884	176.78	18.490	226.15	106.54	291.32	163.79
201500	17	117.26	13.431	166.91	13.967	208.63	82.475	296.73	153.90
203000	18	116.47	11.954	173.97	16.717	225.57	90.709	298.54	142.21
204500	19	118.28	14.169	159.32	18.961	222.78	102.59	277.11	137.69
210000	20	117.72	12.662	183.57	25.896	220.96	86.290	289.92	141.35
211500	21	116.52	12.008	170.94	16.547	244.60	110.92	318.03	141.16
213000	22	118.02	12.292	170.24	13.039	240.16	105.27	308.38	135.74
214500	23	120.12	9.728	191.85	12.493	259.57	108.17	316.10	135.19
220000	24	118.42	11.761	180.19	19.495	212.15	66.556	312.84	135.70
221500	25	116.35	10.001	182.53	17.136	220.84	69.317	311.18	130.15
223000	26	116.84	9.0467	196.40	19.265	242.82	89.586	295.35	128.80
230002	27	118.51	8.1094	204.43	12.706	245.95	96.577	290.54	124.80
231502	28	116.89	7.7379	200.13	17.257	265.35	109.72	312.93	132.40



**Table 6 (Cont'd) – True height profile calculations – Zone 4**

Day  
341

Time	No.	h <sub>0</sub> E	h <sub>1</sub> mE	f <sub>0</sub> E <sup>2</sup>	h <sub>0</sub> F	f <sub>0</sub> F <sup>2</sup>	h <sub>1</sub> mF1	f <sub>0</sub> F1 <sup>2</sup>	h <sub>1</sub> mF2	f <sub>0</sub> F2 <sup>2</sup>
			h <sub>1</sub> SE	f <sub>1</sub> SE <sup>2</sup>						
233002	29	90	117.12	21252	198.55	9.9244	245.83	81.389	304.32	124.96
234503	30	90	120.52	56138	187.17	9.5273	212.06	51.515	268.81	99.013
200003	31		118.53	6.6642	196.62	7.4470	225.63	52.491	289.41	101.57
011502	32	90	171.35	.03524	219.08	11.755	252.79	67.608	308.94	96.258
			116.28	4.4413						
003002	33		118.54	71325	169.35	5.0580	234.80	39.798	289.32	89.669
004502	34		153.30	0	216.90	6.4606	236.74	43.803	293.27	75.692
			116.94	2.9086						
010002	35		116.77	3.3001	189.93	2.2723	246.64	46.944	293.68	68.548
011502	36		118.21	4.9984	209.72	7.5691	247.65	39.487	293.21	58.438
014502	37		116.86	.99613	212.54	2.8687	247.13	18.779	293.78	55.250
020002	38		118.51	1.1310	209.03	5.2371	242.36	32.245	298.31	49.063
021503	39		121.85	1.1697	209.27	4.4560	231.32	17.746	280.74	45.185
023003	40		118.40	1.2529	194.19	3.1372	228.56	28.030	265.72	37.089
030002	41		131.05	0	216.61	.00236	248.03	20.451	266.40	23.319
			117.15	.8914						
031502	42		127.83	0	198.45	.05182	218.39	10.012	252.40	16.154
			116.66	.8936						
033002	43		129.29	0	191.28	0	249.93	10.220	327.06	16.822
			118.74	.8441						
034502	44		135.45	0	226.14	0	262.97	10.116	308.01	16.233
			123.59	.9491						
040003	45		129.18	0	208.08	.1460	244.51	9.1902	300.10	16.015
			122.71	.5175						
041502	46		130.72	0	221.01	0	241.96	5.2595	305.11	16.648
			118.70	.9614						
						</				

DATA PAPER (11 COLUMNS) NPD-GEM-3900/215-44)

GPO 936-172

Table 7 — True height profile calculations — Zone 5

$h_b E = 90 \text{ km}$  (this page)

Time (HMS)		No.	$h_m E$	$f_o E^2$	$h_b F$	$f_o F^2$	$h_m F1$	$f_o F1^2$	$h_m F2$	$f_o F2^2$
Day 340	160517	1	111.44	7.2980	186.16	5.4091	213.41	63.735	234.41	80.503
	162017	2	105.45	7.1628	170.16	1.9966	208.72	58.013	260.97	84.767
	163517	3	106.47	8.1595	172.17	7.4276	212.90	67.685	250.63	89.599
	165017	4	112.00	8.4195	182.72	8.6389	213.07	59.009	267.02	103.35
	170517	5	107.57	8.9341	176.67	8.6787	202.48	56.701	250.45	100.97
	172017	6	108.72	9.4308	168.34	10.473	210.50	62.988	283.80	115.36
	173517	7	105.45	9.6001	178.37	13.651	226.15	91.777	263.29	121.71
	175017	8	109.54	10.537	186.64	21.675	216.35	82.527	263.19	130.07
	180517	9	107.14	10.026	173.03	11.582	218.96	87.462	276.32	134.18
	182017	10	111.99	10.637	194.35	19.736	219.59	72.723	279.98	134.46
	185011	11	110.04	13.136	161.60	15.506	218.15	71.071	267.04	138.42
	190500	12	112.43	12.941	189.72	20.464	241.74	107.92	300.70	140.87
	192000	13	113.33	13.577	169.76	18.279	223.71	77.214	279.53	142.81
	193500	14	112.86	11.513	178.73	24.765	217.91	85.784	288.83	140.35
	195000	15	114.69	13.054	179.48	17.533	226.79	80.855	292.92	139.40
	200500	16	106.23	11.413	176.20	15.623	222.98	71.321	313.90	160.60
	202000	17	102.57	9.140	190.50	21.890	221.48	71.772	282.65	155.25
	203500	18	105.04	13.282	170.76	8.5367	210.13	59.361	278.95	146.28
	205000	19	109.62	10.024	184.59	4.0318	218.41	29.243	283.78	137.66
	210500	20	110.75	12.624	174.80	14.938	196.77	51.122	287.80	125.58
	212000	21	110.14	12.166	172.93	11.827	196.64	42.198	338.62	132.46
	213500	22	104.92	11.127	141.99	9.8470	221.38	55.767	288.42	128.20
	215000	23	105.82	9.8793	197.25	21.767	224.30	82.029	277.35	121.60
	220500	24	111.77	11.350	180.32	10.478	218.26	61.253	317.10	120.99
	222000	25	107.81	10.353	165.85	10.398	212.55	54.669	285.72	109.10
	223500	26	97.135	7.7584	163.21	3.3101	219.94	56.454	288.72	103.43
	225017	27	106.36	9.0488	167.83	8.0595	223.22	60.202	305.25	106.69
	230517	28	103.92	7.6162	172.42	5.7734	250.56	86.316	302.11	106.99
	232017	29	101.27	7.7309	179.58	10.422	248.93	83.172	295.97	119.21

**Table 7 (Cont'd) – True height profile calculations – Zone 5**

Time	No.	h <sub>b</sub> E	h <sub>m</sub> E h <sub>s</sub> E	f <sub>o</sub> E <sup>2</sup> f <sub>s</sub> E <sup>2</sup>	h <sub>b</sub> F	f <sub>o</sub> F <sup>2</sup>	h <sub>m</sub> F1	f <sub>o</sub> F1 <sup>2</sup>	h <sub>m</sub> F2	f <sub>o</sub> F2 <sup>2</sup>
Day 340										
2335/17	30	90	102.19	5.7004	195.62	13.452	249.46	96.149	281.52	115.12
2350/17	31		107.45	4.7068	179.11	5.2675	231.39	83.085	291.46	114.61
Day 341										
0005/17	32		99.863	2.2571	186.08	8.7079	216.33	54.923	278.92	102.30
0020/17	33		97.591	2.1090	172.94	6.8647	230.40	59.804	289.09	101.84
0035/17	34		105.40	2.0149	200.62	8.5510	232.91	58.014	279.71	93.506
0050/17	35		96.453	1.4714	177.53	4.6124	239.76	63.553	281.17	82.789
0105/17	36		121.00	0	205.06	6.93965	252.36	58.676	291.01	78.671
			99.631	1.7098						
0120/17	37	100	127.78	0	205.05	0.11585	233.01	37.386	282.22	68.730
			105.90	1.7506						
0135/17	38	100	119.18	0	212.56	0	223.13	20.601	295.35	55.535
			102.79	1.3122						
0150/17	39	100	123.85	0	203.03	0	240.23	29.528	296.01	51.418
			102.62	1.6987						
0205/17	40	100	116.93	0	210.69	0.12787	241.91	13.127	294.84	50.450
			101.91	1.2015						
0220/17	41	100	125.12	0	197.84	2.0243	228.00	30.672	265.56	44.532
			103.84	1.7020						
0235/17	42	100	121.86	0	211.01	0.00016	228.28	22.547	262.11	34.863
			103.79	1.4462						
0250/17	43	100	118.35	0	180.00	0	214.67	14.679	286.42	29.705
			102.07	1.3019						
0305/17	44	100	116.37	0	183.62	0	206.61	11.971	260.92	21.606
			100.0	1.3155						
0320/17	45	100	131.88	0	179.29	0	212.37	6.9971	292.44	20.559
			105.61	2.1020						
0335/17	46	100	123.65	0	206.44	0	224.96	9.5281	275.29	17.372
			101.88	1.7420						
0350/17	47	100	114.14	0	236.21	0	249.34	6.1917	282.57	14.277
			102.94	1.8964						
0405/17	48	100	117.73	0	188.87	0.1181	220.90	6.8643	273.03	12.386
			100.20	1.4021						

DATA PAPER (11 COLUMN) NDT-GEN-9908'21544)

GPO 026-172

Table 8 — True height profile calculations — Zone 6

$h_b E = 90 \text{ km. (this page)}$

Time (HMS)		No.	$h_m E$	$f_o E^2$	$h_b F$	$f_o F^2$	$h_m F1$	$f_o F1^2$	$h_m F2$	$f_o F2^2$
Day	16 10 12	1	109.32	5.6033	168.70	5.3227	218.76	42.132	260.20	74.065
340	16 25 40	2	111.66	5.9261	197.06	14.205	215.00	45.394	265.57	89.133
	16 40 12	3	110.97	6.3061	185.51	11.180	205.71	40.851	261.15	89.697
	16 55 12	4	112.77	6.6604	177.47	10.150	205.07	33.495	249.16	86.936
	17 10 12	5	104.23	7.3045	155.91	12.380	219.47	64.922	289.17	98.562
	17 25 12	6	113.68	9.1487	200.09	12.708	225.37	58.064	262.90	91.464
	17 40 12	7	110.98	7.0115	170.97	2.3357	218.33	35.877	265.63	106.07
	17 55 12	8	109.38	9.2849	176.53	7.4150	217.79	67.066	298.41	107.10
	18 10 12	9	100.50	7.2050	164.53	14.550	204.44	54.257	303.09	122.52
	18 25 12	10	100.68	7.9156	165.11	10.121	236.45	98.441	275.83	122.29
	18 40 00	11	104.30	9.2544	197.95	22.928	246.52	123.73	263.09	134.87
	18 55 00	12	111.22	10.629	188.29	16.938	242.14	111.62	280.64	131.76
	19 10 00	13	101.42	9.3342	187.65	12.290	223.82	84.691	290.42	143.18
	19 25 00	14	108.77	10.680	186.54	11.617	248.27	117.41	279.85	145.12
	19 40 00	15	107.42	10.889	178.53	17.287	247.28	120.11	323.50	163.30
	19 55 00	16	104.49	12.323	172.16	17.460	248.36	133.83	282.10	159.00
	20 10 00	17	110.81	11.593	150.10	13.082	207.77	47.979	267.90	149.86
	20 25 00	18	106.21	10.566	209.27	27.993	225.31	87.136	288.39	143.34
	20 40 00	19	98.575	8.8695	172.06	13.702	224.16	100.24	288.82	153.10
	20 55 00	20	99.287	9.6843	169.01	9.5530	207.57	75.502	286.75	142.42
	21 10 00	21	104.16	10.006	159.14	9.9892	222.03	91.435	298.15	139.78
	21 25 00	22	98.825	9.1456	177.10	9.1245	219.10	74.184	306.03	140.67
	21 40 00	23	100.43	8.7036	164.75	7.6917	241.74	102.17	305.05	131.30
	21 55 00	24	98.079	8.1333	188.98	20.656	226.93	80.992	284.61	126.32
	22 10 00	25	97.697	7.1832	182.30	11.366	243.53	99.253	335.91	151.78
	22 25 00	26	99.066	7.0772	186.41	7.8361	255.71	114.68	290.35	134.98
	22 55 12	27	100.42	5.5534	182.72	13.235	245.60	104.44	320.71	138.25
	23 10 12	28	107.57	6.5593	198.41	17.833	227.25	70.785	292.03	129.74

**Table 8 (Cont'd) – True height profile calculations – Zone 6**

Time	No.	h <sub>b</sub> E	h <sub>s</sub> E	f <sub>s</sub> E <sup>2</sup>	h <sub>b</sub> F	f <sub>b</sub> F <sup>2</sup>	h <sub>m</sub> F1	f <sub>o</sub> F1 <sup>2</sup>	h <sub>m</sub> F2	f <sub>o</sub> F2 <sup>2</sup>
232512	29	90	103.48	6.3688	208.04	5.0167	249.94	83.436	317.16	123.03
234012	30		100.82	8.0414	180.42	8.4724	243.68	76.479	294.93	121.30
235312	31		98.955	5.0156	187.98	11.997	239.18	83.536	287.69	107.71
Day 341										
001012	32		103.96	6.3292	207.99	6.8836	251.05	72.115	306.36	113.46
002512	33		102.80	5.7533	206.52	4.1002	239.20	63.239	280.73	100.44
004012	34		98.365	4.8596	184.54	4.0736	244.30	72.854	276.21	86.586
005512	35		96.157	4.0490	189.26	3.2918	238.67	52.938	328.18	87.616
011012	36		100.02	4.1185	198.20	10.763	235.91	47.442	279.82	68.546
012512	37		148.01	0	193.40	3.8537	234.70	38.137	315.91	59.623
			102.81	3.6155						
014012	38		99.746	3.0173	198.07	1.9931	251.46	37.415	298.69	50.766
015512	39		139.17	0	213.60	2.4240	289.04	41.053	311.51	43.671
			103.18	2.8788						
021012	40		101.19	2.3352	206.77	8.0163	242.56	27.837	307.38	48.356
022512	41		114.62	0	232.53	151.38	246.36	19.228	273.01	37.908
			97.340	1.3824						
024012	42	100	116.75	0	204.35	1.07875	229.55	21.690	278.79	33.607
			104.15	1.0080						
031012	43	100	116.84	0	217.99	0	250.15	20.758	280.15	26.658
			103.52	1.0657						
032512	44	100	116.84	0	203.64	0	222.75	13.235	258.96	21.711
			103.83	1.0404						
034012	45	100	109.03	0	184.43	1.02688	208.04	9.6441	246.52	13.697
			101.77	1.5812						
035512	46	100	110.94	0	179.47	0	213.83	4.4904	236.47	11.253
			102.06	1.7105						
041012	47	100	110.43	0	203.16	0	215.35	5.8887	248.63	8.5091
			100.0	1.8556						

DATA PAPER (1) COLUMN(1) NDB-604-959/21-40

SP9 936-172

nighttime hours, as expected. Further, these curves are shifted with respect to each other for the different paths in a manner consistent with solar zenith angle variations. The sun is most directly overhead at different universal times (Greenwich Meridian Time) for the six midpath points. The solar zenith angle  $\chi$  at an observation point is the angle made by the line of sight from the observation point to the sun with the vertical, which is directly overhead from the observation point. From the observed dependence it is expected that if an ionospheric parameter were plotted as a function of  $\cos \chi$ , or some power of it, the dependence might appear as a noisy variation about a straight line. This straight line would be a trend line from which a prediction of the ionospheric parameter could be simply made. Evidently, the daytime dependence on solar zenith angle is more fundamental than the dependence on time.

The transformation from time to solar zenith angle at an observation point is part of MINIMUF [Rose, Martin, and Levine, 1978a], a computerized algorithm for predicting F MUF values, based on a statistical ionospheric model with sunspot number as the driving parameter. Later updates of this algorithm are contained in [Rose and Martin, 1978b; Rose, 1979; Sailors (1-6), 1984]. Part of the algorithm has been used to convert universal time to  $\cos \chi$  and  $\cos \chi_{\text{eff}}$  at F2 layer heights. Here,  $\chi$  is the actual solar zenith angle and  $\chi_{\text{eff}}$  is the effective solar zenith angle. The latter incorporates a correction for the well-known lag between the solar source term and the ionospheric response in the upper F layer region. For the time period of interest, the lag effect is small; calculated actual and effective solar zenith angles are nearly equal. The plan is to plot ionospheric parameters associated with the upper F layer region (i.e.,  $h_m F1$ ,  $f_o F1^2$ ,  $h_m F2$ ,  $f_o F2^2$ , and  $Y2$ ) as a function of  $\cos \chi_{\text{eff}}$ , or some power of it, and the other parameters as a function of  $\cos \chi$ , or some power of it. The conversion from time to actual and effective solar zenith angles is given for midpath points X1-X6 of Figure 2 in Tables 9-14.

In deciding what power of  $\cos \chi$  to use as the independent variable, one may recall the predictions of the simple Chapman Layer Theory [e.g., Chamberlain, 1978], whereby the rate equation for electron density  $N_m$  at the maximum of the layer, which is directly proportional to  $f_m^2$  at the maximum, can be written as

$$\frac{dN_m}{dt} = C + q \cos \chi - L, \quad (7)$$

where  $C$  is a constant source term which is not dependent on  $\chi$ ,  $q$  is a constant in another source term which gives the solar influence, and  $L$  is a loss term which has one of two common forms:

$$L = \begin{aligned} & \alpha N_m^2 && (\alpha\text{-layer}) \\ & \beta N_m && (\beta\text{-layer}) \end{aligned} \quad (8)$$

In quasi-equilibrium, which applies to ionospheric layers most of the time, the left side of (7) can be approximately set to zero. The result is that  $N_m^2$  varies linearly with  $\cos \chi$  in  $\alpha$ -layer theory, and  $N_m$  varies linearly with  $\cos \chi$  in  $\beta$ -layer theory.

Chapman-Layer theory is too simplified for the upper F layer region of the ionosphere, where other source terms arise from diffusive transport along and, to a lesser extent, across magnetic field lines. Nevertheless, it will be of

Table 9 — Time to solar zenith angle — Path 1 (cf. Table 3)

## X1 Coordinates:

LAT= 36.1745 LON(W)= 119.6655  
MO= 12 DY= 6

No.	HOUR(UT)		COS(X)	COS(XEFF)
1	15.9219	Day	0.277201	0.265900
2	16.1719	340	0.304440	0.293593
3	16.4219		0.330445	0.320096
4	16.6719		0.355111	0.345302
5	16.9219		0.378337	0.369107
6	17.1719		0.400029	0.391417
7	17.4219		0.420099	0.412139
8	17.6719		0.438467	0.431191
9	17.9219		0.455056	0.448494
10	18.1719		0.469801	0.463980
11	18.4219		0.482642	0.477584
12	18.6719		0.493526	0.489252
13	18.9167		0.502242	0.498753
14	19.1667		0.509132	0.506459
15	19.4219		0.514037	0.512208
16	19.6719		0.516735	0.515740
17	19.9167		0.517347	0.517172
18	20.1667		0.515897	0.516561
19	20.4219		0.512259	0.513776
20	20.6667		0.506737	0.509067
21	20.9167		0.499065	0.502215
22	21.1667		0.489369	0.493327
23	21.4167		0.477689	0.482438
24	21.6667		0.464072	0.469594
25	21.9167		0.448575	0.454847
26	22.1667		0.431258	0.438255
27	22.4167		0.412194	0.419887
28	22.9219		0.368648	0.377650
29	23.1719		0.344798	0.354394
30	23.4219		0.319551	0.329702
31	23.6719		0.293008	0.303673
32	23.9219		0.265277	0.276413
33	0.1719	Day	0.236471	0.248032
34	0.4219	341	0.206706	0.218646
35	0.6719		0.176103	0.188374
36	0.9219		0.144787	0.157337
37	1.1719		0.112883	0.125663
38	1.4219		0.080522	0.093480
39	1.6719		0.047834	0.060917
40	1.9219		0.014952	0.028108
41	2.1719		0.014952	0.012302
42	2.4219		0.014952	0.010856
43	2.6719		0.014952	0.009580
44	3.1717		0.014952	0.007462
45	3.4219		0.014952	0.006585
46	3.6719		0.014952	0.005811
47	3.9219		0.014952	0.005128
48	4.1719		0.014952	0.004525

Table 10 — Time to solar zenith angle — Path 2 (cf. Table 4)

X2 Coordinates:

LAT= 36.4979      LON(W)= 118.3753

MO= 12      DY= 6

No.	HOUR(UT)		COS(X)	COS(XEFF)
1	16.0042	Day	0.292350	0.281428
2	16.2542	340	0.318583	0.308141
3	16.5042		0.343522	0.333602
4	16.7542		0.367064	0.357706
5	17.0042		0.389114	0.380357
6	17.2542		0.409582	0.401461
7	17.5042		0.428385	0.420933
8	17.7542		0.445447	0.438695
9	18.0042		0.460698	0.454673
10	18.2542		0.474077	0.468803
11	18.7542		0.495006	0.491295
12	19.0042		0.502472	0.499567
13	19.2500		0.507821	0.505721
14	19.5000		0.511214	0.509940
15	19.7500		0.512529	0.512087
16	20.0000		0.511761	0.512151
17	20.2542		0.508847	0.510083
18	20.5000		0.503995	0.506044
19	20.7500		0.497028	0.499896
20	21.0000		0.488042	0.491716
21	21.5000		0.464162	0.469401
22	21.7500		0.449365	0.455357
23	22.0000		0.432742	0.439462
24	22.2500		0.414360	0.421781
25	22.5000		0.394293	0.402385
26	23.0042		0.349041	0.358382
27	23.2542		0.324414	0.334318
28	23.5042		0.298468	0.308895
29	23.7542	Day	0.271309	0.282217
30	0.0042	341	0.242760	0.254075
31	0.2544		0.213552	0.225258
32	0.5042		0.183541	0.195589
33	0.7542		0.152749	0.165091
34	1.0042		0.121335	0.133921
35	1.2544		0.089392	0.102170
36	1.5042		0.057156	0.070074
37	1.7542		0.024651	0.037657
38	2.0042		0.024651	0.012646
39	2.2542		0.024651	0.011160
40	2.5042		0.024651	0.009849
41	2.7542		0.024651	0.008691
42	3.0042		0.024651	0.007670
43	3.2542		0.024651	0.006769
44	3.5042		0.024651	0.005974
45	3.7542		0.024651	0.005272
46	4.0042		0.024651	0.004652
47	4.2542		0.024651	0.004106



Table 11 — Time to solar zenith angle — Path 3 (cf. Table 5)

## X3 Coordinates:

LAT= 35.1834      LON(W)= 116.9689  
 MO= 12      DY= 6

No.	HOUR(UT)		COS(X)	COS(XEFF)
1	16.0853	Day	0.324808	0.313914
2	16.3353	340	0.350867	0.340500
3	16.5853		0.375516	0.365716
4	16.8353		0.398654	0.389463
5	17.0853		0.420190	0.411643
6	17.3353		0.440036	0.432169
7	17.5853		0.458113	0.450956
8	17.8353		0.474348	0.467930
9	18.0853		0.488676	0.483023
10	18.3353		0.501039	0.496174
11	18.8333		0.519622	0.516383
12	19.0833		0.525841	0.523438
13	19.3333		0.529945	0.528389
14	19.5833		0.531919	0.531215
15	19.8333		0.531754	0.531905
16	20.0833		0.529450	0.530457
17	20.3333		0.525018	0.526876
18	20.5833		0.518475	0.521176
19	20.8333		0.509847	0.513381
20	21.0833		0.499169	0.503521
21	21.3333		0.486484	0.491637
22	21.5833		0.471843	0.477776
23	21.8333		0.455305	0.461994
24	22.0833		0.436936	0.444354
25	22.8353		0.371431	0.380851
26	23.0853		0.346535	0.356549
27	23.3353		0.320246	0.330814
28	23.5853		0.292670	0.303748
29	23.8353		0.263916	0.275460
30	0.0853	Day 341	0.233905	0.245839
31	0.3353		0.203224	0.215530
32	0.5853		0.171725	0.184353
33	0.8353		0.139534	0.152433
34	1.0853		0.106781	0.119900
35	1.3353		0.073599	0.086884
36	1.5853		0.040120	0.053518
37	1.8353		0.006479	0.019937
38	2.0853		0.006479	0.012170
39	2.3353		0.006479	0.010740
40	2.5853		0.006479	0.009478
41	3.0853		0.006479	0.007382
42	3.3353		0.006479	0.006514
43	3.5853		0.006479	0.005749
44	3.8353		0.006479	0.005073
45	4.0853		0.006479	0.004477

Table 12 — Time to solar zenith angle — Path 4 (cf. Table 6)

x4 Coordinates:

LAT= 38.673      LON(W)= 113.5913

MO= 12      DY= 6

No.	HOUR(UT)		COS(X)	COS(XEFF)
1	16.0008	Day	0.301289	0.291490
2	16.2506	340	0.324639	0.315342
3	16.5114		0.347594	0.338863
4	16.7506		0.367268	0.359090
5	17.0006		0.386343	0.378777
6	17.2506		0.403819	0.396896
7	17.5006		0.419623	0.413371
8	17.7506		0.433689	0.428134
9	18.0008		0.445972	0.441138
10	18.2508		0.456393	0.452300
11	18.7500		0.471513	0.468946
12	19.0000		0.476173	0.474388
13	19.2500		0.478862	0.477866
14	19.5000		0.479568	0.479365
15	19.7500		0.478288	0.478879
16	20.0000		0.475027	0.476410
17	20.2500		0.469800	0.471969
18	20.5000		0.462627	0.465573
19	20.7500		0.453538	0.457249
20	21.0000		0.442571	0.447032
21	21.2500		0.429772	0.434963
22	21.5000		0.415193	0.421094
23	21.7500		0.398895	0.405481
24	22.0000		0.380945	0.388188
25	22.2500		0.361418	0.369289
26	22.5000		0.340394	0.348860
27	23.0006		0.294156	0.303706
28	23.2506		0.269185	0.279218
29	23.5006		0.243099	0.253574
30	23.7508		0.215976	0.226850
31	0.0008	Day	0.187738	0.198934
32	0.2506	341	0.159079	0.170582
33	0.5006		0.129728	0.141490
34	0.7506		0.099840	0.111812
35	1.0006		0.069537	0.081670
36	1.2506		0.038946	0.051189
37	1.7506		0.038946	0.011231
38	2.0006		0.038946	0.009911
39	2.2508		0.038946	0.008745
40	2.5008		0.038946	0.007718
41	3.0008		0.038946	0.006011
42	3.2506		0.038946	0.005305
43	3.5006		0.038946	0.004682
44	3.7506		0.038946	0.004132
45	4.0008		0.038946	0.003646
46	4.2506		0.038946	0.003218

Table 13 — Time to solar zenith angle — Path 5 (cf. Table 7)

## X5 Coordinates:

LAT= 34.7007 LON(W)= 119.437  
MO= 12 DY= 6

No.	HOUR(UT)	COS(X)	COS(XEFF)
1	16.0881 Day	0.312181	0.300857
2	16.3381 340	0.339366	0.328546
3	16.5881	0.365192	0.354920
4	16.8381	0.389555	0.379872
5	17.0881	0.412359	0.403303
6	17.3381	0.433510	0.425119
7	17.5881	0.452926	0.445232
8	17.8381	0.470527	0.463562
9	18.0881	0.486244	0.480035
10	18.3381	0.500014	0.494586
11	18.8364	0.521441	0.517632
12	19.0833	0.529003	0.526020
13	19.3333	0.534553	0.532419
14	19.5833	0.537962	0.536685
15	19.8333	0.539217	0.538802
16	20.0833	0.538312	0.538760
17	20.3333	0.535251	0.536562
18	20.5833	0.530047	0.532214
19	20.8333	0.522720	0.525734
20	21.0833	0.513299	0.517150
21	21.3333	0.501822	0.506494
22	21.5833	0.488336	0.493809
23	21.8333	0.472894	0.479147
24	22.0833	0.455558	0.462566
25	22.3333	0.436398	0.444132
26	22.5833	0.415489	0.423920
27	22.8381	0.392475	0.401580
28	23.0881	0.368301	0.378030
29	23.3381	0.342651	0.352966
30	23.5881	0.315629	0.326489
31	23.8381	0.287343	0.298704
32	0.0881 Day	0.257674	0.269461
33	0.3381 341	0.227280	0.239475
34	0.5881	0.195974	0.208528
35	0.8381	0.163882	0.176745
36	1.0881	0.131132	0.144253
37	1.3381	0.097857	0.111183
38	1.5881	0.064189	0.077667
39	1.8381	0.030264	0.043839
40	2.0881	0.030264	0.013429
41	2.3381	0.030264	0.011851
42	2.5881	0.030264	0.010458
43	2.8381	0.030264	0.009229
44	3.0881	0.030264	0.008145
45	3.3381	0.030264	0.007188
46	3.5881	0.030264	0.006343
47	3.8381	0.030264	0.005598
48	4.0881	0.030264	0.004940

Table 14 — Time to solar zenith angle — Path 6 (cf. Table 8)

**X6 Coordinates:**

LAT= 41.8965      LON(W)= 122.1268

MO= 12      DY= 6

No.	HOUR(UT)	COS(X)	COS(XEFF)
1	16.1700 <i>Day</i>	0.228846	0.219205
2	16.4278 <i>340</i>	0.252777	0.243542
3	16.6700	0.274222	0.265408
4	16.9200	0.295204	0.286861
5	17.1700	0.314928	0.307092
6	17.4200	0.333310	0.326014
7	17.6700	0.350272	0.343546
8	17.9200	0.365741	0.359615
9	18.1700	0.379651	0.374152
10	18.4200	0.391944	0.387094
11	18.6667	0.402436	0.398247
12	18.9167	0.411366	0.407864
13	19.1667	0.418543	0.415744
14	19.4167	0.423937	0.421852
15	19.6667	0.427524	0.426162
16	19.9167	0.429290	0.428657
17	20.1667	0.429226	0.429324
18	20.4167	0.427332	0.428163
19	20.6667	0.423618	0.425176
20	20.9167	0.418099	0.420378
21	21.1667	0.410798	0.413789
22	21.4167	0.401746	0.405436
23	21.6667	0.390983	0.395355
24	21.9167	0.378553	0.383590
25	22.1667	0.364511	0.370190
26	22.4167	0.348914	0.355213
27	22.9200	0.313079	0.320539
28	23.1700	0.293229	0.301219
29	23.4200	0.272130	0.280617
30	23.6700	0.249872	0.258818
31	23.9200	0.226548	0.235917
32	0.1700 <i>Day</i>	0.201805	0.211526
33	0.4200 <i>341</i>	0.176730	0.186791
34	0.6700	0.150900	0.161258
35	0.9200	0.124426	0.135037
36	1.1700	0.097421	0.108240
37	1.4200	0.069999	0.080980
38	1.6700	0.042279	0.053375
39	1.9200	0.014378	0.025541
40	2.1700	0.014378	0.010521
41	2.4200	0.014378	0.009284
42	2.6700	0.014378	0.008193
43	3.1700	0.014378	0.006381
44	3.4200	0.014378	0.005631
45	3.6700	0.014378	0.004970
46	3.9200	0.014378	0.004386
47	4.1700	0.014378	0.003870

some interest to see if the dependence of  $fO F2^4$  on  $\cos X_{\text{eff}}$  tends to be linear, as in the  $\alpha$ -layer theory, or if the dependence of  $fO F2^2$  on  $\cos X_{\text{eff}}$  is more nearly linear, as in the  $\beta$ -layer theory. In addition to these choices, the MINIMUF ionospheric model assumes that  $fO F2^2$  varies linearly with  $(\cos X_{\text{eff}})^{1/2}$ . These three choices have been investigated, as shown in the example of Figure 29, where calculated  $fO F2^2$  values for Path 1 in the time interval 1555-2210 (UT) have been plotted vs  $(\cos X_{\text{eff}})^{1/2}$ . These values, shown as pluses in Figure 29, are connected by straight lines, and the result is a noisy variation about a fairly well-defined background trend. This trend is generally upward with increasing values of the independent variable. It is believed that the noise present arises mainly from wave-like (e.g., TID's) disturbances in the ionosphere, or a superposition thereof, which are present much of the time. Some noisy appearance may result from calculational inaccuracies, which are difficult to assess. From the standpoint of making predictions of  $fO F2^2$ , it is the background trend in Figure 29 which is of interest [Reilly, 1984b]. Three dotted trend lines are shown in Figure 29. Trend Line 1 is a linear regression analysis (best linear least-squares fit) of the calculated  $fO F2^2$  values on  $(\cos X_{\text{eff}})^{1/2}$ , which corresponds to the MINIMUF form. Trend Line 2 shows some curvature on this plot, since it is determined from the linear regression analysis of  $fO F2^2$  on  $\cos X_{\text{eff}}$ , which corresponds to the  $\beta$ -layer theory. Trend Line 3 also shows curvature, since it is determined from the linear regression analysis of  $fO F2^4$  on  $\cos X_{\text{eff}}$ , which corresponds to  $\alpha$ -layer theory. Despite the different appearance of the three trend lines outside the region of calculations, all three fit the calculations quite well. Still, the fit of Trend Line 2 to the calculations is found to be somewhat better in this case, and in the  $fO F2^2$  variations for the five other paths, than the fit of Trend Lines 1 and 3. Indeed, it was found that the extrapolations based on Trend Line 3 were quite erroneous in some cases. All the other ionospheric parameters were treated similarly. The general conclusion was that, for simplicity, the choice of independent variable as  $\cos X$  or  $\cos X_{\text{eff}}$ , as in Trend Line 2, was advisable, since good fits and reasonable extrapolations were always obtained. For the display of results of the true height profile calculations, the independent variable  $\cos X_{\text{eff}}$  will subsequently be chosen for the parameters  $hmF1$ ,  $fO F1^2$ ,  $hmF2$ , and  $fO F2^2$ , and the corresponding Trend Line calculations will involve a linear regression analysis of these parameters on this independent variable. Similarly, the independent variable will be  $\cos X$  for the parameters  $hmE$ ,  $fO E^2$ ,  $hbF$ , and  $fbF^2$ . The difference between values of these two independent variables is very small for the time period of interest, but it can be significant for summertime operations.

Of further note in Figure 29 is the predicted behavior of  $fO F2^2$  from MINIMUF, shown for the observed 10.7 cm radio flux value of 210.4 for December 6, 1982. This translates to a sunspot number of 167. It is seen that the MINIMUF 3.5 line in Figure 29 intersects the calculated results in four places, so that sounder-determined  $fO F2^2$  results at these intersection points, if used to update MINIMUF 3.5 with an effective sunspot number [Uffelman, Harnish, and Goodman, 1984], would determine the MINIMUF line shown in Figure 29. This line is seen to have the wrong slope, which makes its usefulness for predictions questionable. Although MINIMUF is apparently based on an oversimplified ionospheric model [Reilly, 1984b], the preceding defect will likely be shared by all statistical models which are driven by only a few parameters, such as the sunspot number. It will be argued that the data from a configuration of sounders can be analyzed to give superior capability for HF propagation assessment.

Zone 1, Day 340, 15:55:19 - 22:10

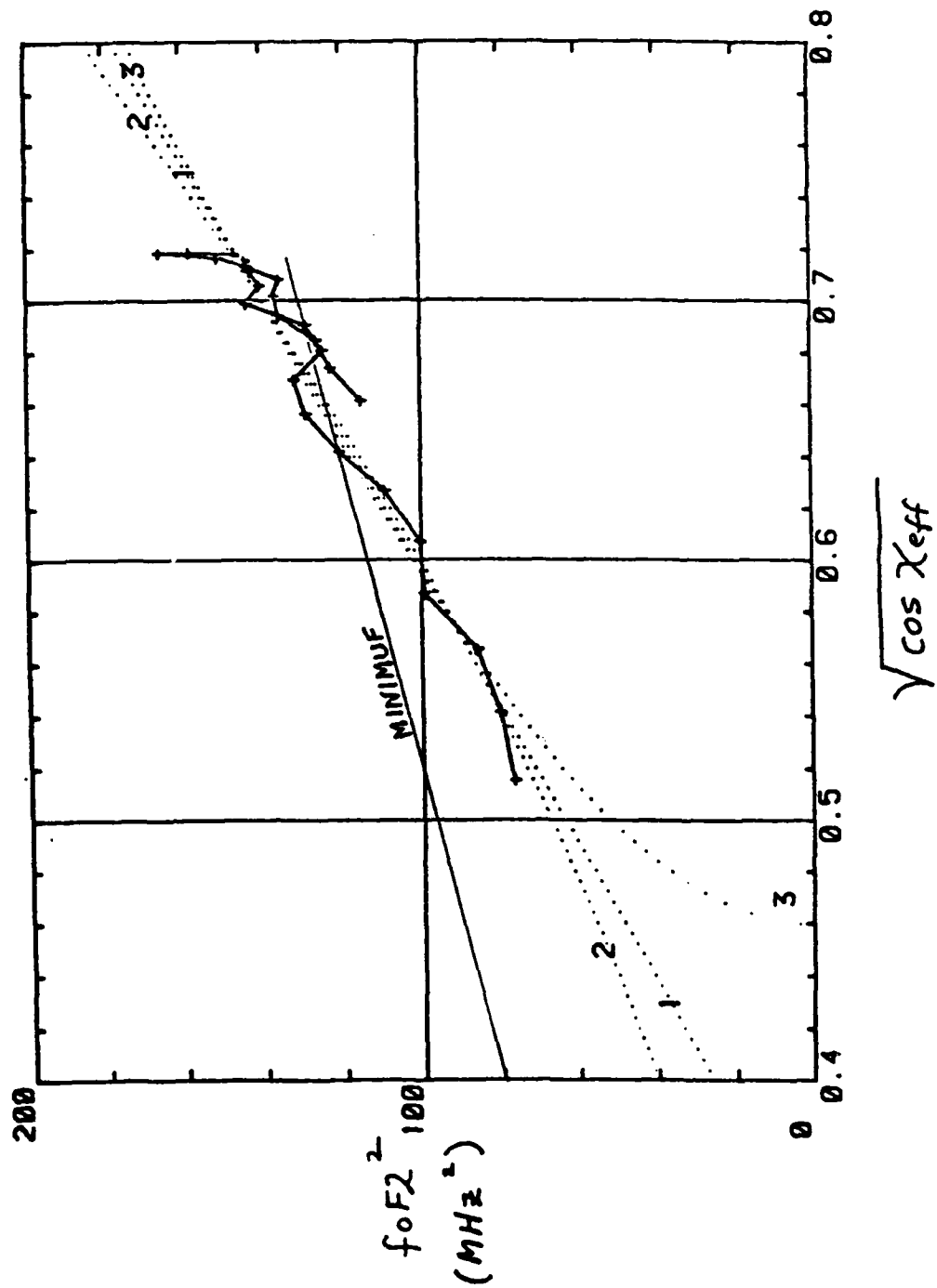


Fig. 29 — Solar zenith angle (effective) dependence of  $f_oF2^2$

Tables 3-14 can be used to plot the variation of the ionospheric parameters with either  $\cos X$  or  $\cos X_{\text{eff}}$ . These plots are displayed by parameter for all six paths in the Appendices. Appendix B displays the variation of  $fOF2^2$  with  $\cos X_{\text{eff}}$  for X1-X6, plus the corresponding results for the vertical-incidence sounders which were available for comparison. Appendix C displays the variation of  $hmF2$  with  $\cos X_{\text{eff}}$  for X1-X6, and Appendices D and E show this variation for  $fOF1^2$  and  $hmF1$ , respectively. The variation of the parameter  $fbF^2$  with  $\cos X$  is displayed in Appendix F for X1-X6, and corresponding plots for  $hbF$ ,  $fOE^2$ , and  $hmE$  are given in Appendices G, H, and I, respectively. The results are discussed next.

The results for  $fOF2^2$  vs.  $\cos X_{\text{eff}}$  are plotted in Appendix B. They are the pluses connected by the solid lines. Generally speaking, they appear as a slightly noisy variation about a roughly linear background variation. The results start out in the middle of the figure around 1600 UT (0800 PST), advance up the line at fifteen minute intervals to a maximum around 2000 UT and come back down the line until, at around 2200, the results advance up to a higher line and come down it to a point near the left margin of the figure, which corresponds to the beginning of nighttime conditions in the F2 layer at around 0200 UT (1800 PST). From here (until 0400 UT) the values tend to decrease along a steep line near the left margin. Calculated results are found at fifteen minute intervals. They are seen in these figures to be spread out more for larger solar zenith angles. Also shown in each figure is a set of dotted trend lines, each determined by a linear regression analysis (best linear least-squares fit) on a portion of the results. For example, in the results for X1, four such trend lines are shown. Trend line 1 (L1) is found by fitting points 1-9, and with the fifteen minutes/point conversion, this corresponds to the time interval 1600-1800 UT. Similarly, L2 is associated with 1600-2000, L3 with all the daytime points from 1600-0200, and L4 with 2300-0200. Greater detail of the correspondence between the plotted point and time can be found from Tables 3 and 9. Close inspection reveals that it takes 1-2 hours to establish a trend line that will be accurate for predictions ahead for one hour or more. Frequently (except for X6), the trend line established between 1600 and 1800 UT will be good until about 2200, near which there will be a transition up to a higher trend line. This trend line can be established between 2300 and 0030 UT, and it will be good until about 0200 in this case. For best accuracy the trend line should be updated as often as possible, but it is convenient that predictive capability is good one or more hours ahead. This allows more than enough time for the data to be collected and processed and for the trend line information to be disseminated to the field, where it is needed for the SSL or other HF system application.

Available vertical ionogram results were scaled for  $fOF2^2$  values, and these results are interspersed with the X1-X6 results in Appendix B. The NAS results were placed after the X1 results for comparison, as is logical from Figure 2. Similarly, VBG was put after X5. There was only one DRS ionogram, and the result of scaling it is shown in the X4 plot. The results for Fort Ord (R in Figure 2) are shown at the end of Appendix B. In general, the comparisons between calculated  $fOF2^2$  values for X1-X6 are in excellent agreement with corresponding results scaled from vertical ionograms.

Trend line information for the eight parameters in Appendices B-I is given by the A and B coefficients of

$$P_i = A(P_i) + B(P_i) \cos X_{\text{eff}} \quad (9)$$

$$(P_1 = fOF2^2, P_2 = hmF2, P_3 = fOF1^2, P_4 = hmF1)$$

or

$$P_i = A(P_i) + B(P_i) \cos X \quad (10)$$

$$(P_5 = fbF^2, P_6 = hbF, P_7 = fOE^2, P_8 = hmE)$$

Frequent updating of the A and B coefficients is advisable for optimum accuracy in a prediction scheme, but not necessarily too frequent in the case for  $fOF2^2$ , as just seen. Other parameters may require different treatment, as will be seen. The set of A and B coefficients for the ionospheric parameters will be of use to SSL and other HF systems in the field, as discussed later.

The effective solar zenith angle dependence of  $hmF2$  for points X1-X6 in Figure 2 is displayed in Appendix C. The dependence on  $\cos X_{eff}$  is mildly increasing in the morning (local time) and nearly constant in the afternoon. If the A and B coefficients are frequently updated, there should be no problem in using the associated trend lines for predictions. If, however, the trend lines are not frequently updated, and it is desired to use them for long-range predictions, special procedures are indicated. In this case, the results of Appendix C suggest that if a trend line is established (using, e.g., 1-2 hours of sounder measurements) during early morning hours, it should be used for predictions only during the morning hours (i.e., when  $\cos X_{eff}$  is increasing with time). When the trend line is established during the early afternoon hours for long-range afternoon predictions, it would be wise to assume that  $B(hmF2) = 0$ , in which case  $A(hmF2)$  is just given by the arithmetical average of the  $hmF2$  determinations. Trend lines L5 in the plots for X4-X6 show the pitfall which could otherwise develop.

The effective solar zenith angle dependence of  $fOF1^2$  is shown in Appendix D. Its appearance is similar to that for  $fOF2^2$ . The parameter increases roughly linearly with  $\cos X_{eff}$  in the morning and decreases, again roughly, linearly with this parameter in the afternoon until sunset, beyond which point the decrease is steeper in appearance. Frequent updating of the trend line is called for, but, in the absence of this, longer-range predictions with the determined trend lines have to be made. There are limitations to the success of this. A closer look at the dependence of  $fOF1^2$  reveals three segments: the linear increase in the morning, a transition segment in the early afternoon (e.g., between 2000 and 2200 UT), and subsequently a different linear decrease in the afternoon until sunset. The trend lines established in any one of these segments is not expected to predict well in the other segments. This applies similarly to  $fOF2^2$ . Predictions within a segment should be reasonably successful. The danger of using a trend line in the transition segment to predict in the late afternoon segment is shown by L5 in the X5 and X6 plots.

The plots for  $hmF1$  are shown in Appendix E. The background dependence of this parameter on solar zenith angle is weak. Frequent updating is again advisable, but, in lieu of this, long-range predictions based on  $B(hmF1) = 0$  should be quite successful and safe. If this is not assumed, the disparity between L1 and L2 for X4, and between L5 and L4 for X6 shows what could happen in long-range predictions.

The solar zenith angle dependence of  $fbF^2$  is shown in Appendix F. The same division of this dependence into three segments (morning, early afternoon, late afternoon) is seen here as for the other density parameters,  $fOF1^2$  and  $fOF2^2$ . In each of these segments the background dependence of  $fbF^2$  is increasing with  $\cos X$ , but, once again, the trend line in one



segment cannot be expected to necessarily predict well into other segments. Otherwise, the trend line predictions should work quite well.

Plots of  $hbF$  are contained in Appendix G. This height parameter, like the others, has only a weak dependence on solar zenith angle. Frequent updating of the trend lines will give optimum accuracy, but safe and acceptable long-range predictions can be made on the basis of the assumption that  $B(hbF)=0$ . The pitfall of making long-range predictions without this assumption is seen from L5 in the X5 plot.

The dependence of  $fOE^2$  on solar zenith angle is displayed in Appendix H. After sunrise this parameter exhibits a noisy increase up a line until noon when it starts to come back down a zigzag path about a similar line. In the evening it begins to intersect the horizontal axis, and in some cases is spiky in appearance at this point as sporadic E becomes the dominant contribution. This spikiness has to do with the treatment of the E layer in the true height profile calculation. Sometimes it is handled as in Figure 4, and sometimes as in Figure 8, where only a nominal E layer contribution is calculated. The X4 plot shows a particularly erratic behavior (e.g., L1) in the morning region, where only a weak portion of the E layer was visible on the ionograms. The spiky appearance toward sunset had to do with the ambiguity of where the regular, blanketing E layer left off and the thin, patchy sporadic E layer began. Frequent updating of the trend line is called for. For long-range predictions, the trend line determined should have positive slope, and is subject to the three-segment considerations discussed previously, although prediction from the first segment to the third seems better in this case than previously. A predicted negative value of  $fOE^2$  should be set to zero.

The parameter  $hmE$  is plotted in Appendix I. It is nearly constant until around sunset when it begins to jump up to higher values. Again, this marks the appearance of sporadic E layer conditions, and the conversion from Figure 4 to Figure 8 in the true height profile calculations. Frequent updating of the trend line is desired, but for long-range predictions of the E layer and the E-F transition region, the following type of procedure can be followed. A trend line can be established for  $fOE^2$  in the afternoon and used to predict values down to the horizontal axis. Similarly, a trend line can be established for  $hmE$  during the same afternoon period. It should have the characteristic that  $B(hmE) \approx 0$ , or else this condition can be rigorously enforced, to be safe. Hence, the point  $(fOE^2, hmE)$  is predicted, and the point  $(fbF^2, hbF)$  is similarly predicted from a trend line determination. The E-F transition line from the former point to the latter should have positive slope. If not, move  $(fOE^2, hmE)$  up the reentrant line with negative slope until the new E-F transition line is vertical. This will define the ionosphere up to the bottom of the F layer. The approximations involved are acceptable, if one recalls that the reentrant region is ambiguous anyway, the E layer calculations are approximate, and the important F layer calculations are insensitive to small alterations of the E layer.

It has been estimated in the preceding discussion of the plots that it might take one to two hours of sounder measurements to establish a trend line for the background dependence of an ionospheric parameter. The appearance of the parameter is noisy, and another guideline would be to process something like a full cycle of noise deviation to get the trend line information. The recommendations about how to use the trend lines for long-range predictions were based on analysis of data during a twelve hour period during December 6-7. Numerous other time periods remain to be analyzed, and the results will be of interest with regard to the preceding and further observations. For example, the nighttime situation has not been fully elucidated by the present analysis.

### 3D. Trend Lines Compared

A comparison of trend line behavior at the various sounder control points will provide some insight into how the information about the ionosphere at sounder control points (transmitter positions for vertical-incidence sounders and midpath points for oblique-incidence sounders) can be used to infer and predict the ionosphere along unsounded paths. Recall that there were basically three time segments in the daytime during each of which ionospheric trend lines could be established and used successfully: morning, early afternoon, and late afternoon. Trend lines for the first and third segments will be compared here. The first segment is given by the trend line L2 in Appendices B-I, which was established between 1600 and 2000 UT. The third segment is given by the trend line L4, which was established between about 2230 and 0200 UT, except for  $fO E^2$  for X2 and X4, where early afternoon hours were used. The trend line comparisons, by parameter, are shown in Appendix J.

The L2 plot for  $fOF2^2$  in Appendix J is considered first. The trend lines, other than 4 and 6, are close to each other, as expected by the proximity of the associated control points in Figure 2. Further, the lines seem to occur in the right order; 8 and 0 are close to 1, and 7 is close to 5. Curiously, 4 and 6 are close together here. One might try to justify this on the basis of the calculated magnetic dip angles. This angle is measured upward from the magnetic field vector at a point to the local horizontal plane. Values for X1-X6 are found to be  $61.7^\circ$ ,  $62.2^\circ$ ,  $61.3^\circ$ ,  $65.0^\circ$ ,  $60.4^\circ$ , and  $66.0^\circ$ , respectively. The formation dynamics of the upper F layer include a contribution of enhanced diffusion charge transport along magnetic field lines. Hence, in the vertical distribution of ionospheric charge and the parameters of the F2 layer, it stands to reason that there could be a dependence on magnetic dip angle. The L2 lines do seem to be strongly correlated to the magnetic dip angle in this case. In the next plot, i.e., the L4 lines of  $fOF2^2$ , it is found, however, that this correlation with magnetic dip angle is not as impressive. The slopes of the 6 and 4 lines differ substantially. The sounder control points in Figure 2, which are geographically in close proximity to each other, do again show strongly correlated trend behavior.

The next two plots show the trend lines for  $hmF2$ . The L2 trend lines show that this parameter tends to increase in the morning, and the L4 lines show that it tends to stay constant in the afternoon. Once more, the different slopes of L2 lines 4 and 6 tend to indicate that geographical proximity of an arbitrary point to each of the sounder control points is a more important consideration for a spatial interpolation scheme than the magnetic dip angle value in relation to these values for the sounder control points. The other trend lines of these plots are also consistent with this observation.

The trend line plots for  $fOF1^2$  are qualitatively similar to those for  $fOF2^2$ . The same comments apply. It is interesting that the L2 lines 4 and 6 are fairly close to each other again.

The trend line plots for  $hmF1$  follow. They are quite similar to the  $hmF2$  plots. The fact that the L2 line 2 is up with 4 and 6 may reflect the drift problem mentioned for sounder 2 in Section 2A, which would tend to cause overestimated values of the height parameters. Similarly, one cannot attach too much significance to the decreasing trend of L4 line 2 at this point.

The trend lines for  $fbF^2$  which follow tend to show a good deal more variation than seen in the preceding plots. There is virtually no apparent dependence on magnetic dip angle, nor is any expected this low in the F layer. The fact is that the lower ionospheric parameters are subject more to the vicissitudes of the true height profile calculations, including the E

layer approximations and a necessarily approximate reentrant procedure. This, and the fact that this parameter is part of a procedure for fitting an idealized profile to a calculated true height profile, appear to account for the variability in the  $fbF^2$  trend lines. Nevertheless, the trend line results are deemed to be useful in the interpolation scheme to be discussed later. There really is not very much variation in the  $hbF$  trend lines which follow. The parameter is nearly constant on a given trend line. The last two trend line plots are of the parameter  $fOE^2$ , which exhibit the strong solar dependence expected during the daytime period. The L4 lines 1 and 2 were determined using data in the early afternoon. Hence, they do not include data for which sporadic E behavior exerts an influence. The plots for  $hmE$  and  $hbE$  have not been included, but, disregarding the influence of sporadic E, they would appear to have only a very weak dependence on solar zenith angle. In fact,  $hbE=90$  km was the assumption about the bottom of the E layer under these conditions.

This leads into the question of the specification of the E layer under sporadic E conditions and nighttime conditions. Some consideration was given to this in Section 3C. A procedure would be to use the trend lines established in the afternoon without the influence of sporadic E conditions for  $hbE$ ,  $hmE$ , and  $fOE^2$ . Then, as previously discussed, the  $fOE^2$  trend line would be used to predict this parameter down to the horizontal axis ( $fOE^2=0$ ). The  $hmE$  trend line would predict  $hmE$ , and  $hbE=90$  km in this case. Then, if the line connecting ( $fOE^2$ ,  $hmE$ ) with ( $fbF^2$ ,  $hbF$ ) is reentrant, i.e., has negative slope, the former point could be moved up a reentrant line (e.g., with slope  $-12.5$  km/MHz<sup>2</sup>) toward the vertical axis until the line from it to ( $fbF^2$ ,  $hbF$ ) is vertical. Of course, the other parameters are straightforwardly predicted from their trend lines. This would complete the ionospheric specification, from which relatively accurate SSL calculations could be made, in conjunction with the interpolation scheme discussed next.

#### 4. INTERPOLATION OF SOUNDER RESULTS TO UNSOUNDED PATHS

In SSL a measurement of frequency, elevation angle, and azimuth angle is made on the incoming wavefront. These are initial conditions in the calculation of the raypath to the HF transmitter through an ionosphere which is specified at only a relatively few sounder control points. The necessary transition from ionospheric knowledge at these points to specification of the ionosphere along the SSL raypath is the subject of this section.

As is well known, the ionosphere is a fluctuating medium. The results of Section 3C are further evidence of this. Rapid fluctuations will often not be correlated between different sounder control points in Figure 2, but the background dependence will be. Indeed, statistical models of the ionosphere, though often inadequate for accurate SSL calculations, make global predictions of ionospheric characteristics, which represent the background dependence. Ionospheric fluctuations affect SSL determinations, which amount to fixing the HF transmitter at the center of a scatter plot of fixes [Reilly and Coran, 1983b]. Fluctuations affect the scatter of points, but it is hoped that the center of the scatter plot is associated with the background dependence of the ionosphere. This is where the trend lines of the last section come in. They are assumed to represent correlated motion of the ionosphere on the time scale used to establish these trend lines, and are found to predict quite well. Fluctuations generally tend to diminish the accuracy of the SSL determination, but proper use of these trend lines should represent a substantial improvement in SSL technology. This remains to be tested in future research.

The specification of the ionosphere along an unsounded SSL path can be carried out by interpolating the A and B coefficients of Equations (9) and (10) in Section 3C for the trend lines of the ionospheric parameters at the sounder control points (cf. Figure 2). An example is shown in Figure 30, where the sounder control points of Figure 2 are shown along with a pair of dashed raypaths. The receiver R is at point 0 in Figure 30, and the control points X1-X6 are at points 1-6 in Figure 30. Five sample raypath points (not on straight lines in the general case) are shown as X-marks, and are labelled a-e. Only the trend line coefficients for 1-6 have been found, but it will be supposed that they have also been found for 0. Raypath point a is interior to the triangles associated with the points 0,1, and 6 or 0,2, and 6, and either set of three control points is thus suitable for specification of the ionosphere at point a by interpolation of the trend line coefficients at these three points. Point a is also interior to triangle 0,4,6, but for accuracy's sake, only the smallest possible triangle is of interest. If latitude is denoted by L, longitude by  $\ell$ , and  $W_1$  is a trend line coefficient ( $A(P_i)$  or  $B(P_i)$  in Equations (9) or (10)), then a suitable interpolation for a point interior to a triangle of sounder control points is

$$W_1 = AL + B\ell + C \quad (11)$$

where L and  $\ell$  refer to the point in question, and the constant coefficients A, B, and C are found from the three equations which evaluate equation (11) at the three sounder control points. A possible alternative scheme is to perform a weighted average of  $W_1$  values at the sounder control points, where the weighting factor for each sounder control point term is the inverse of the range from the point in question to the sounder control point. A calculation of solar zenith angle (effective or actual) at point a will thus enable the specification of ionospheric parameters at point a from the interpolated trend line coefficients and Equations (9) and (10). It is straightforward to also find the latitude and longitude derivatives of these parameters at point a, from which ionospheric tilt parameters can be specified. With this information the next raypath increment from point a can be calculated in a ray-tracing routine.

Suitable interpolation triangles for raypath points b-d are 246, 015, and 125, respectively. Point e is just outside triangle 235, but it is close enough that extrapolation from these points with (11) should be pretty good. Extrapolation is usually more risky, however, and the necessity of it equates to a deficiency in the sounder network distribution. Note that, in the absence of trend line coefficients from point 0, the triangle for point a is 256, and point c would involve a risky extrapolation from triangle 125. Information for control point 0 can be obtained from true height profile calculations on the vertical-incidence sounder data for Fort Ord. The inclusion of the control point at the receiver is generally advantageous for triangular interpolation possibilities.

There is another scheme for specifying the ionosphere along unsounded paths which may be advantageous for raypath points outside interpolation triangles. The idea would be to use a statistical ionospheric model which incorporates principles of ionospheric dynamics and is consistent with averages of past observed ionospheric behavior on a large geographical scale. The ionospheric specification at sounder control points could be used to update parameters of the model ionosphere in the program, which would then be used to predict the ionosphere along the unsounded path.

It would not be too difficult, in principle, to incorporate interpolation and extrapolation schemes in a computer ray-tracing routine. The result would

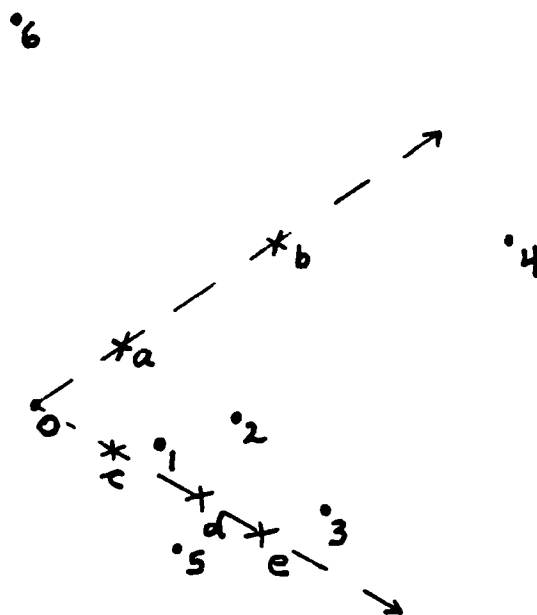


Fig. 30 — SSL-BCT sounder control points (dots - cf. Figure 2) and sample raypaths (dashed) with sample points (X-marks) along them

be an automatic, relatively accurate SSL capability. Actual implementation of these ideas await future research and development.

## 5. MODIFICATION OF SSL TECHNIQUES

A generalization of the simple SSL method of the Introduction (Section 1), which should improve accuracy without sacrificing too much in the way of simplicity, is to try to use ionospheric characteristics at the SSL midpath, if it is believed that radiation reached the receiver by a one-hop mode. The first step is to use ionospheric characteristics at some sounder control point, e.g., one near the direction of the incoming wave front, in the manner discussed in the Introduction. It was found that the vertical ionogram could be simply used within the approximations that the ionosphere exhibits no tilts, i.e., it is spherically symmetric, and that the ionosphere is nearly flat for the portion of the raypath in it. A not too much more complicated alternative is to use the parameters from the true height profile calculation. As noted in connection with Equation (4) of Section 2B, the idealized profile fit based on these parameters lends itself very easily to the range calculation in a spherically symmetric ionosphere. Having calculated the range, it is a simple matter to infer the midpath point, and the second step is to infer the ionosphere at this point and repeat the range calculation. Inferring the midpath ionosphere is done in the manner described in the preceding section. It involves the interpolation of ionospheric trend line parameters at other sounder control points. The second step is repeated, now with possible inclusion of a simple tilt model, in an iterative fashion until the calculated HF transmitter position converges to the desired accuracy. It is anticipated that only a few iterations would be needed.

An alternative SSL technique is more complicated, but also is more accurate, since it would accurately take account of longitudinal and transverse ionospheric tilts. It was alluded to in the preceding paragraph. It would involve a full-blown ionospheric ray-tracing program, with initial conditions given by the SSL measurements and with ionospheric characteristics updated frequently in the raypath calculations by means of interpolation of trend line parameters for ionospheric parameters determined at the control points of a sounder network.

Computer automation will facilitate the calculations in any modification of SSL techniques. The most difficult part of the envisioned SSL system is the deployment and maintenance of a sounder network.

## 6. DISCUSSION

In the Introduction there was a discussion of present state-of-the-art SSL technology, in which severe, simplifying approximations are made for the properties of the ionosphere between the receiver and the HF transmitter, whose location is to be determined. The oblique-incidence and vertical-incidence sounder data of the SSL-BCT project in December, 1982, provided, and still provide, an opportunity to assess the impact of proper accounting of ionospheric properties on SSL technology. But several computational difficulties stood in the way. The analysis hinged on the ability to process the ionograms from the oblique-incidence sounder network, which constituted the major part of the data base. The technology had been developed for vertical-incidence sounders. The author developed a large part of it recently for oblique-incidence sounders. The method of obtaining ionospheric true height profiles from oblique ionograms is delineated in Section 2, where it is also shown that a true height profile could be

characterized accurately and conveniently by a set of parameters. The correspondence between the calculated true height profile and the ionosphere at the sounder midpath is also confirmed here. The method was applied to the set of oblique ionograms from SSL-BCT for December 6-7 (UT), which spanned the local time period in fifteen minute intervals from the morning hours of December 6 after sunrise into the nighttime, a few hours after sunset. Details of the data set and the results of analysis on it are contained in Section 3.

It was found, not surprisingly, that the daytime ionosphere was well-characterized by the zenith angle of the sun, which measures at a point in the F layer the angle that the sun makes with the overhead direction, with some accounting for the time lag between solar perturbation and upper ionospheric response. When the ionospheric parameters were plotted against the cosine of this angle, they were found in Section 3 to show a noisy behavior about quite well-defined trend lines, which are thus used to characterize the background dependence on the ionosphere. These trend lines, updated as frequently as is convenient, could be used to predict the background dependence of the ionosphere at the sounder control points, and it was shown how to do this. It was also seen from comparison of the trend lines at the sounder control points that the background dependence at these points seemed to be correlated.

Correlation of the background dependence of the ionosphere at sounder control points is the basis for specifying the ionosphere on raypaths between the SSL receiver and the HF transmitter. These raypaths practically never include the sounder control points. In Section 4 it was shown how to perform spatial interpolation of trend line parameters at the vertices of sounder control point triangles for the purpose of specifying the ionosphere along raypath portions within these triangles. Other possibilities for inferring ionospheric properties along unsounded paths were mentioned. These involve the updating of the parameters of a statistical model ionosphere with sounder results, and this method may prove to be especially useful for inferring ionospheric properties on raypaths which are outside the aforementioned control point triangles.

In Section 5 it was discussed in detail how a proper HF propagation assessment with ionospheric sounders will result in a modification of SSL technology. The data from either vertical-incidence or oblique-incidence sounders can be used for this purpose to an essentially equivalent effect. The important thing is to establish a strategic distribution of sounder control points. Practical considerations, such as cost, safety, and security of transmitter and receiver location, will also be used to determine the mix of oblique- and vertical-incidence sounders. Trend line parameters at the sounder control points can be radioed to the SSL receiver position, where the HF transmitter location can be computed. An improvement in accuracy over present methods can be obtained by inferring the ionosphere at midpath between the receiver and transmitter, in the manner discussed in Section 5. Of course, if the raypath between receiver and transmitter is inferred to involve more than one hop, the ionosphere should be specified at all of the ionospheric reflection points. With this information, standard approximations can be used to calculate the HF transmitter location. For greatest accuracy, a ray-tracing routine with ionospheric specification along the raypath can be used in the manner discussed. No formidable obstacles appear to stand in the way of these modifications to SSL technology, once the commitment to deploy the sounder network has been made.

Several tasks remain in the analysis of SSL-BCT data. Several of the other time periods in the data base can be analyzed to provide additional

information. In particular, techniques for characterizing and interpolating nighttime ionospheric properties need to be developed. Further, the actual computation of HF transmitter positions can be carried out using the methodology of this report. The appropriate incorporation of this into a ray-tracing program needs to be further developed. Greater accuracy in the interpolation of ionospheric parameters will be obtained from additionally processing the vertical ionograms at Fort Ord. The success of the various SSL techniques can be quantitatively evaluated by comparing actual and calculated HF transmitter positions. Basic information about ionospheric effects will be obtained. Comparison of these results with the contractor results will also be of interest in this regard. Further, the ionospheric effects have to be subtracted out to get a better understanding of errors in measurement techniques used by the contractors.



# REFERENCES

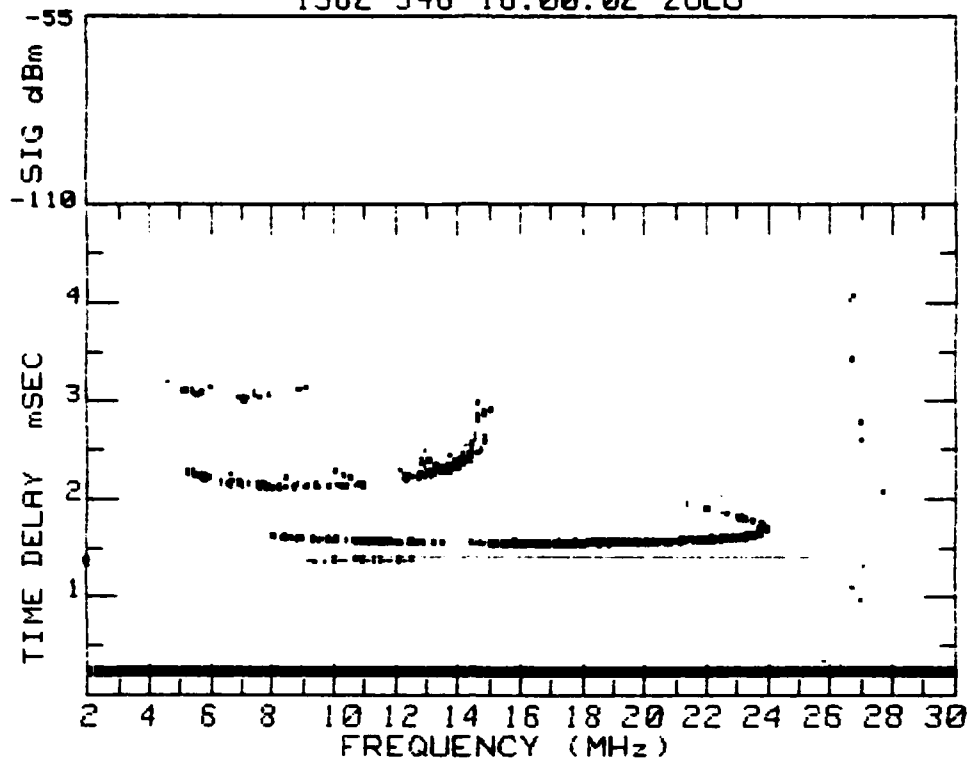
1. Basler, R.P. and T.D. Scott (1973), "Ionospheric Structure from Oblique-Backscatter Soundings," Radio Sci. 8 (5), pp. 425-429.
2. Budden, K.G. (1966), Radio Waves in the Ionosphere, Cambridge University Press, London.
3. Chamberlain, J.W. (1978), Theory of Planetary Atmospheres, Chap. 5, Academic Press, New York.
4. Daehler, M. (1983), "Single Site Location Baseline Certification Test Data Base Description," NRL Memo. Rpt. 5180.
5. Davies, K. (1969), Ionospheric Radio Waves, Blaisdell Publishing Co., Waltham, MA.
6. Kopka, H. and H.G. Moller (1968), "MUF Calculations Including the Effect of the Earth's Magnetic Field," Radio Sci. 3 (1), pp. 53-56.
7. Reilly, M.H. (1983a), "Techniques for Locating a Remote HF Transmitter from Single-Site Measurements," NRL Memo. Rpt. 5145.
8. Reilly, M.H. and J. Coran (1983b), "Confidence Region for the Evaluation of HF DF Single-Site Location Systems," NRL Memo. Rpt. 5164.
9. Reilly, M.H. (1984a), "Ionospheric True Height Profiles from Oblique Ionograms," presented at the Ionospheric Effects Symposium, 1 May 1984, Alexandria, VA. To be published in Radio Science in 1985 in a special issue on IES papers.
10. Reilly, M.H. and E.K. Yamamura (1984b), "Oblique Ionograms and HF Propagation Assessment," MILCOM 84 Conference Record, IEEE Military Communications Conference, Paper 8.3, Los Angeles, CA.
11. Rose, R.B., J.W. Martin, and P.H. Levine (1978a), "MINIMUF-3: A Simplified hf MUF Prediction Algorithm," WOSC TR 186, San Diego, CA 92152.
12. Rose, R.B. and J.W. Martin (1978b), "MINIMUF-3.5: A Simplified hf MUF Prediction Algorithm," WOSC TD 201, San Diego, CA 92152.
13. Rose, R.B. (1979), "Further Verification of the MINIMUF-3.5 hf MUF Prediction Algorithm for: (1) Frequencies Above 32 MHz, (2) Path Lengths of Less Than 250 Mmi," WOSC TN 758, San Diego, CA 92152.
14. Sailors, D.B. (1984), "MINIMUF-B: An Improved Version of MINIMUF 3.5," in Preprints of Proceedings, IES '84, The Effect of the Ionosphere on C<sup>3</sup>I Systems, Paper 1-6, Alexandria, VA.
15. Smith, W. (1939), "The Relation of Radio Skywave Transmission to Ionospheric Measurements," Proc. IRE 27, pp. 332-347.
16. Uffelman, D.R., L.O. Harnish, and J.M. Goodman (1984), "HF Frequency Management by Frequency-Sharing as Assisted by Models Updated in Real Time," NRL Memo. Rpt. 5284.

## APPENDIX A

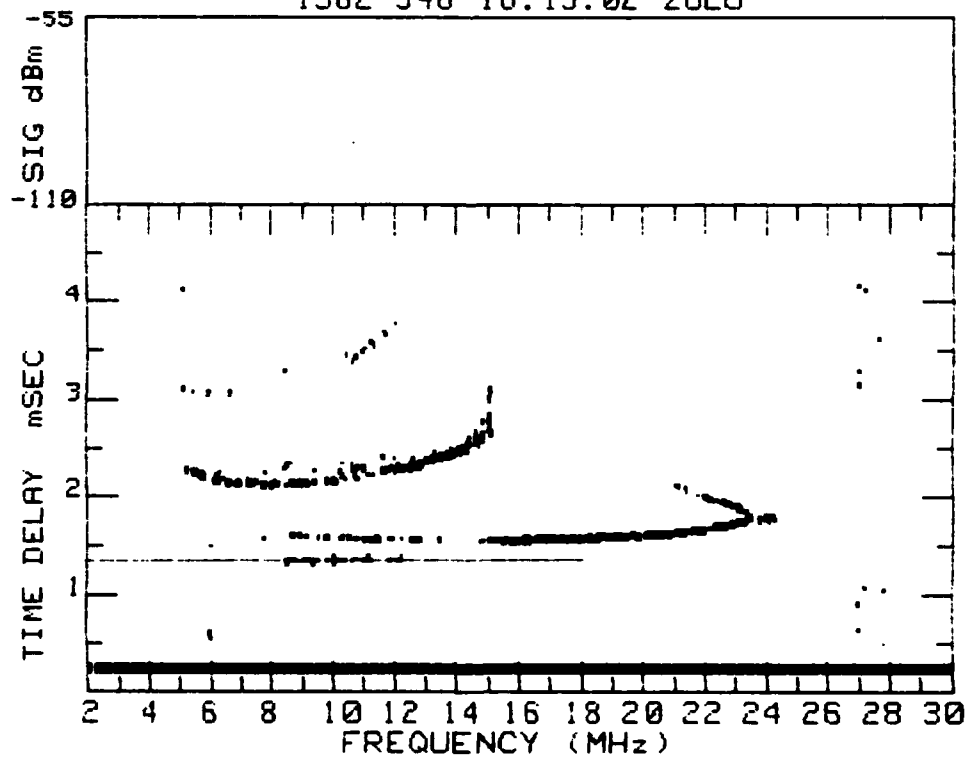
### Comparison Between Calculated and Experimental Vertical Ionograms

Path 4 oblique ionograms (shown) are analyzed to obtain true height profiles (nine-parameter solutions), which are used to calculate equivalent vertical ionograms. These are compared in the following with ordinary mode traces of vertical ionograms measured at Fort Ord (FO) and Desert Research Station (DRS). See the description of the text. Times for the associated ionograms are listed in the legends for these comparisons.

SSL OIS#2 ZONE 4 ERIE,CO TO FT ORD,CA  
1982 348 16:00:02 ZULU



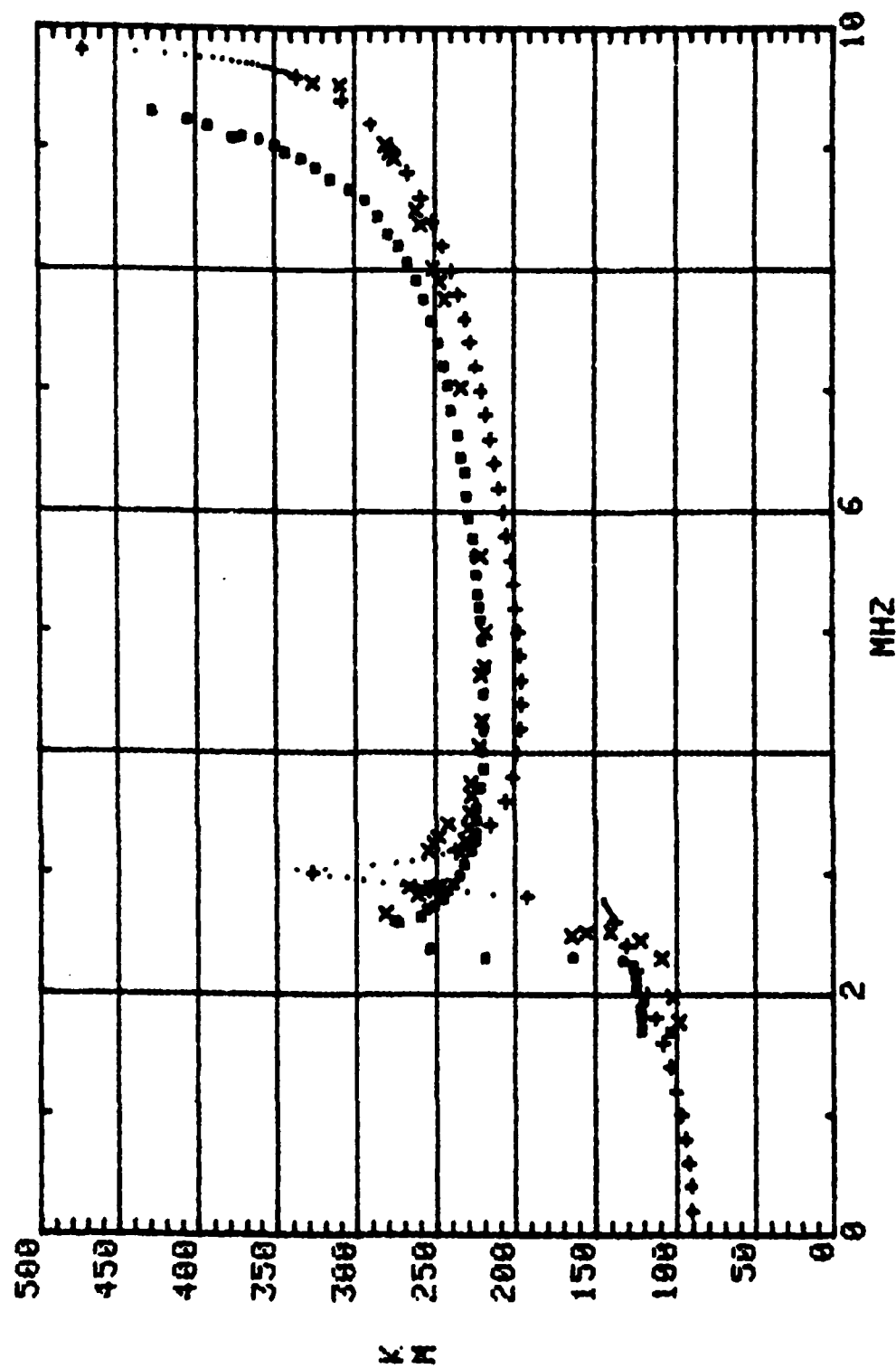
SSL OIS#2 ZONE 4 ERIE,CO TO FT ORD,CA  
1982 348 16:15:02 ZULU



Day 348, 1600

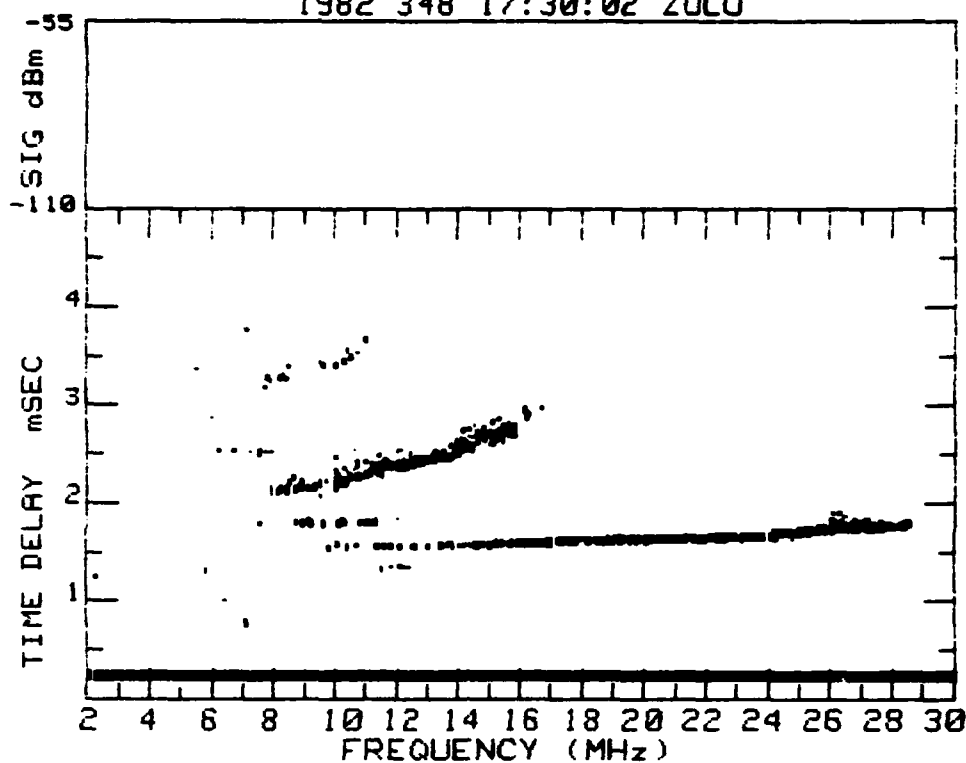
# VERTICAL IONOGRAM

+++... OI 16:00:07  
xxx DRS 16:00  
... FO 15:58

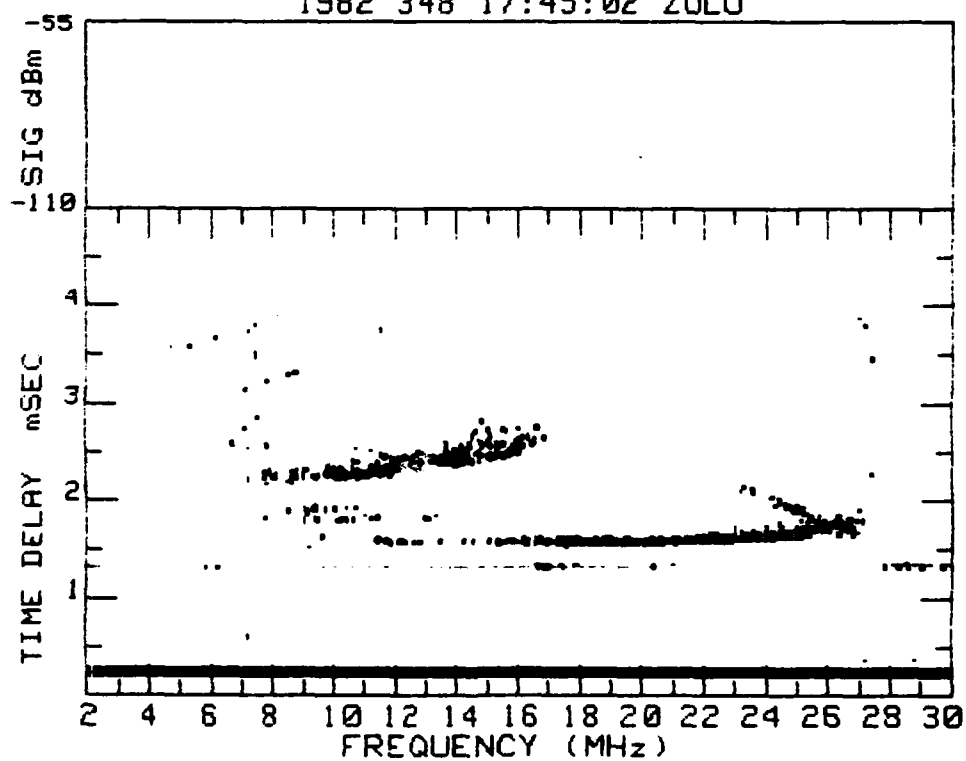




SSL OIS#2 ZONE 4 ERIE,CO TO FT ORD,CA  
1982 348 17:30:02 ZULU



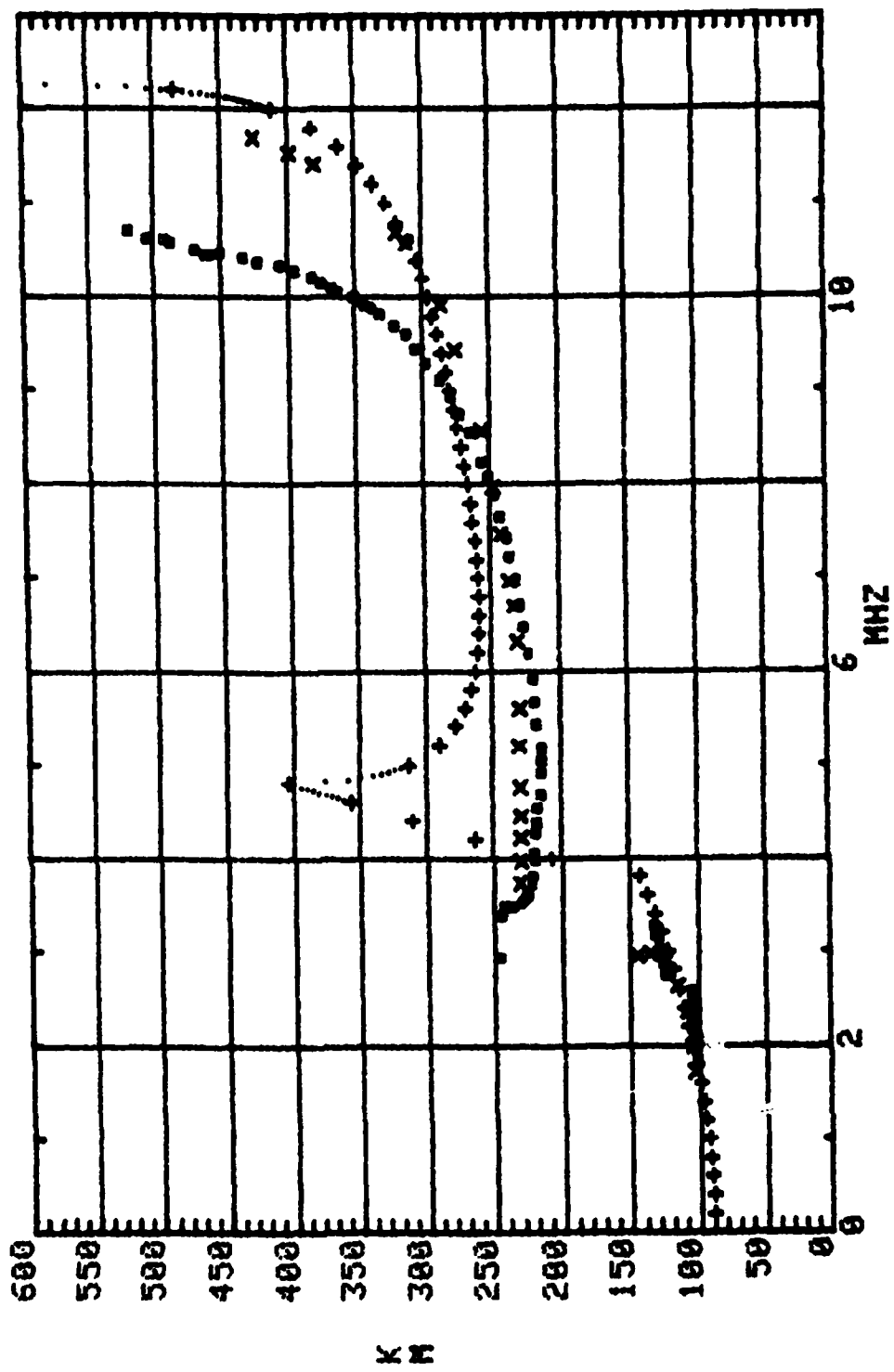
SSL OIS#2 ZONE 4 ERIE,CO TO FT ORD,CA  
1982 348 17:45:02 ZULU



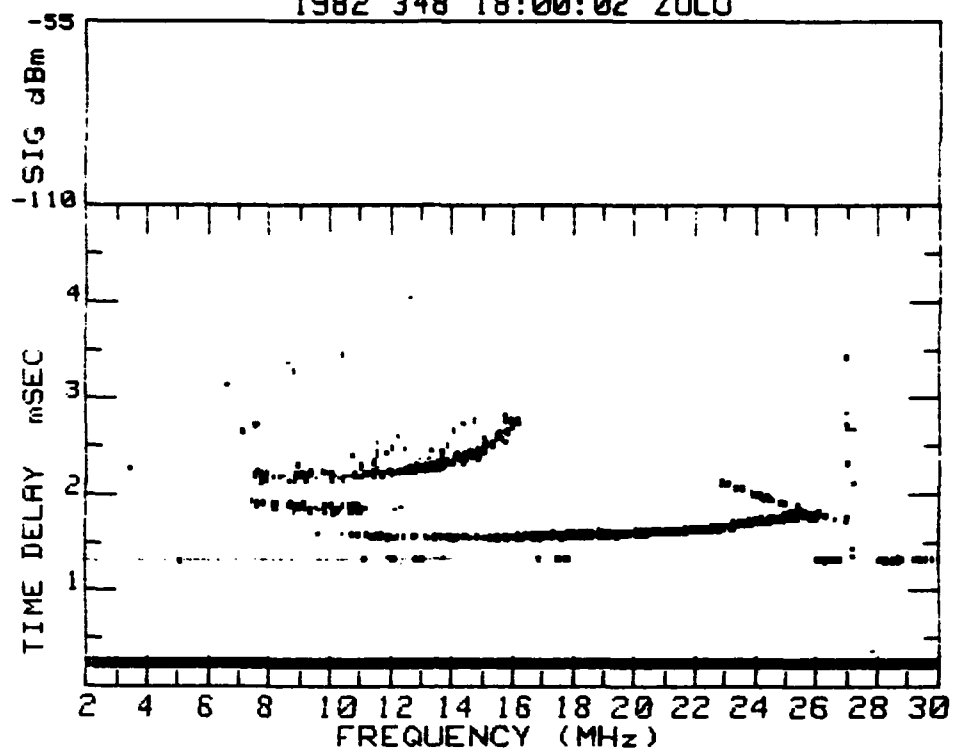
Day 348, 1745

VERTICAL IONOGRAM

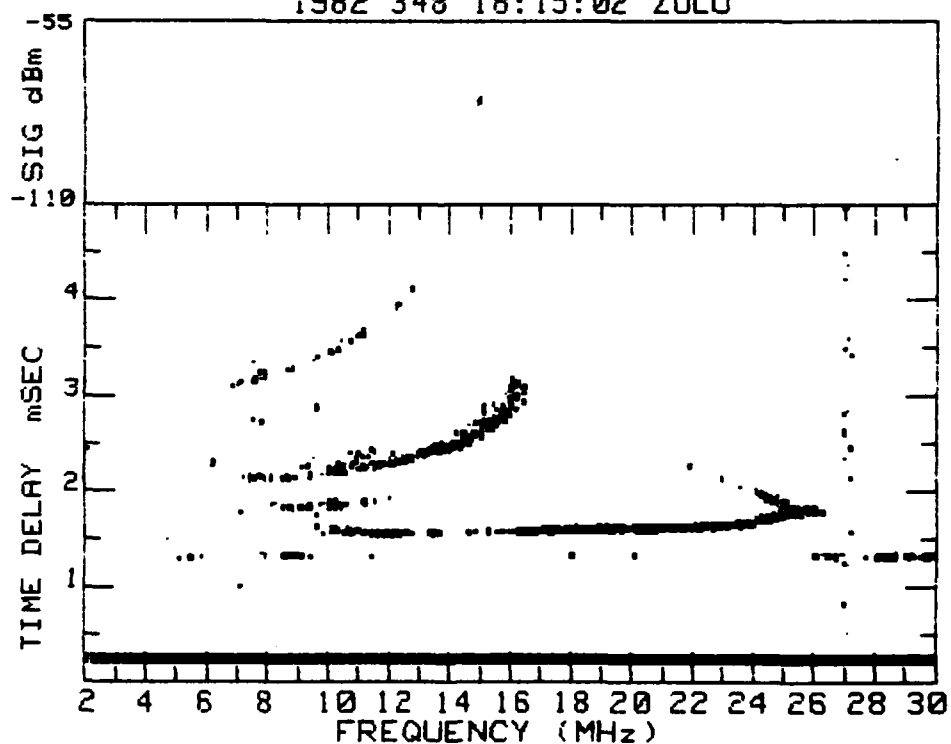
+++... OI 17:45:02  
 xxx DRS 17:45  
 ■■■ FO 17:44



SSL OIS#2 ZONE 4 ERIE,CO TO FT ORD,CA  
1982 348 18:00:02 ZULU



SSL OIS#2 ZONE 4 ERIE,CO TO FT ORD,CA  
1982 348 18:15:02 ZULU





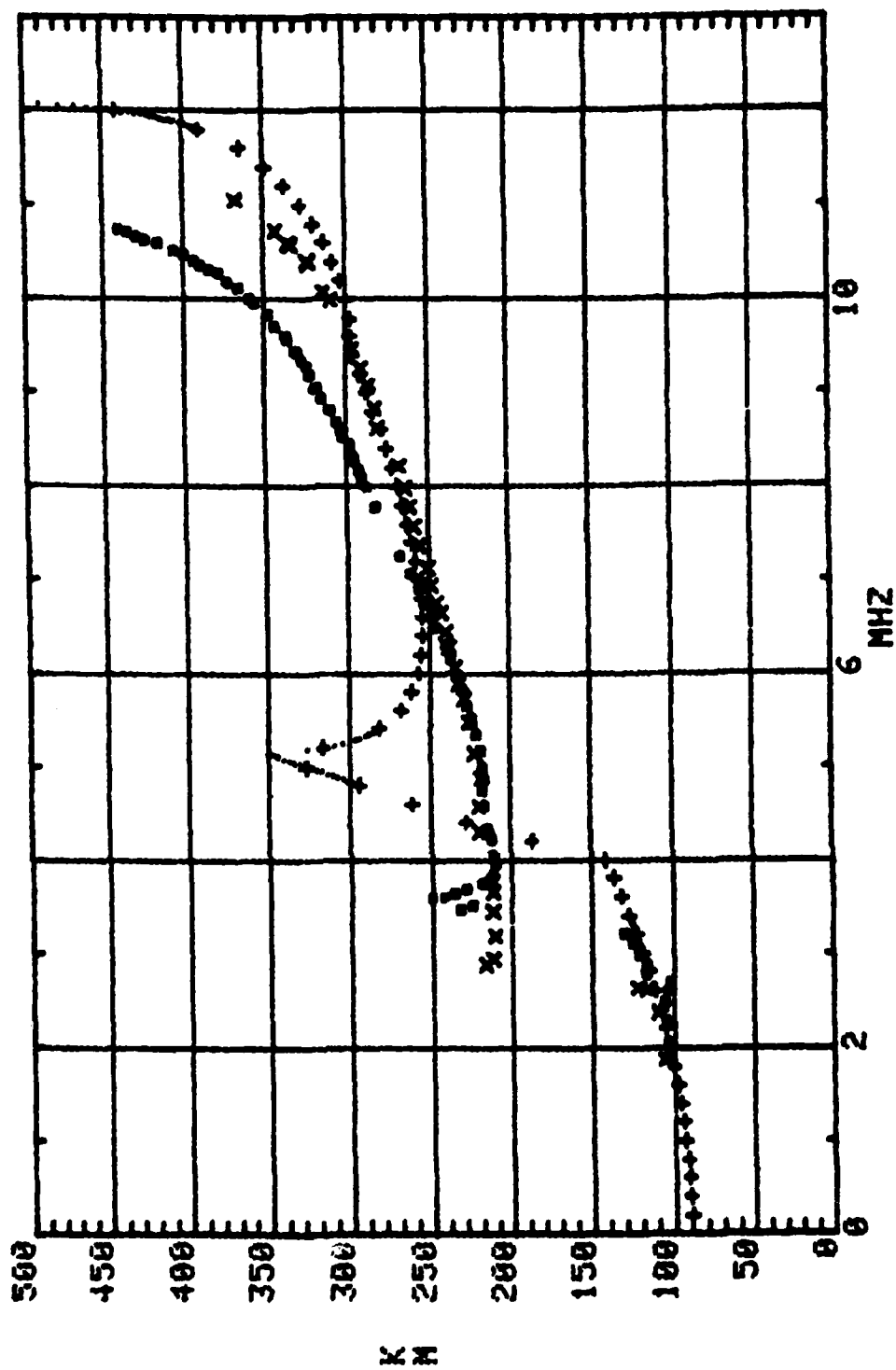
Day 348, 1800

VERTICAL IONOGRAM

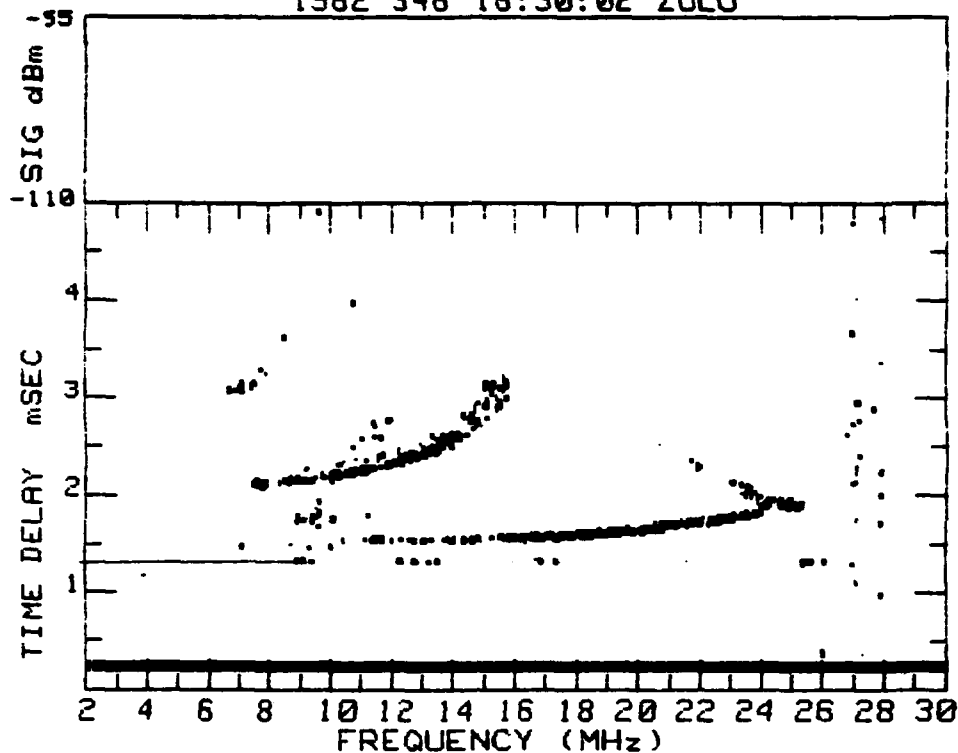
+++ OI 18:00:02

xxx DRS 18:00

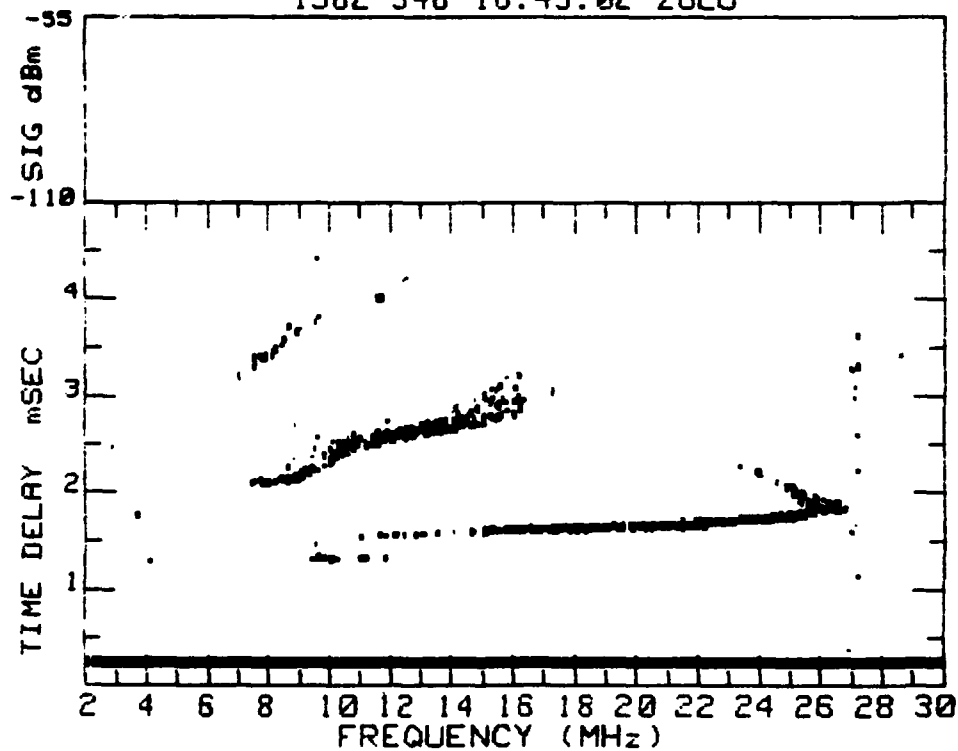
■ FO 17:59



SSL OIS#2 ZONE 4 ERIE,CO TO FT ORD,CA  
1982 348 18:30:02 ZULU



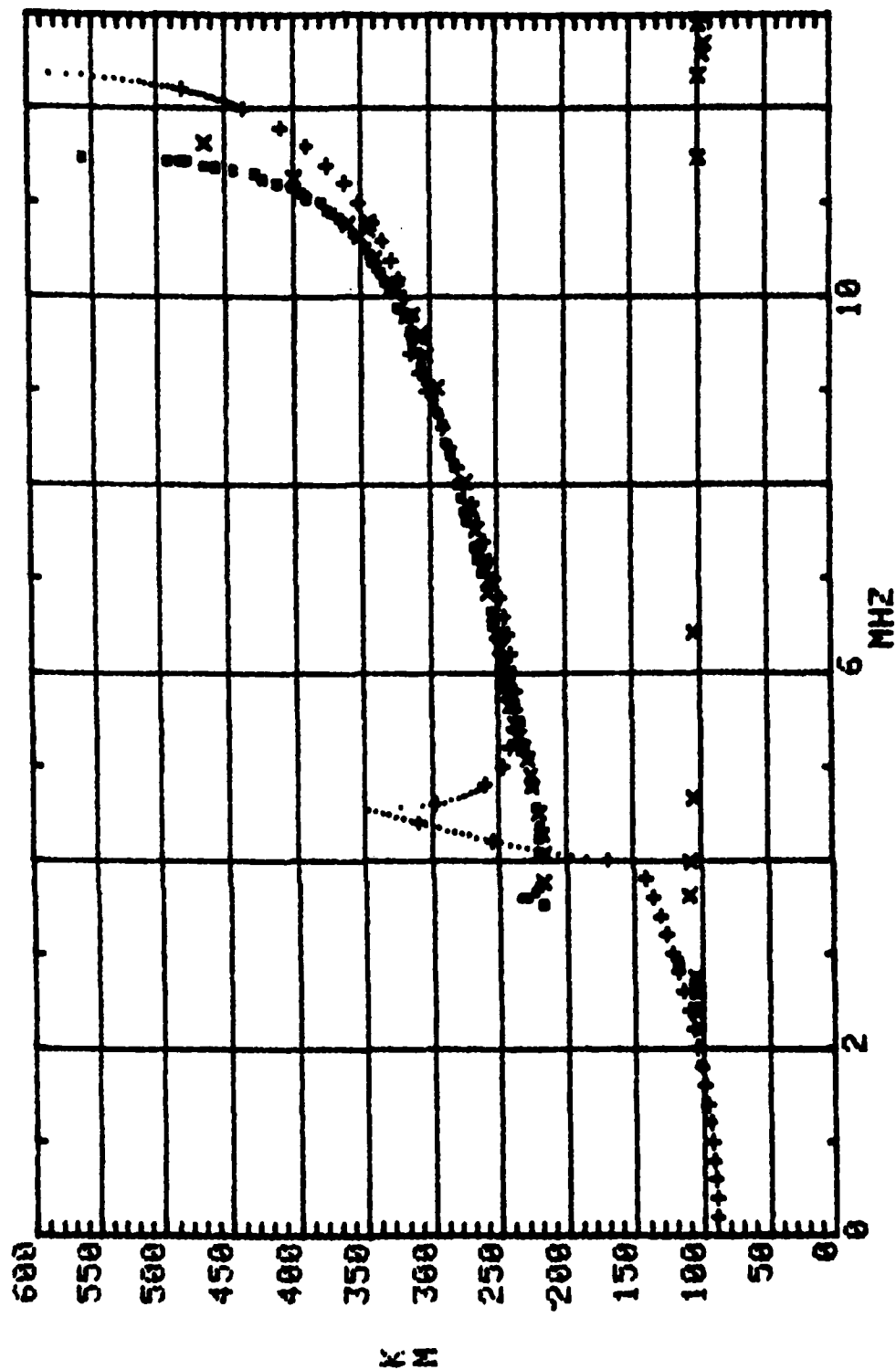
SSL OIS#2 ZONE 4 ERIE,CO TO FT ORD,CA  
1982 348 18:45:02 ZULU



Day 348, 1830

# VERTICAL IONOGRAM

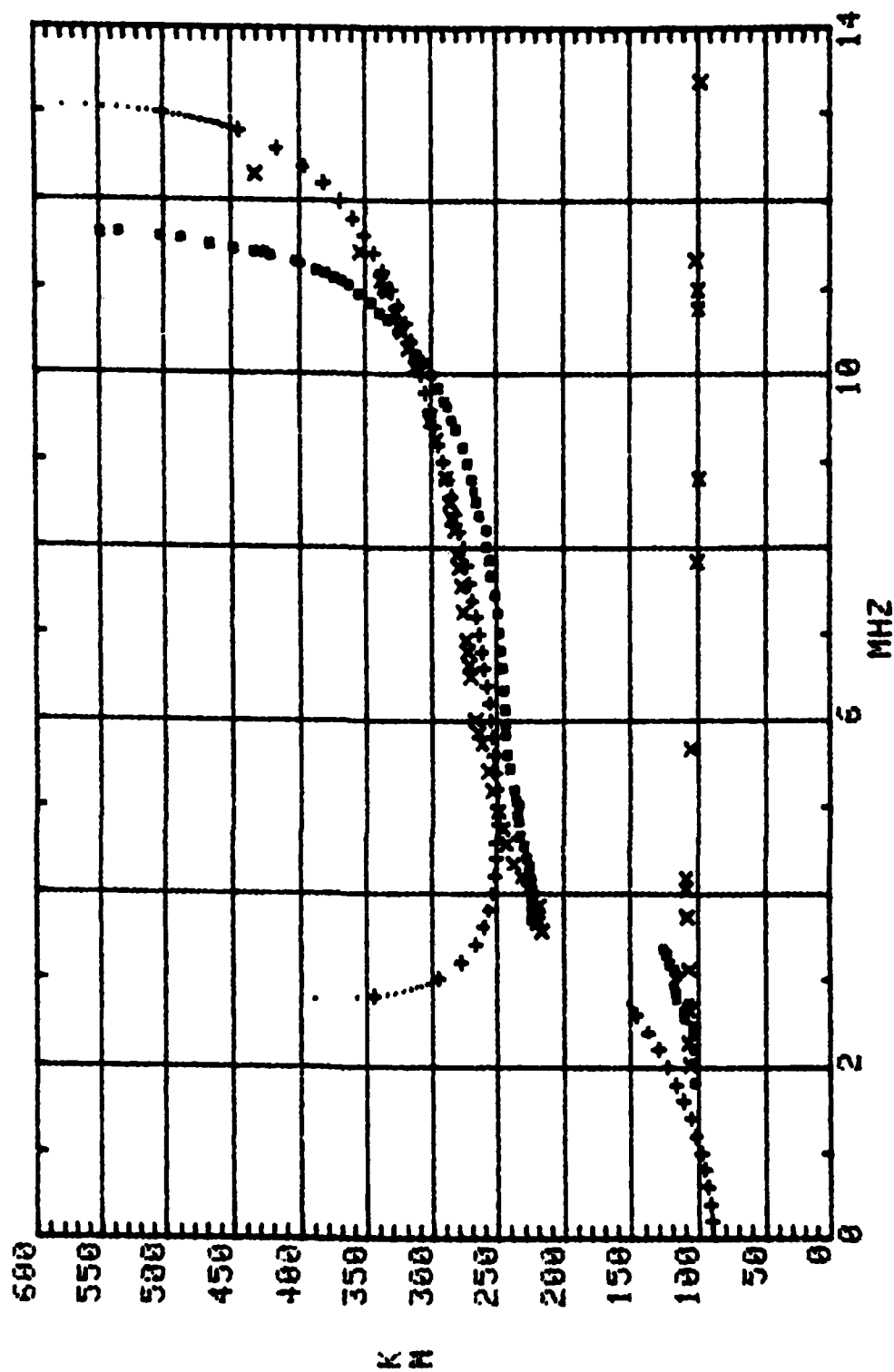
+++...	OI	18:30:02
xxx	DRS	18:30
■■■	FO	18:29



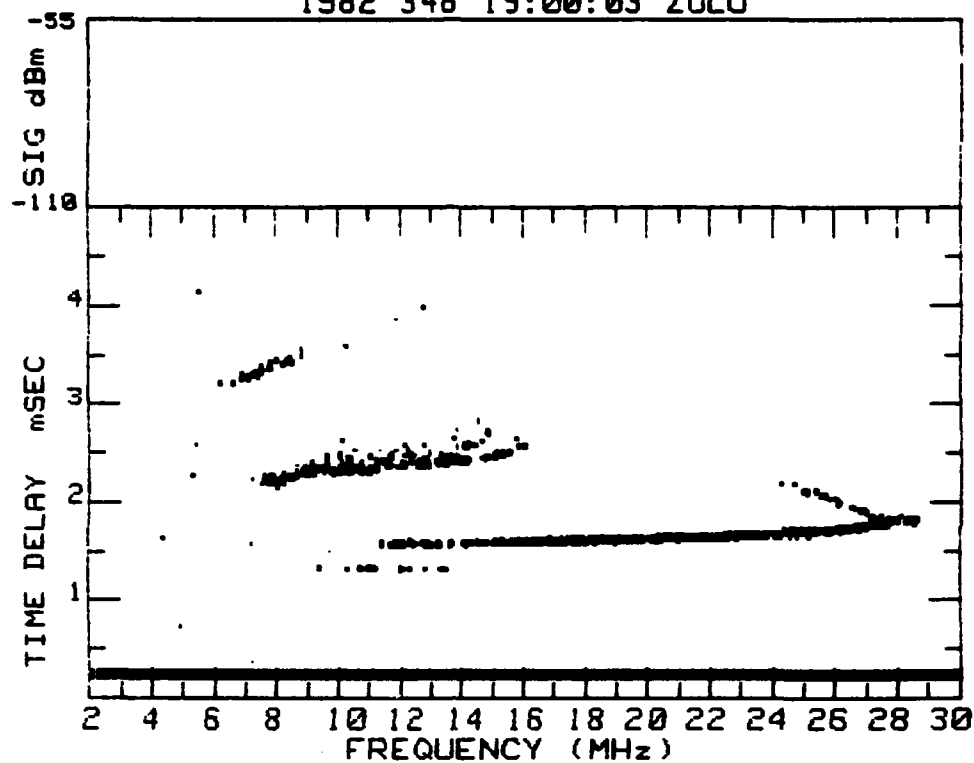
0348, 1845

VERTICAL IONOGRAM

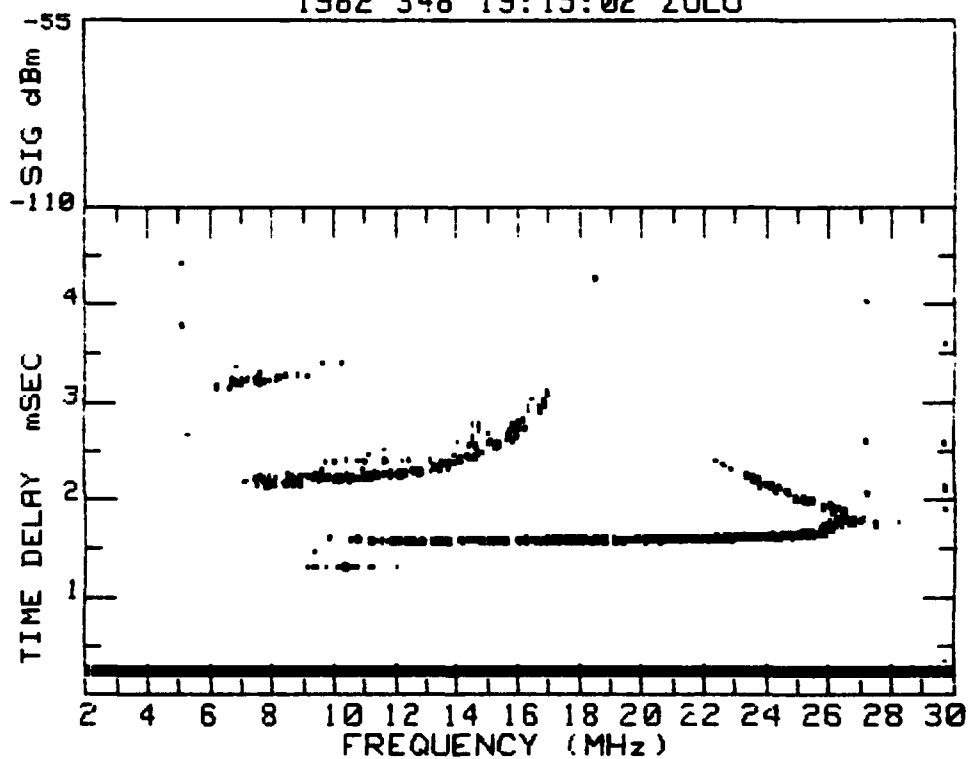
+++--- OI 18:45:02  
 xxx DRS 18:45  
 ■■■ FO 18:44



SSL OIS#2 ZONE 4 ERIE,CO TO FT ORD,CA  
1982 348 19:00:03 ZULU



SSL OIS#2 ZONE 4 ERIE,CO TO FT ORD,CA  
1982 348 19:15:02 ZULU



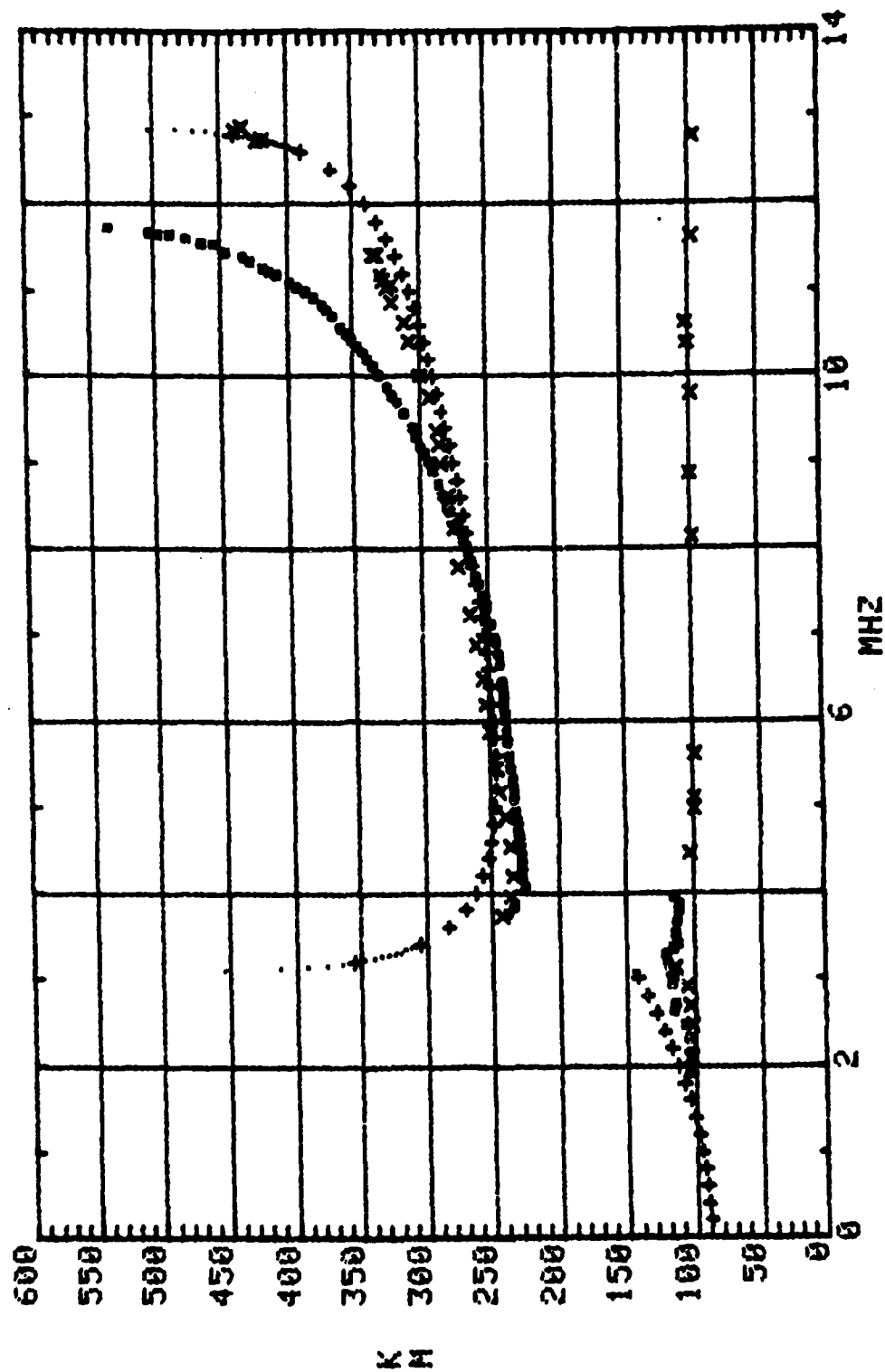
D348, 1900

VERTICAL IONOGRAM

+++ OI 19:00:03

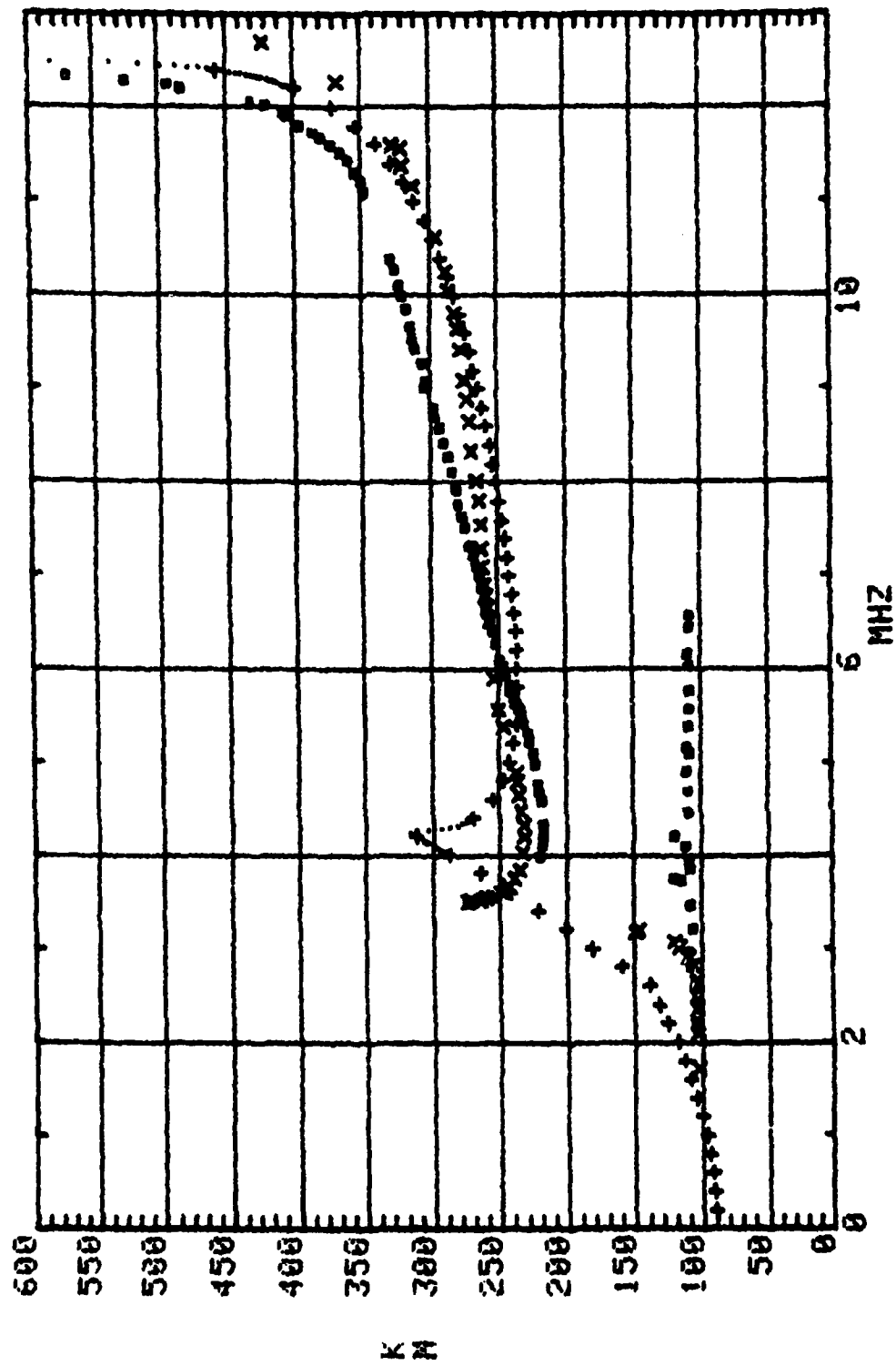
xxx DRS 19:00

■■■ FO 18:59

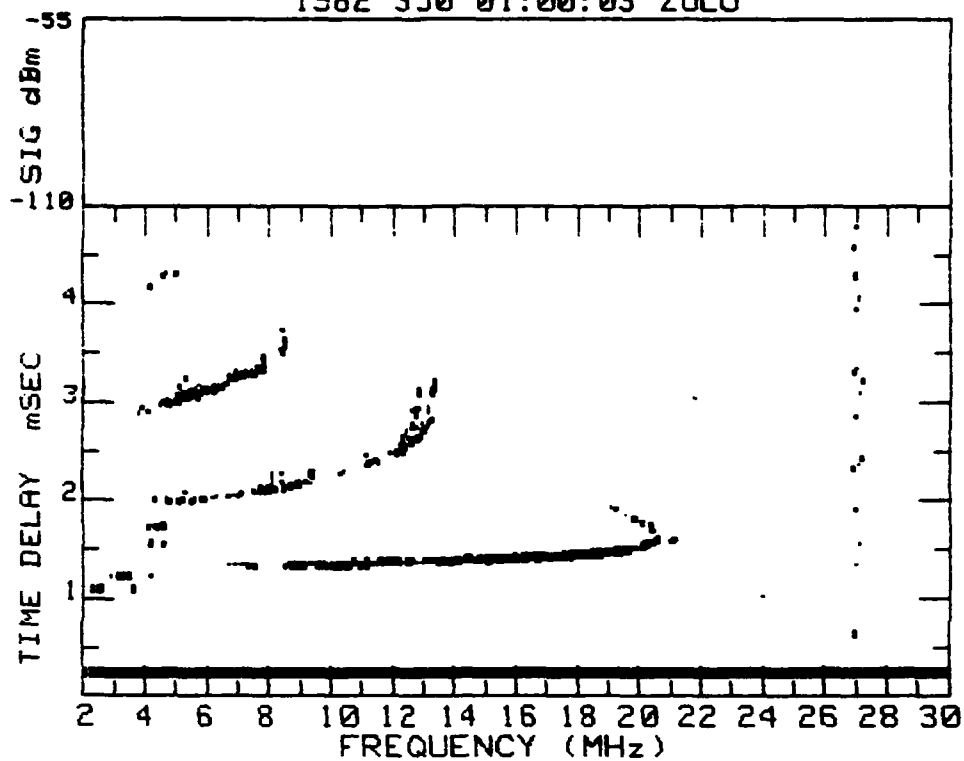


# VERTICAL LONGRAN

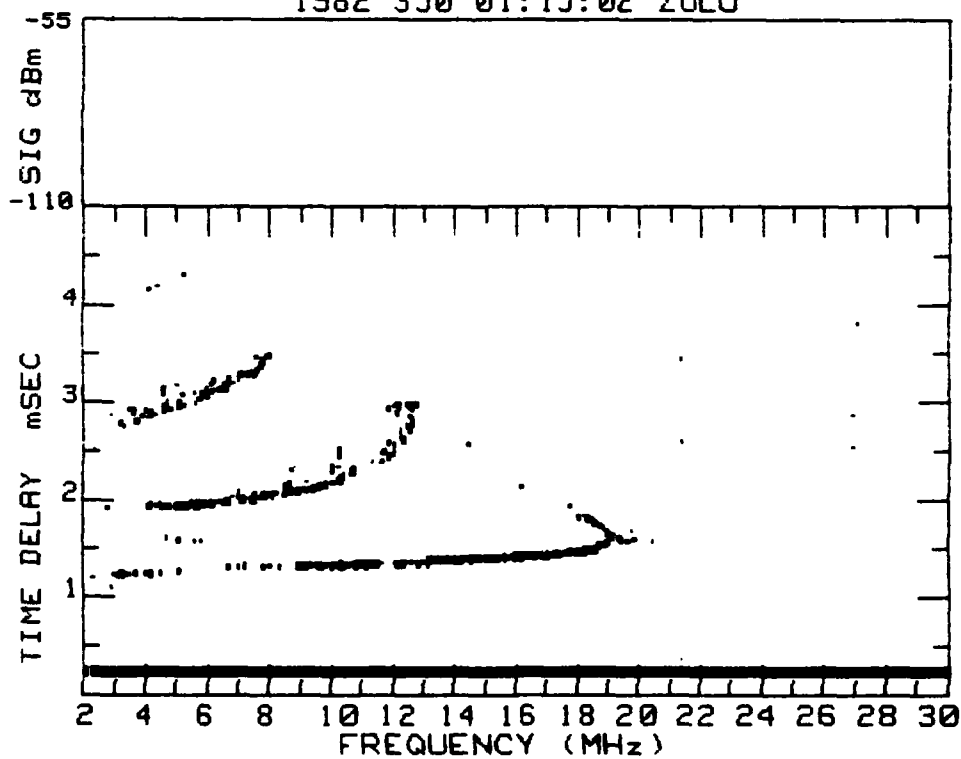
+++-	OI	19:15:02
xx	DRS	19:15
■ ■ ■	FO	19:15



SSL OIS#2 ZONE 4 ERIE,CO TO FT ORD,CA  
1982 350 01:00:03 ZULU



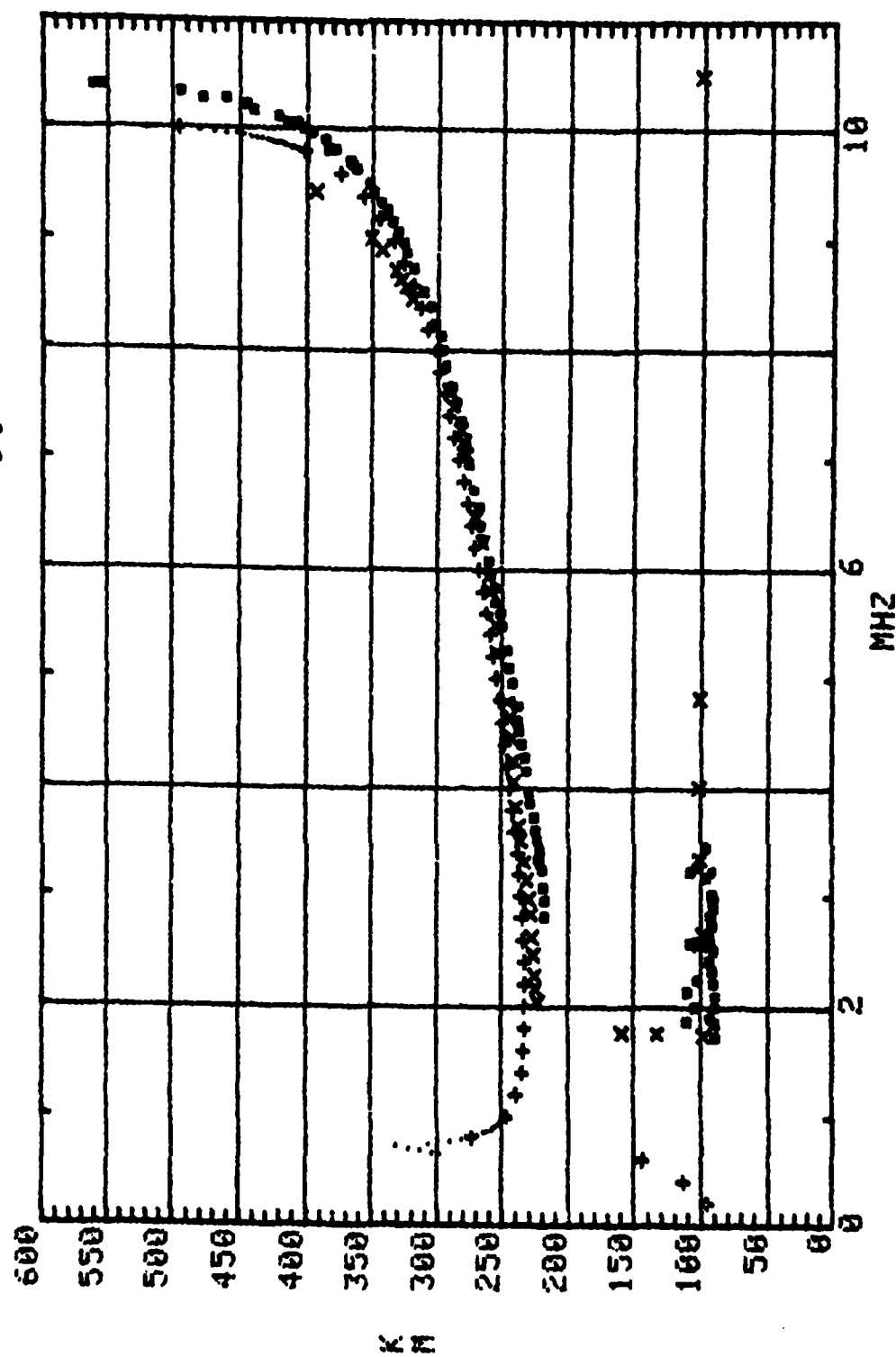
SSL OIS#2 ZONE 4 ERIE,CO TO FT ORD,CA  
1982 350 01:15:02 ZULU





# VERTICAL IDNOGRAM

+++...	OI	01:00:03
xxx	DRS	01:05
###	FO	00:58



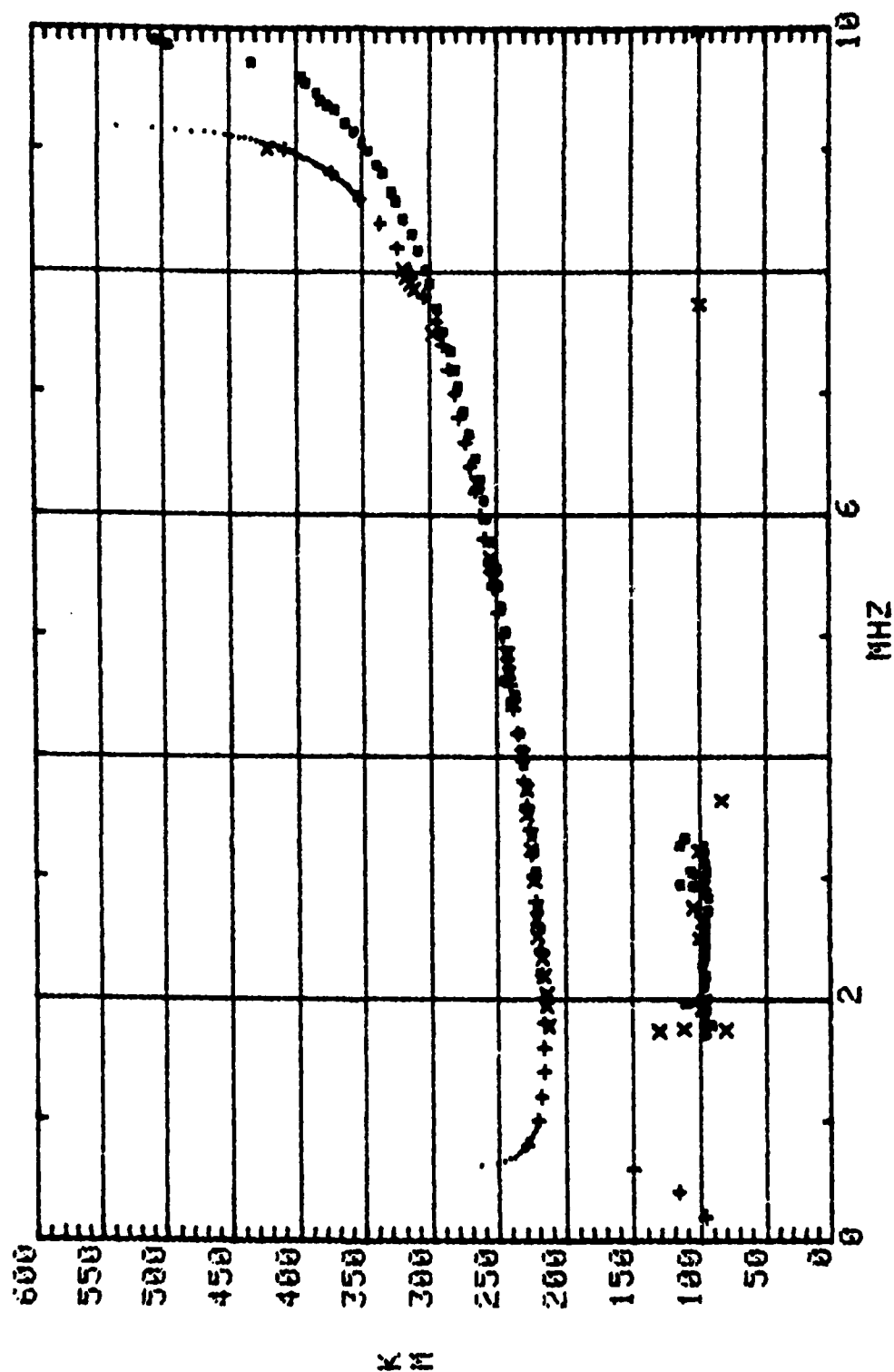
D 350, 0115

# VERTICAL IONOGRAM

+++... OI 01:15:02

xxx DRS 01:15

■ ■ ■ FO 01:13



AD-A157 226

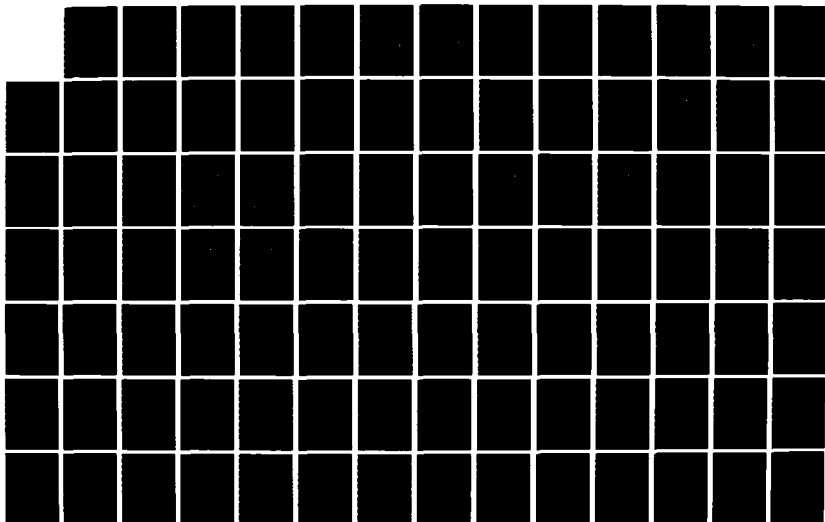
SINGLE SITE LOCATION WITH IONOSPHERIC SPECIFICATION  
FROM OBLIQUE-INCIDENCE SOUNDERS(U) NAVAL RESEARCH LAB  
WASHINGTON DC M H REILLY ET AL. 24 JUN 85 NRL-MR-5586

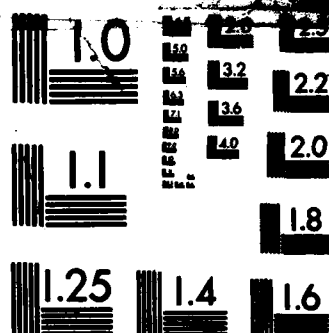
2/3

UNCLASSIFIED

F/G 20/14

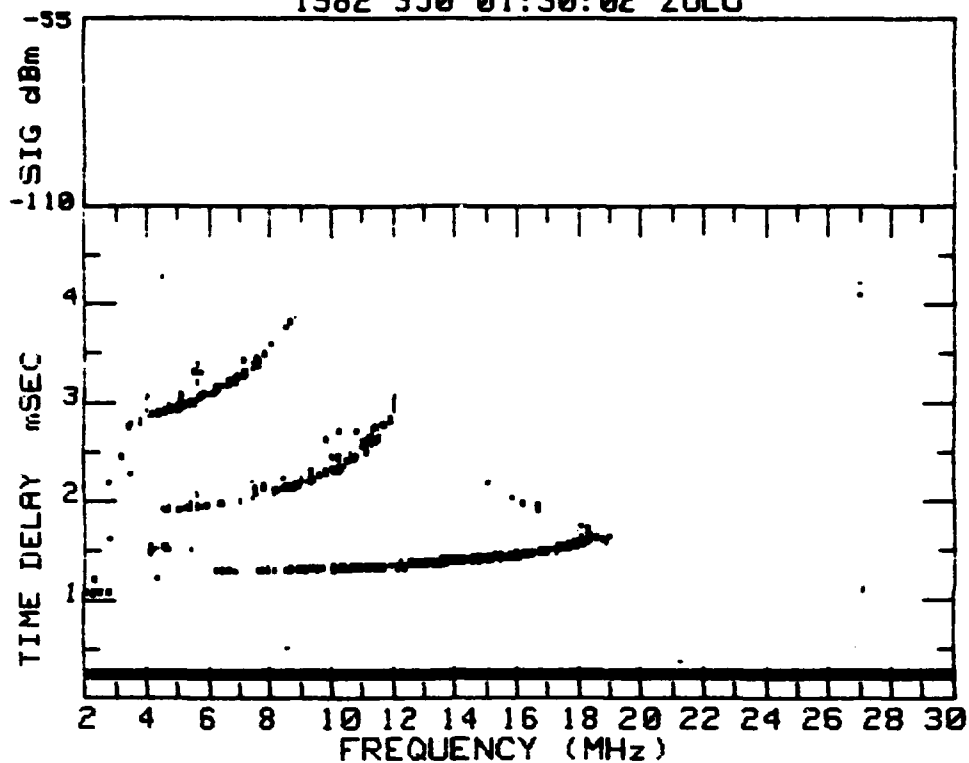
NL



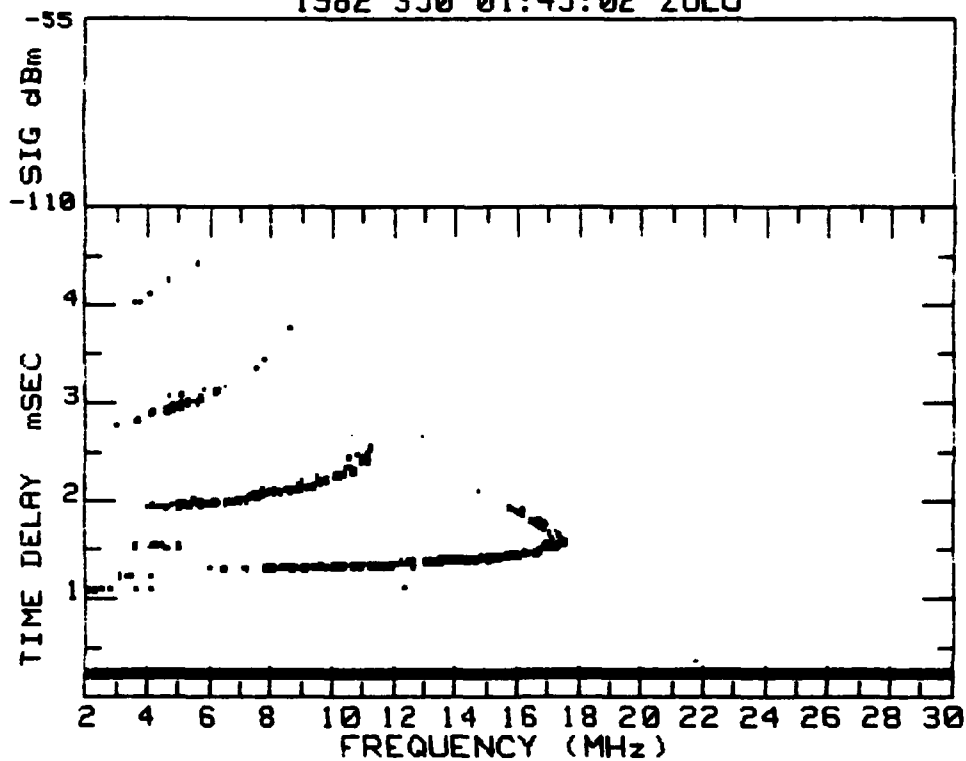


MICROCOPY RESOLUTION TEST CHART  
NATIONAL BUREAU OF STANDARDS-1963-A

SSL OIS#2 ZONE 4 ERIE,CO TO FT ORD,CA  
1982 350 01:30:02 ZULU

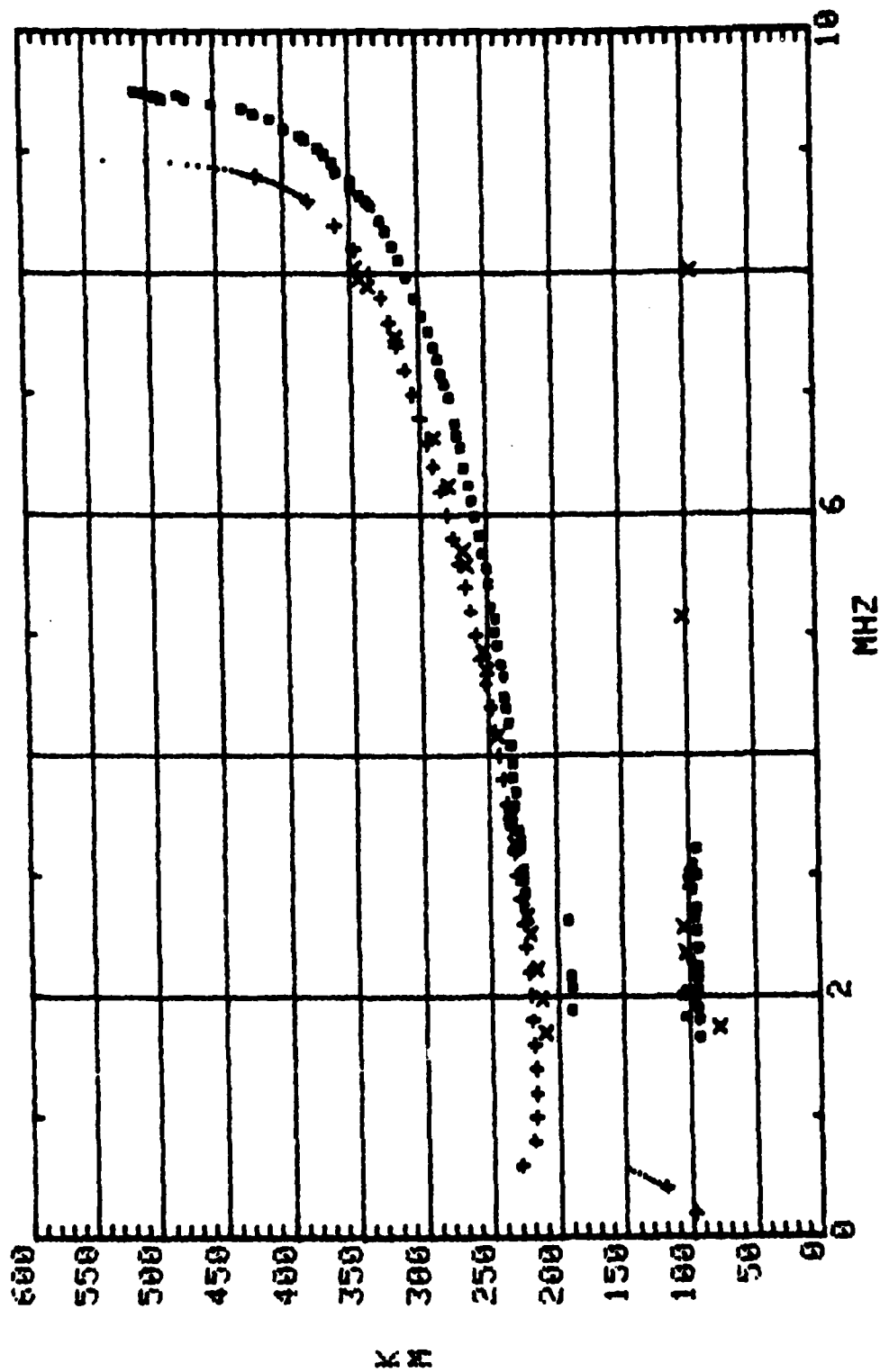


SSL OIS#2 ZONE 4 ERIE,CO TO FT ORD,CA  
1982 350 01:45:02 ZULU



# D350, 0130 VERTICAL IONOGRAM

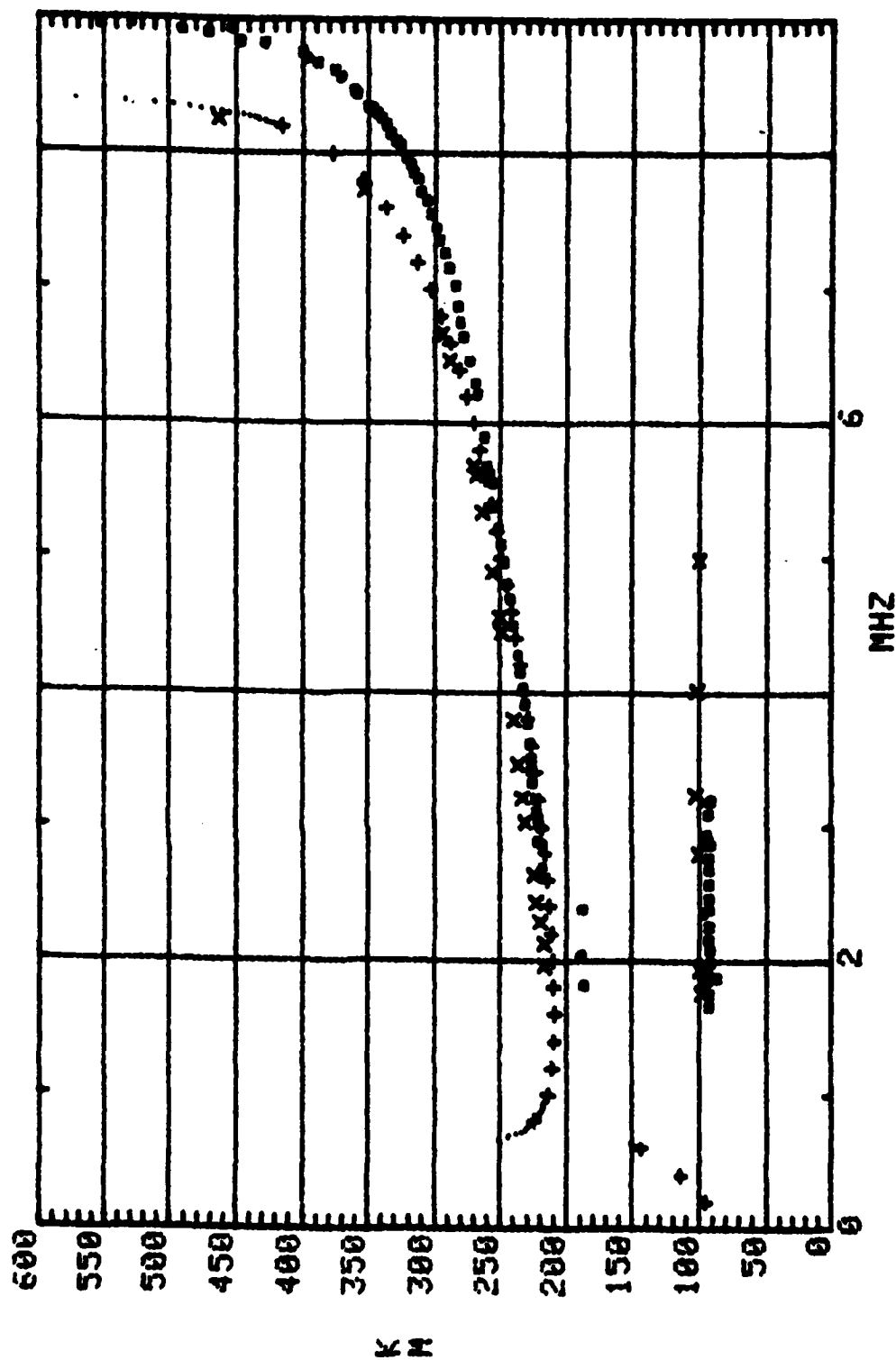
+++... OI 01:30:02  
 xxx DRS 01:30  
 ■■■ FO 01:28



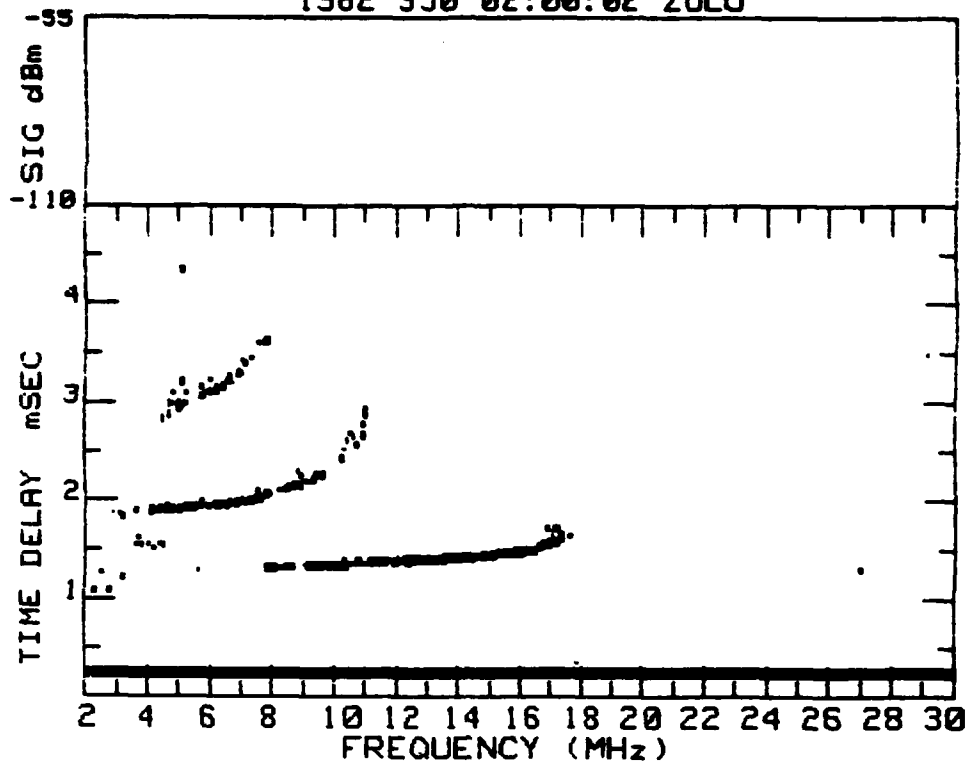
D350, 0145

VERTICAL IONOGRAM

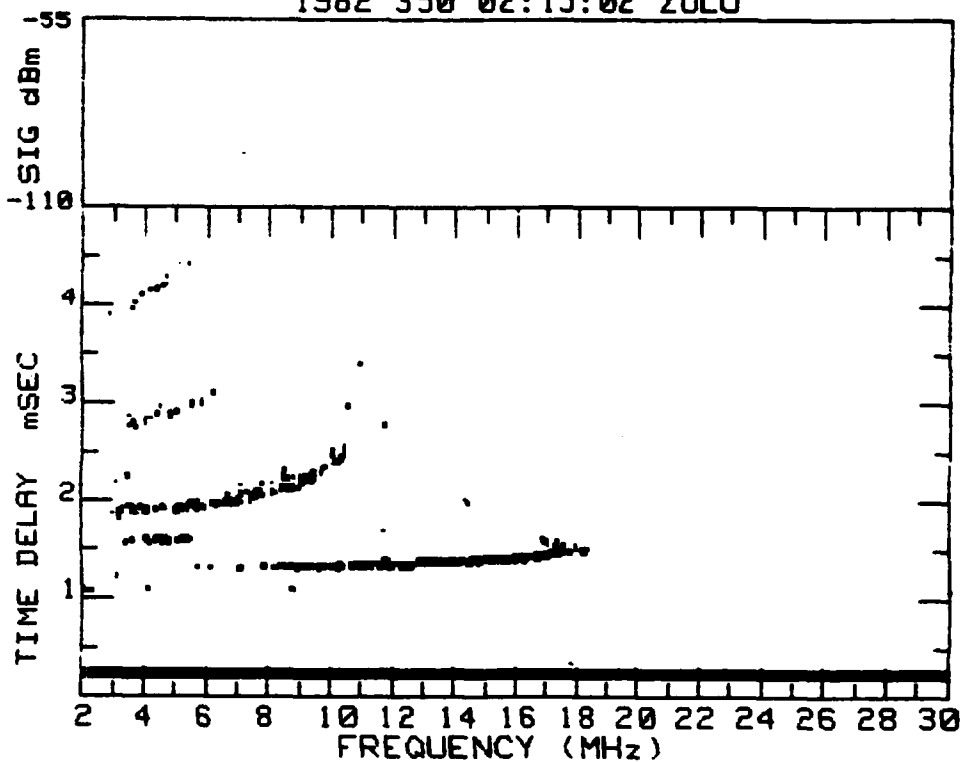
+++... OI 01:45:02  
 xxx DRS 01:45  
 ■■■ FO 01:43



SSL OIS#2 ZONE 4 ERIE,CO TO FT ORD,CA  
1982 350 02:00:02 ZULU



SSL OIS#2 ZONE 4 ERIE,CO TO FT ORD,CA  
1982 350 02:15:02 ZULU





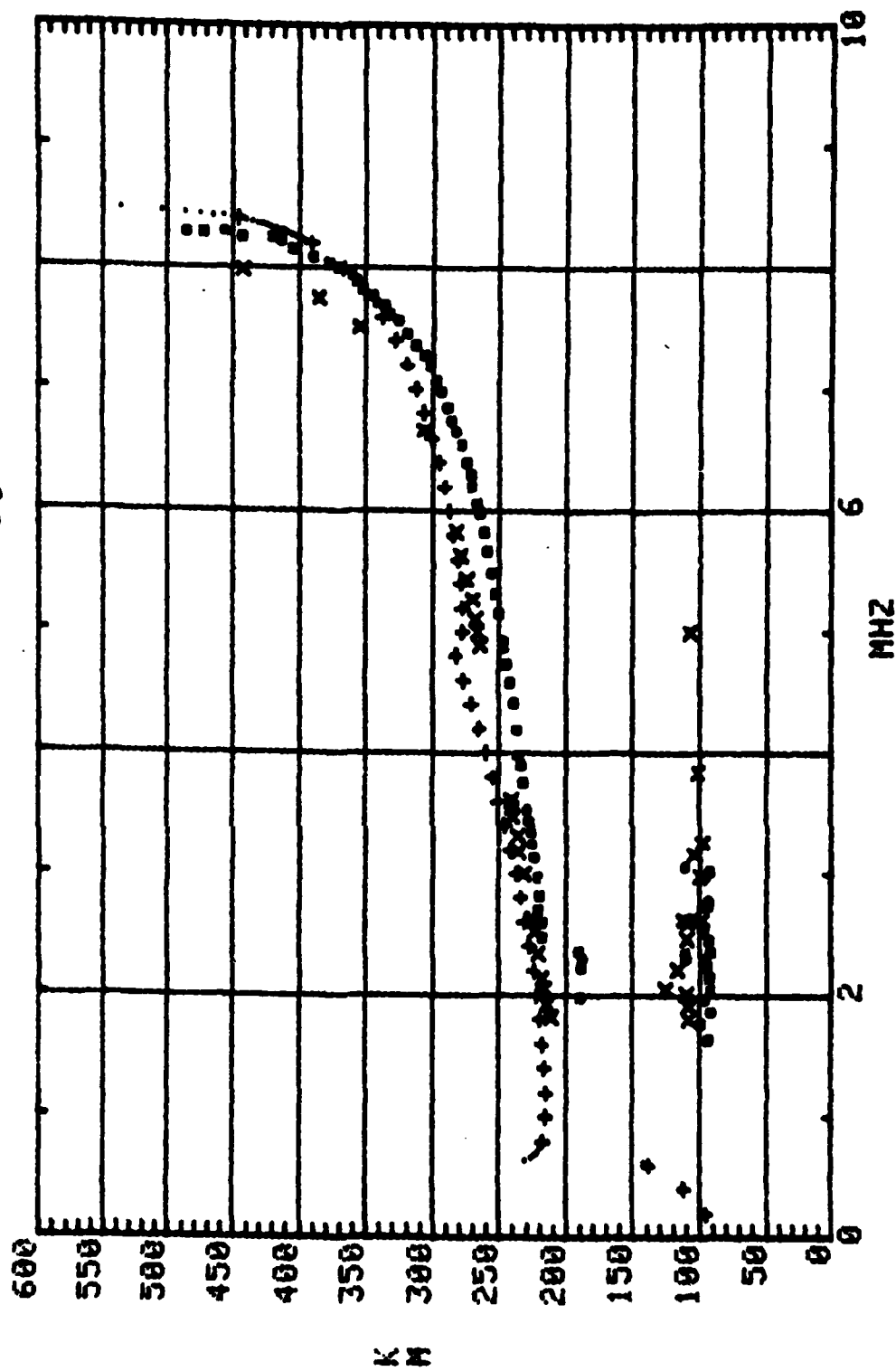
D350, 0200

VERTICAL IONOGRAM

+++... OI 02:00:02

xxx DRS 02:00

... FO 01:58



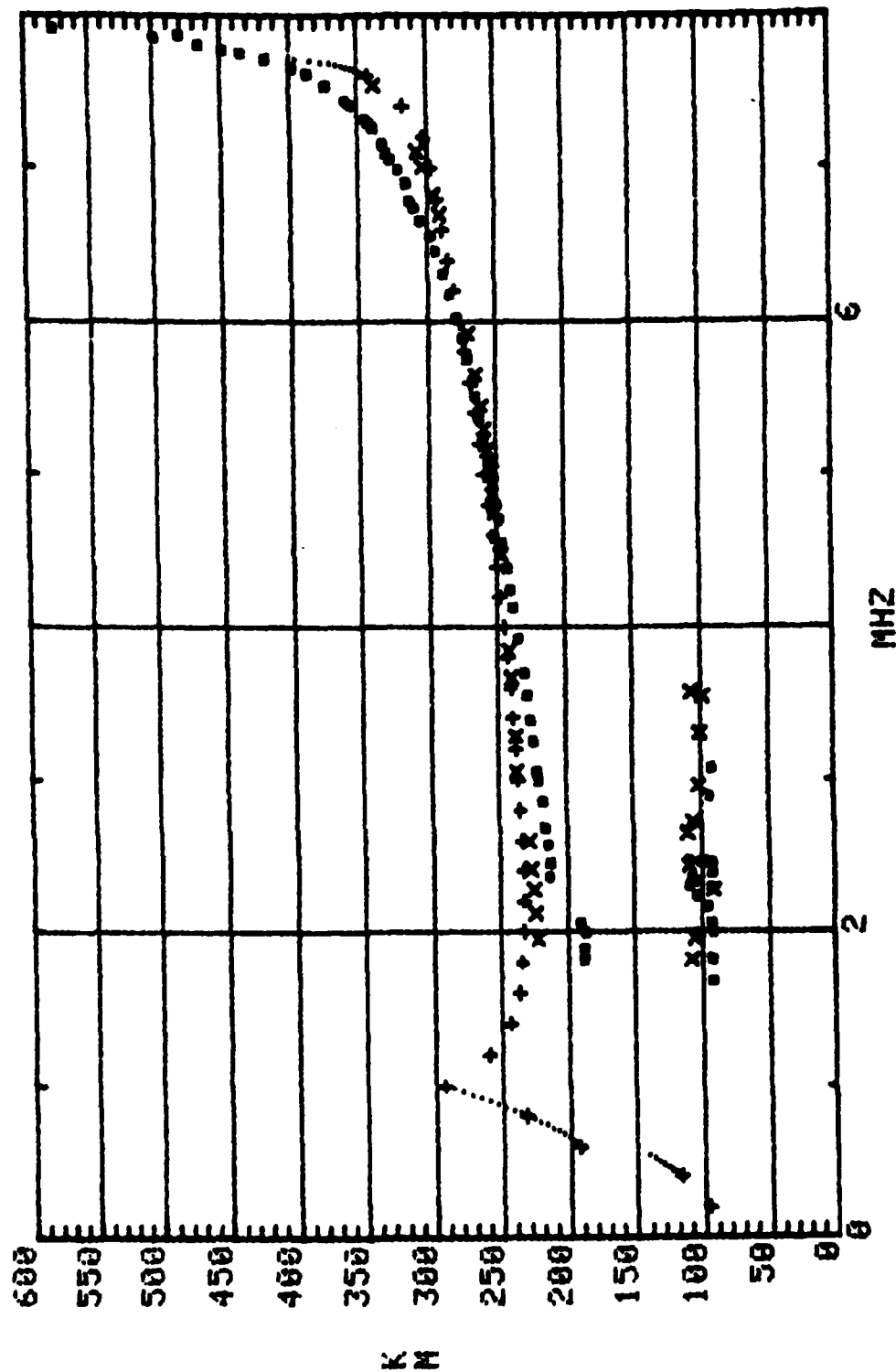
D350, 02:15

VERTICAL IONOGRAM

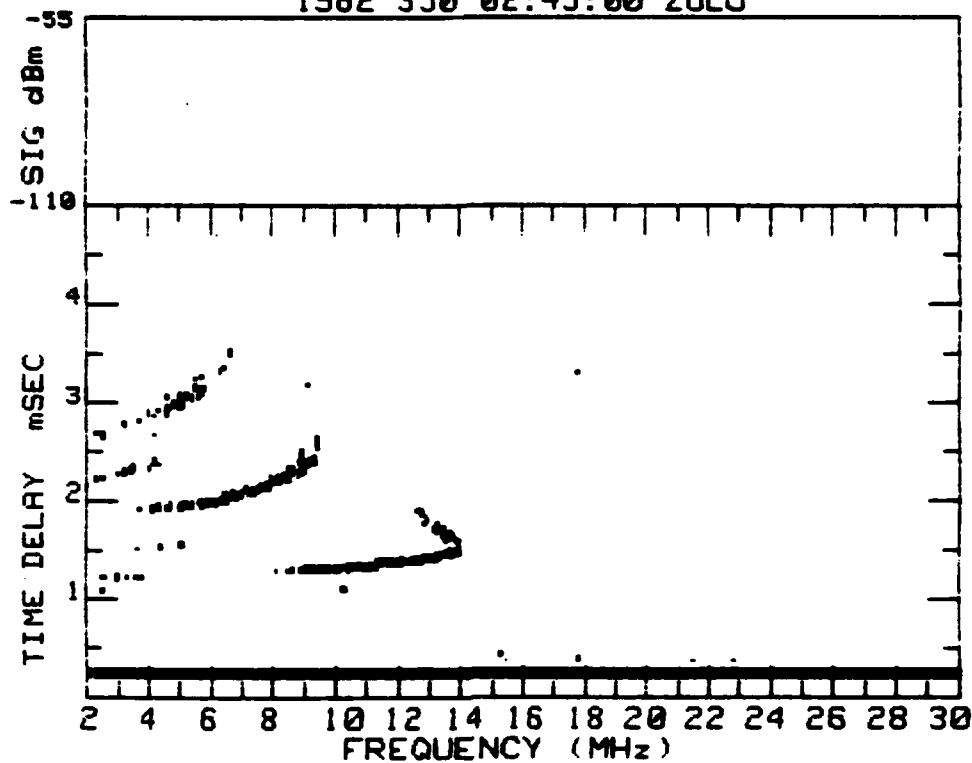
+++... OI 02:15:02

xxx DRS 02:15

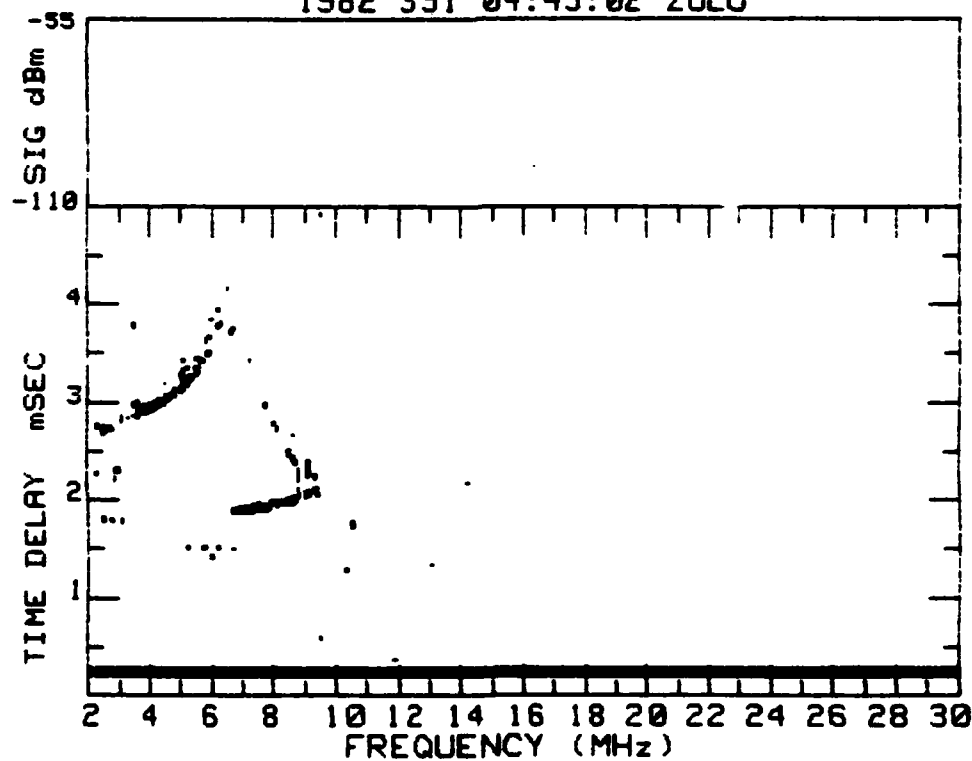
■ ■ ■ FO 02:13



SSL OIS#2 ZONE 4 ERIE,CO TO FT ORD,CA  
1982 350 02:45:00 ZULU



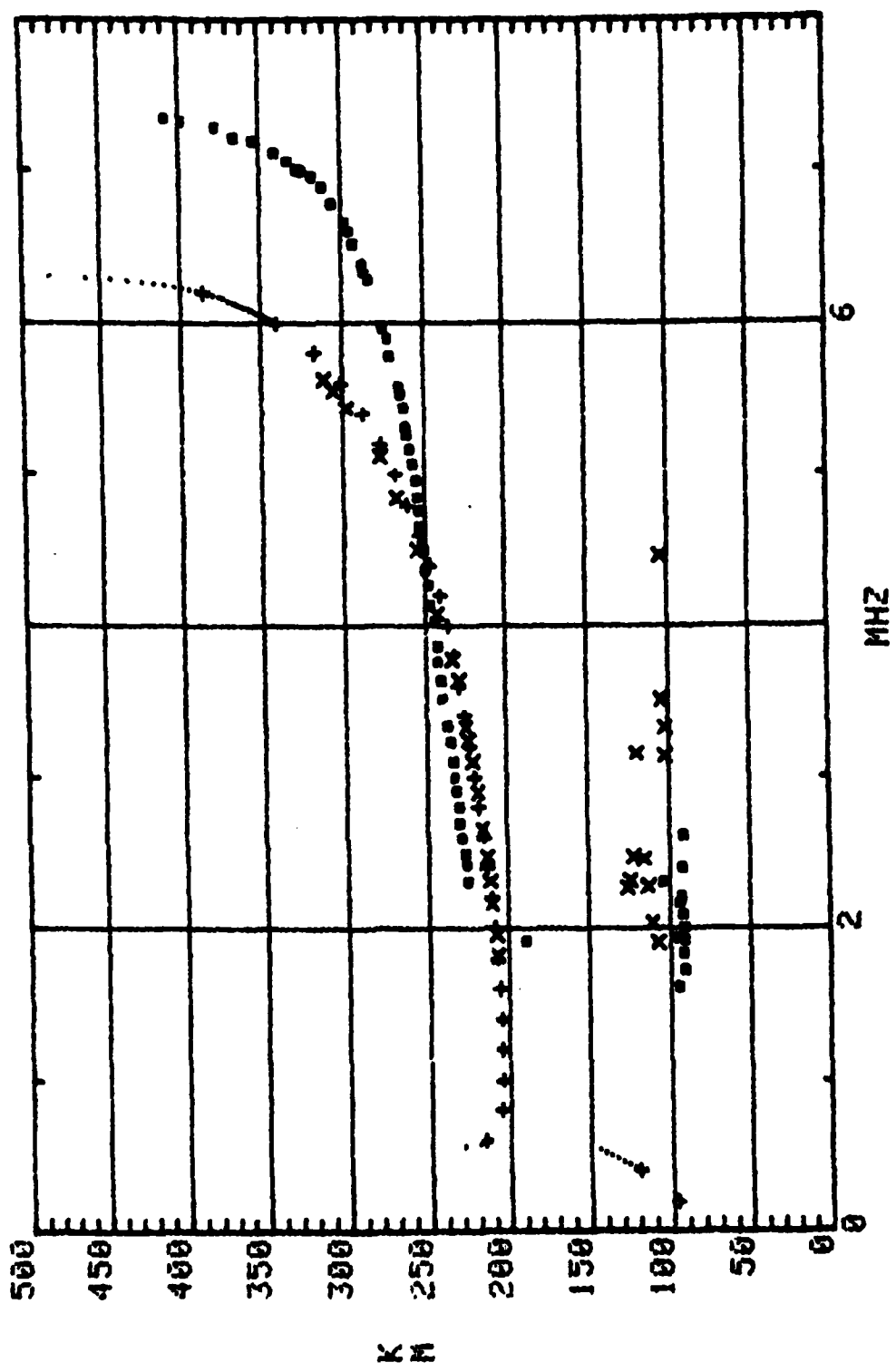
SSL OIS#2 ZONE 4 ERIE,CO TO FT ORD,CA  
1982 351 04:45:02 ZULU



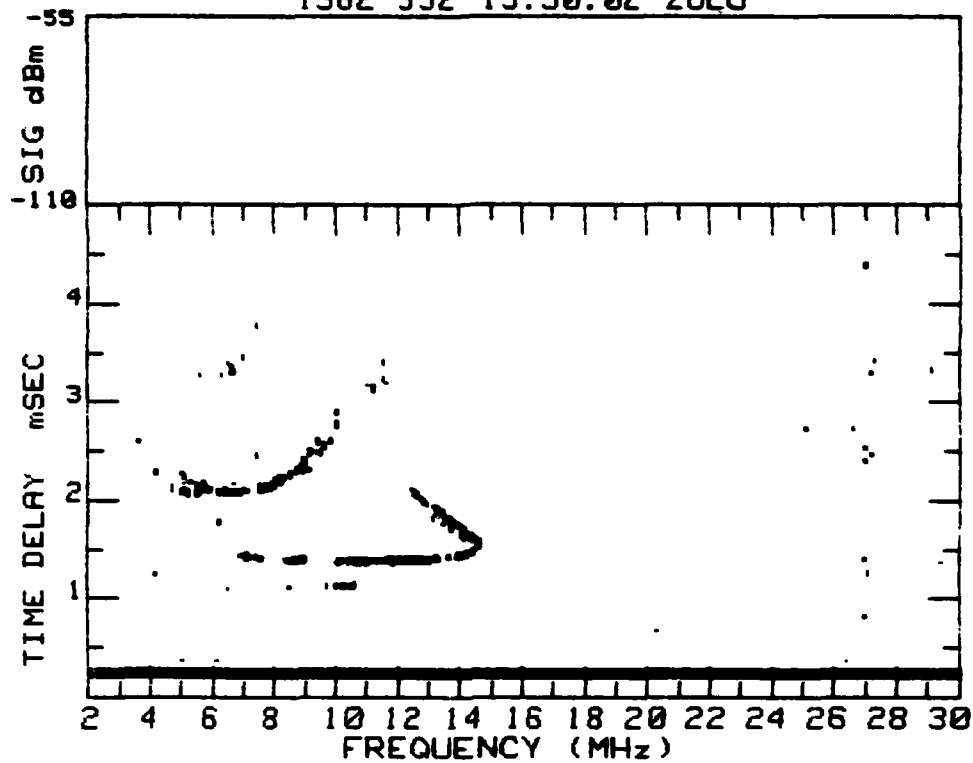
D350, 0245

VERTICAL IONOGRAM

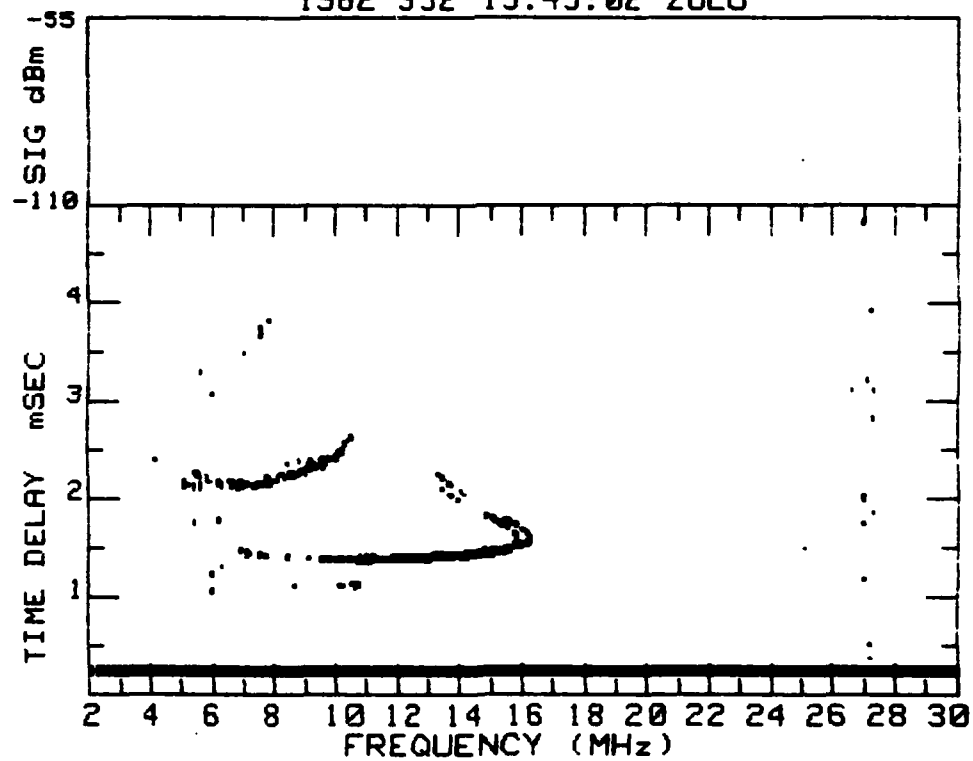
+++... OI 02:45:00  
 xxx DRS 02:45  
 ■■■ FO 02:43



SSL OIS#2 ZONE 4 ERIE,CO TO FT ORD,CA  
1982 352 15:30:02 ZULU



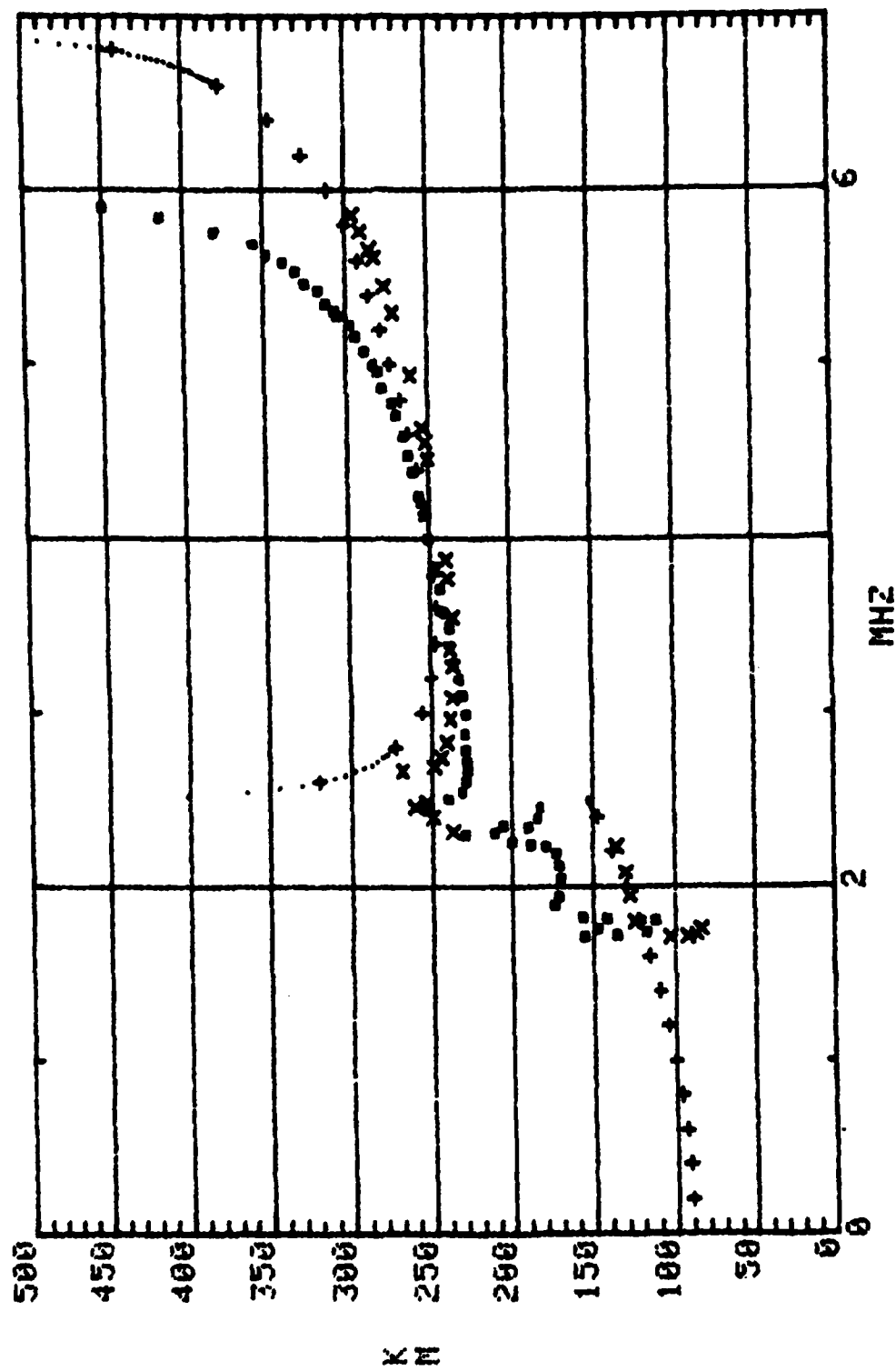
SSL OIS#2 ZONE 4 ERIE,CO TO FT ORD,CA  
1982 352 15:45:02 ZULU



0352, /530

VERTICAL IONOGRAM

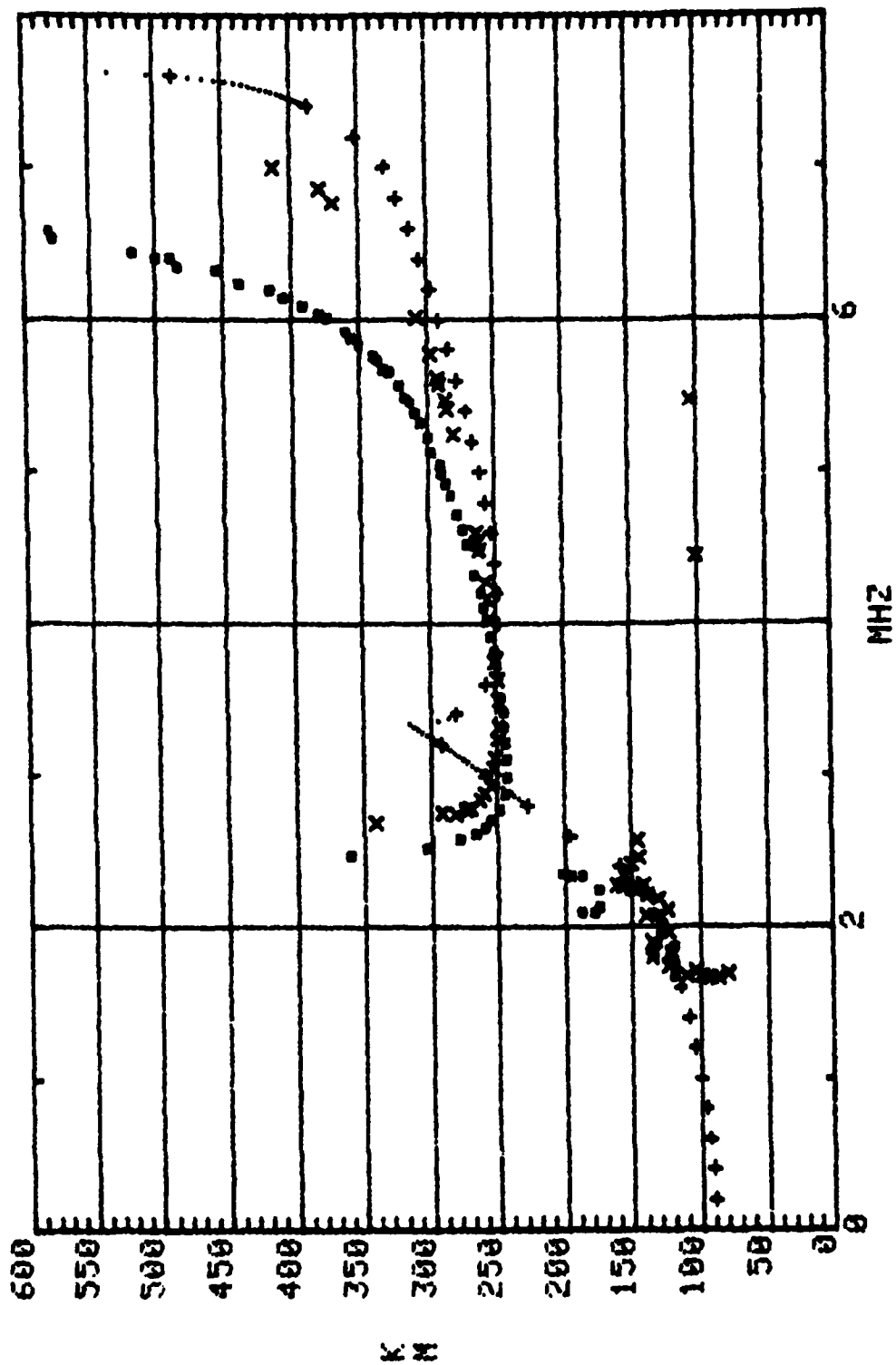
+++...	OI	15:30:02
xxx	DRS	15:30
■■■	FO	15:27



D352, 1545

VERTICAL IONOGRAM

+++... OI 15:45:02  
 xxx DRS 15:45  
 ■■■ FO 15:43



APPENDIX B

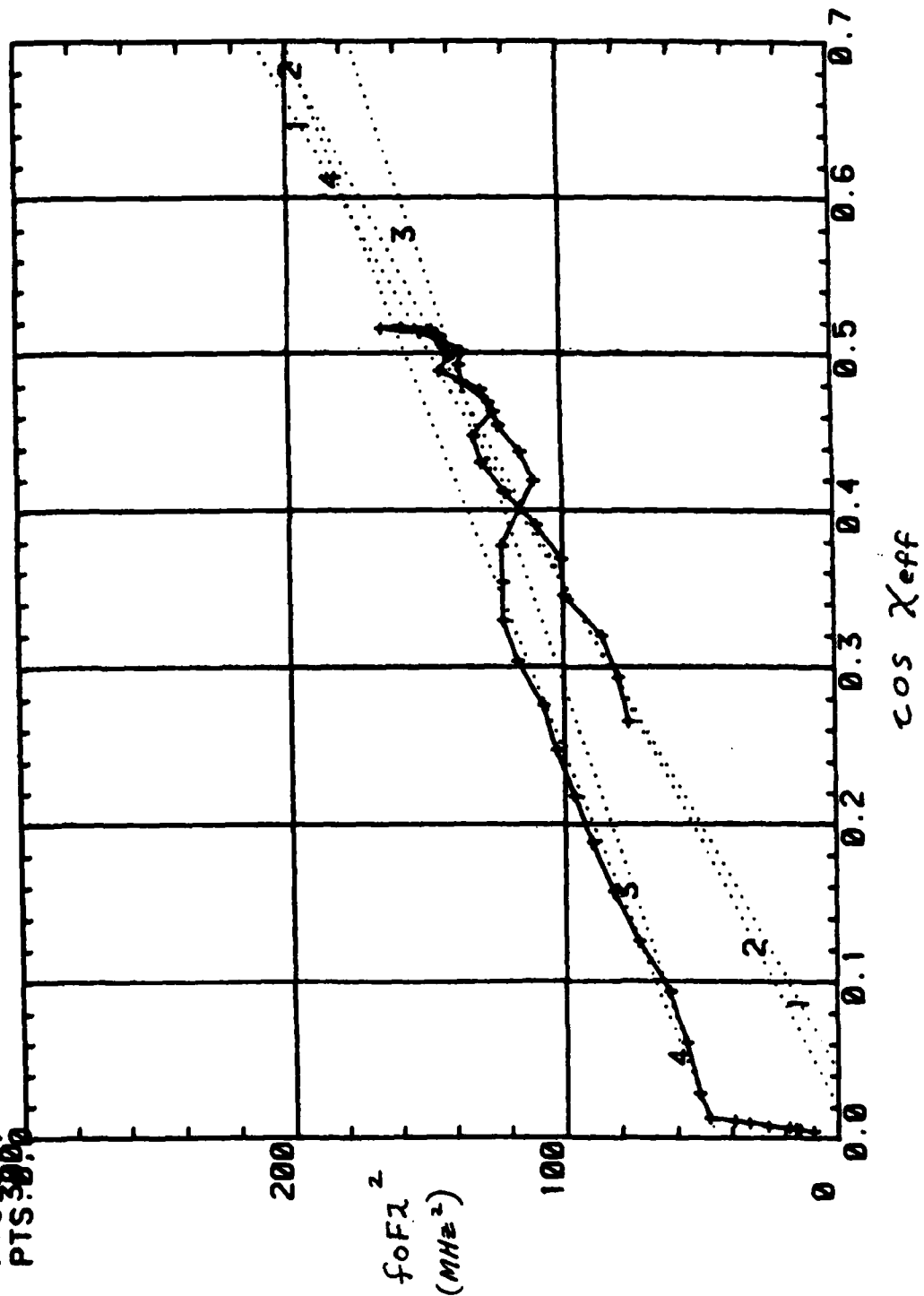
Plots of  $f_oF_2^2$  vs.  $\cos \chi_{eff}$



X1: 0340,1600 - D341,0400 (UT)

TREND LINES:

- L1: PTS.1.9
- L2: PTS.1.17
- L3: PTS.1.41
- L4: PTS.28.41
- L5: PTS.30.0



106 105 104 103 102 101 100 99 98 97 96 95 94 93 92 91 90 89 88 87 86 85 84 83 82 81 80 79 78 77 76 75 74 73 72 71 70 69 68 67 66 65 64 63 62 61 60 59 58 57 56 55 54 53 52 51 50 49 48 47 46 45 44 43 42 41 40 39 38 37 36 35 34 33 32 31 30 29 28 27 26 25 24 23 22 21 20 19 18 17 16 15 14 13 12 11 10 9 8 7 6 5 4 3 2 1 0

NAS: D340, 16:05 - 19:25 (UT)

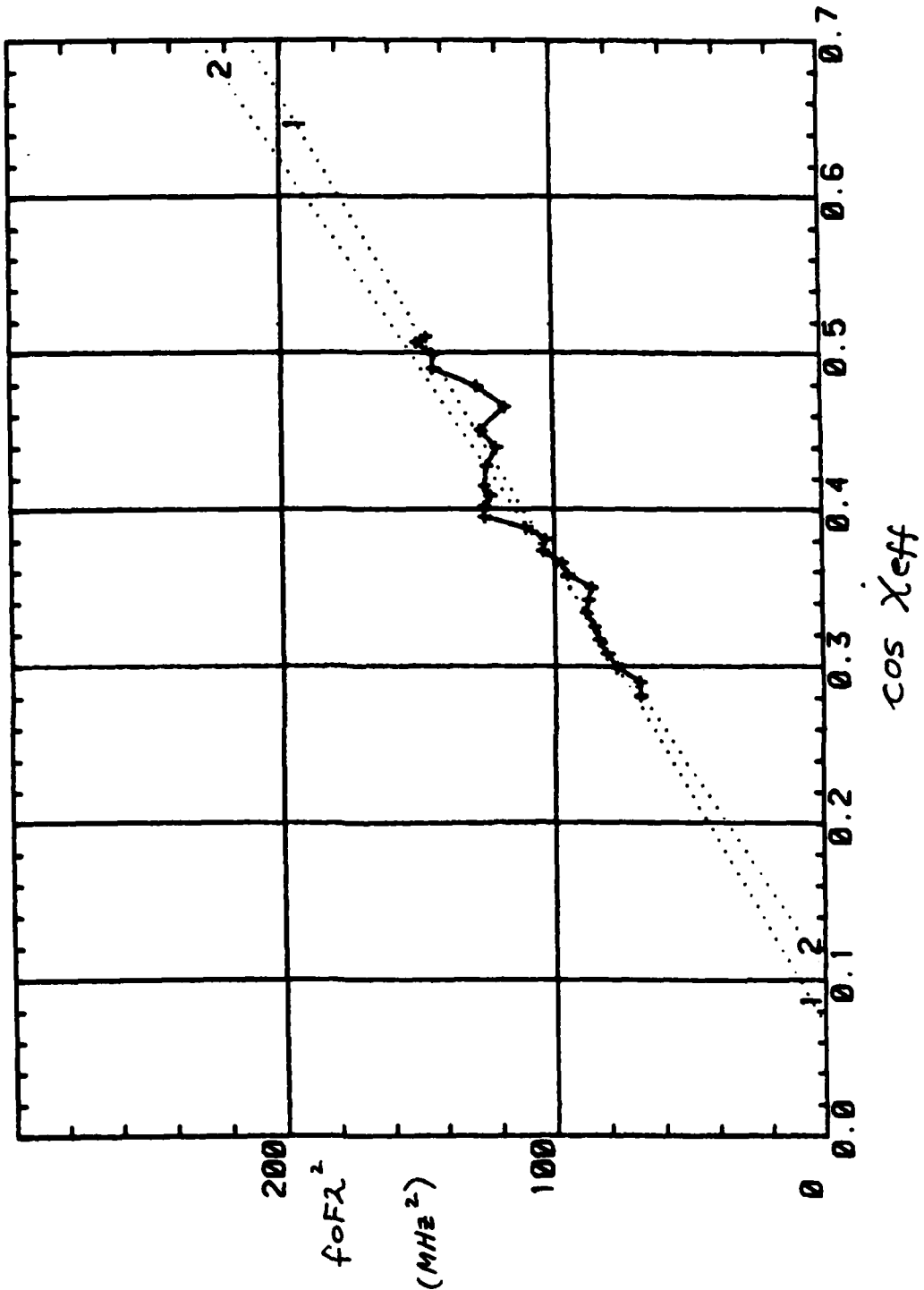
TREND LINES:

L1: PTS.1.27

L2: PTS.1.21

L3: PTS.0.0

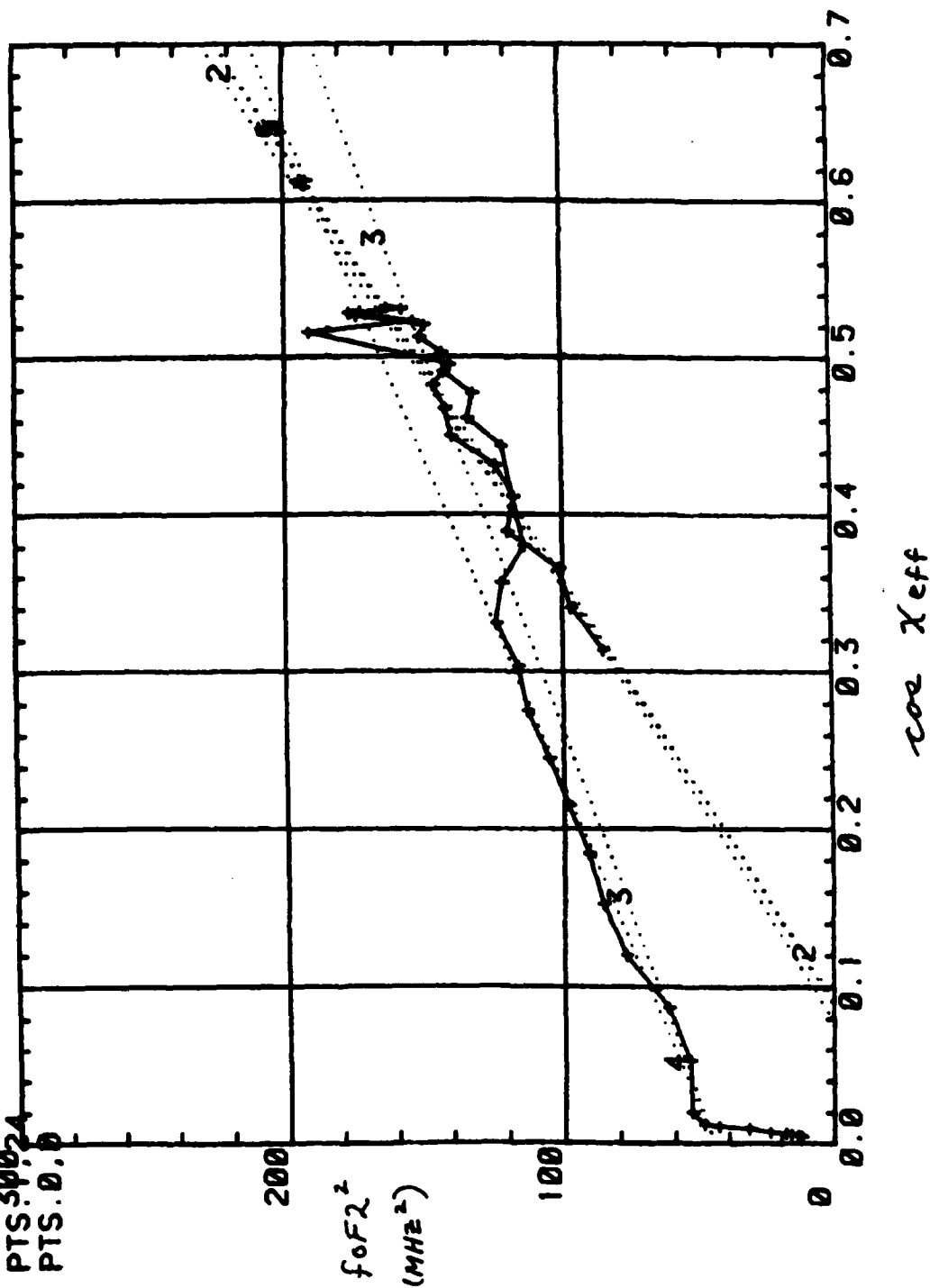
compare with  $X_1$





X3: D340,1600 - D341,0400 (UT)

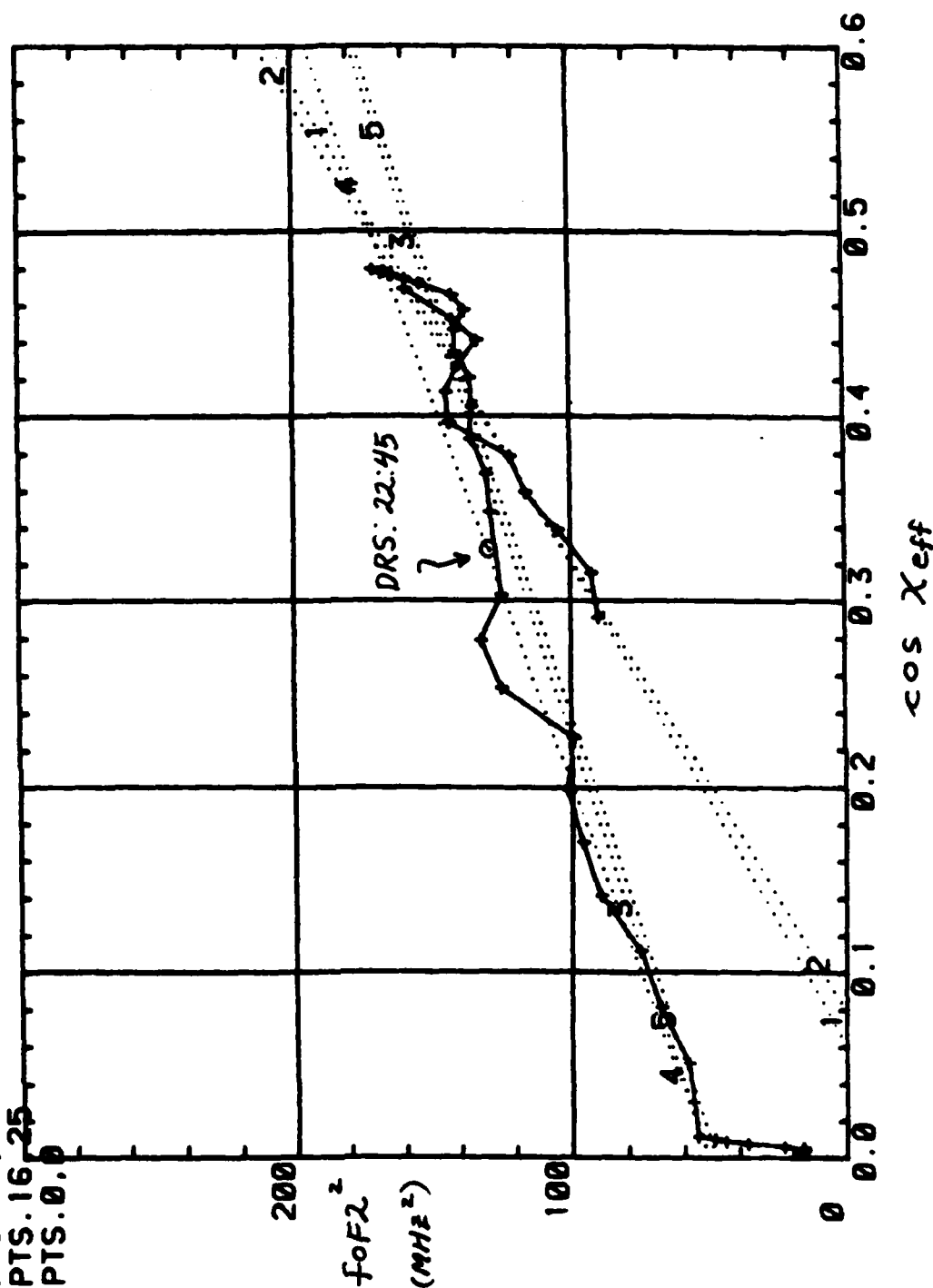
TREND LINES:  
 L1: PTS.1.9  
 L2: PTS.1.16  
 L3: PTS.1.37  
 L4: PTS.27.37  
 L5: PTS.30.24  
 L6: PTS.0.0



X4: D340,1600 - D341, 0400 (UT)

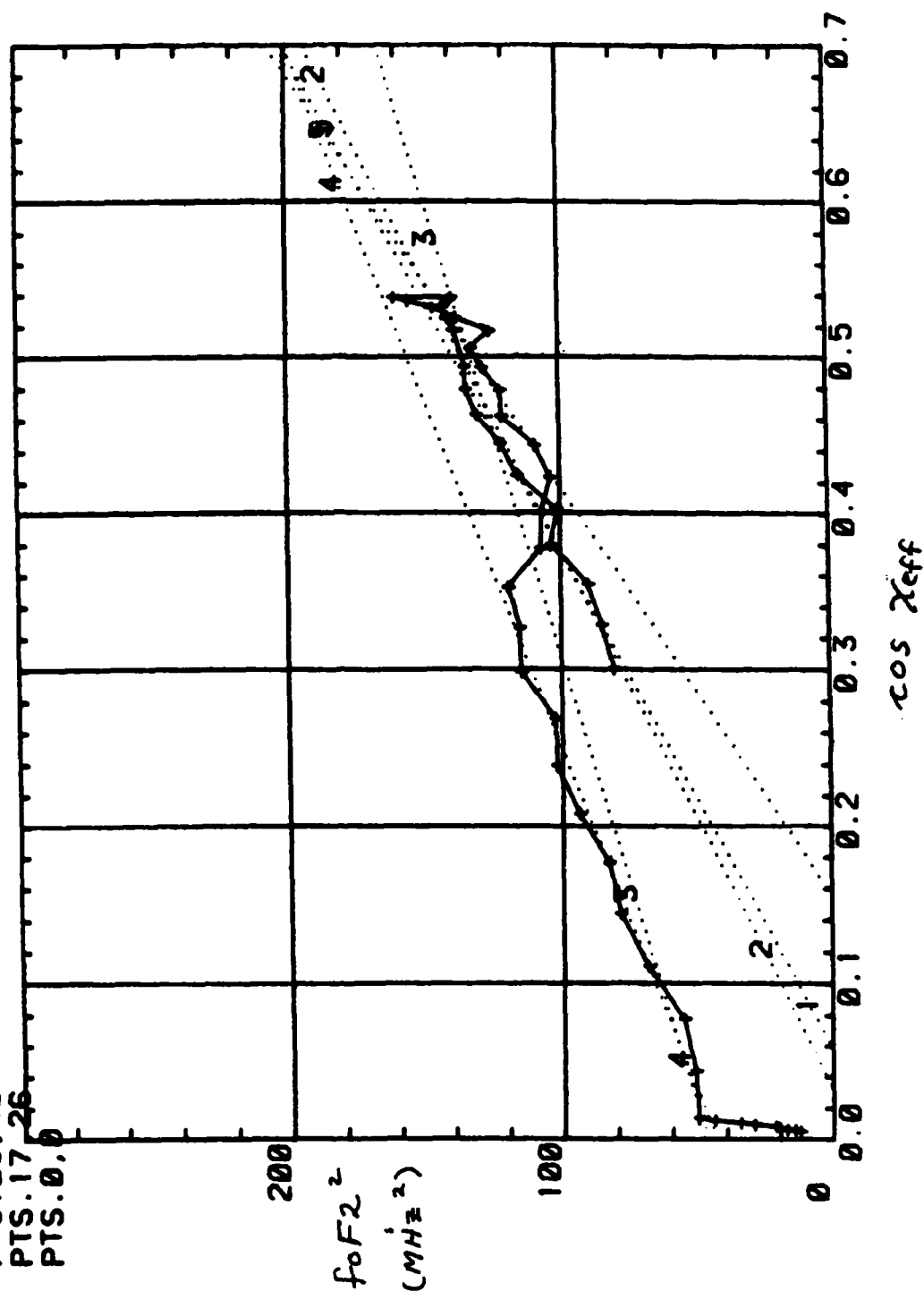
TREND LINES:

- L1: PTS.1.9
- L2: PTS.1.16
- L3: PTS.1.37
- L4: PTS.25.37
- L5: PTS.16.25
- L6: PTS.0.0



X5: D340, 1600 - D341, 0400 (UT)

TREND LINES:  
 L1: PTS. 1.9  
 L2: PTS. 1.16  
 L3: PTS. 1.40  
 L4: PTS. 29.40  
 L5: PTS. 17.26  
 L6: PTS. 0.0



VBG: D340, 1700-2200 (UT)

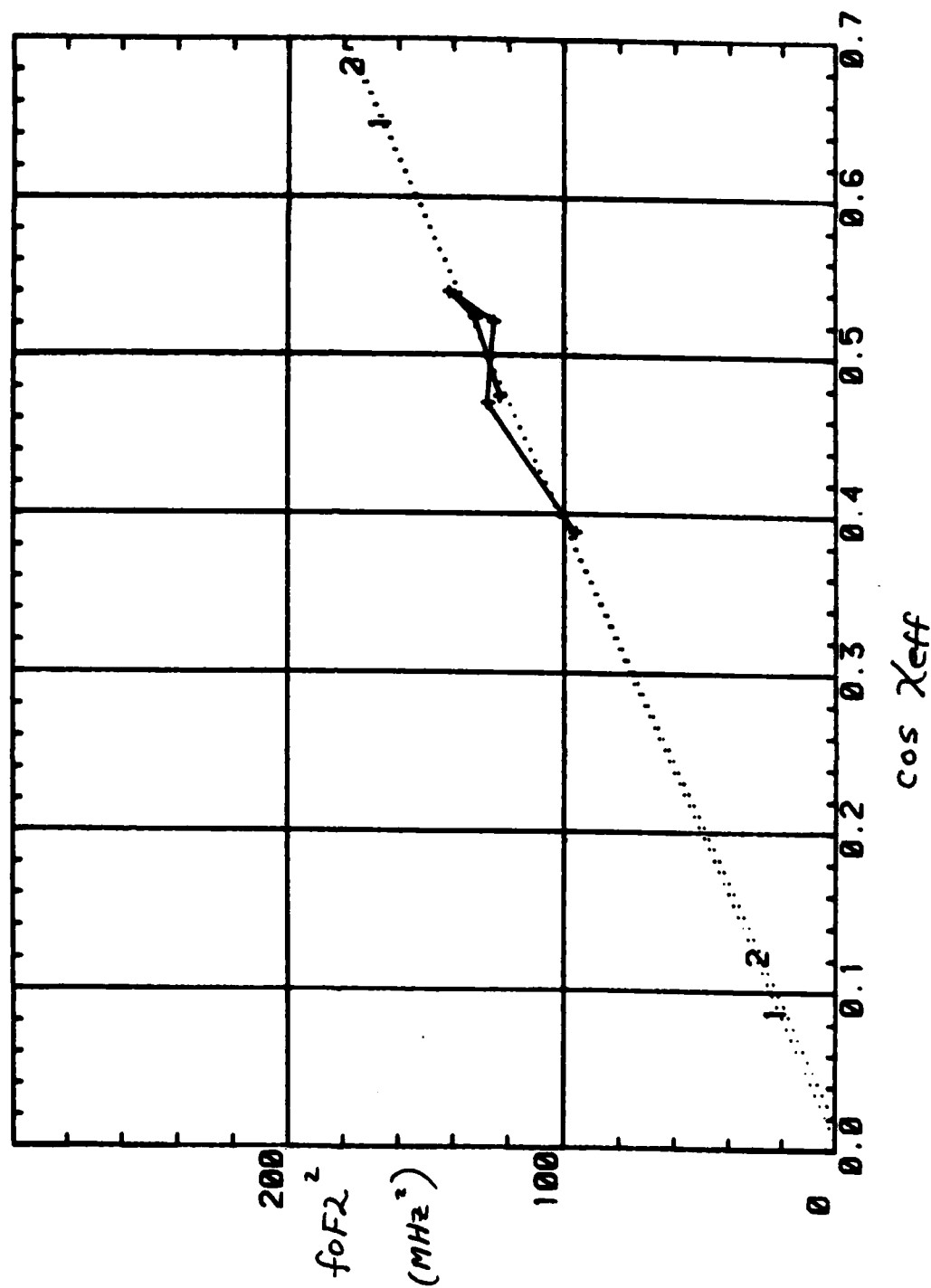
TREND LINES:

L1: PTS.1.6

L2: PTS.1.4

L3: PTS.0.0

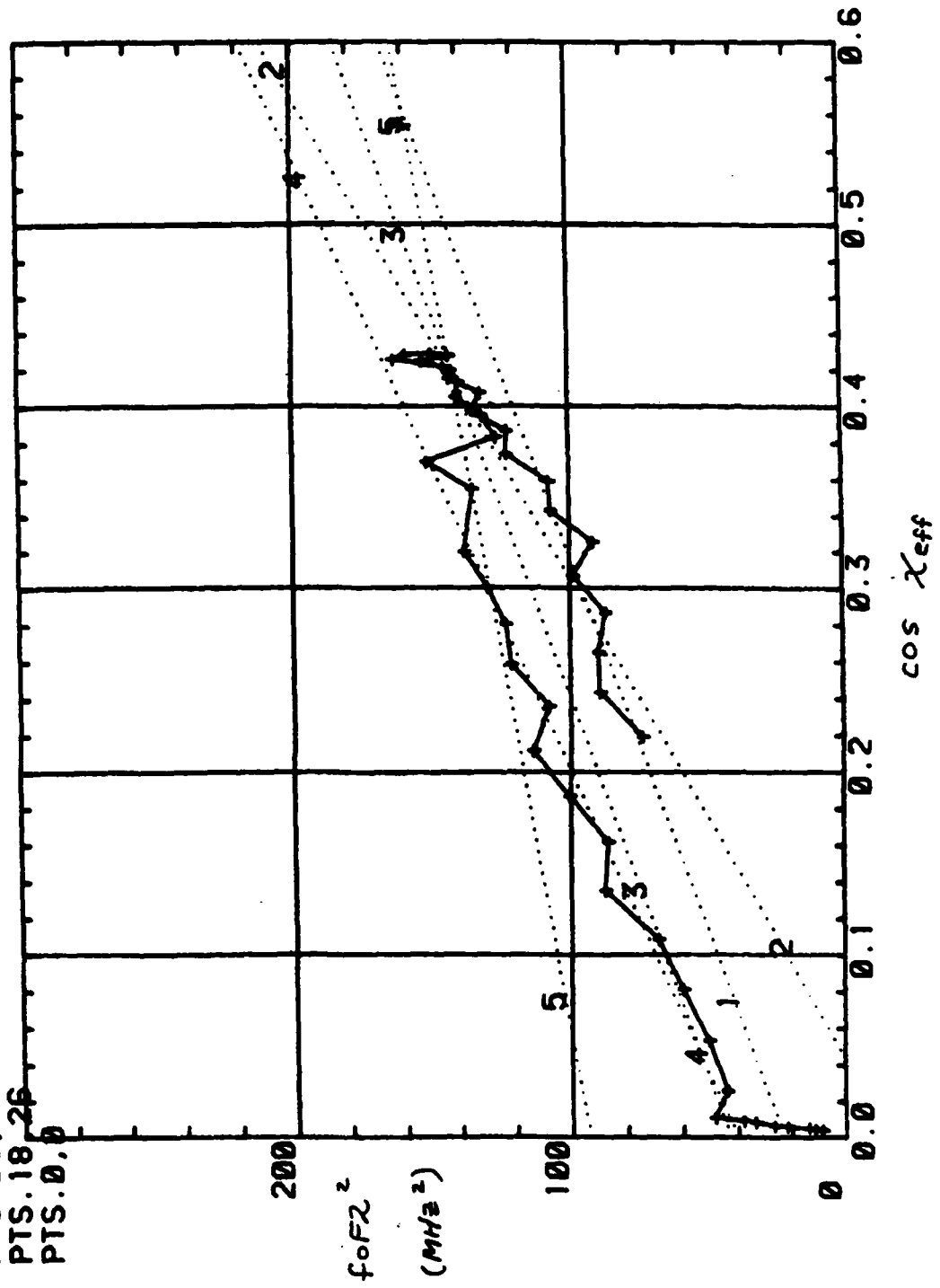
*compare with X5*



X6: D340, 1600 - D341, 0400 (UT)

TREND LINES:

- L1: PTS.1.9
- L2: PTS.1.17
- L3: PTS.1.40
- L4: PTS.25.40
- L5: PTS.18.26
- L6: PTS.0.0

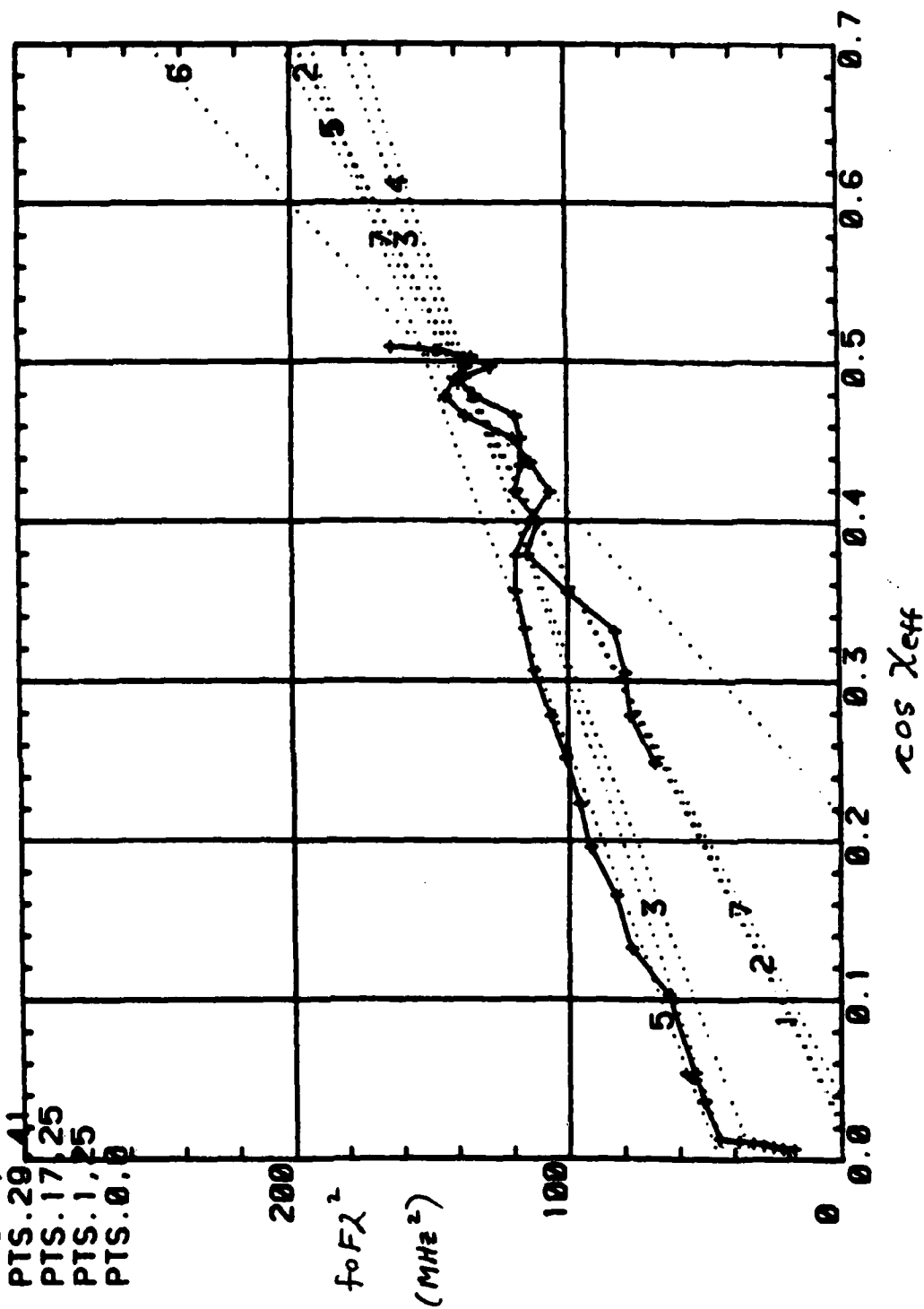




Ft. Ord (R): Day 340, 1600 — Day 341, 03:45 (UT)

TREND LINES:

L1: PTS.1.9  
 L2: PTS.1.17  
 L3: PTS.1.47  
 L4: PTS.1.41  
 L5: PTS.29.41  
 L6: PTS.17.25  
 L7: PTS.1.25  
 L8: PTS.0.0



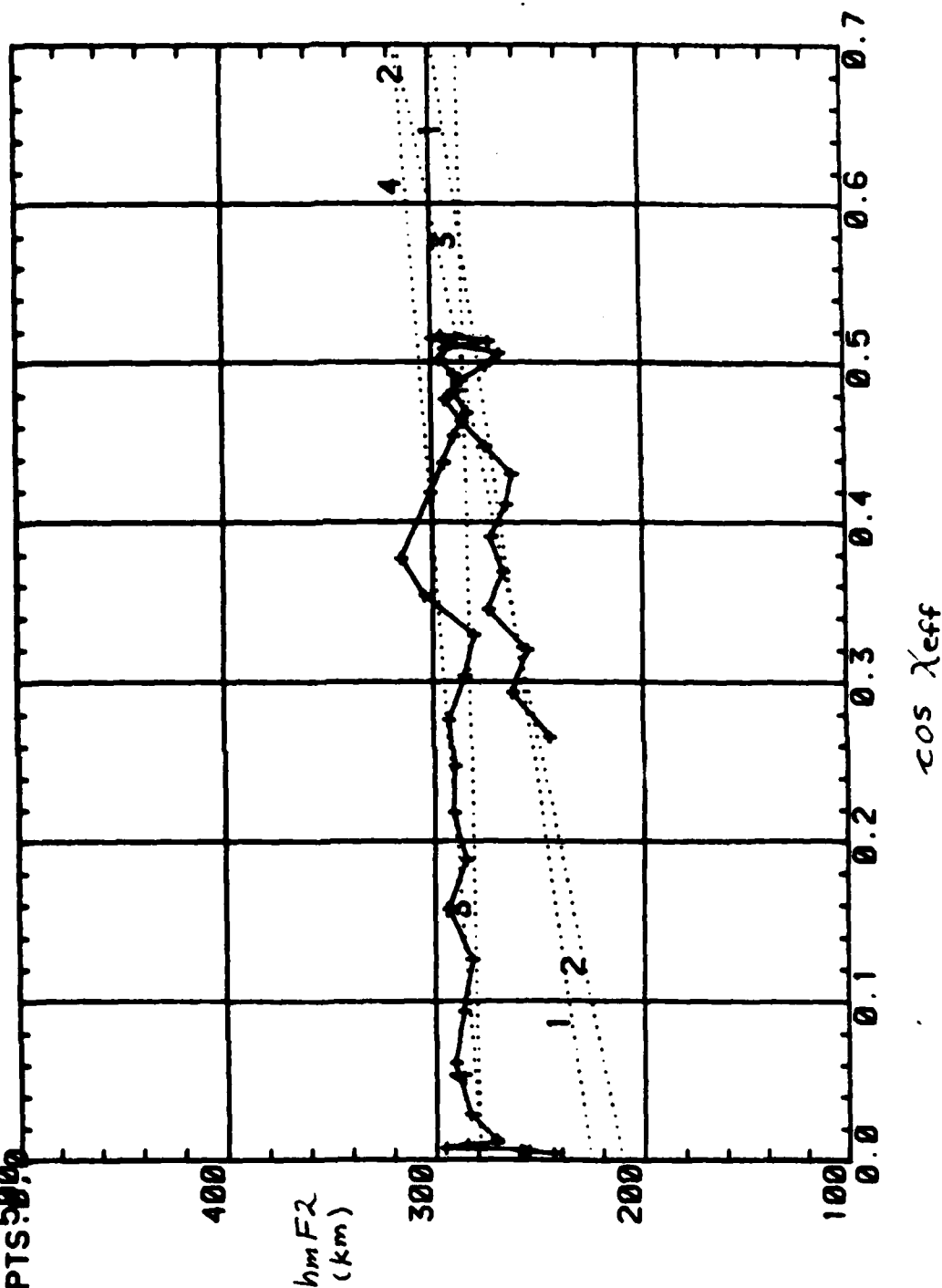
APPENDIX C

Plots of  $h_m F_2$  vs.  $\cos \chi_{off}$

X1: D340, 1600 - D341, 0400 (UT)

TREND LINES:

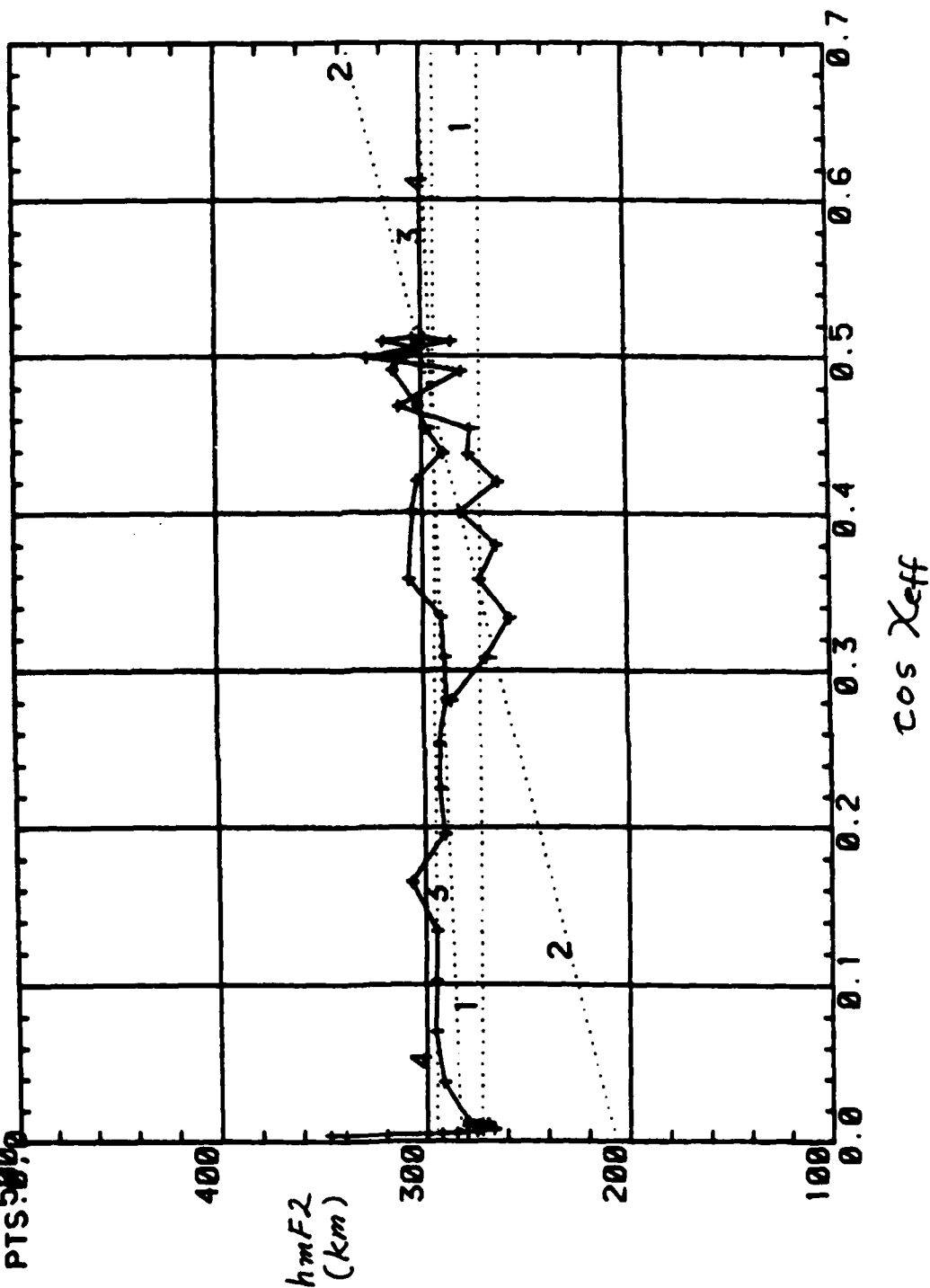
- L1: PTS. 1.9
- L2: PTS. 1.17
- L3: PTS. 1.41
- L4: PTS. 28.41
- L5: PTS. 50.0



X2: D340,1600 - D341,0400 (UT)

TREND LINES:

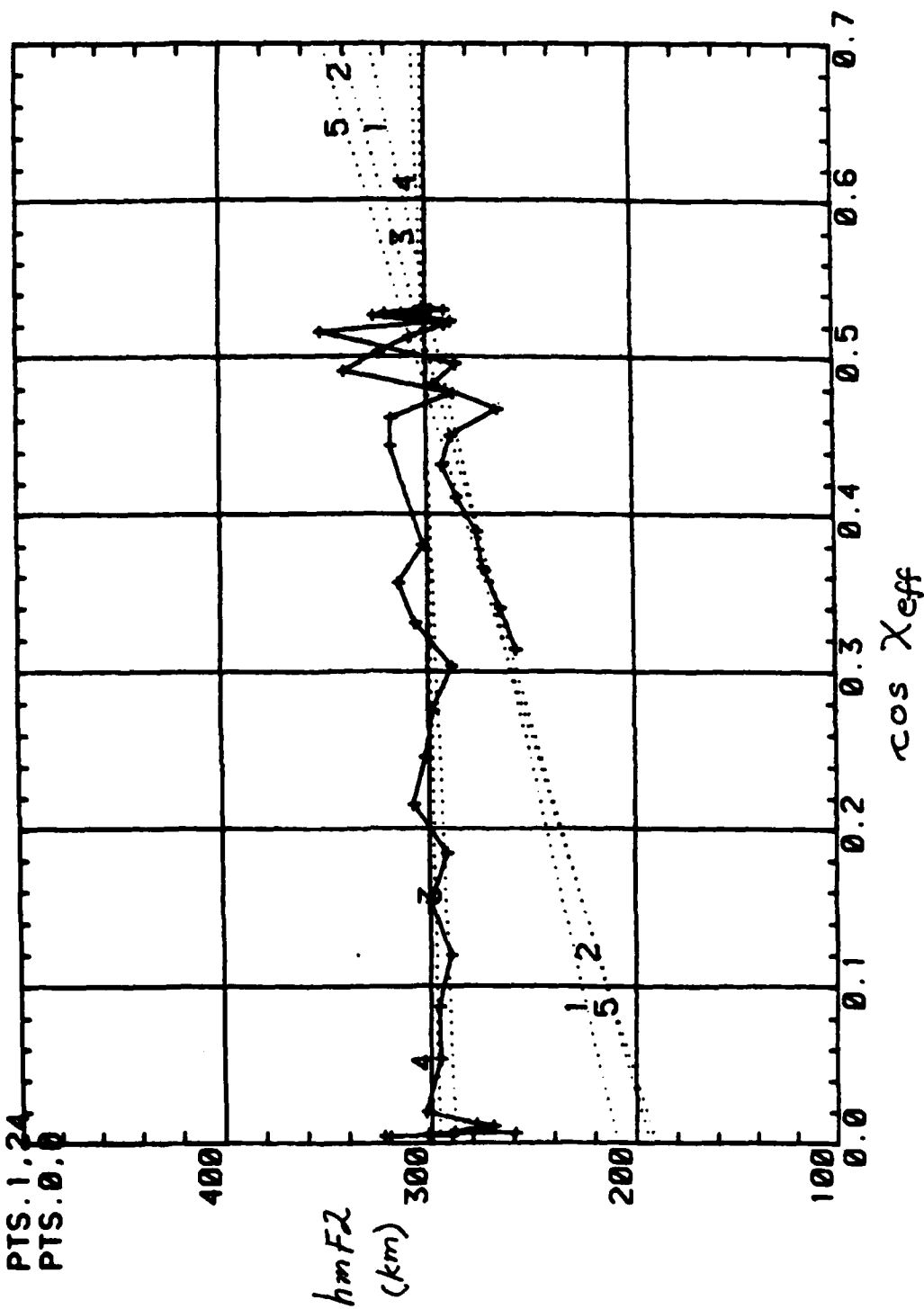
- L1: PTS.1,9
- L2: PTS.1,16
- L3: PTS.1,36
- L4: PTS.26,36
- L5: PTS.50,0



X3: D 340, 1600 - D 341, 0400 (UT)

TREND LINES:

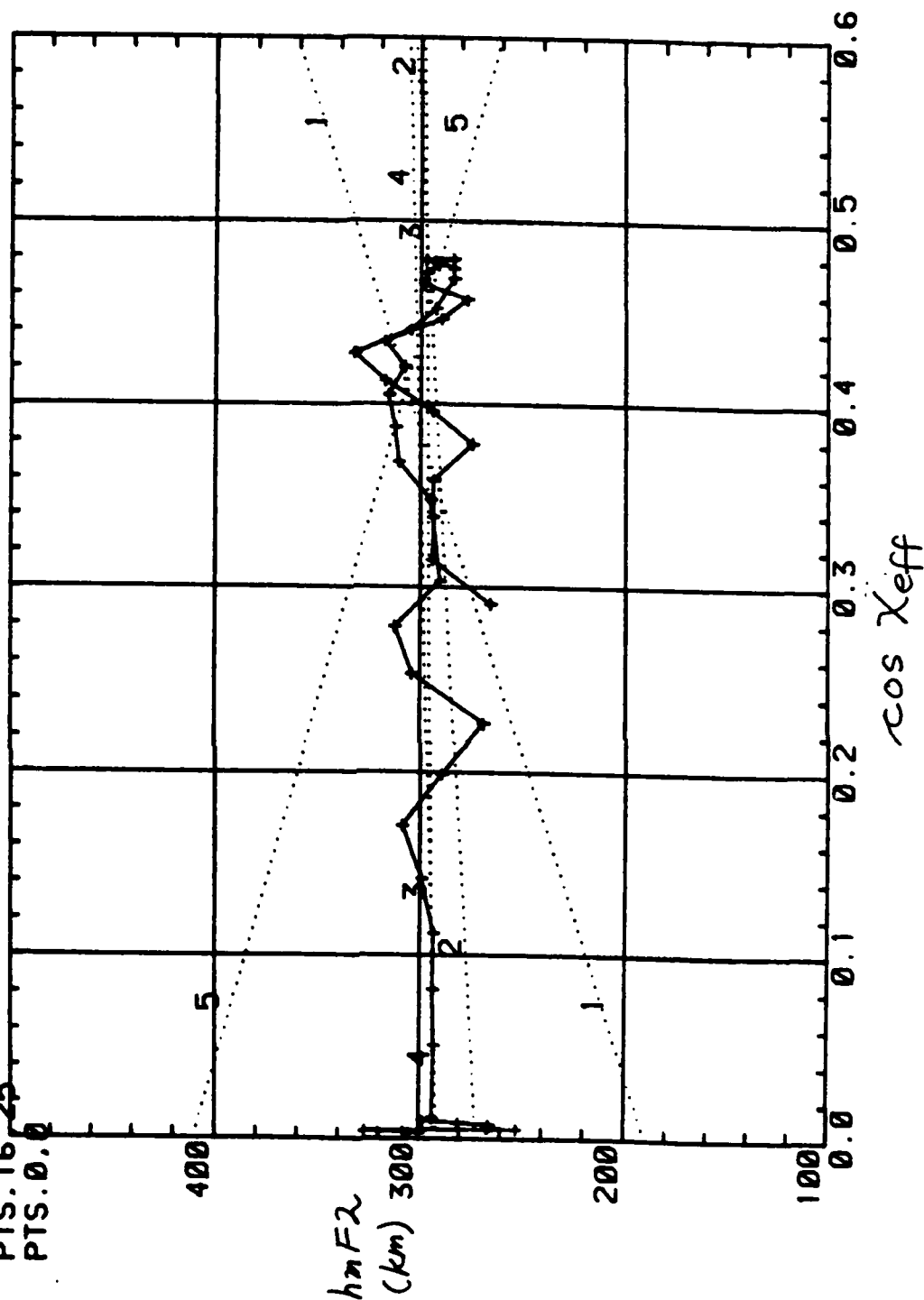
L1: PTS.1.9  
 L2: PTS.1.16  
 L3: PTS.1.37  
 L4: PTS.27.37  
 L5: PTS.1.24  
 L6: PTS.0.0



X4: D 340, 1600 - D 341, 0400 (UT)

TREND LINES:

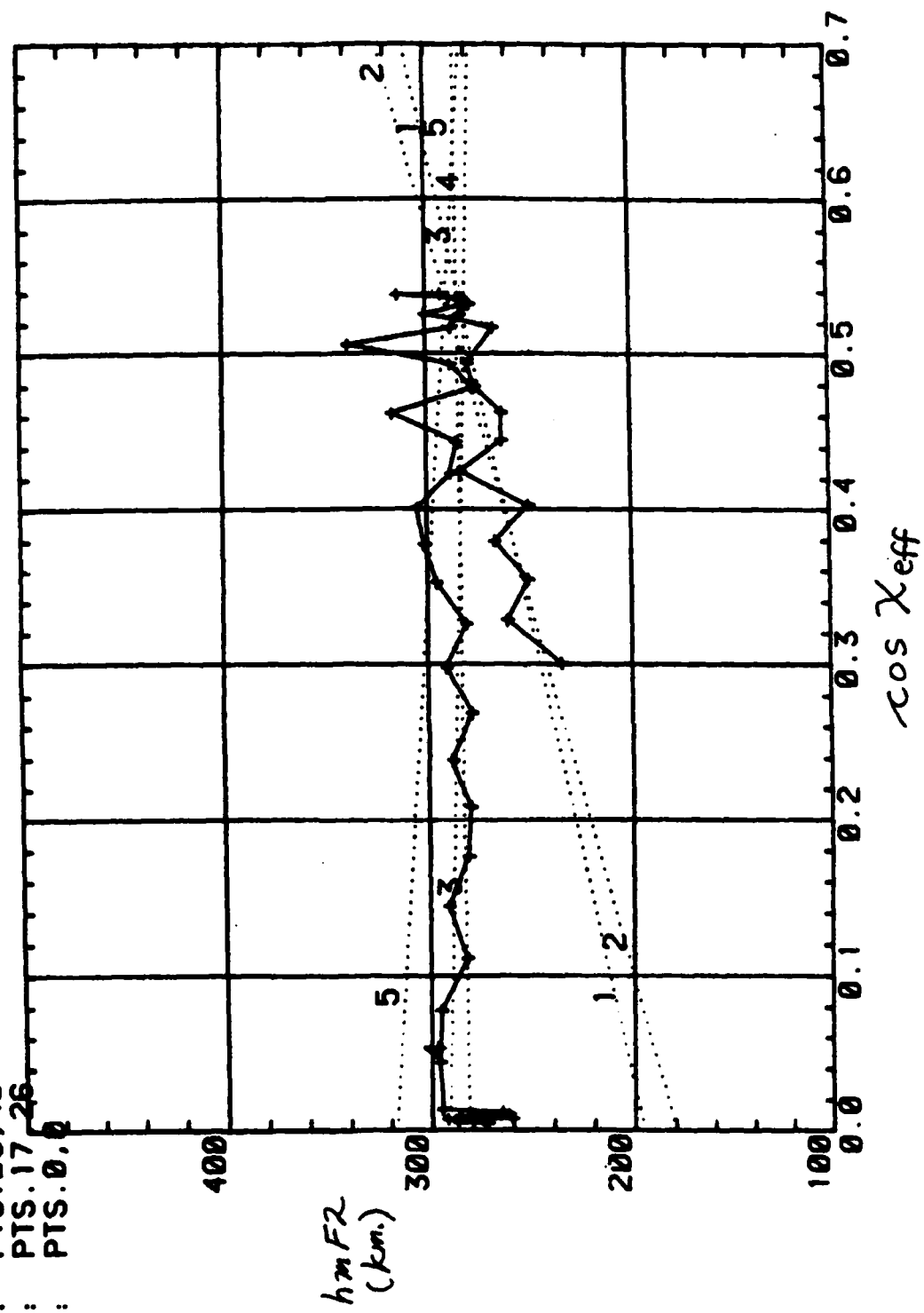
L1: PTS. 1.9  
 L2: PTS. 1.16  
 L3: PTS. 1.37  
 L4: PTS. 25.37  
 L5: PTS. 16.25  
 L6: PTS. 0.0



X5: D340,1600 - D341, 0400 (UT)

TREND LINES:

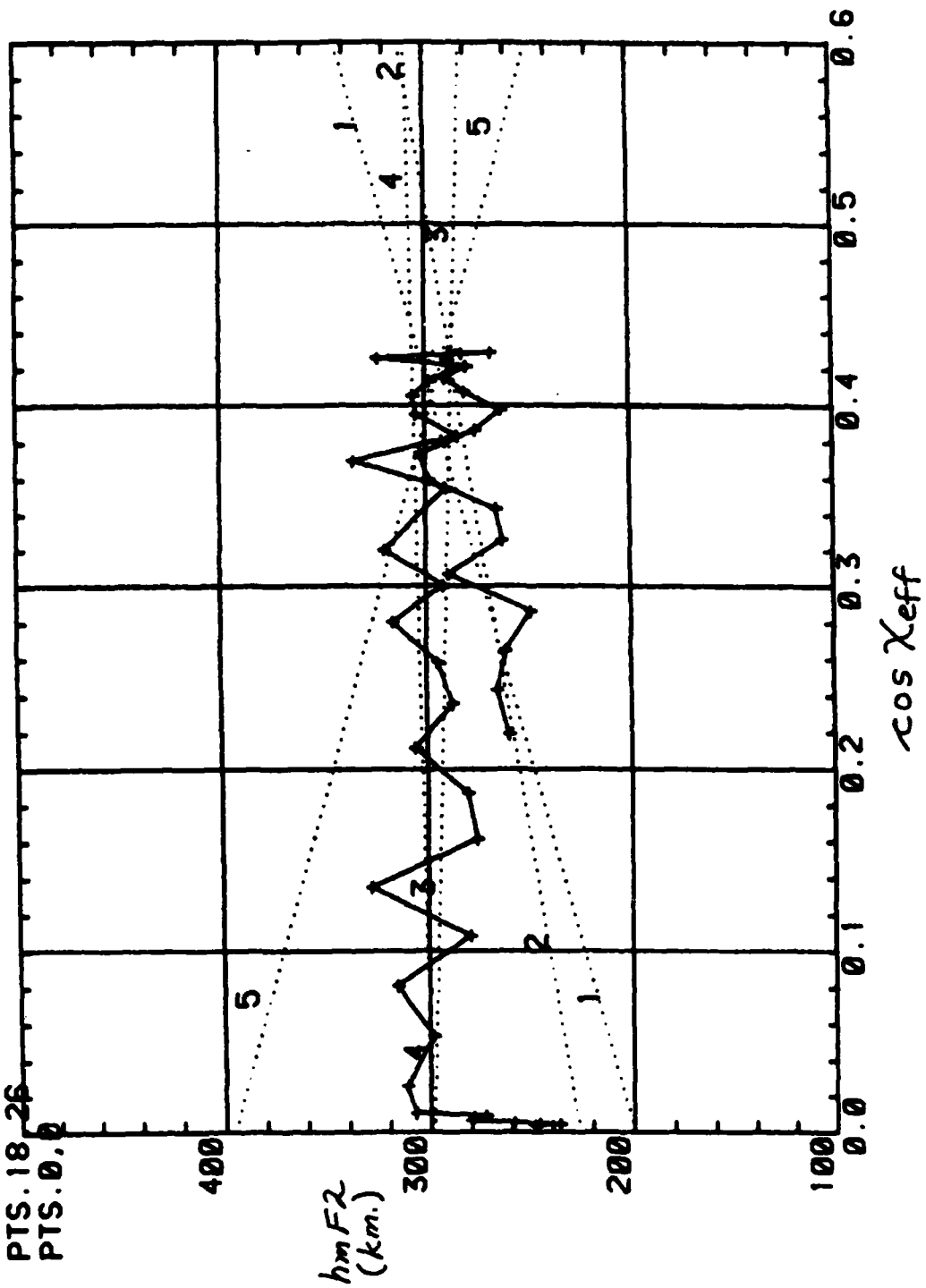
- L1: PTS.1,9
- L2: PTS.1,16
- L3: PTS.1,40
- L4: PTS.29,40
- L5: PTS.17,26
- L6: PTS.0,0



X6: D340, 1600 - D341, 0400 (UT)

TREND LINES:

- L1: PTS. 1, 9
- L2: PTS. 1, 17
- L3: PTS. 1, 40
- L4: PTS. 25, 40
- L5: PTS. 18, 26
- L6: PTS. 0, 0





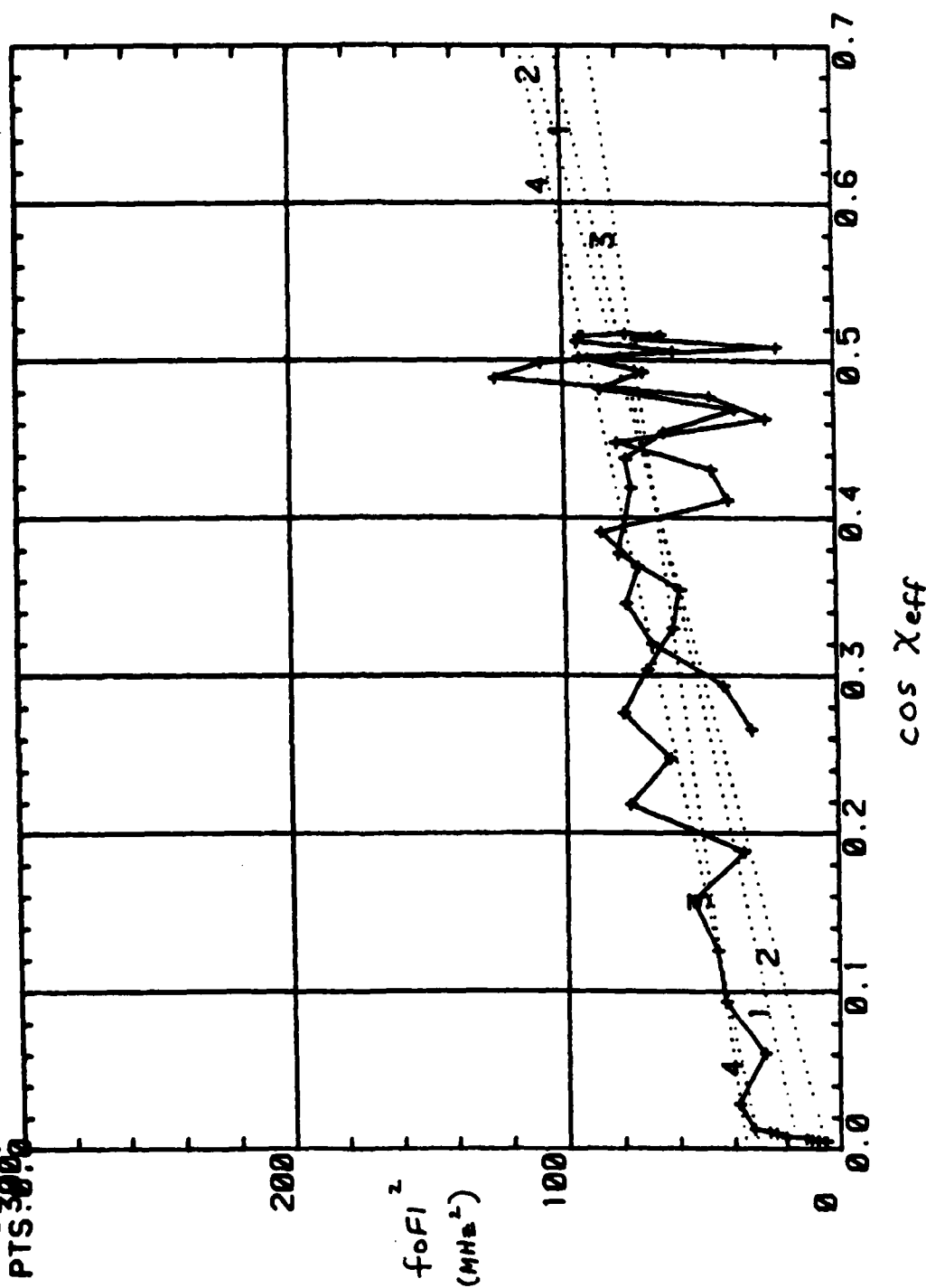
APPENDIX D

Plots of  $f_oF_1^2$  vs.  $\cos \chi_{\text{off}}$

X1: D340,1600 - D341,0400 (UT)

TREND LINES:

L1: PTS.1.9  
 L2: PTS.1.17  
 L3: PTS.1.41  
 L4: PTS.28.41  
 L5: PTS.30.0



X2: D340, 1600 - D341, 0400 (UT)

## TREND LINES:

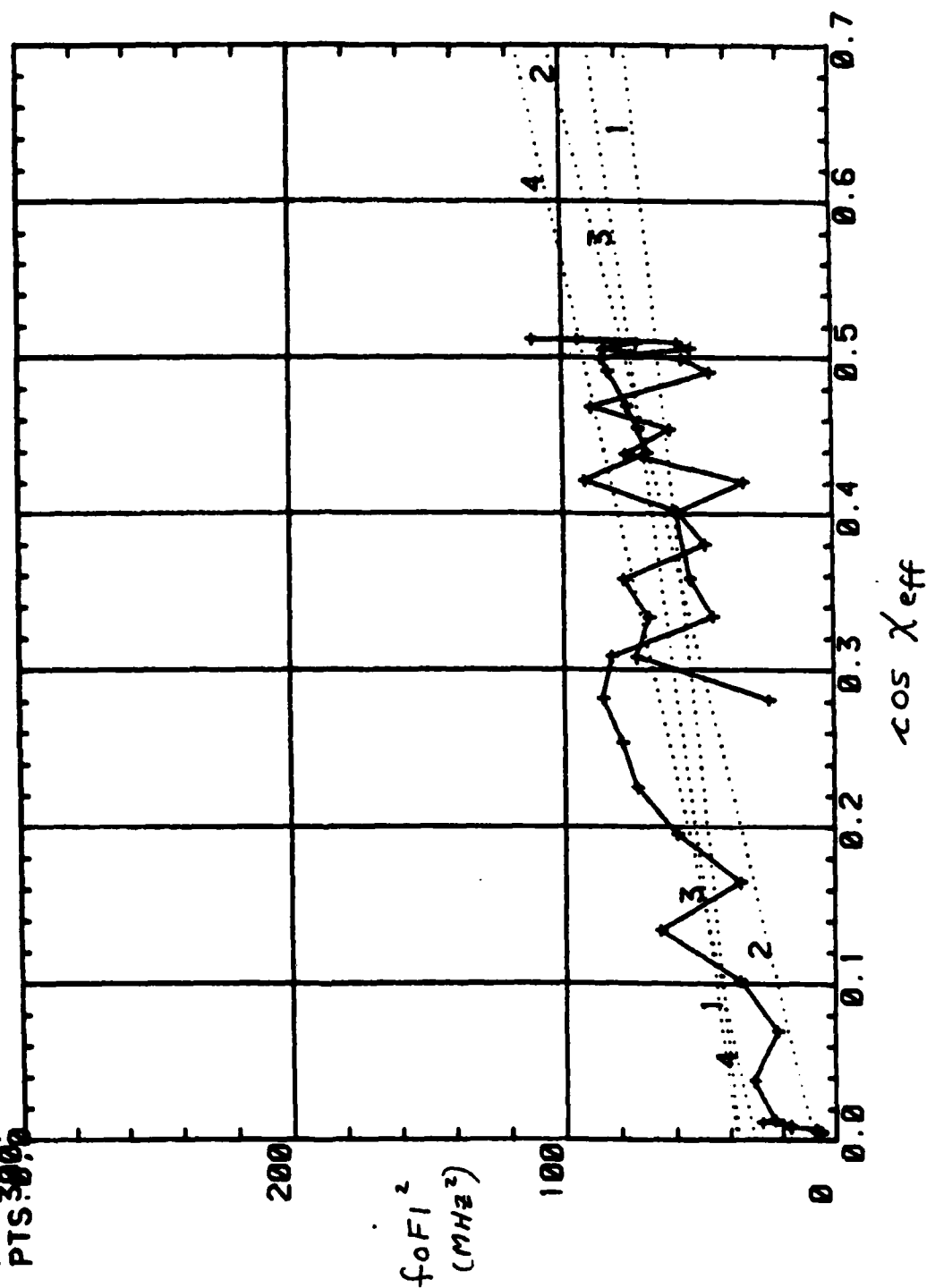
LI: PTS.1,9

**L2: PTS. 1, 16**

**L3: PTS. 1, 36**

**L4: PTS 26, 36**

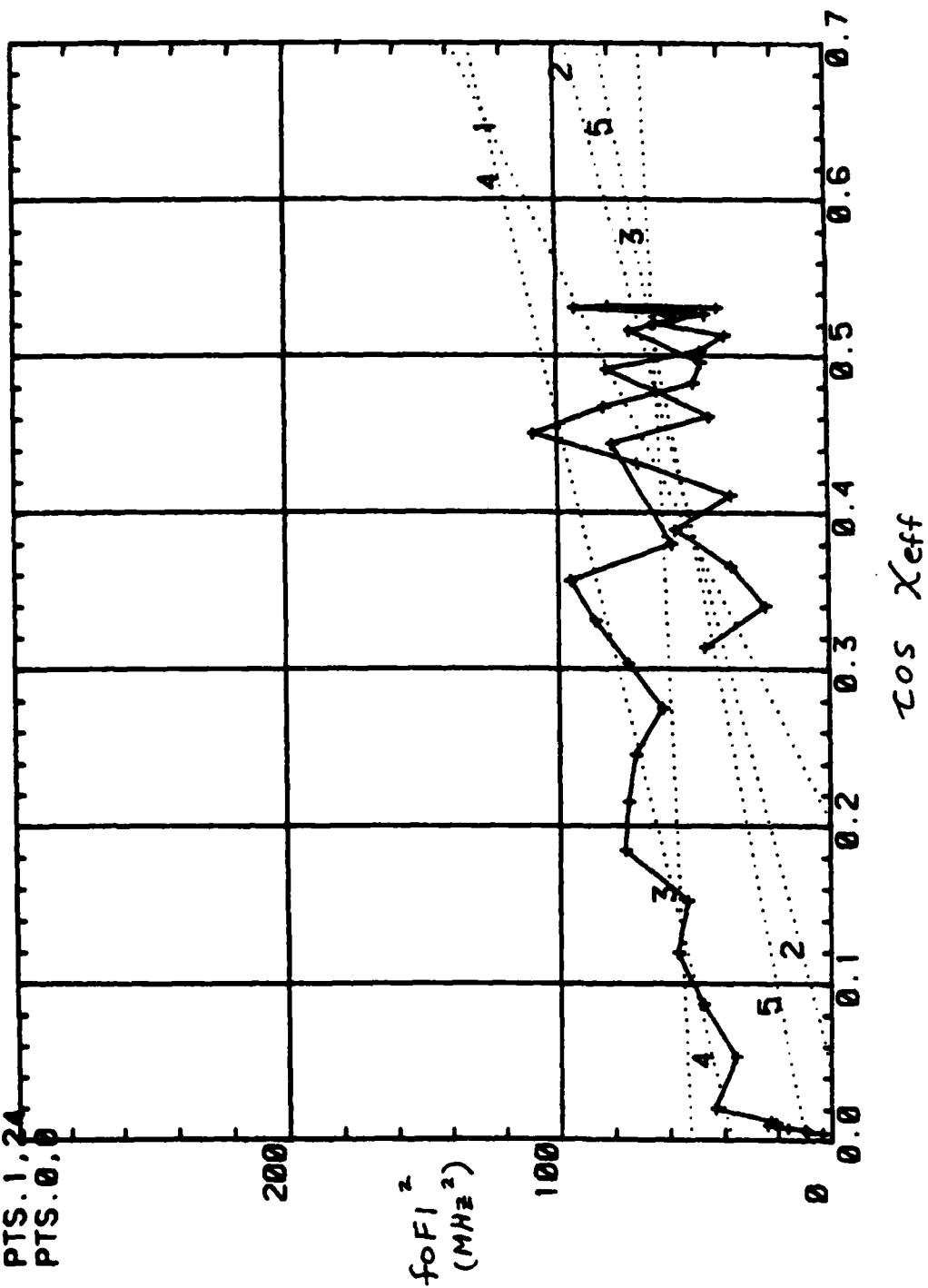
L5: PLS 3909



X3: D340, 1600 - D341, 0400 (UT)

TREND LINES:

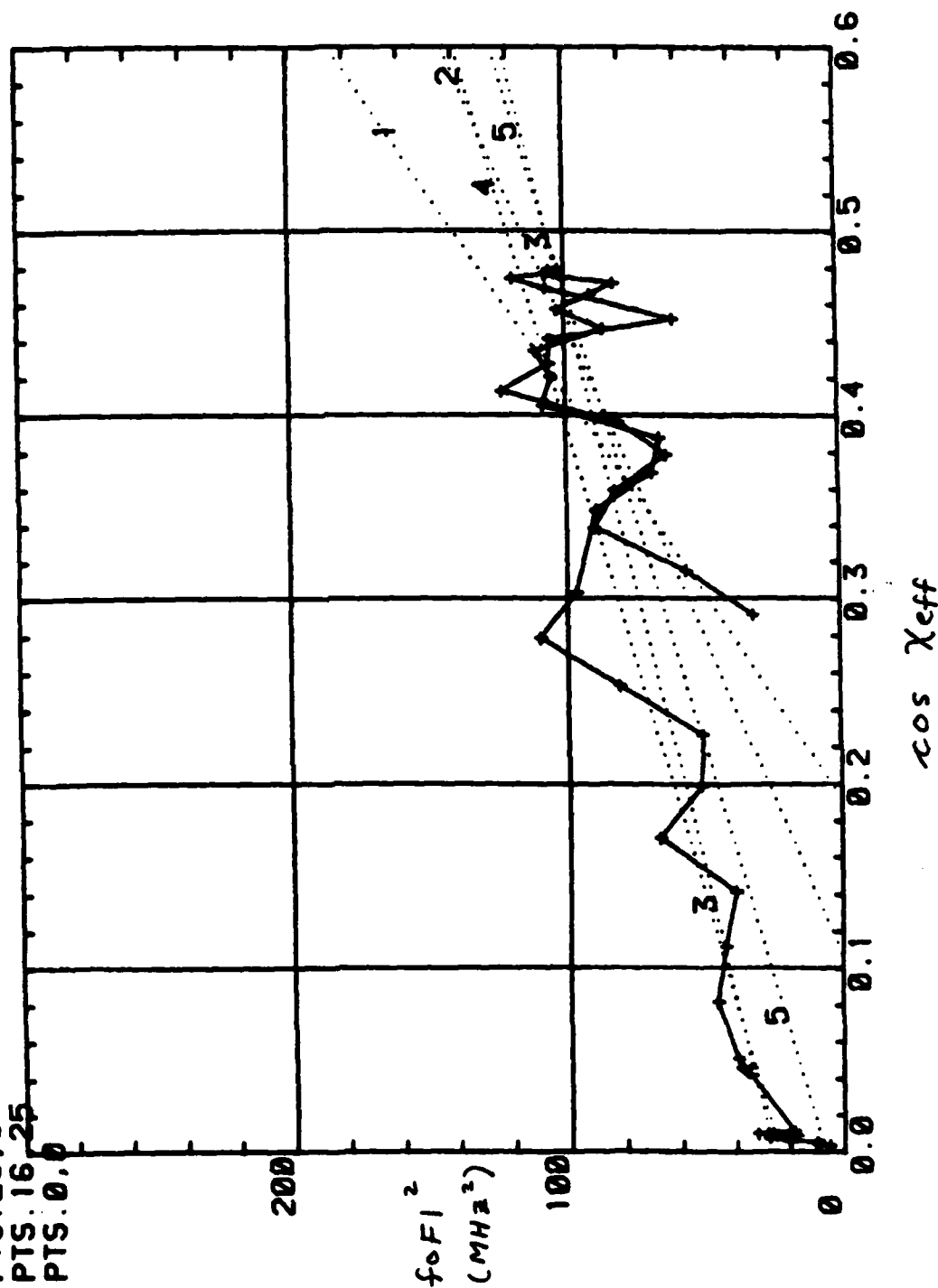
- L1: PTS. 1.9
- L2: PTS. 1.16
- L3: PTS. 1.37
- L4: PTS. 27.37
- L5: PTS. 1.24
- L6: PTS. 0.0



X4: D340, 1600 - D 341, 0400 (UT)

TREND LINES:

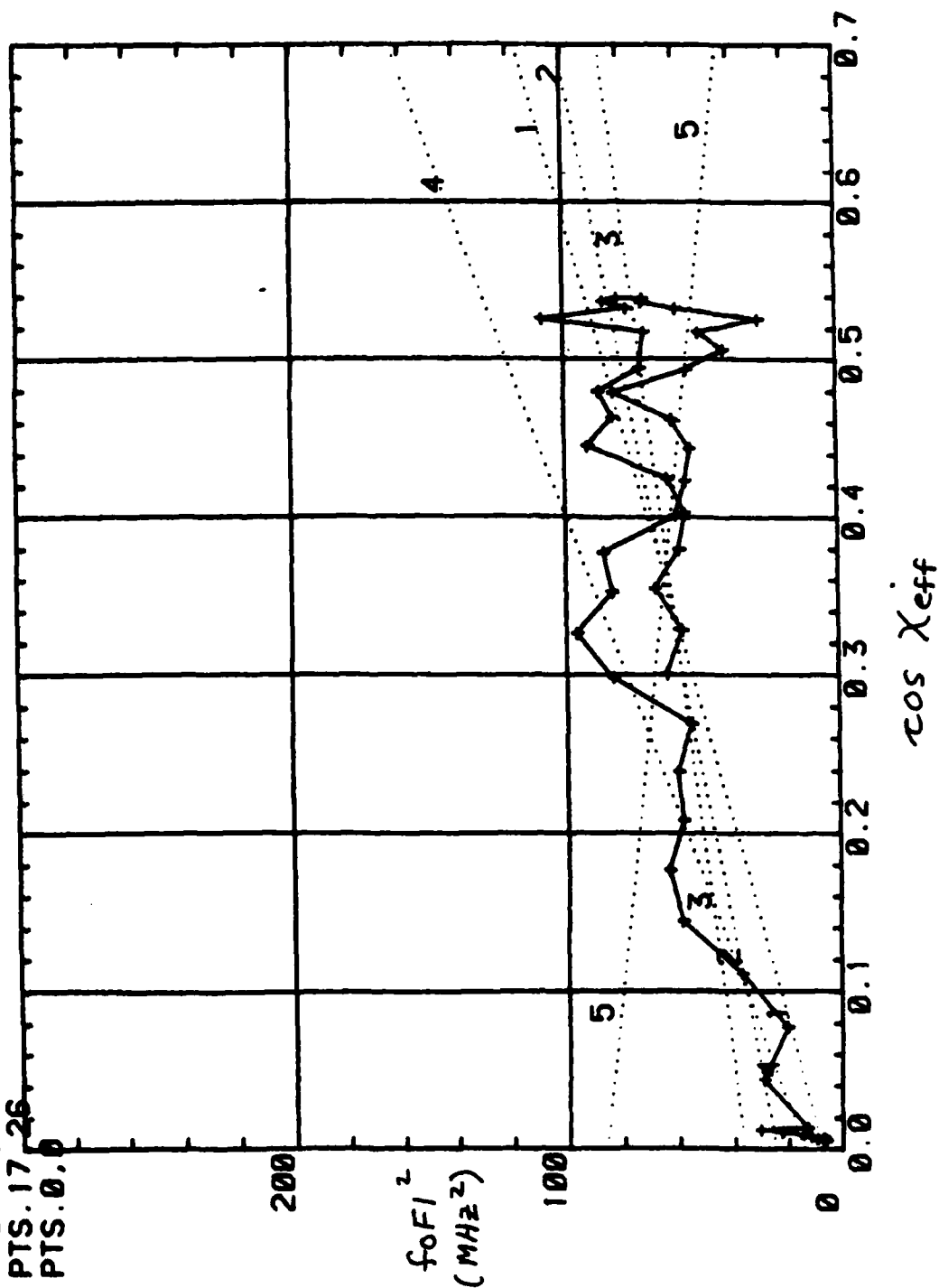
- L1: PTS. 1.9
- L2: PTS. 1.16
- L3: PTS. 1.37
- L4: PTS. 25.37
- L5: PTS. 16.25
- L6: PTS. 0.0



X5: D340, 1600 - D341, 0400 (UT)

TREND LINES:

L1: PTS.1.9  
 L2: PTS.1.16  
 L3: PTS.1.40  
 L4: PTS.29.40  
 L5: PTS.17.26  
 L6: PTS.0.0



X6: D340, 1600 - D341, 0400 (UT)

**TREND LINES:**

**Li: PTS.1,9**

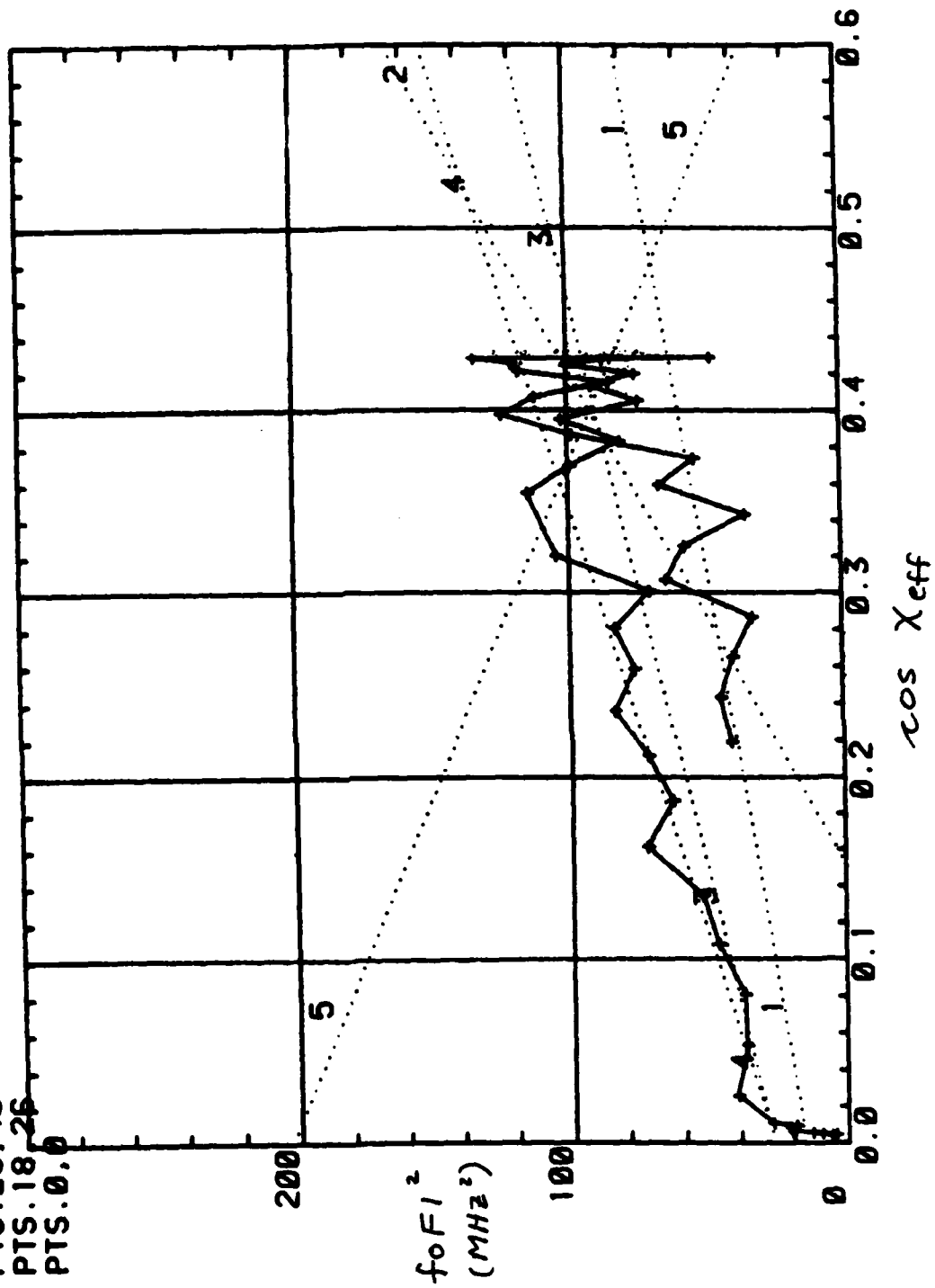
**L2: PTS. 1.17**

**L3: PTS. 1, 40**

**L4: PTS. 25, 40**

LS: PTS. 18, 25

LG: PTS. 0.0



APPENDIX E

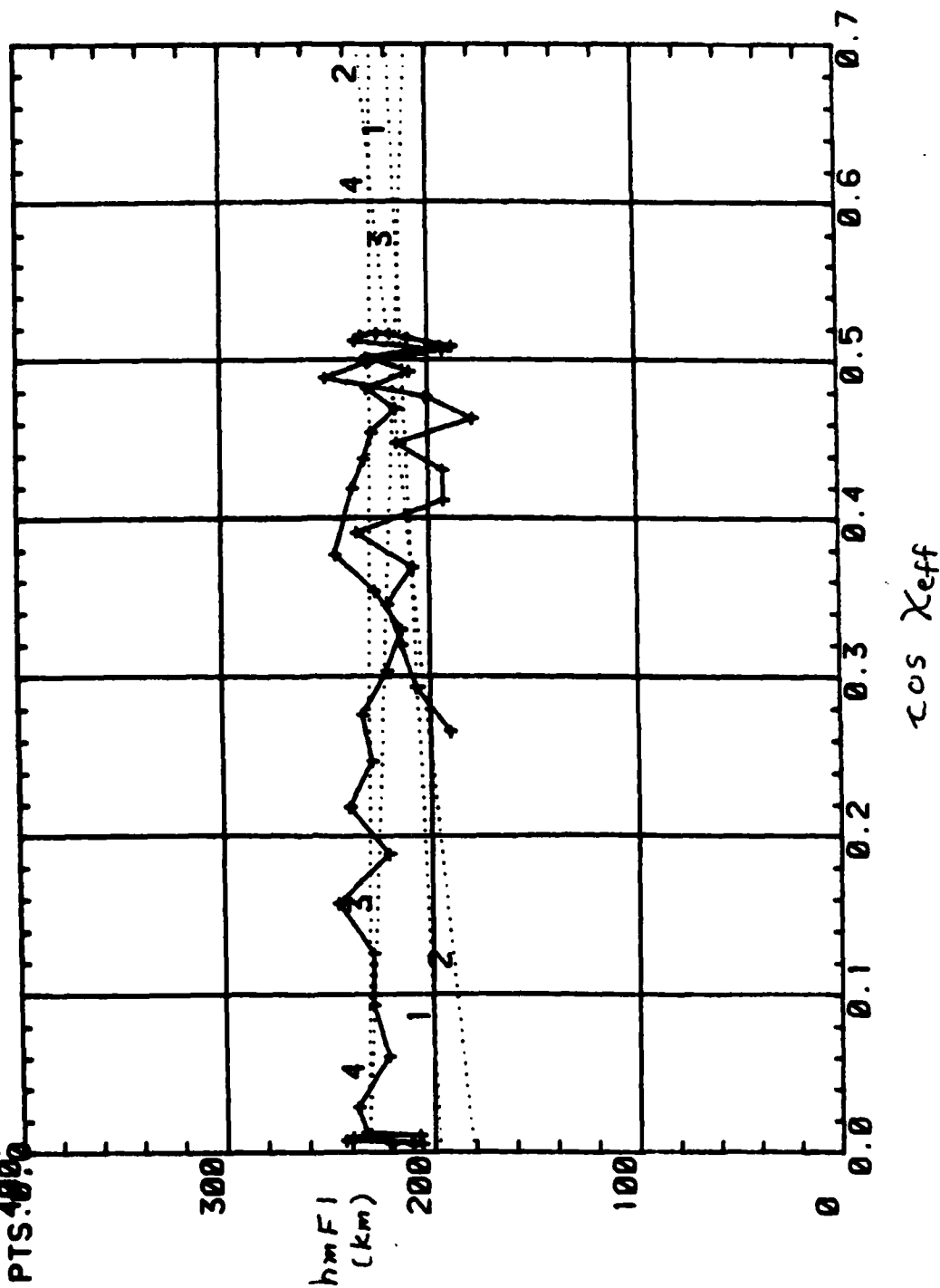
Plots of  $hmF1$  vs.  $\cos X_{eff}$



X1: D340,1600 - D341, 0400 (UT)

TREND LINES:

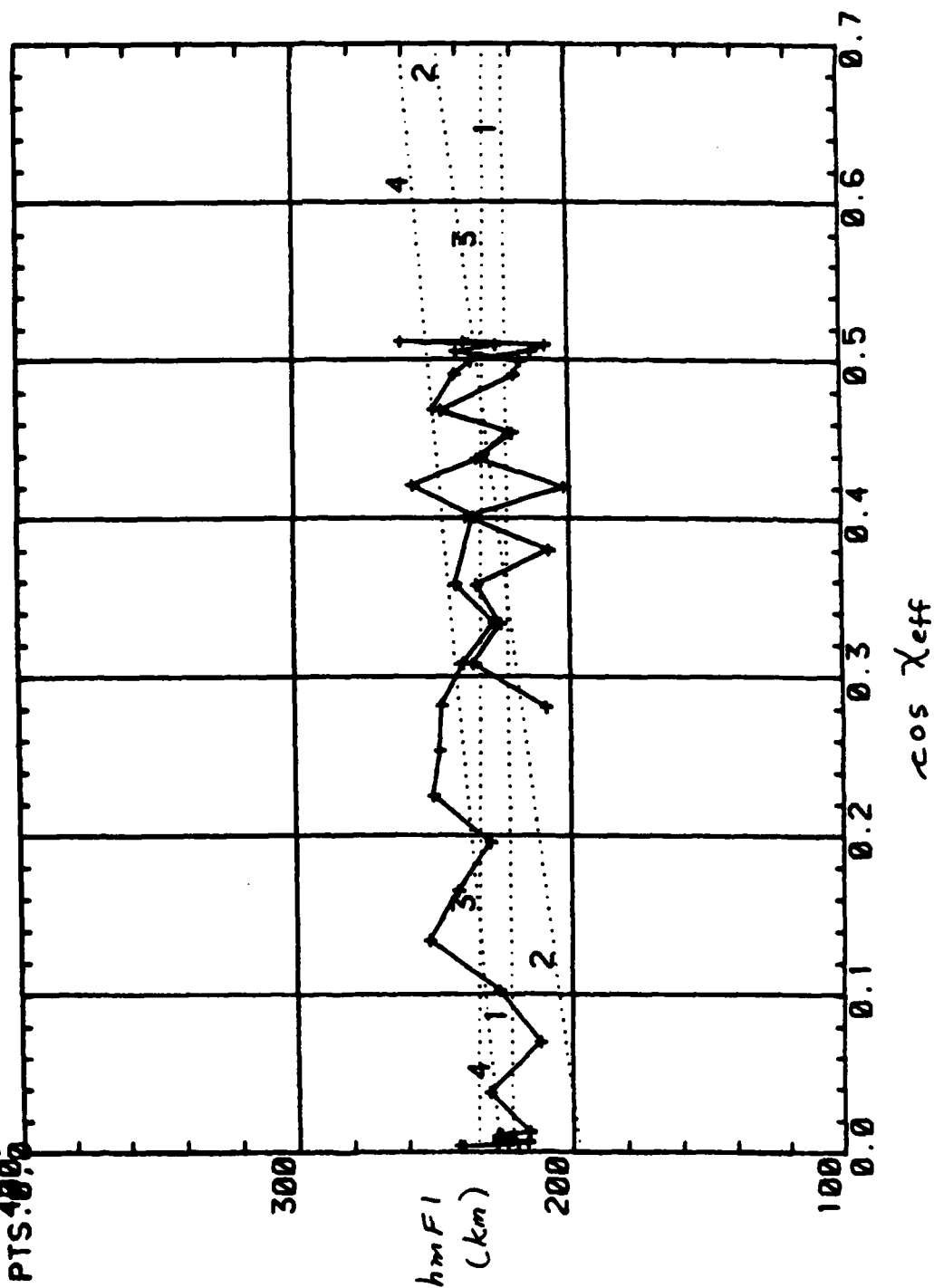
L1: PTS.1.9  
 L2: PTS.1.17  
 L3: PTS.1.41  
 L4: PTS.28.41  
 L5: PTS.40.0



X2: D340, 1600 - D341, 0400 (UT)

TREND LINES:

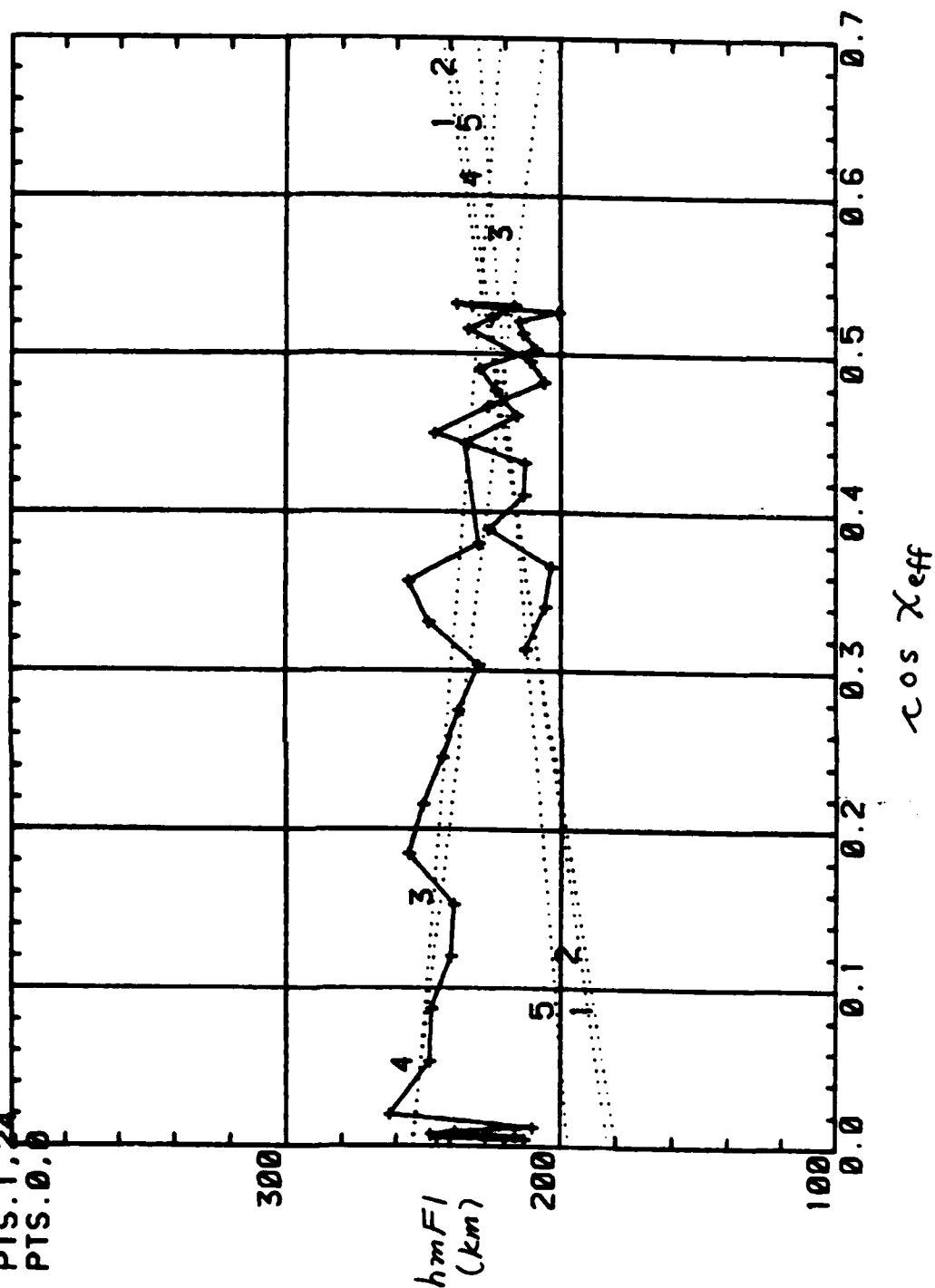
- L1: PTS.1.9
- L2: PTS.1.16
- L3: PTS.1.36
- L4: PTS.26.36
- L5: PTS.40.0



X3: 0340, 1600 - D3 41, 0400 (UT)

TREND LINES:

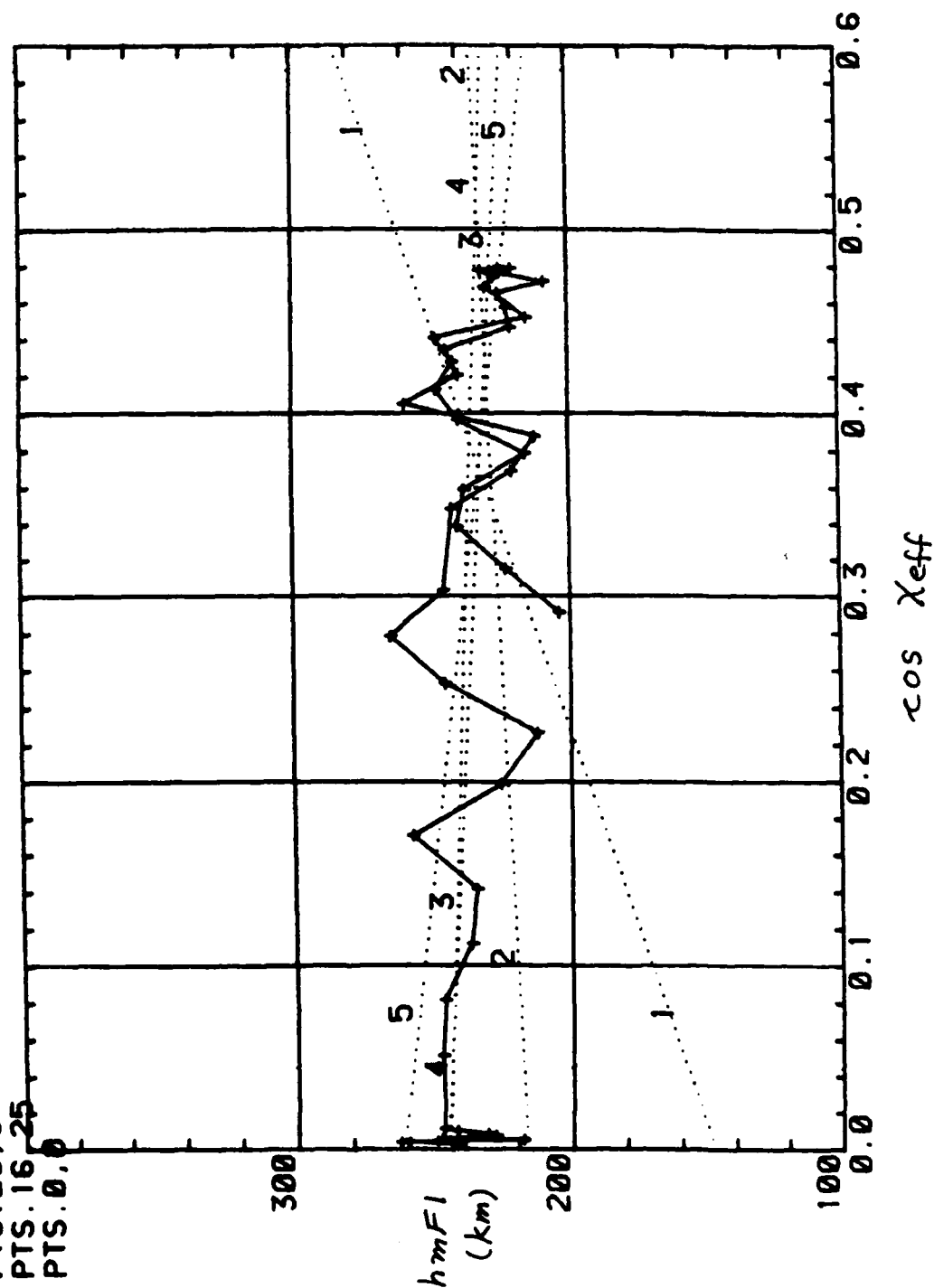
- L1: PTS. 1.9
- L2: PTS. 1.16
- L3: PTS. 1.37
- L4: PTS. 27.37
- L5: PTS. 1.24
- L6: PTS. 0.0



X4: D340,1600 - D341,0400 (UT)

TREND LINES:

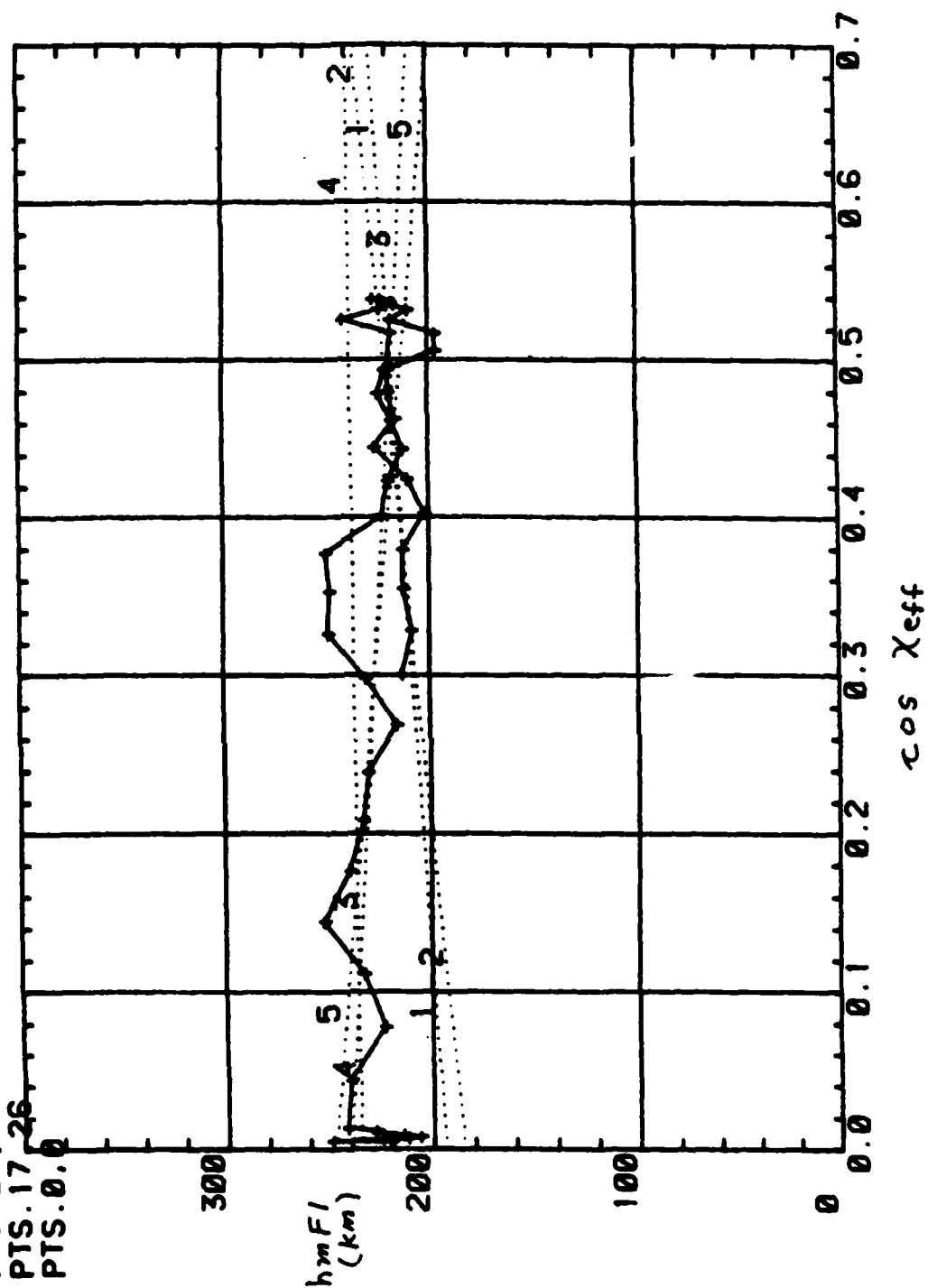
L1: PTS.1,9  
 L2: PTS.1,16  
 L3: PTS.1,37  
 L4: PTS.25,37  
 L5: PTS.16,25  
 L6: PTS.0,0



X5: D340,1600 - D341,0400 (UT)

TREND LINES:

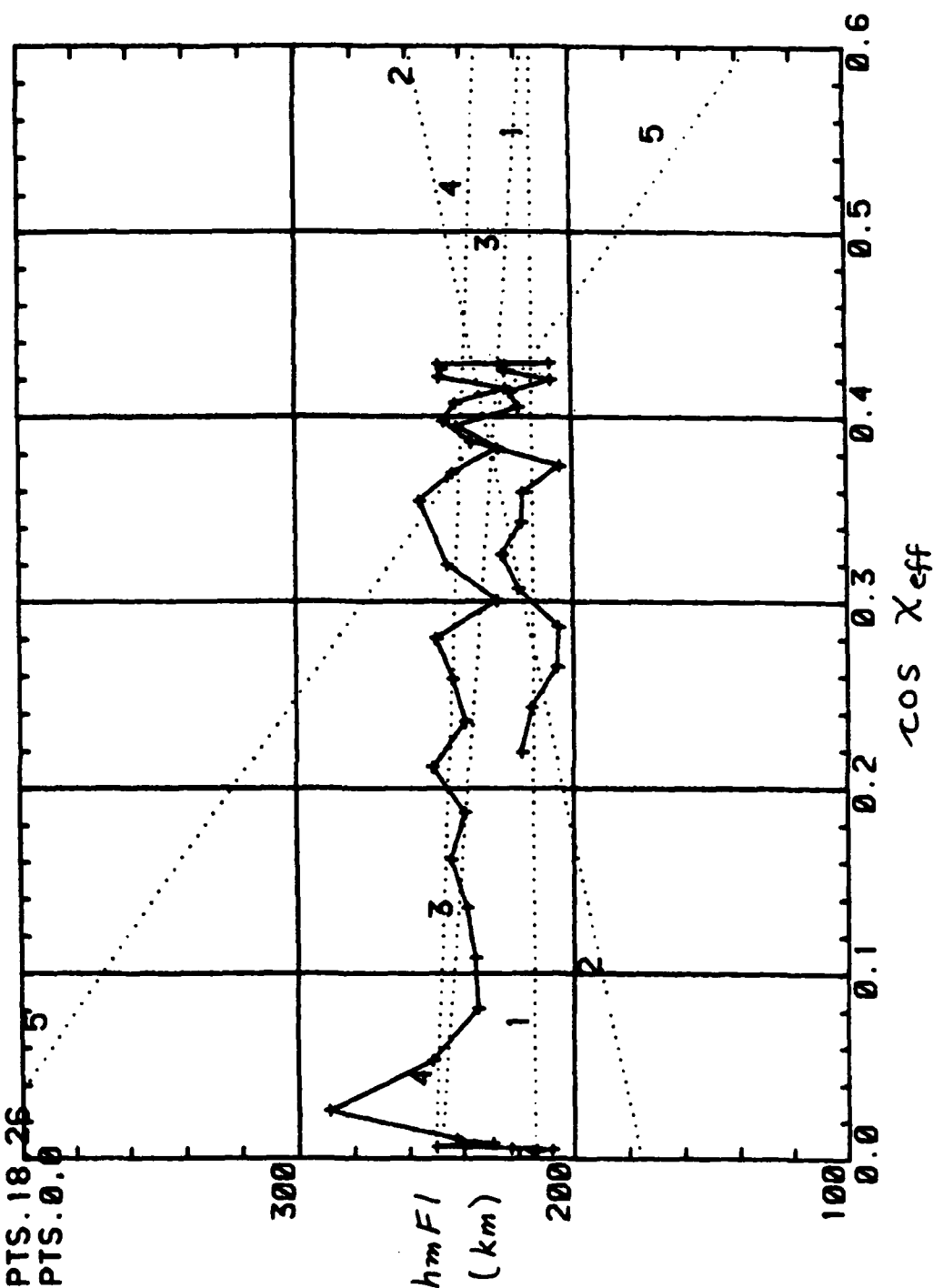
L1: PTS.1.9  
L2: PTS.1.16  
L3: PTS.1.40  
L4: PTS.29.40  
L5: PTS.17.26  
L6: PTS.0.0



X6: D340,1600 - D341,0400 (UT)

TREND LINES:

- L1: PTS.1,9
- L2: PTS.1,17
- L3: PTS.1,40
- L4: PTS.25,40
- L5: PTS.18,26
- L6: PTS.0,0



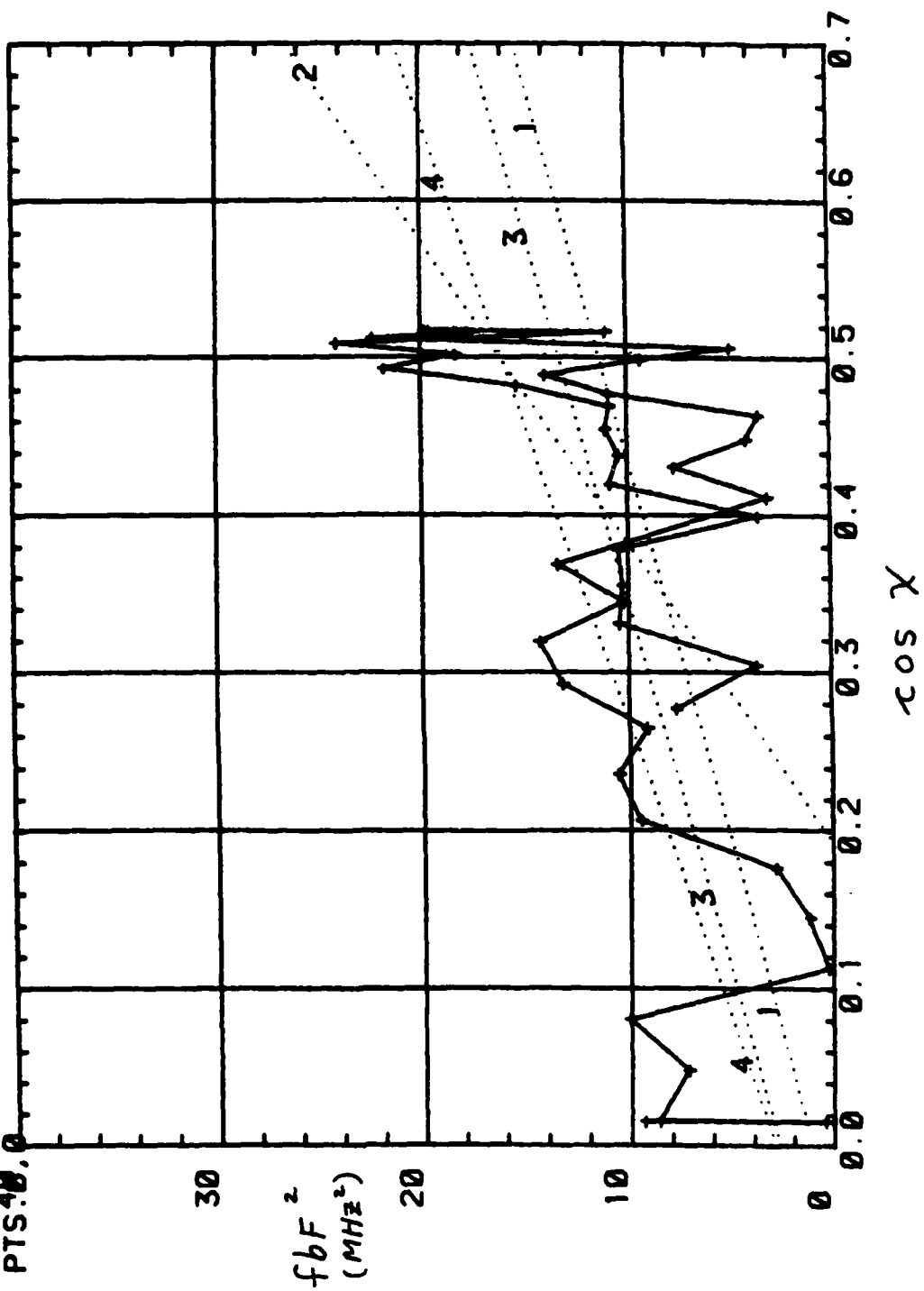
APPENDIX F

Plots of  $fbF^2$  vs.  $\cos \chi$

X1: D340, 1600 - D341, 0400 (UT)

TREND LINES:

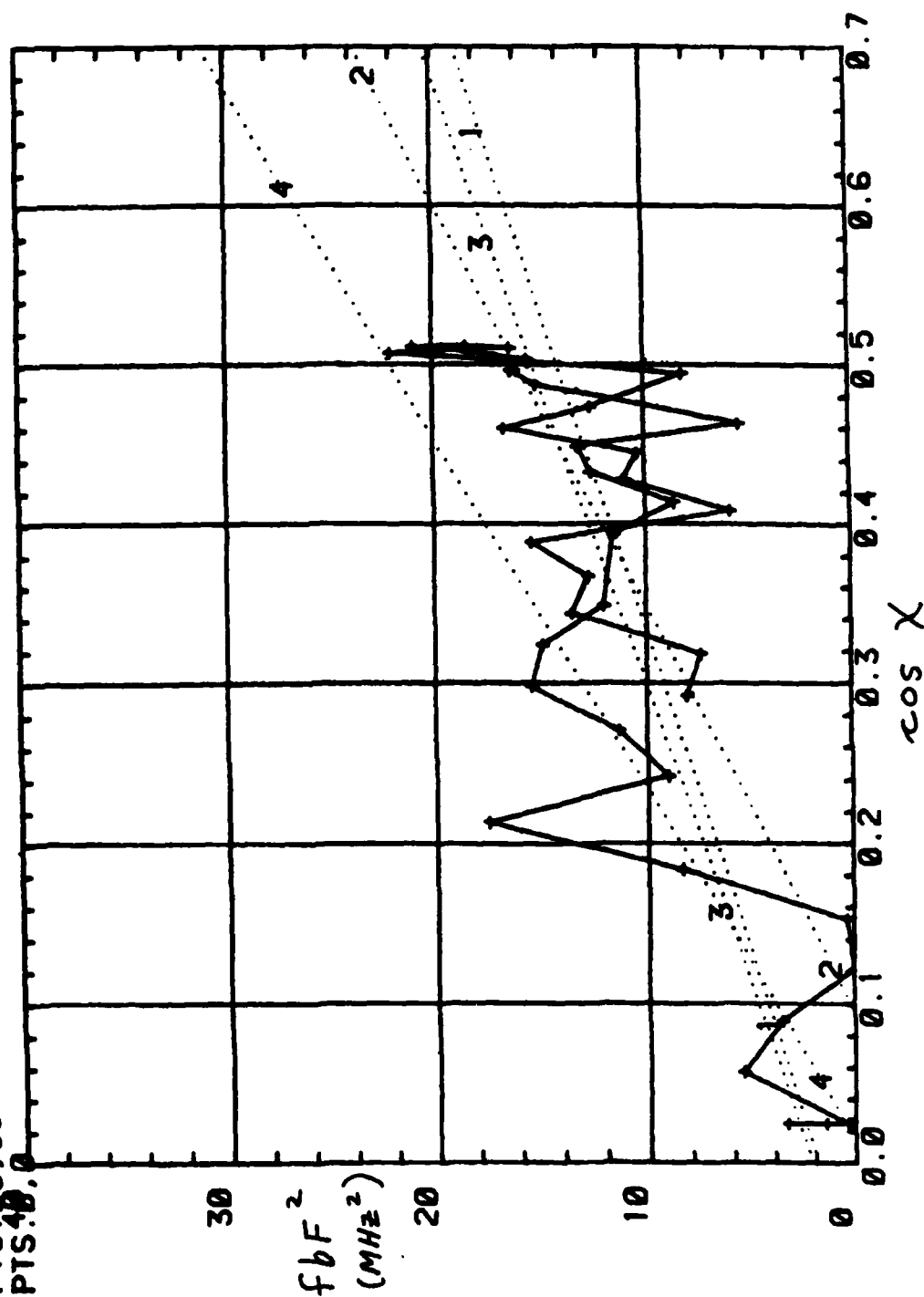
- L1: PTS. 1.9
- L2: PTS. 1.17
- L3: PTS. 1.41
- L4: PTS. 28.41
- L5: PTS. 40.0





X2: D340, 1600 - D341, 0400 (UT)

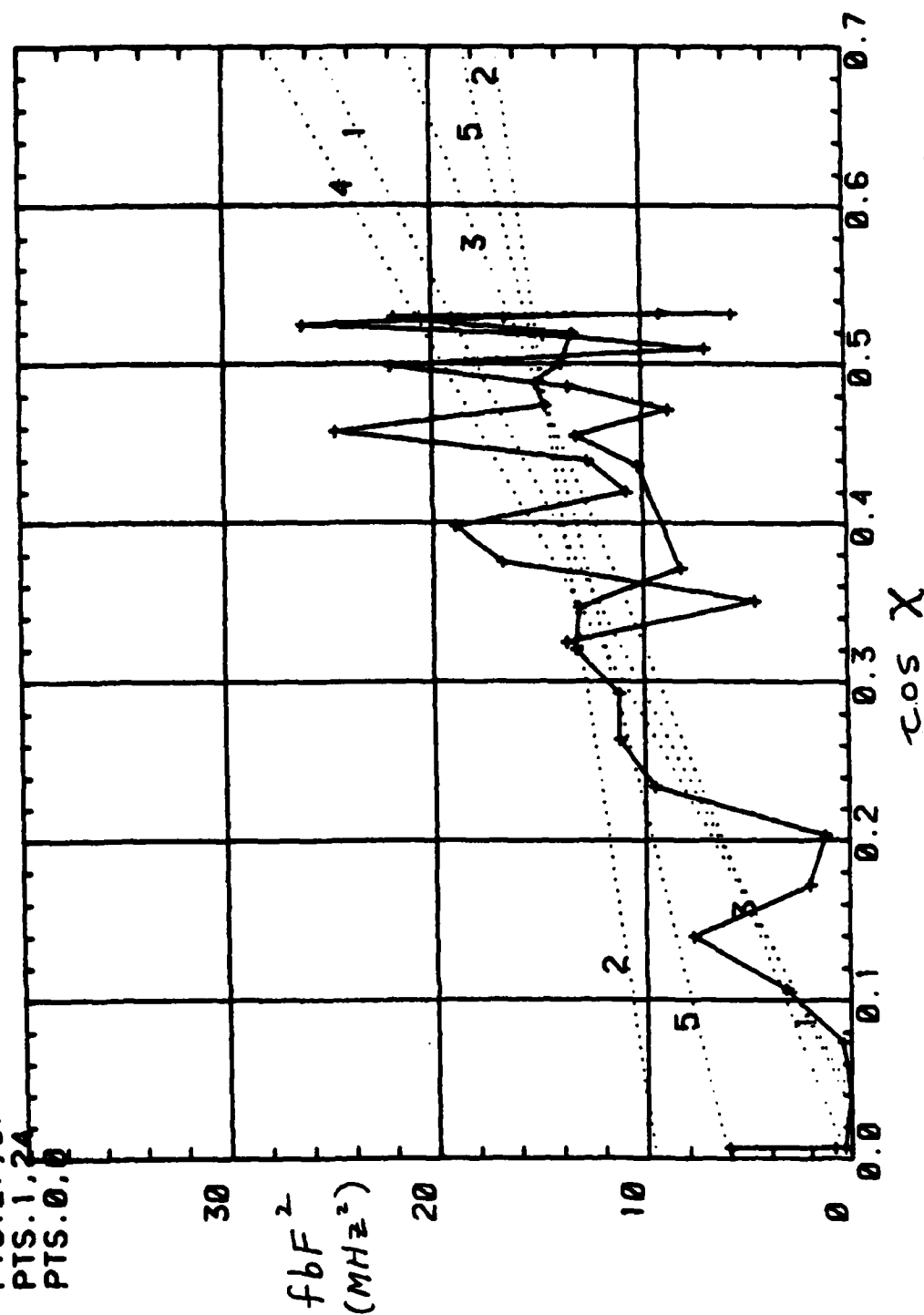
TREND LINES:  
 L1: PTS. 1, 9  
 L2: PTS. 1, 16  
 L3: PTS. 1, 36  
 L4: PTS. 26, 36  
 L5: PTS. 0, 0



X3: D340,1600 - D341,0400 (UT)

TREND LINES:

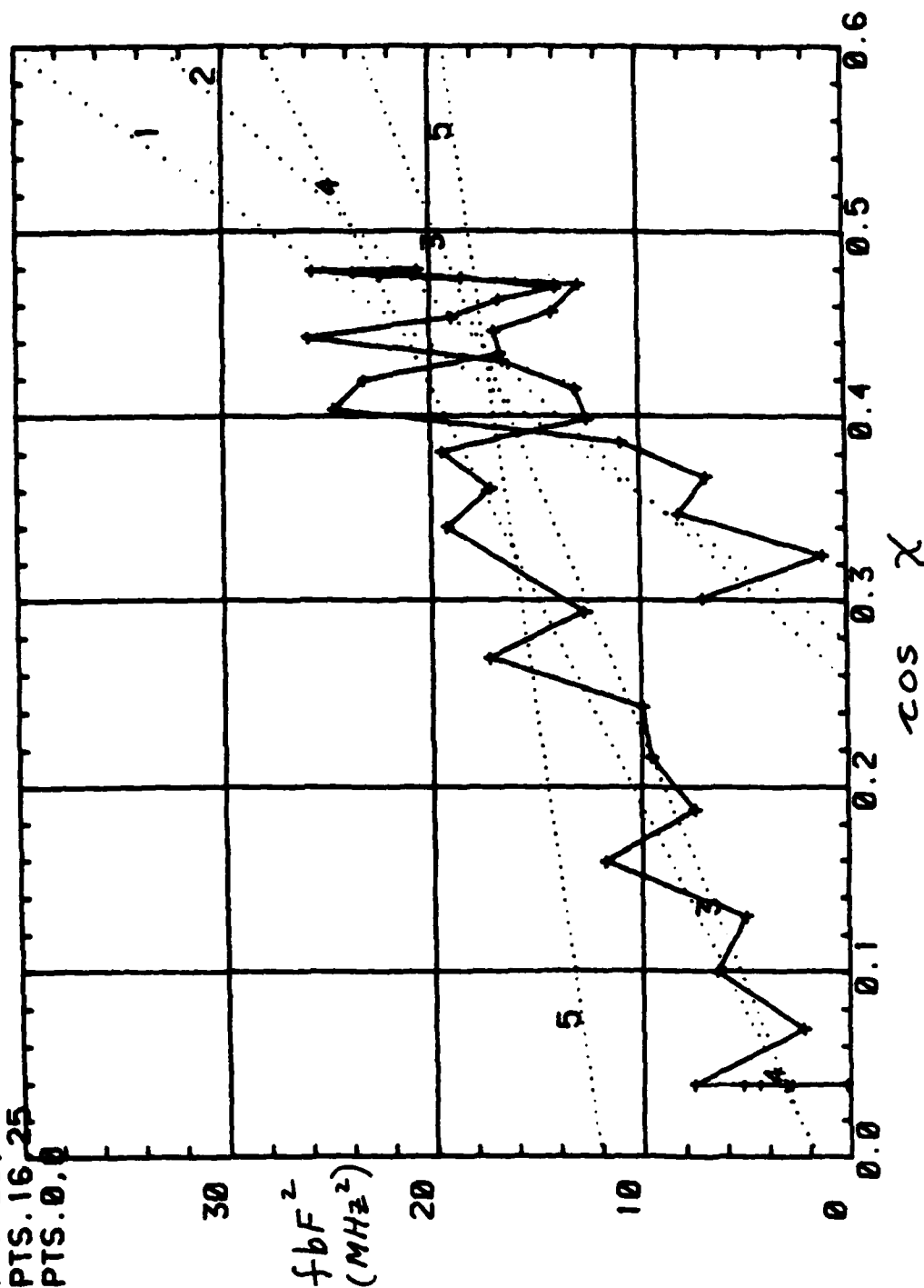
L1: PTS.1,9  
L2: PTS.1,16  
L3: PTS.1,37  
L4: PTS.27,37  
L5: PTS.1,24  
L6: PTS.0,0



X4: D340,1600 - D341,0400 (UT)

TREND LINES:

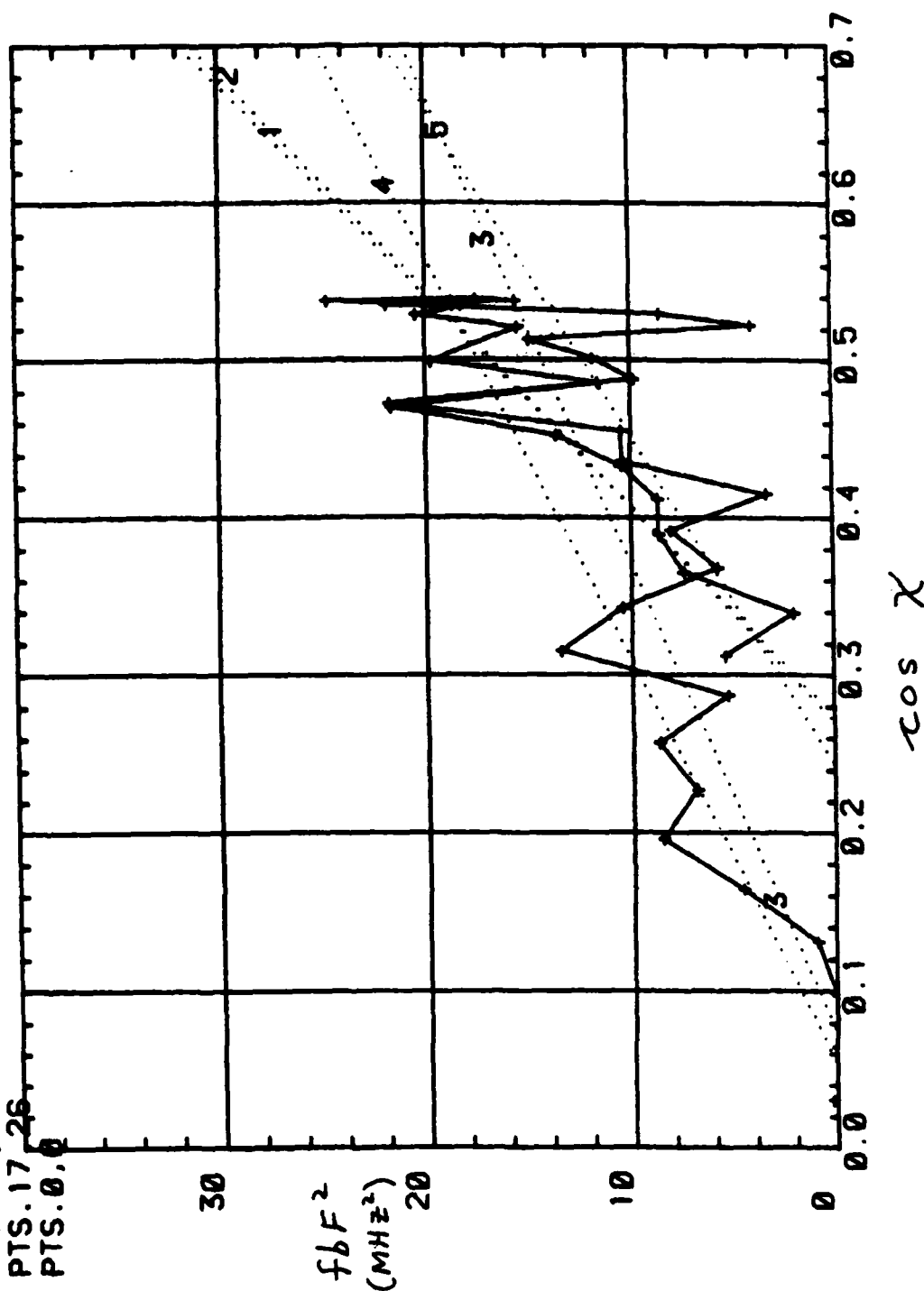
- L1: PTS.1.9
- L2: PTS.1.16
- L3: PTS.1.37
- L4: PTS.25.37
- L5: PTS.16.25
- L6: PTS.0.0



X5: Day 340, 1600 - Day 341, 0400 (UT)

TREND LINES:

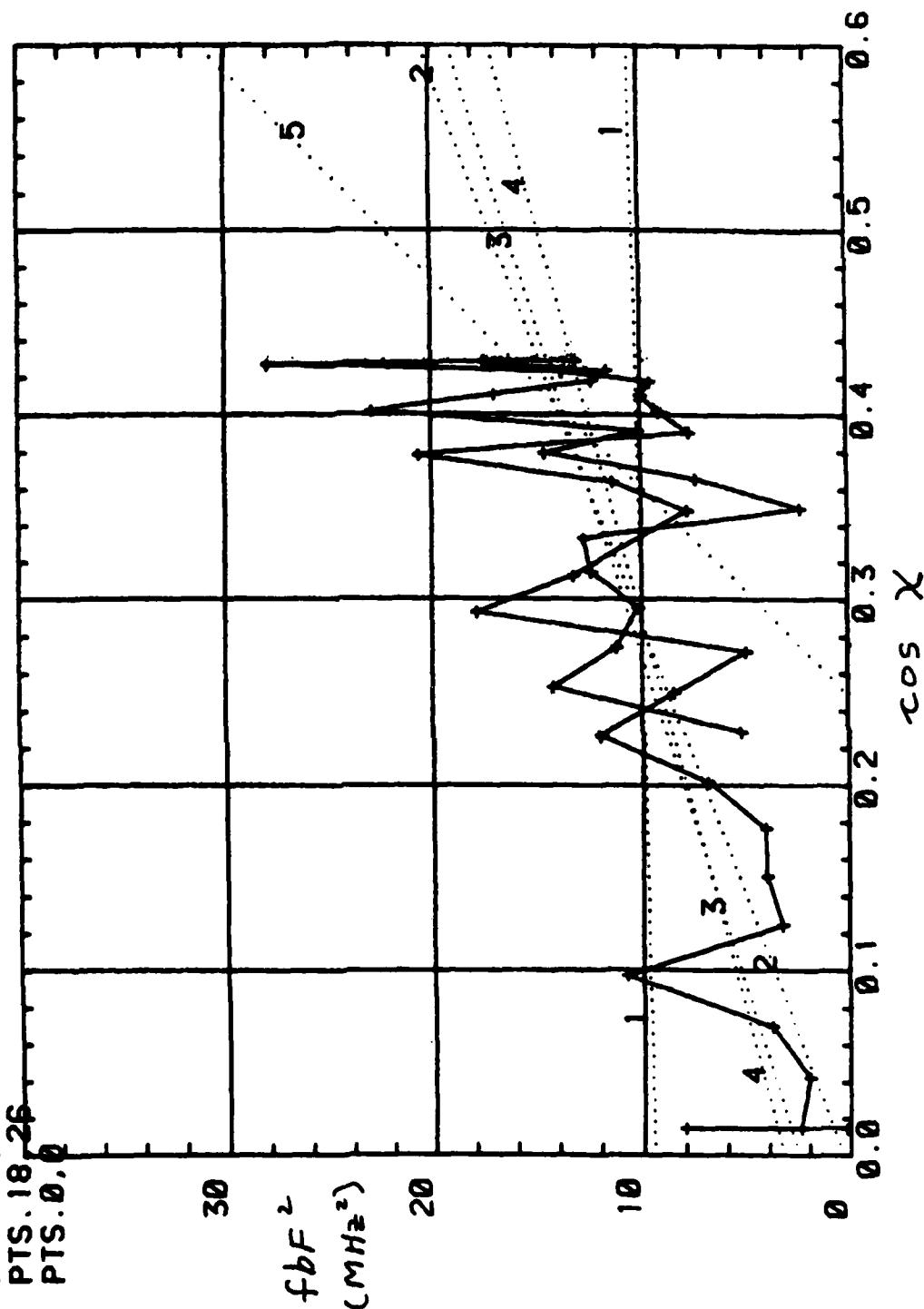
- L1: PTS. 1, 9
- L2: PTS. 1, 16
- L3: PTS. 1, 40
- L4: PTS. 29, 40
- L5: PTS. 17, 26
- L6: PTS. 0, 0



X6: D340, 1600 - D341, 0400 (UT)

TREND LINES:

- L1: PTS.1.9
- L2: PTS.1.17
- L3: PTS.1.40
- L4: PTS.25.40
- L5: PTS.18.26
- L6: PTS.0.0

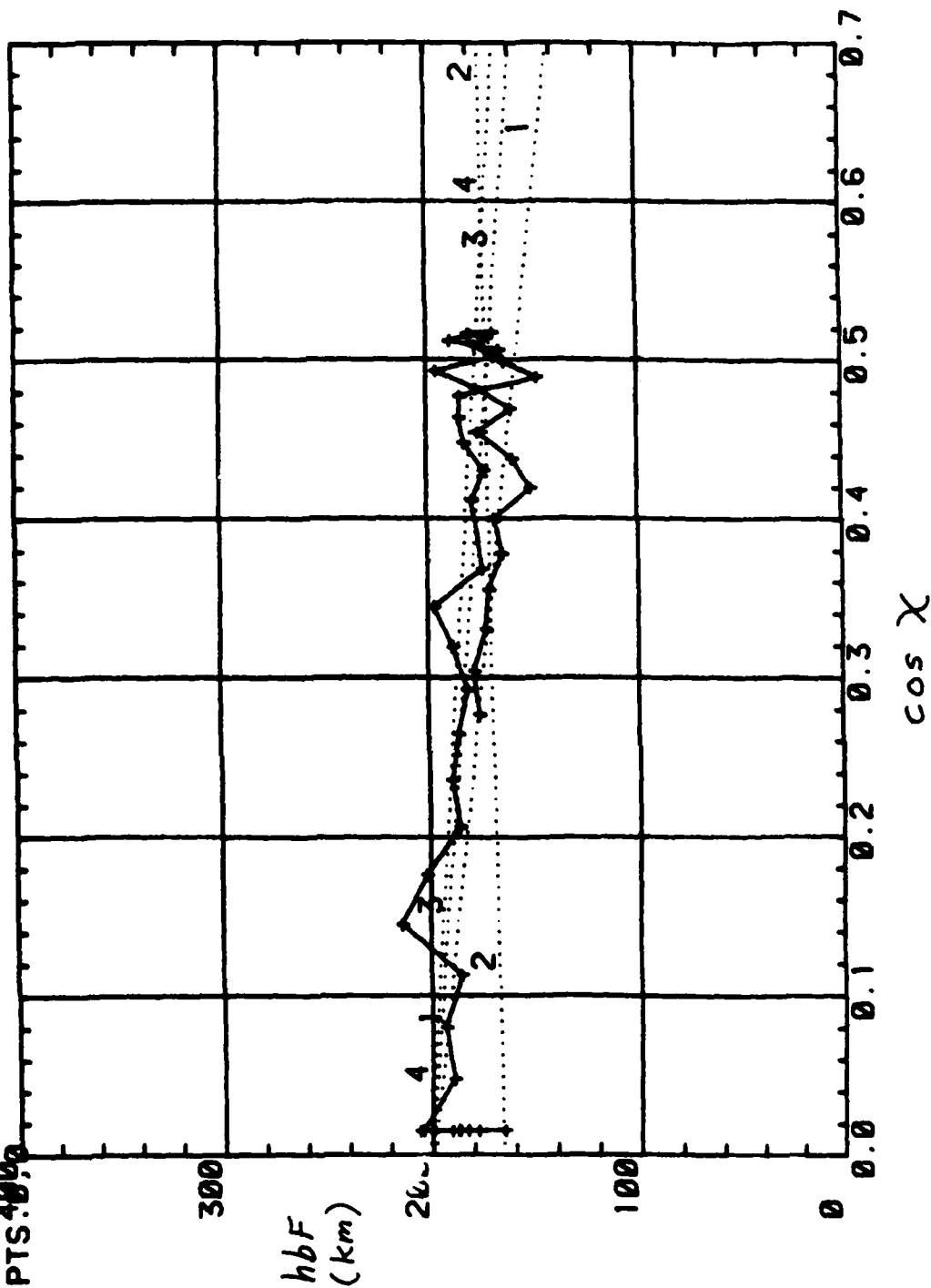


APPENDIX G

Plots of  $hbF$  vs.  $\cos \chi$

X1: D340, 1600 - D341, 0400 (UT)

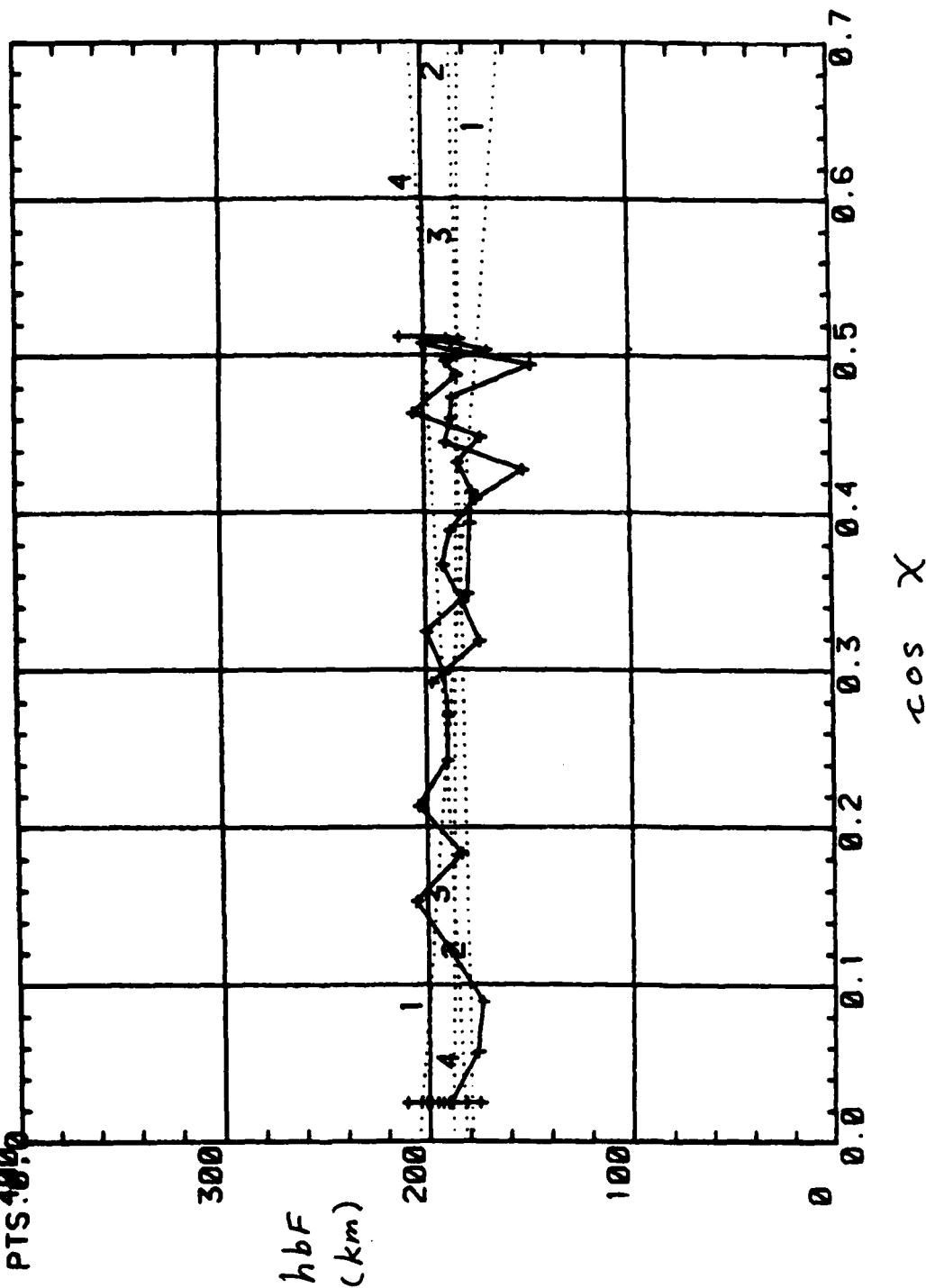
TREND LINES:  
 L1: PTS. 1, 9  
 L2: PTS. 1, 17  
 L3: PTS. 1, 41  
 L4: PTS. 28, 41  
 L5: PTS. 40, 41



X2: D 340,1600 - D 341,0400 (UT)

TREND LINES:

- L1: PTS. 1.9
- L2: PTS. 1.16
- L3: PTS. 1.36
- L4: PTS. 26.36
- L5: PTS. 40.0

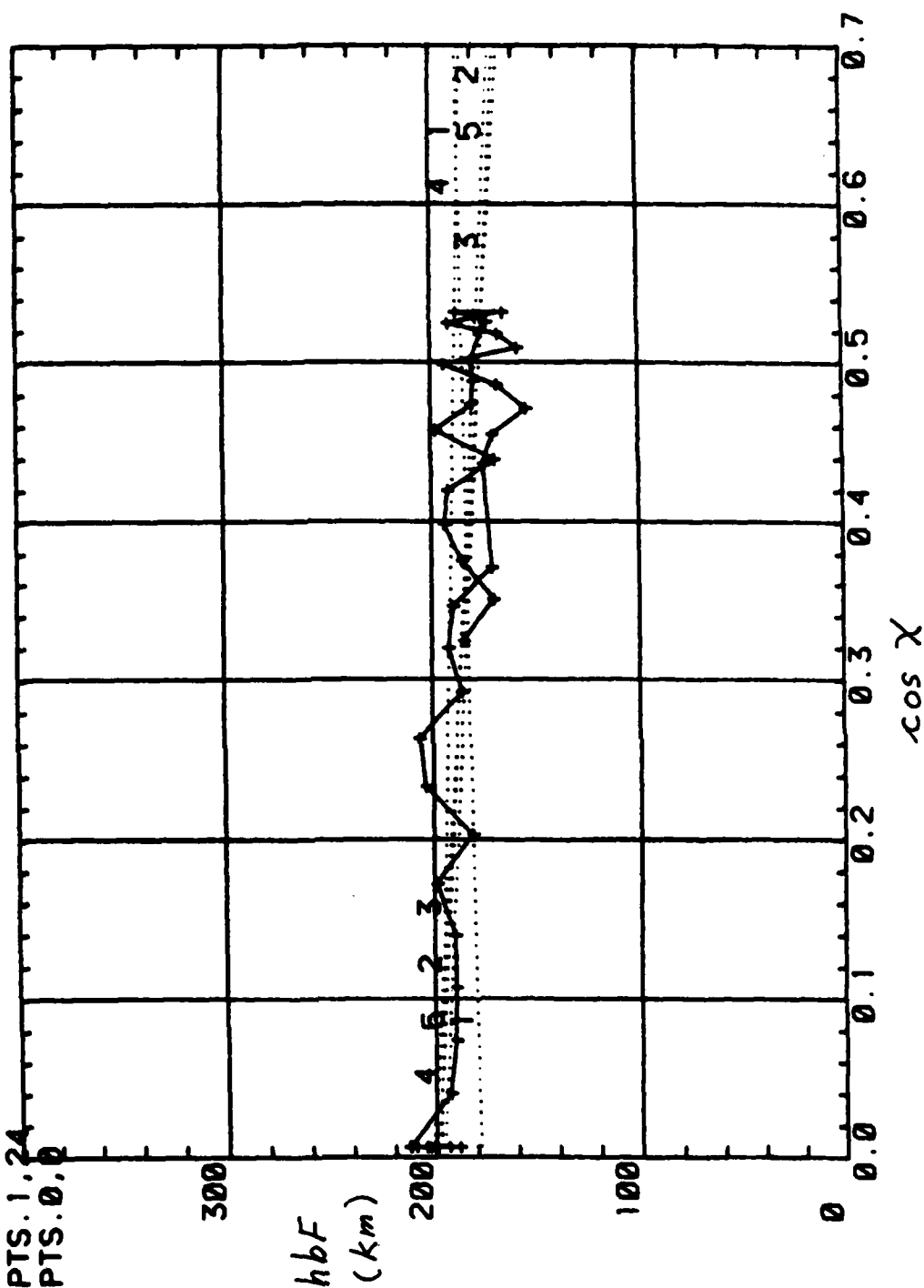




X3: 0340,1600 - D341, 0400 (UT)

TREND LINES:

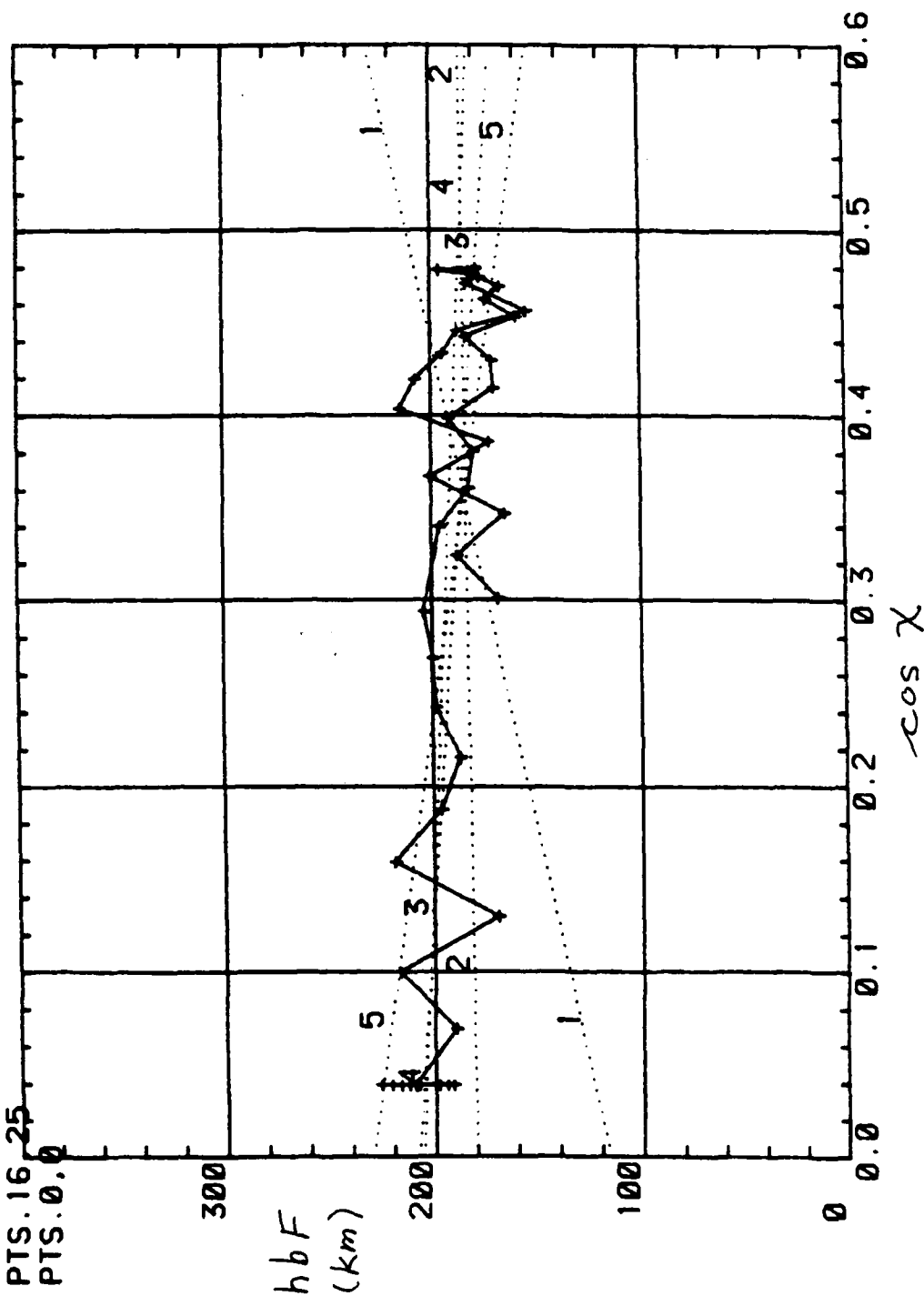
- L1: PTS.1,9
- L2: PTS.1,16
- L3: PTS.1,37
- L4: PTS.27,37
- L5: PTS.1,24
- L6: PTS.0,0



X4: D340, 1600 - D341, 0400 (UT)

TREND LINES:

- L1: PTS. 1, 9
- L2: PTS. 1, 16
- L3: PTS. 1, 37
- L4: PTS. 25, 37
- L5: PTS. 16, 25
- L6: PTS. 0, 0



X5: D340, 1600 - D341, 0400 (UT)

## TREND LINES:

**L1: PTS. 1, 9**

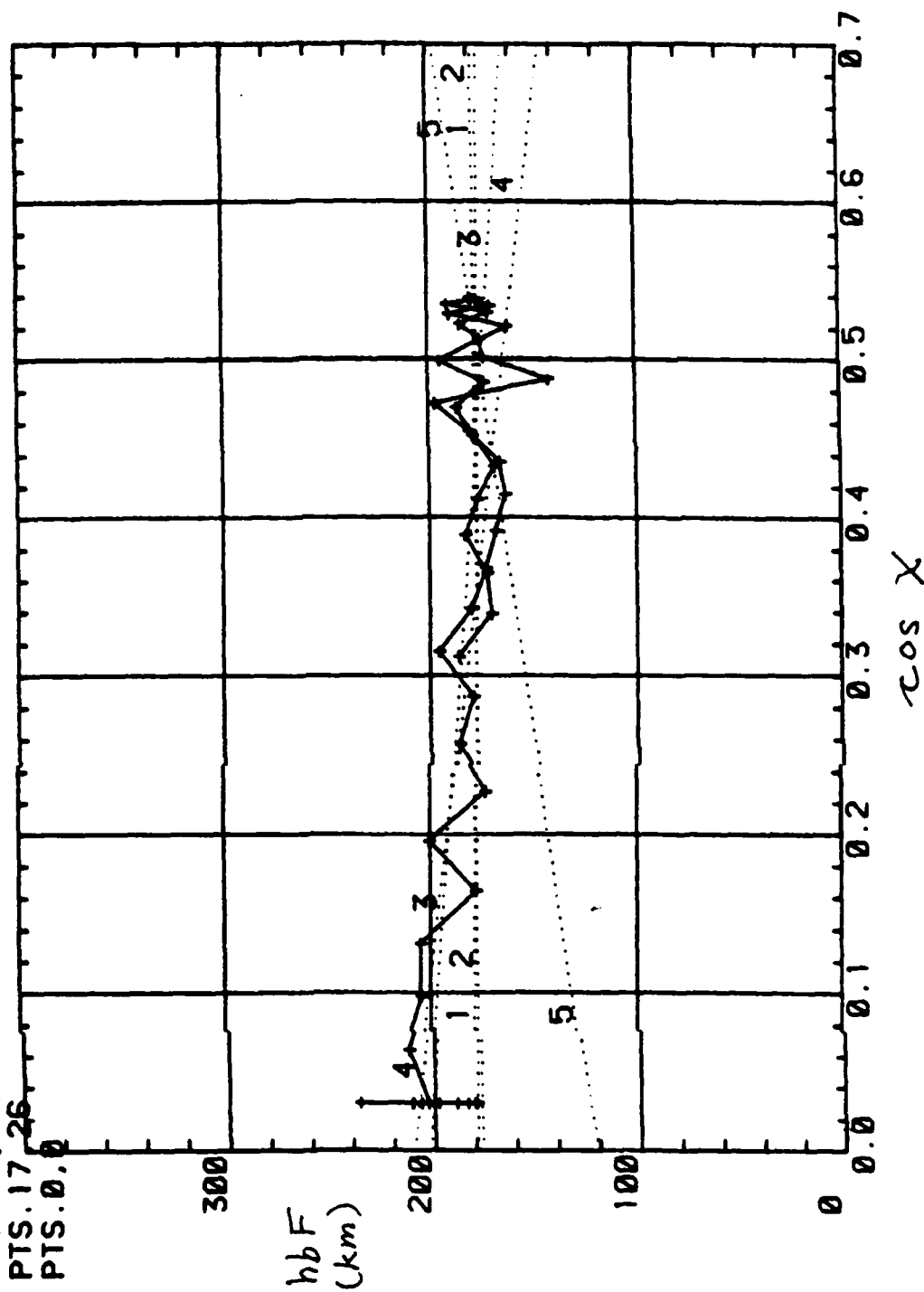
**L2: PTS. 1, 16**

**L3: PTS. 1, 40**

**L4: PTS. 29, 40**

L5: PTS. 17, 26

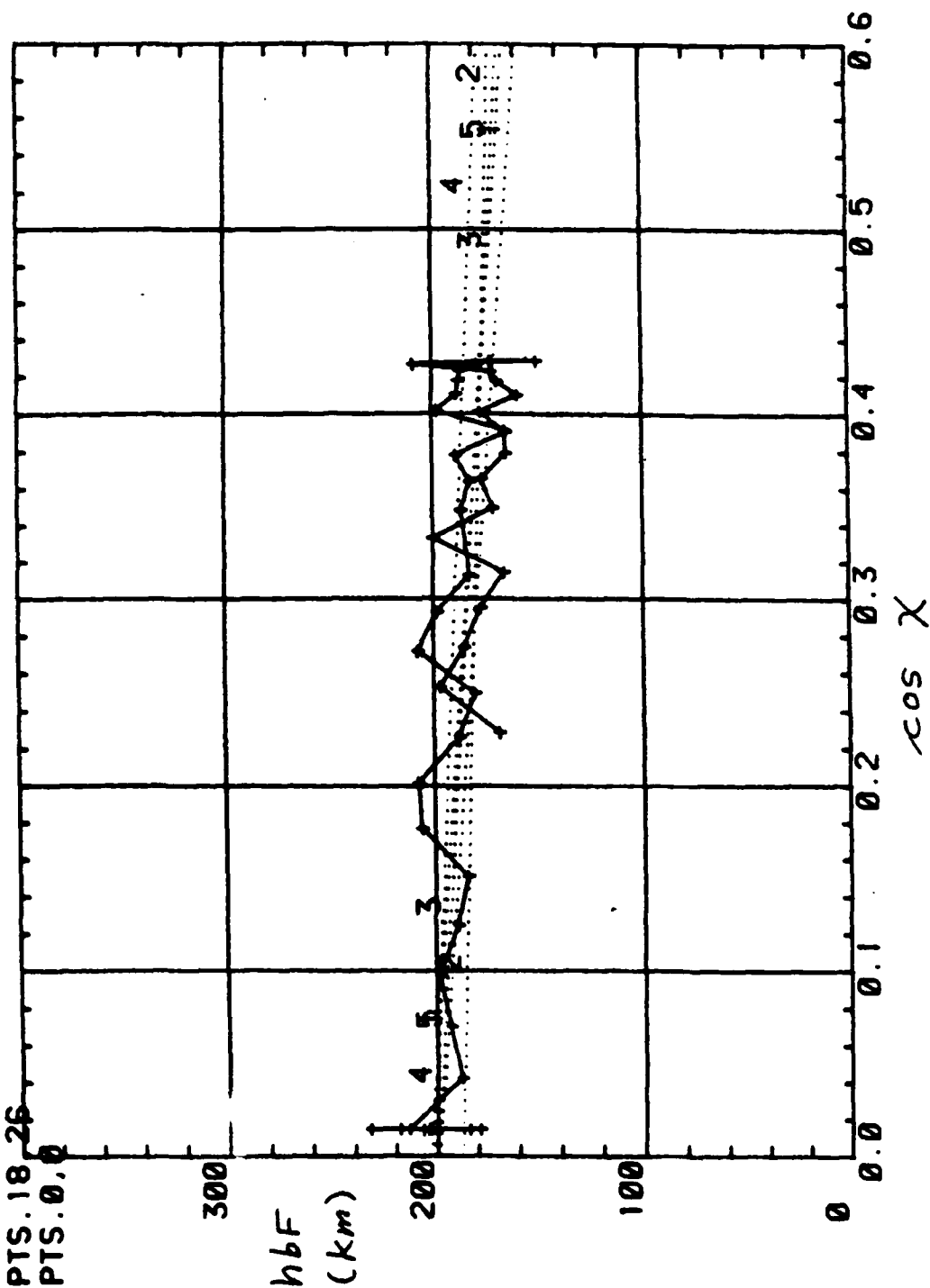
16: PIS. 0. 0.



XG: D340, 1600 - D341, 0400 (UT)

TREND LINES:

- L1: PTS. 1, 9
- L2: PTS. 1, 17
- L3: PTS. 1, 40
- L4: PTS. 25, 40
- L5: PTS. 18, 26
- L6: PTS. 0, 0



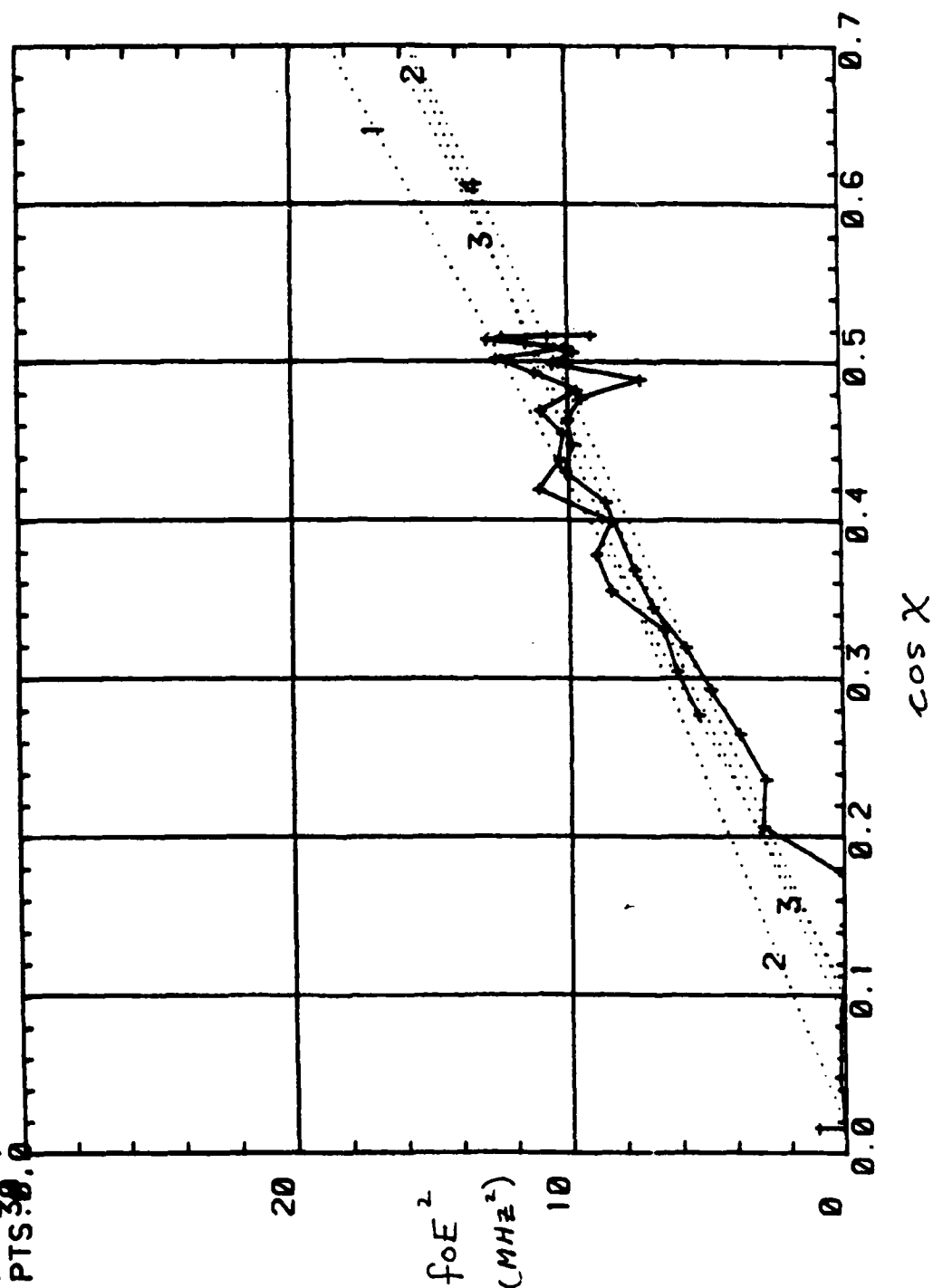
APPENDIX H

Plots of  $f\sigma E^2$  vs.  $\cos \chi$

X1: D340, 1600 - D341, 0400 (UT)

TREND LINES:

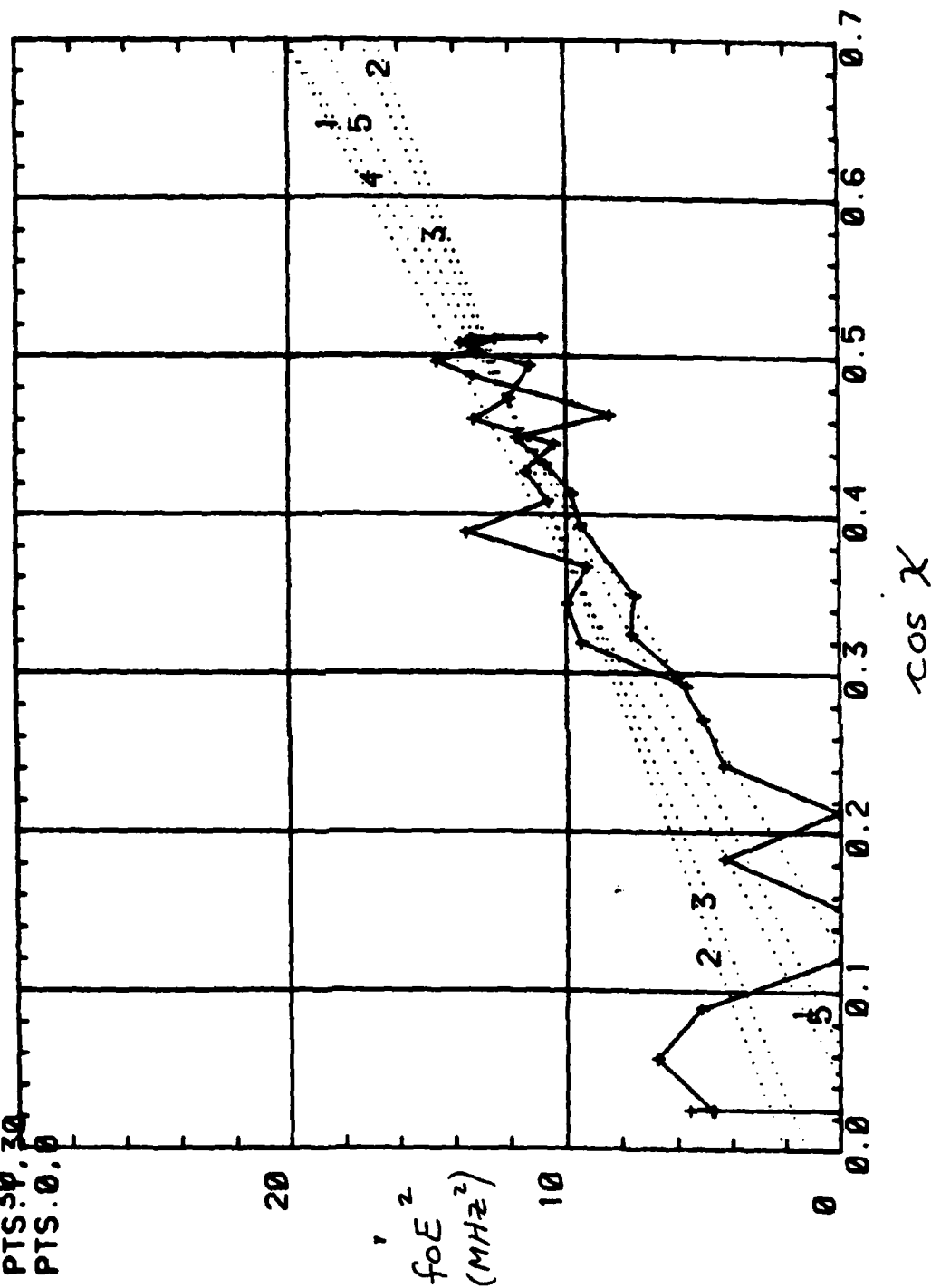
- L1: PTS. 1, 9
- L2: PTS. 1, 17
- L3: PTS. 1, 34
- L4: PTS. 17, 34
- L5: PTS. 30, 0



X2: D340, 1600 - D341, 0400 (UT)

TREND LINES:

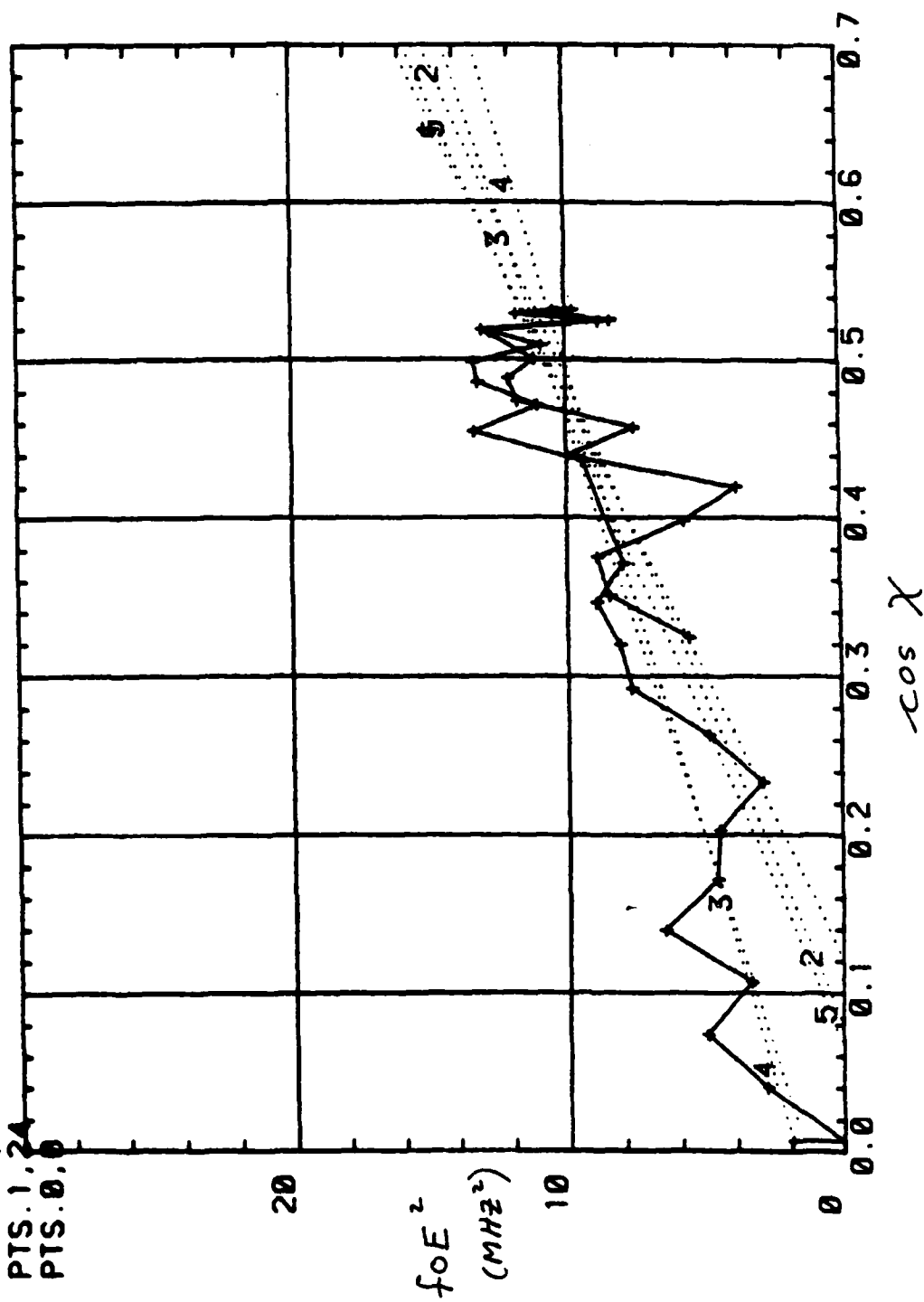
L1: PTS.1.9  
 L2: PTS.1.16  
 L3: PTS.1.23  
 L4: PTS.16.30  
 L5: PTS.30.30  
 L6: PTS.0.0



X3: D 340, 1600 - D 341, 0400 (UT)

TREND LINES:

- L1: PTS. 1, 9
- L2: PTS. 1, 16
- L3: PTS. 1, 30
- L4: PTS. 27, 37
- L5: PTS. 1, 24
- L6: PTS. 0, 0

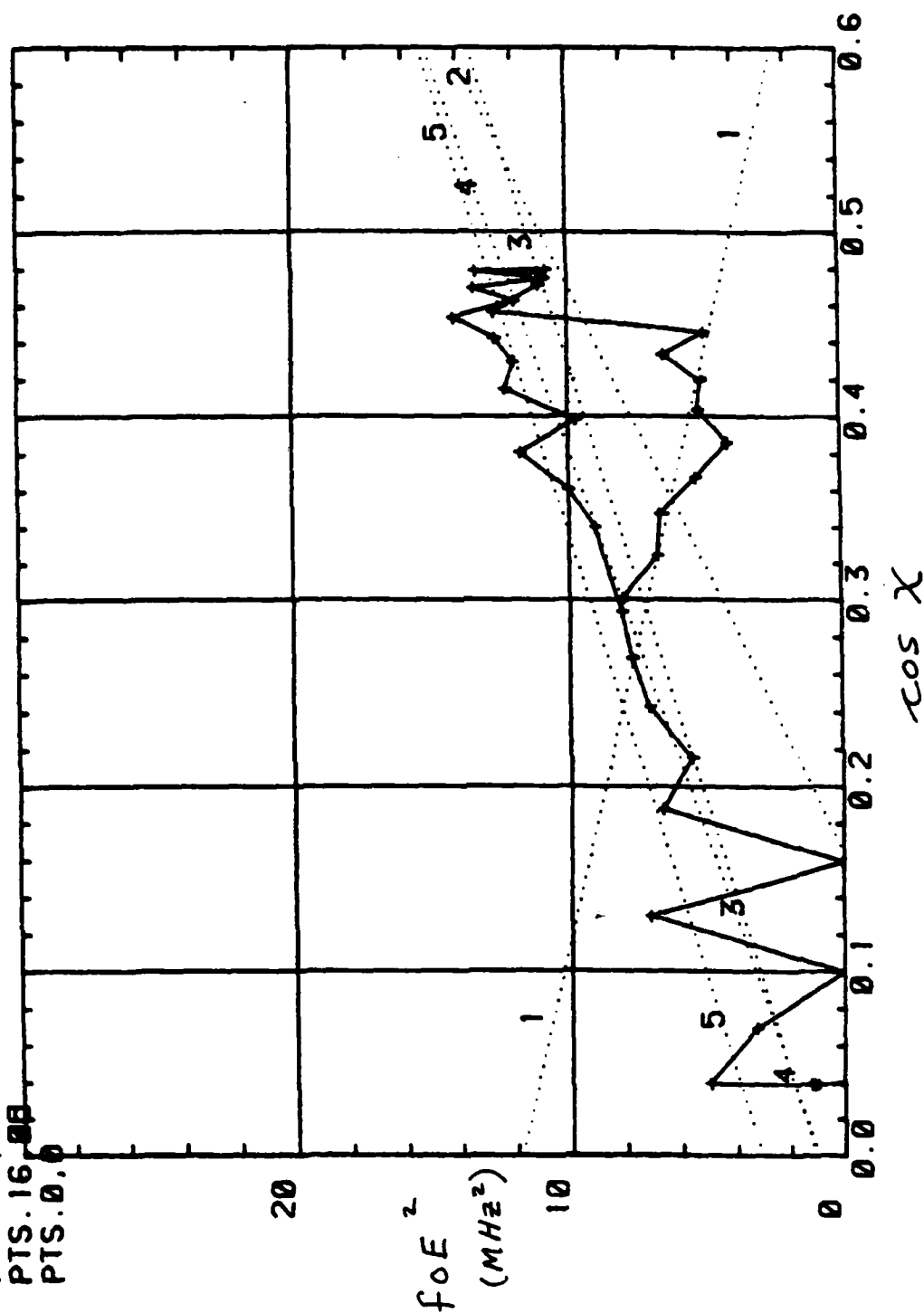




X4: D340, 1600 - D341, 0400 (UT)

TREND LINES:

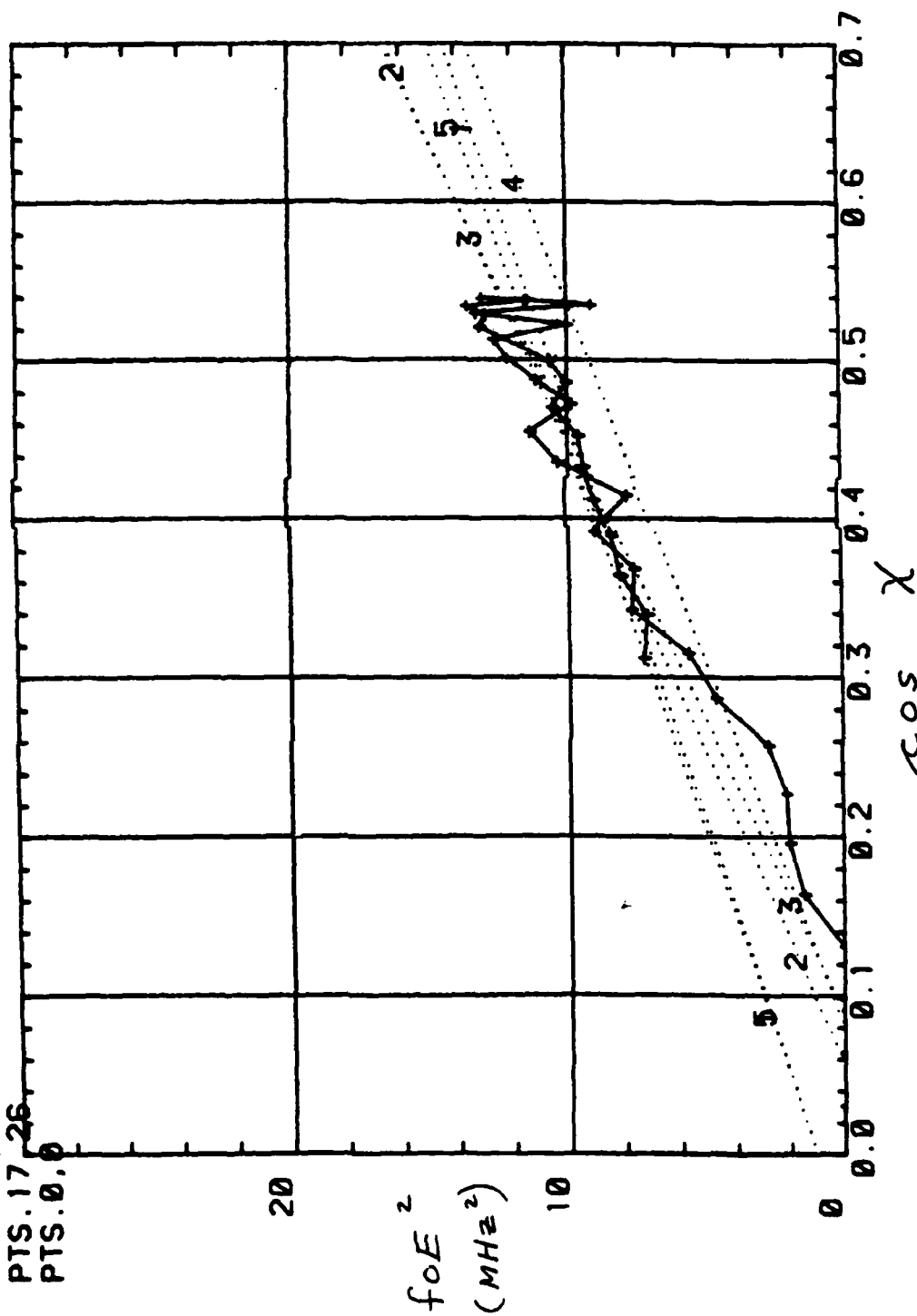
- L1: PTS.1.9
- L2: PTS.1.16
- L3: PTS.1.37
- L4: PTS.25.37
- L5: PTS.16.00
- L6: PTS.0.0



X5: D340, 1600 - D341, 0400 (UT)

TREND LINES:

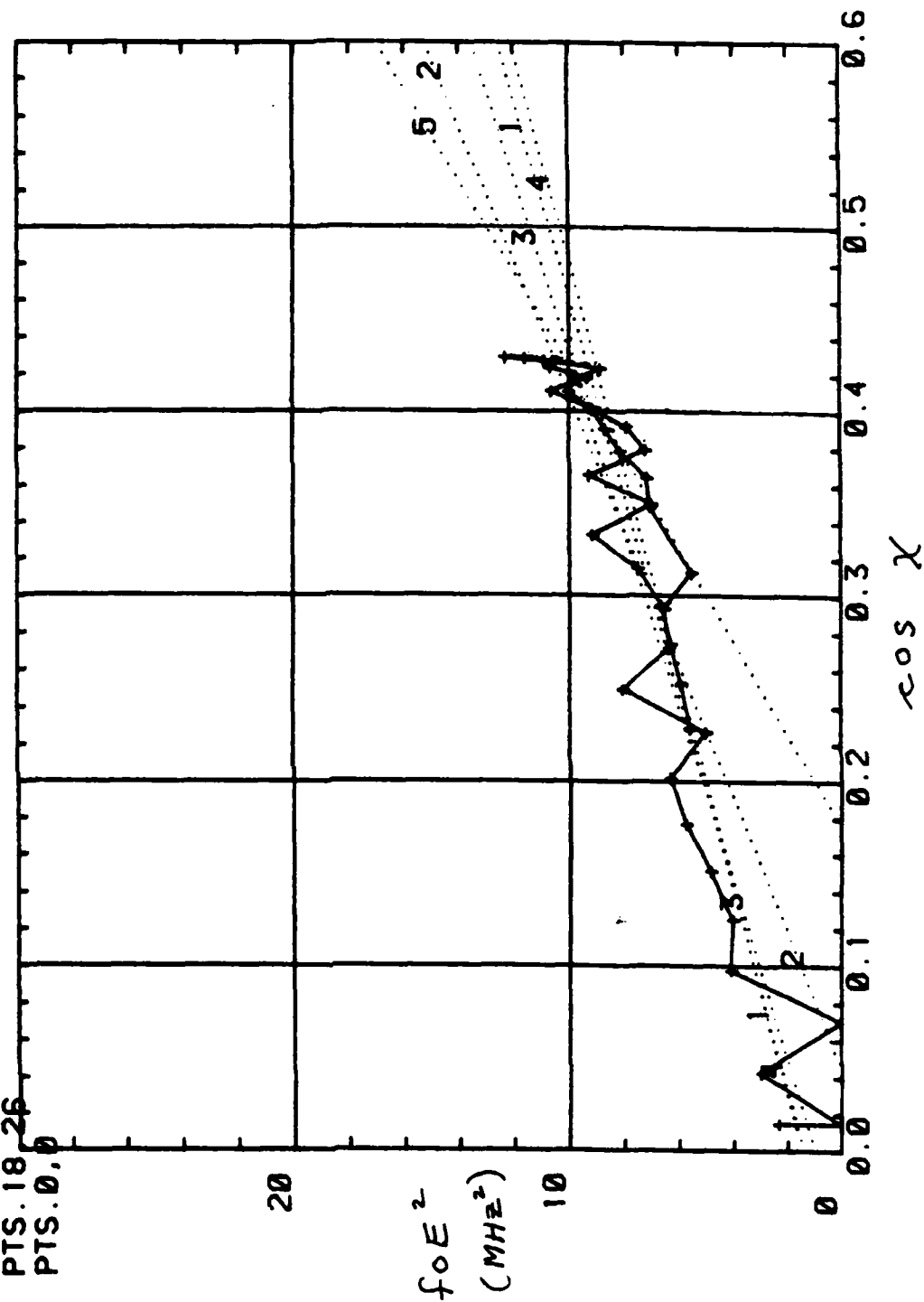
L1: PTS. 1.9  
 L2: PTS. 1.16  
 L3: PTS. 1.40  
 L4: PTS. 29.40  
 L5: PTS. 17.26  
 L6: PTS. 0.0



X6: D340, 1600 - D341, 0400 (UT)

TREND LINES:

- L1: PTS.1.9
- L2: PTS.1.17
- L3: PTS.1.40
- L4: PTS.25.40
- L5: PTS.18.26
- L6: PTS.0.0

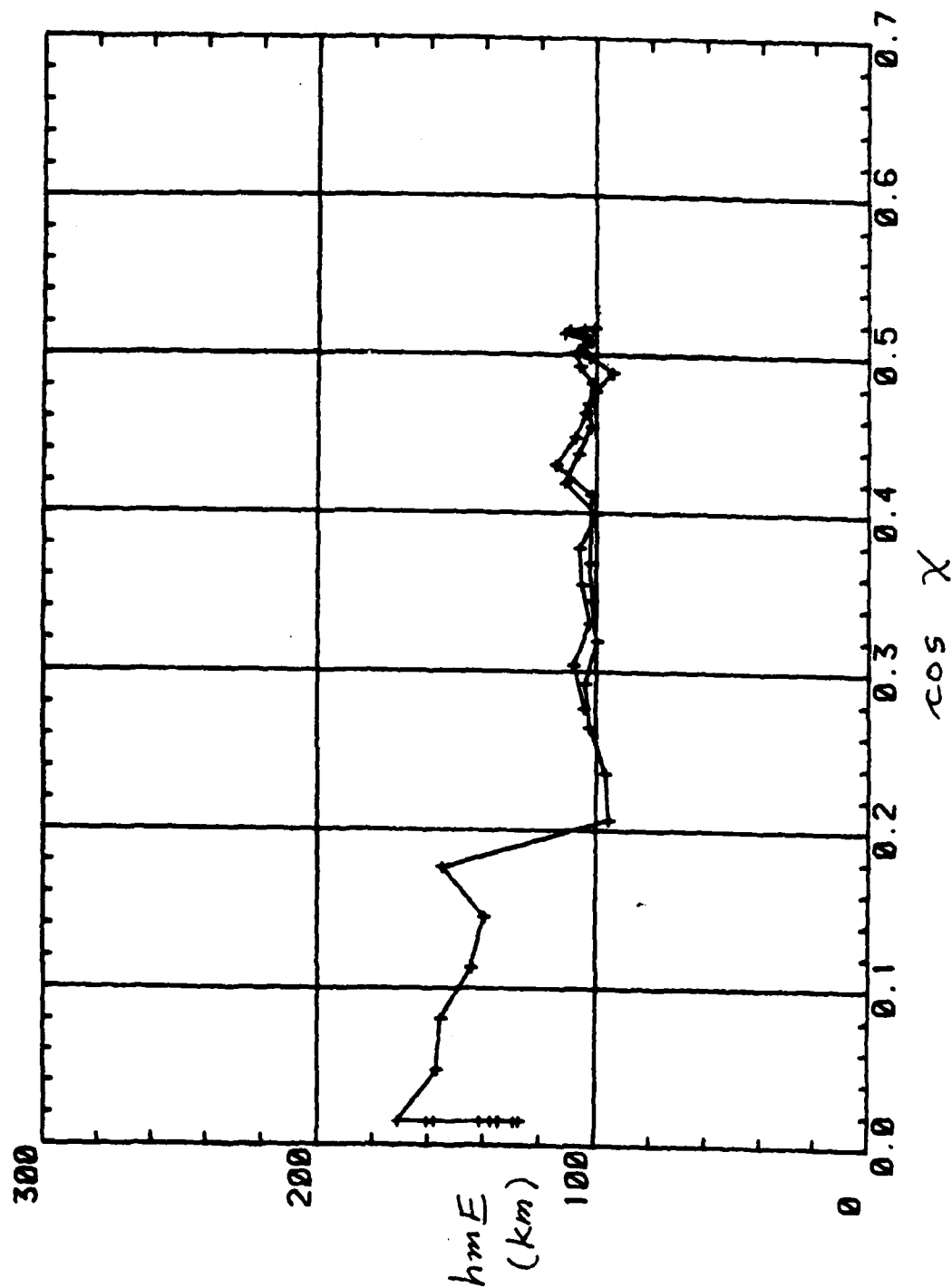


APPENDIX I

Plots of  $\ln E$  vs.  $\cos \chi$

X1: D340,1600 - D341,0400 (UT)

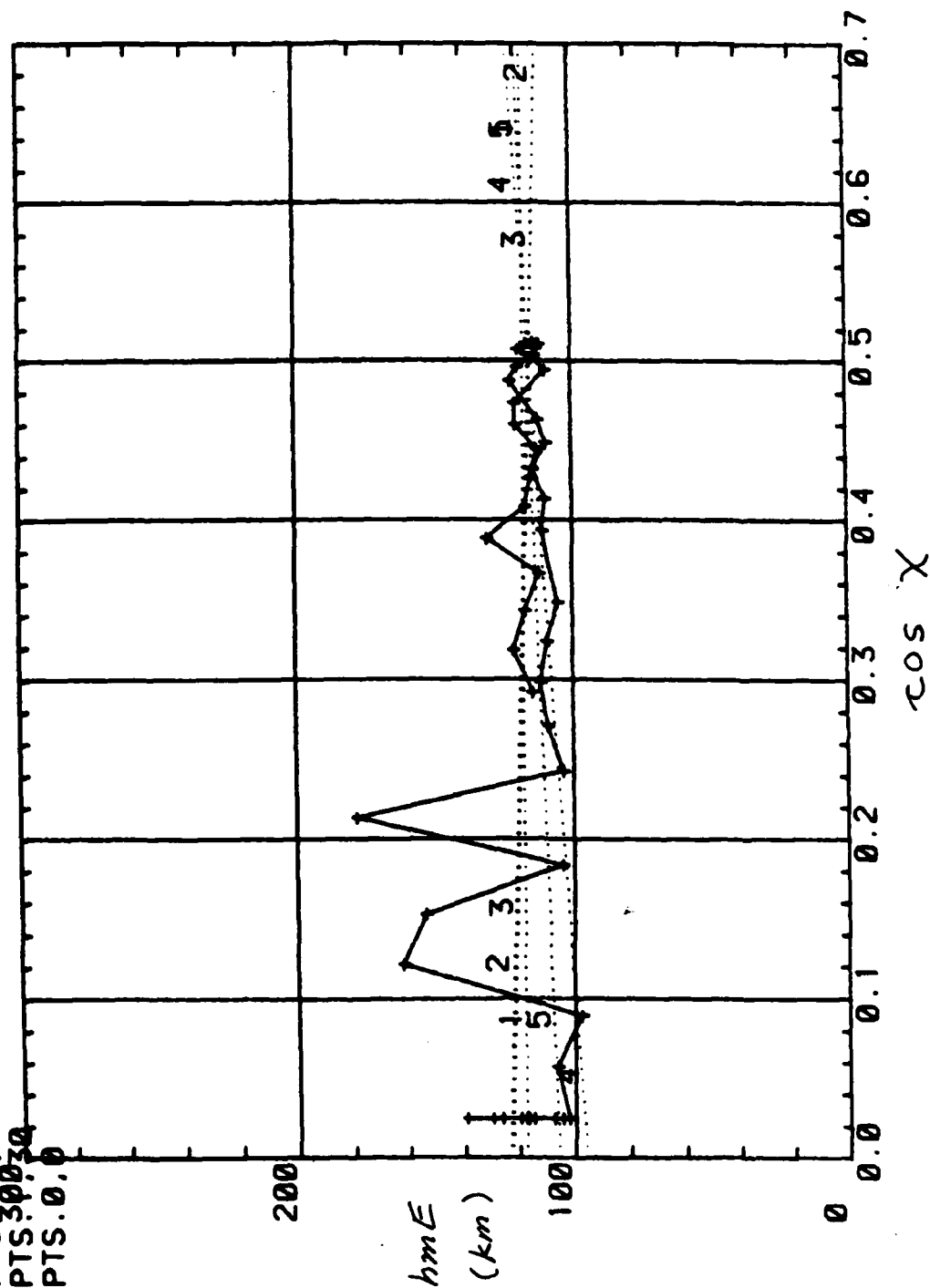
TREND LINES:  
L1: PTS.0,0



X2: D340, 1600 - D341, 0400 (UT)

TREND LINES:

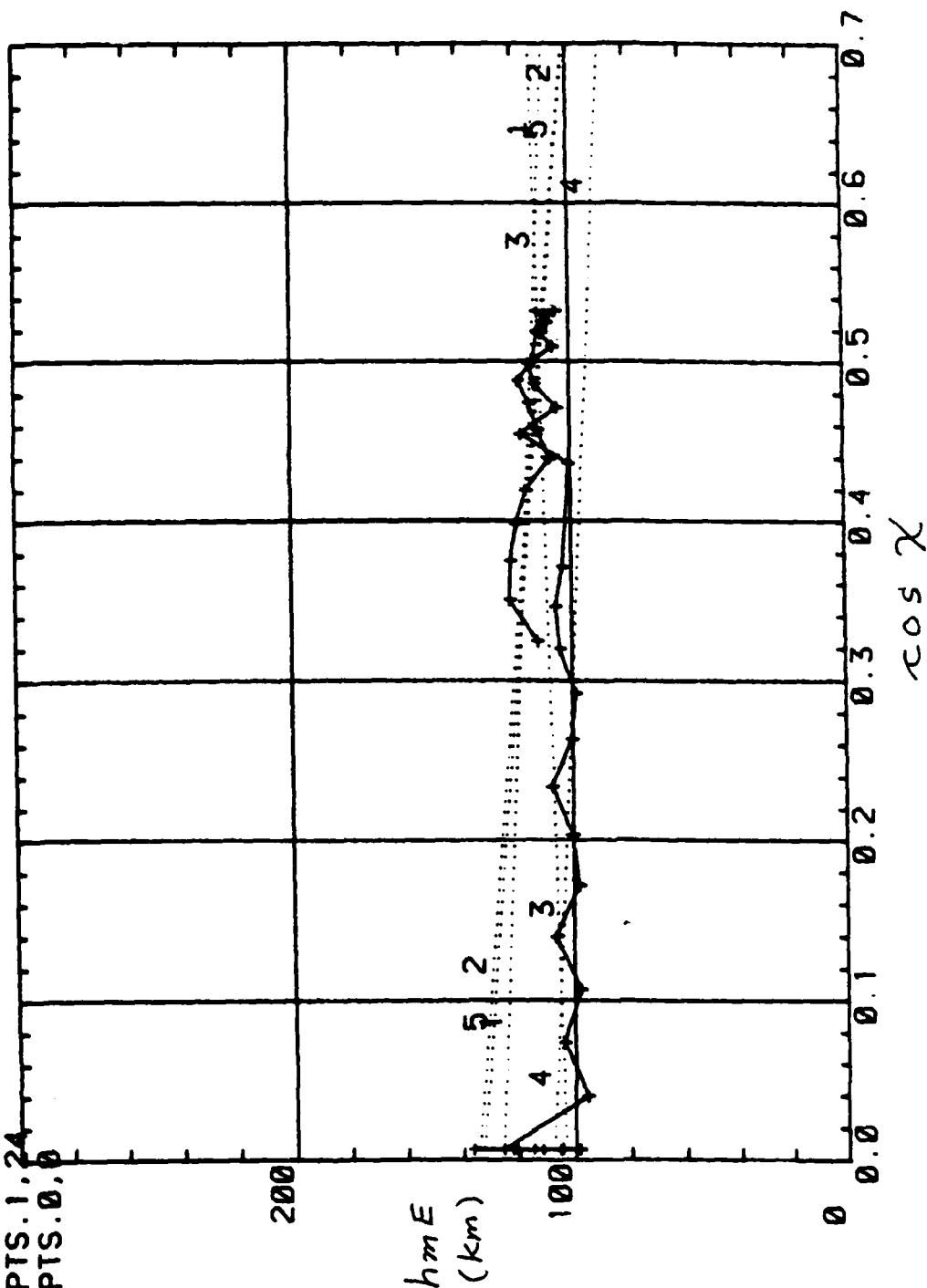
L1: PTS.1.9  
 L2: PTS.1.16  
 L3: PTS.1.23  
 L4: PTS.16.30  
 L5: PTS.30.30  
 L6: PTS.0.0



X3: D340, 1600 -- D341, 0400 (UT)

TREND LINES:

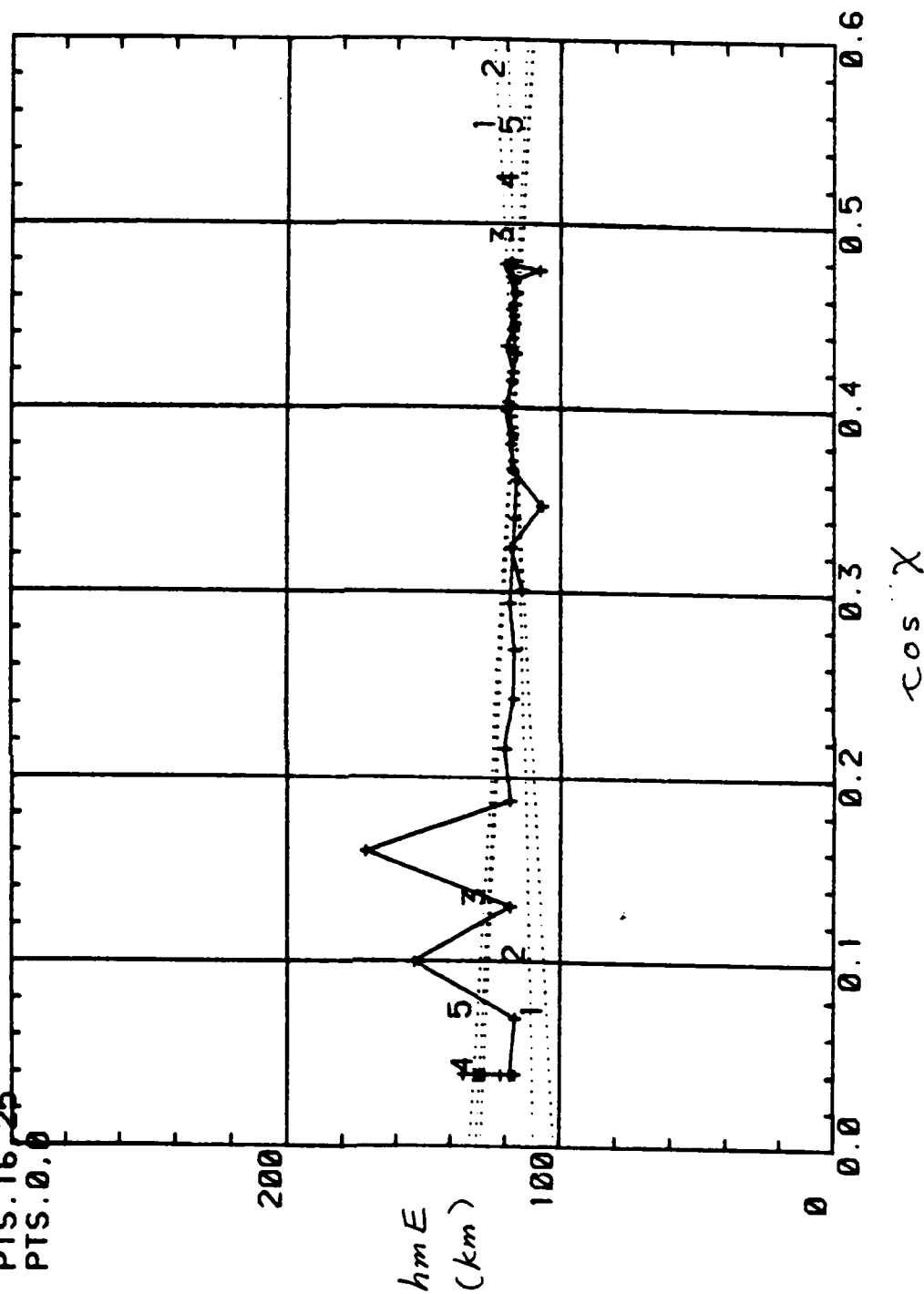
- L1: PTS.1,9
- L2: PTS.1,16
- L3: PTS.1,37
- L4: PTS.27,37
- L5: PTS.1,24
- L6: PTS.0,0



X4: D340,1600 - D341,0400 (UT)

TREND LINES:

- L1: PTS.1,9
- L2: PTS.1,16
- L3: PTS.1,37
- L4: PTS.25,37
- L5: PTS.16,25
- L6: PTS.0,0

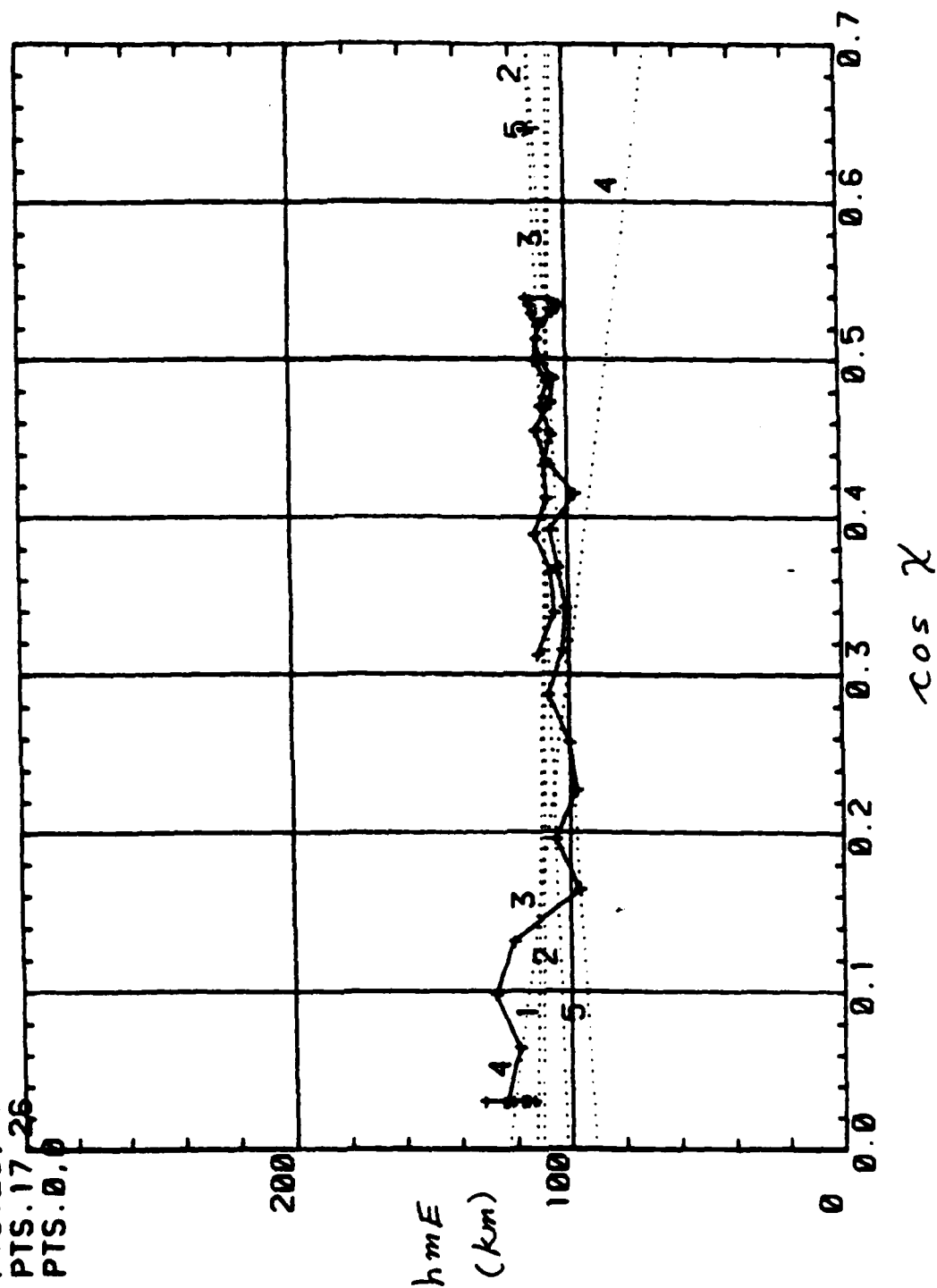




X5: D340, 1600 - D341, 0400 (UT)

TREND LINES:

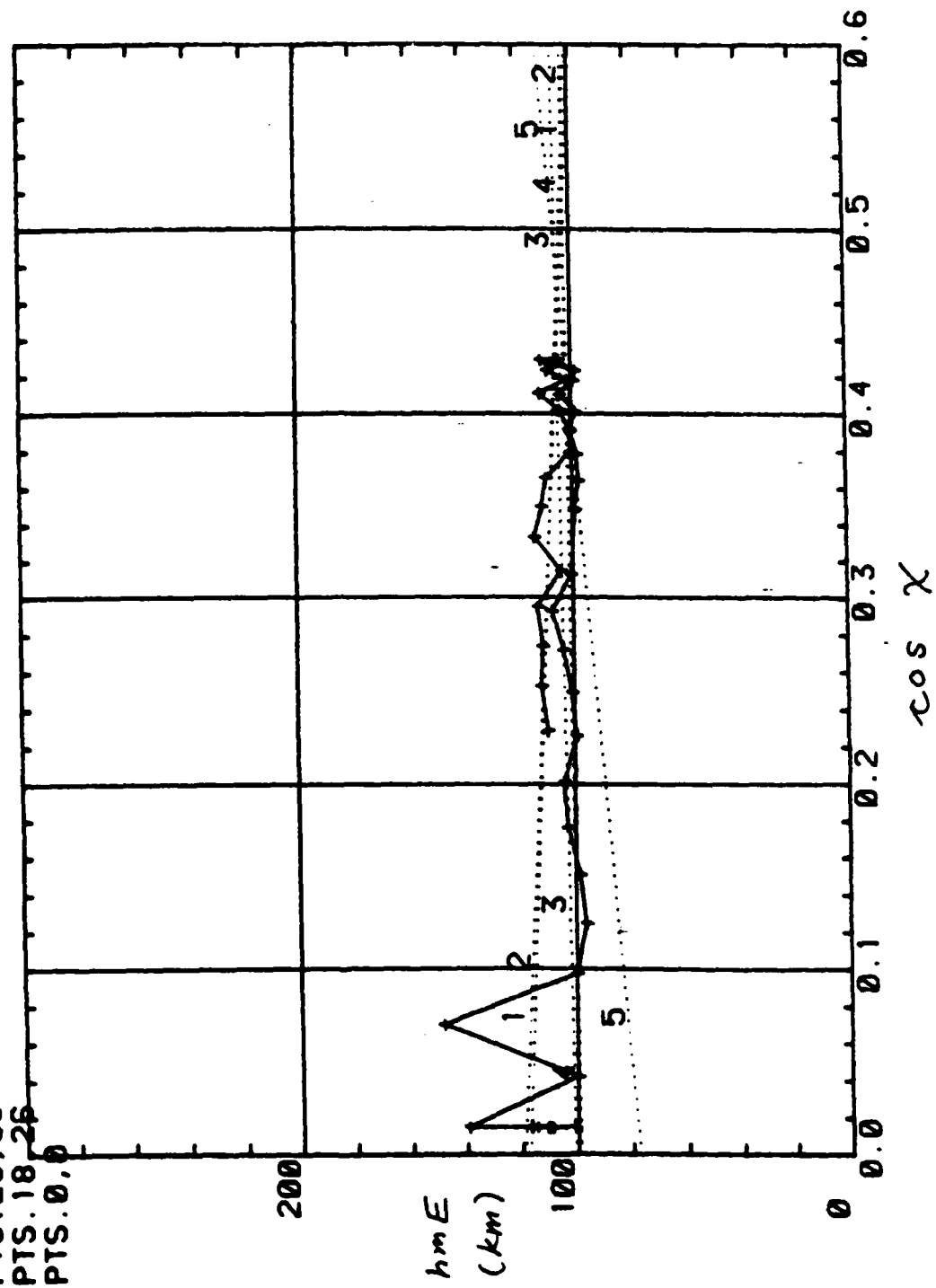
L1: PTS.1,9  
 L2: PTS.1,16  
 L3: PTS.1,40  
 L4: PTS.29,40  
 L5: PTS.17,26  
 L6: PTS.0,0



XG: D340, 1600 - D341, 0400 (UT)

TREND LINES:

- L1: PTS. 1, 9
- L2: PTS. 1, 17
- L3: PTS. 1, 36
- L4: PTS. 25, 36
- L5: PTS. 18, 26
- L6: PTS. 0, 0



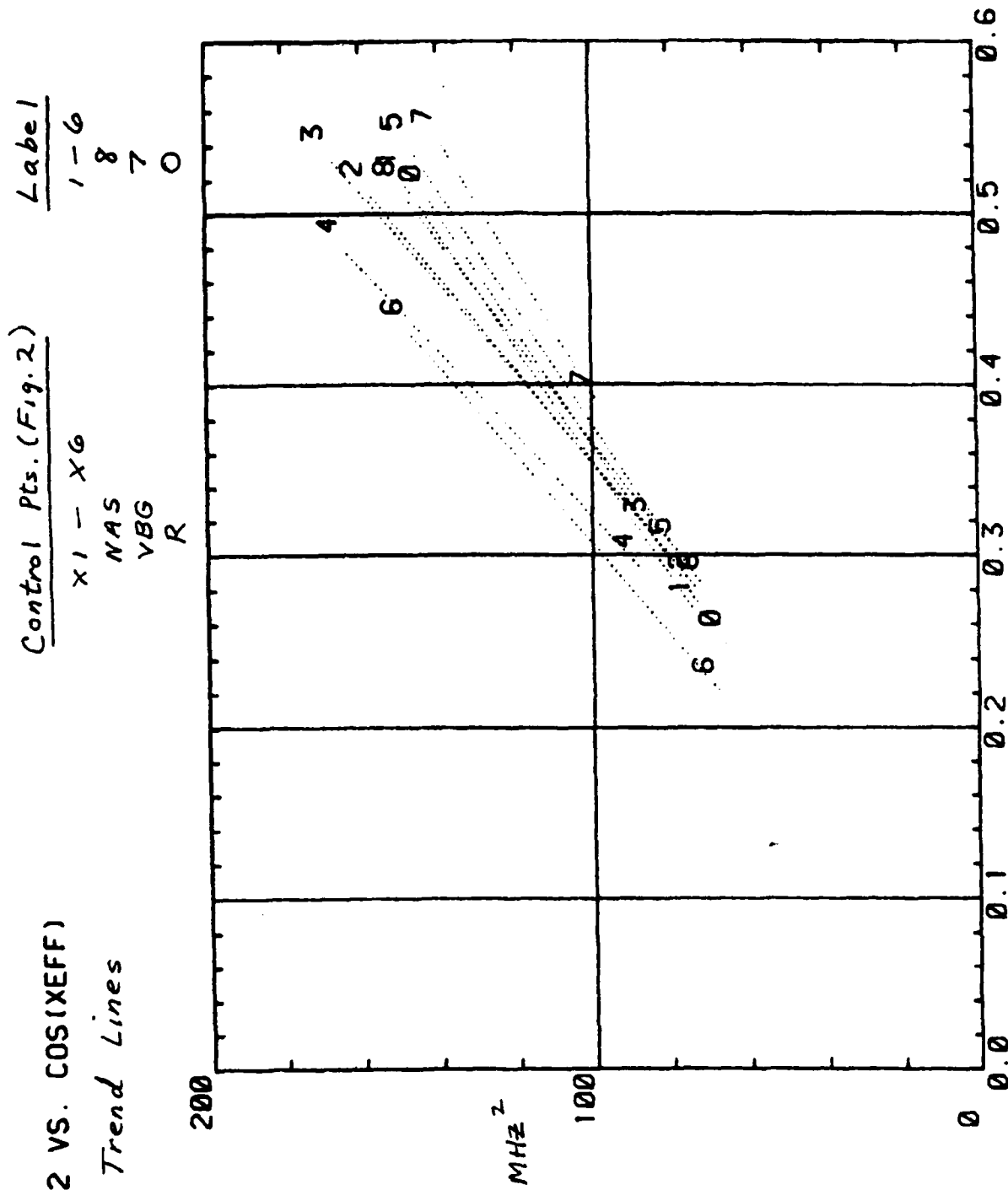
## APPENDIX J

### Comparison of Trend Lines

Trend lines for each of seven ionospheric parameters are plotted together for all the sounder control points. Curves 1-6 refer to control points X1-X6 in Figure 2. Additional trend lines for  $fOF2^2$  from vertical-incidence sounders are plotted for comparison. These are identified in the accompanying legend for the plot. For each parameter there are two plots, one for the morning trend lines, identified as L2 in Appendices B-H, and one for the late afternoon trend lines, identified as L4 in Appendices B-H. The lines are drawn in the intervals for which they were determined by linear regression analysis.

F0F212 VS. COS(XEFF)

L2 Trend Lines



F0F212 VS. COS(XEFF)

L4 Trend Lines

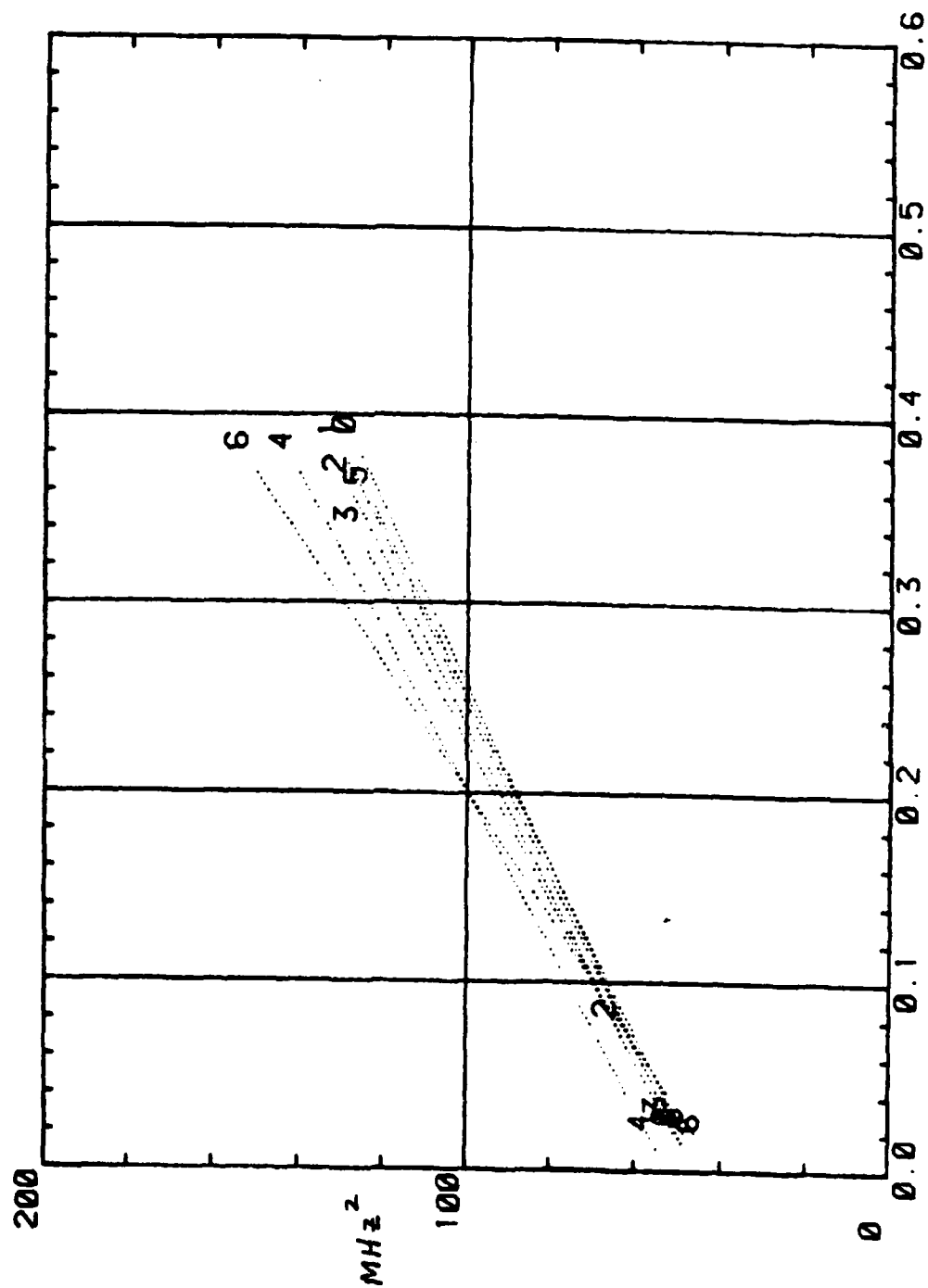
Control Pts. (Fig.2)

1-6

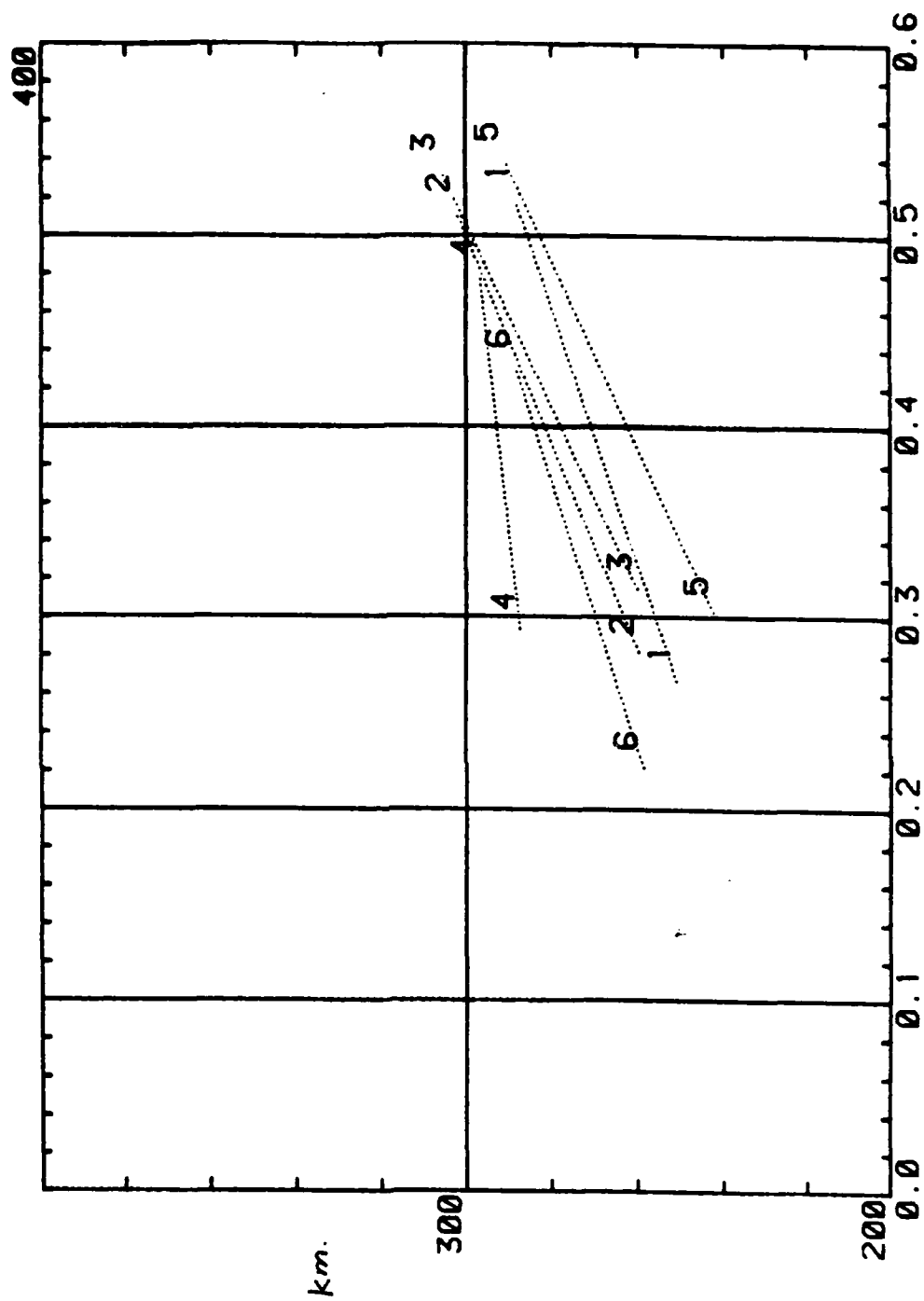
0

X1-X6

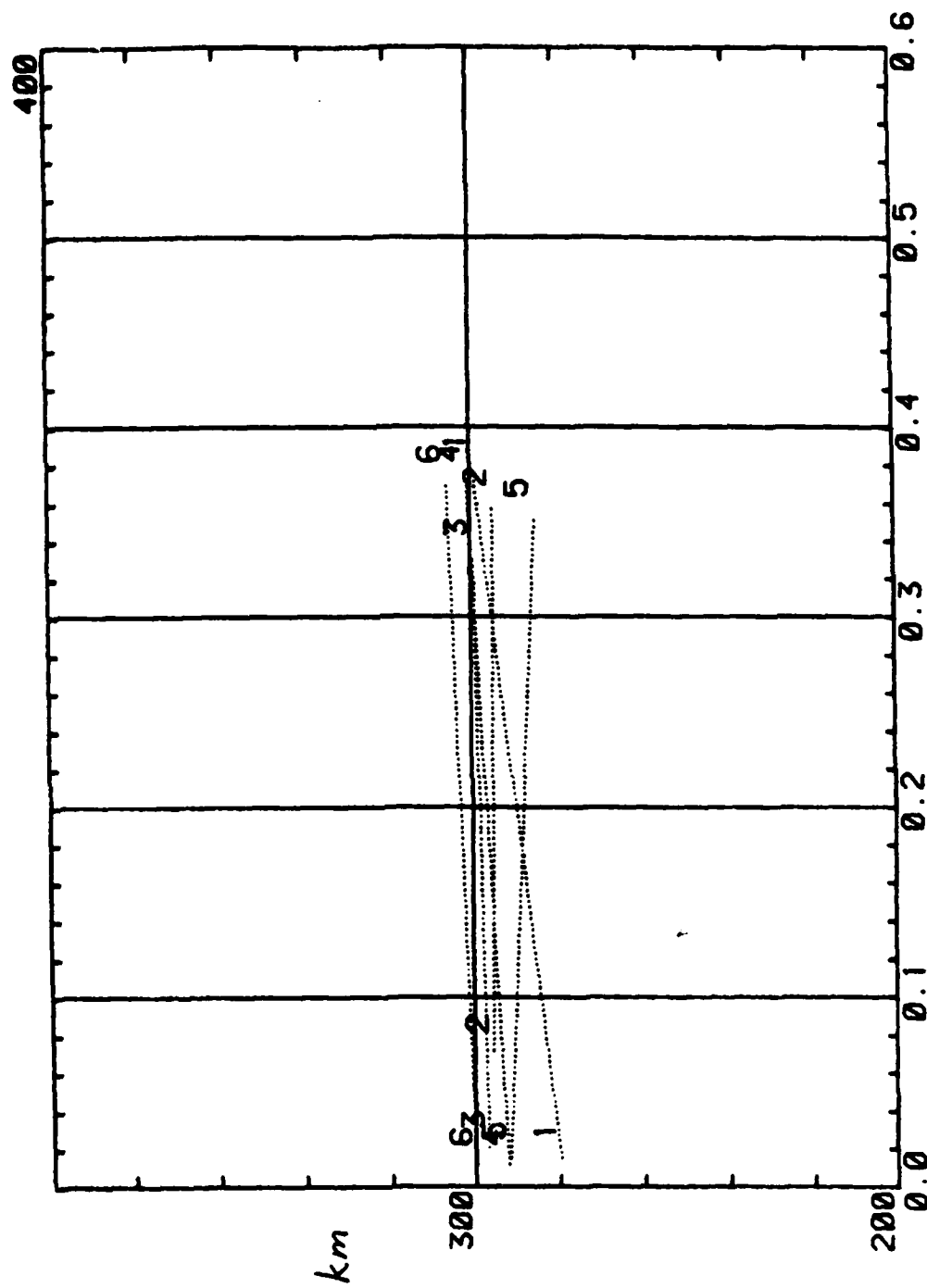
R



# HMF2 VS. COS(XEFF) L2 Trend Lines

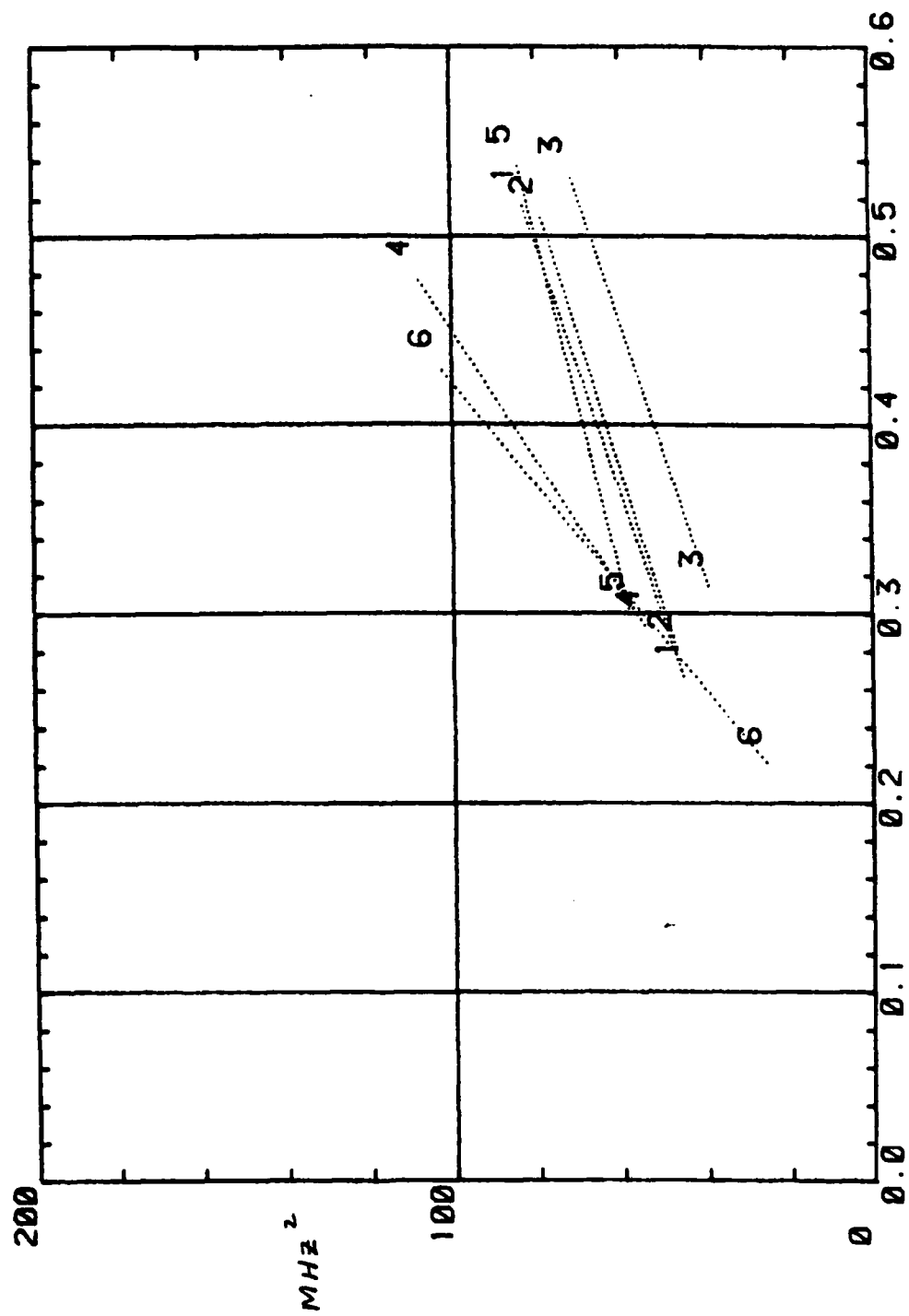


# HMF2 VS. COS(XEFF) L4 Trend Lines



# F0F112 VS. COS(XEFF)

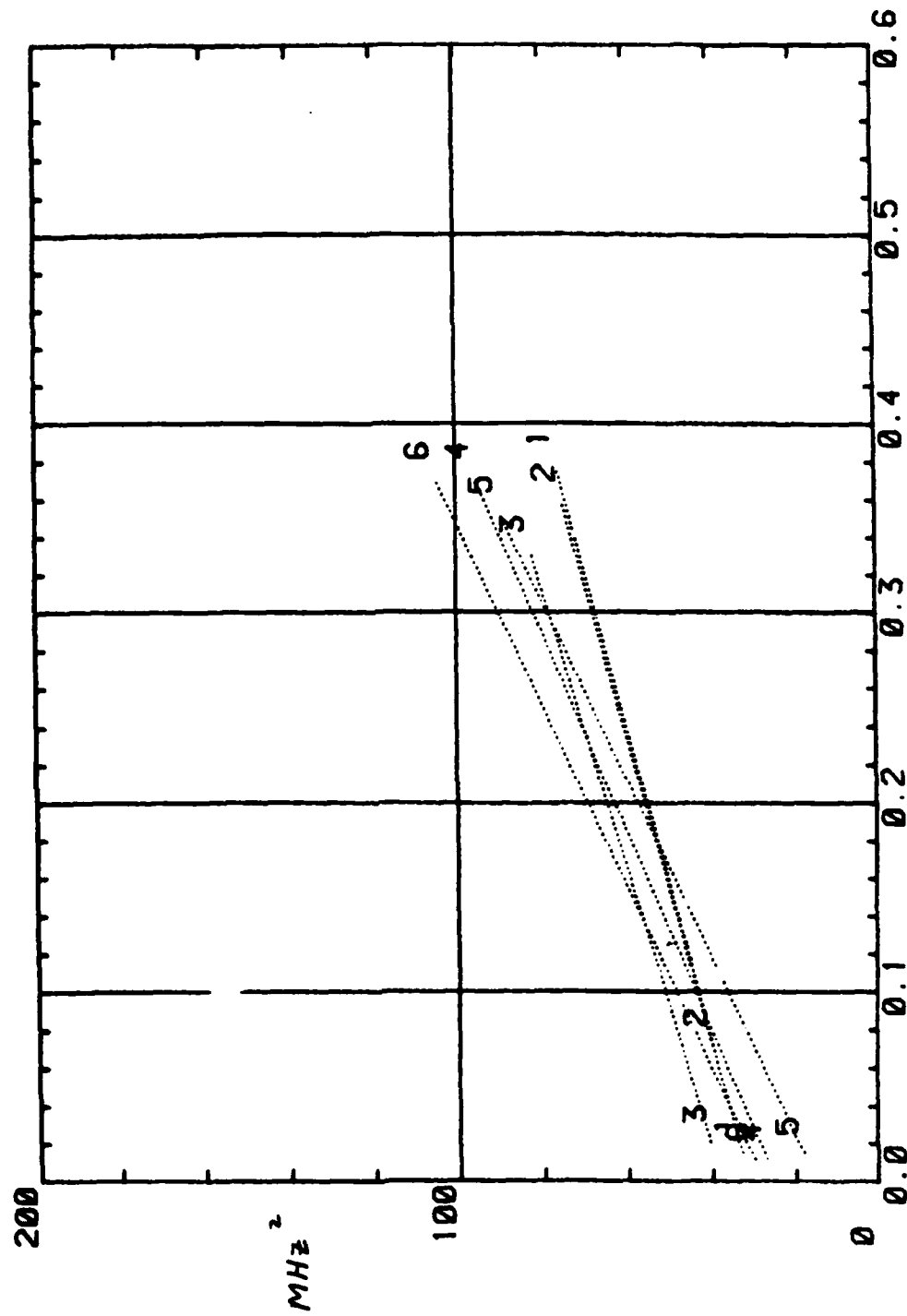
L2 Trend Lines





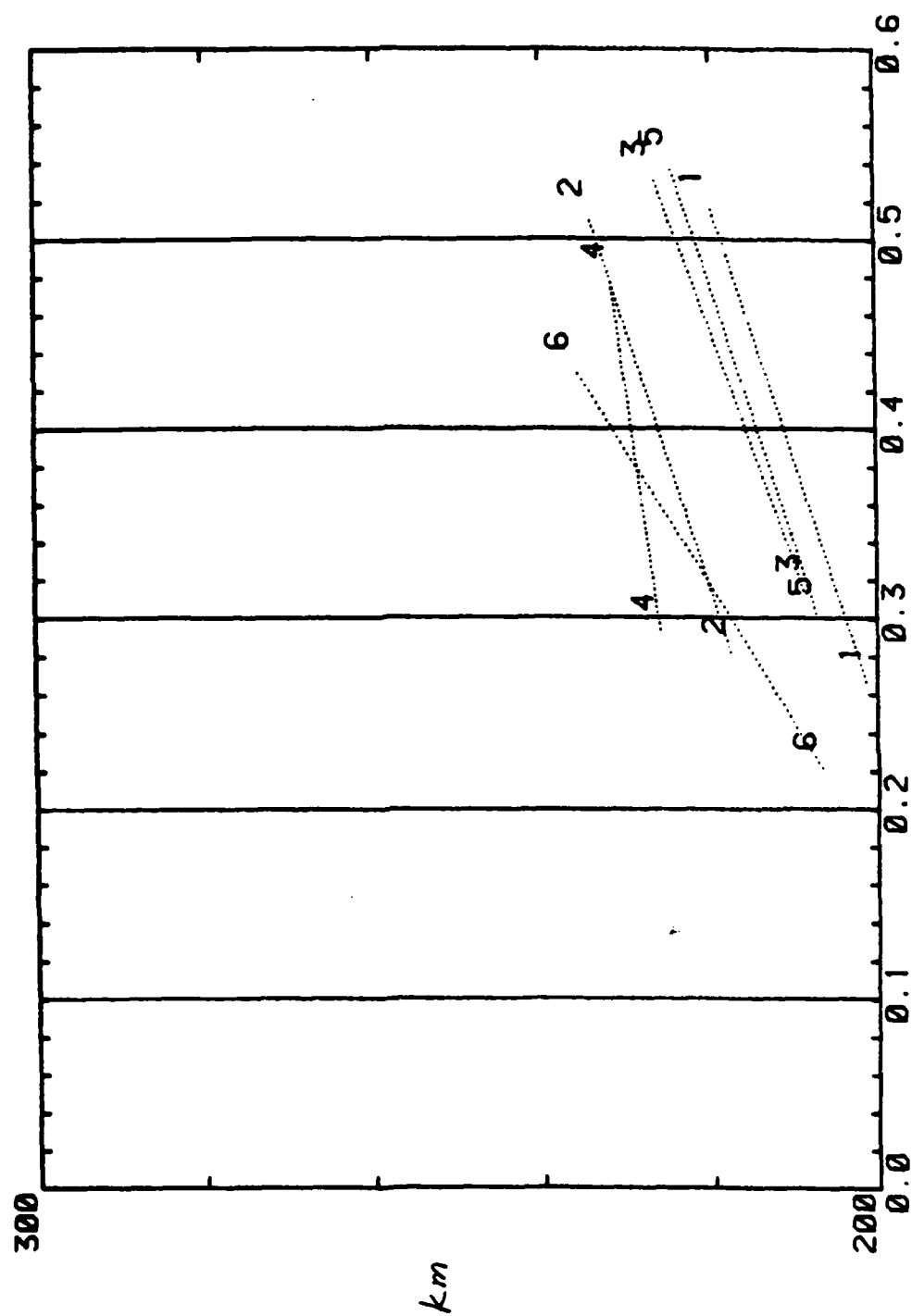
F0F112 VS. COS(XEFF)

L4 Trend Lines



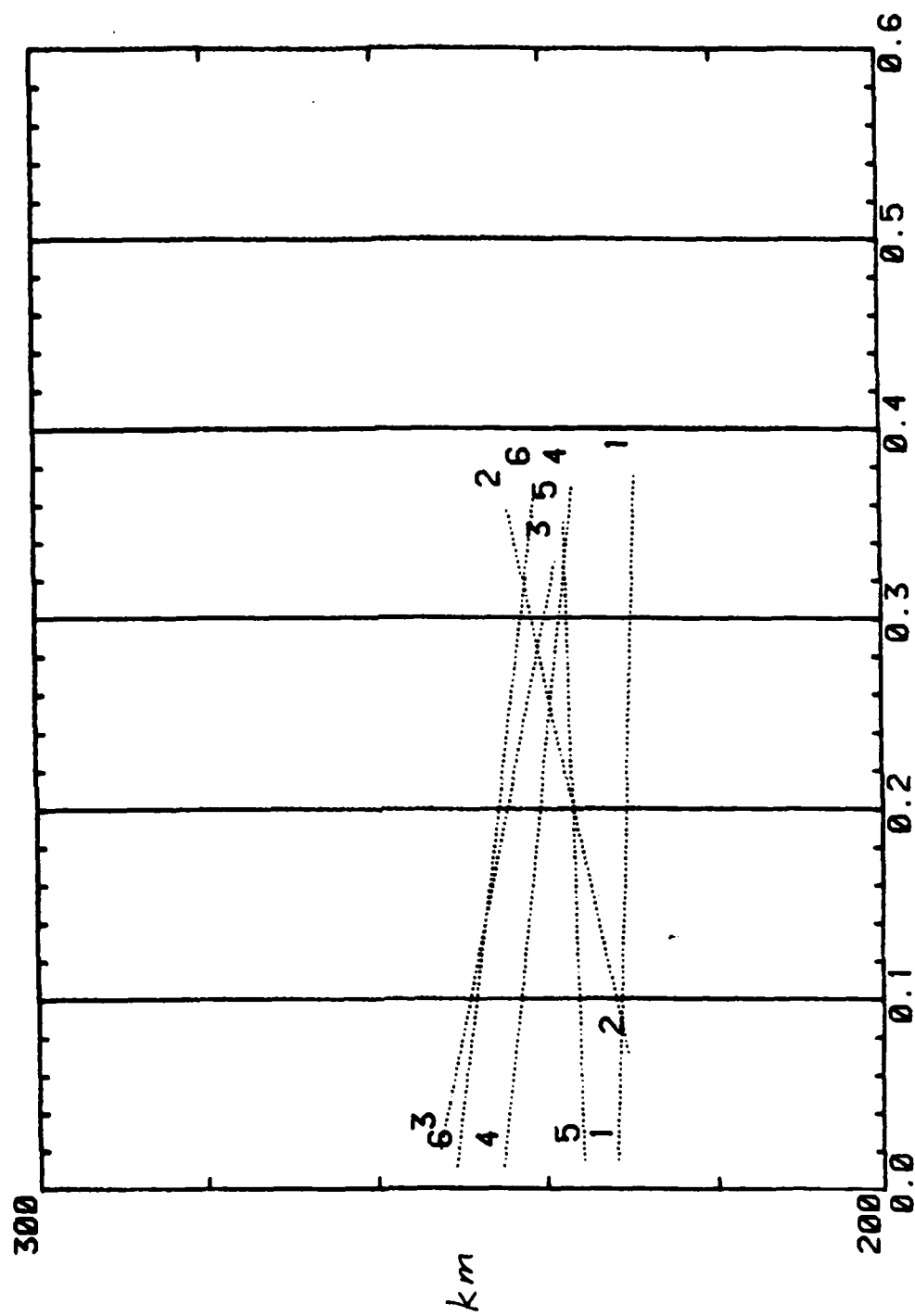
HMF1 VS. COS(XEFF)

L2 Trend Lines



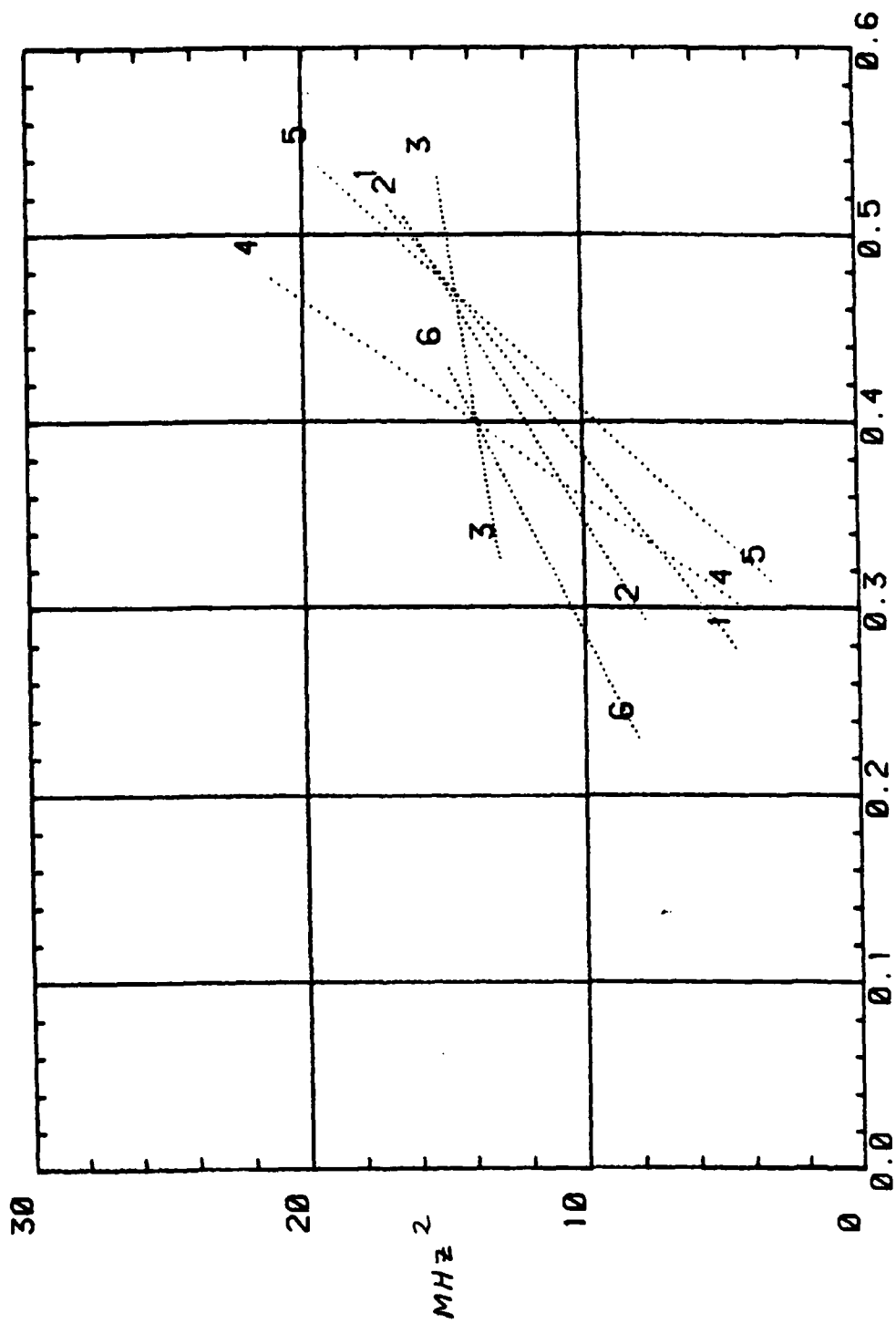
HMF1 VS. COS(XEFF)

L4 Trend Lines

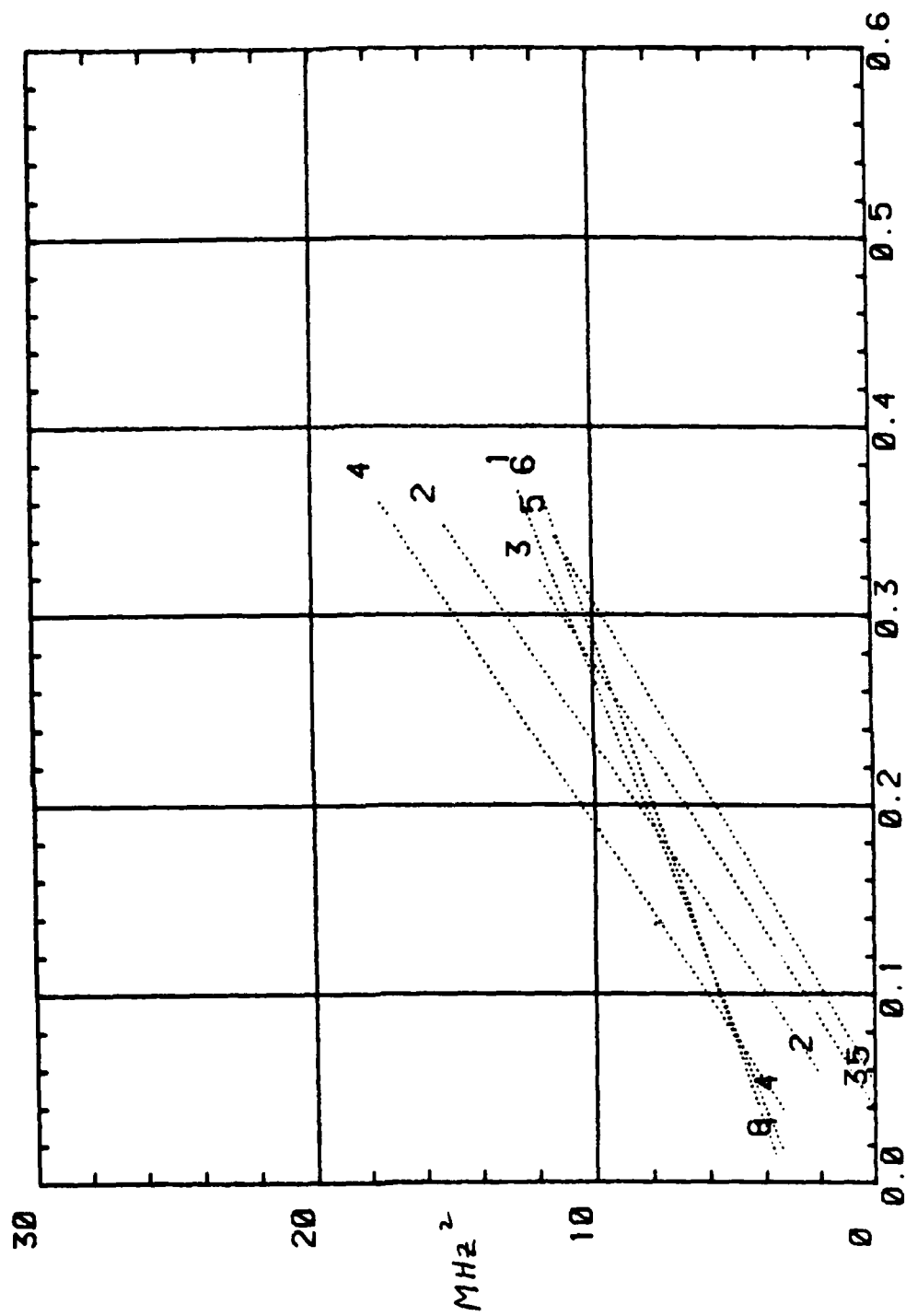


FBF12 VS. COS(X)

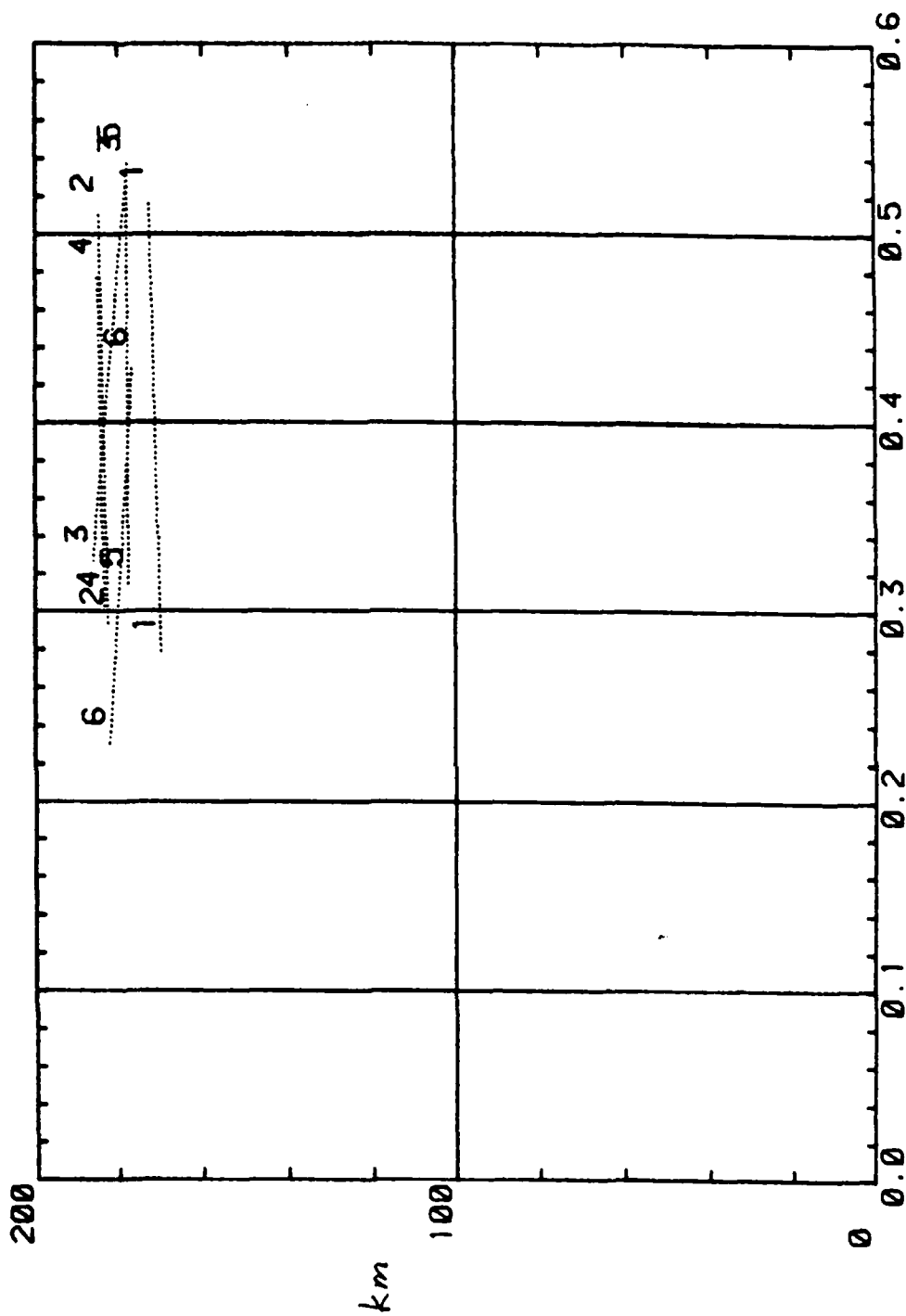
L2 Trend Lines



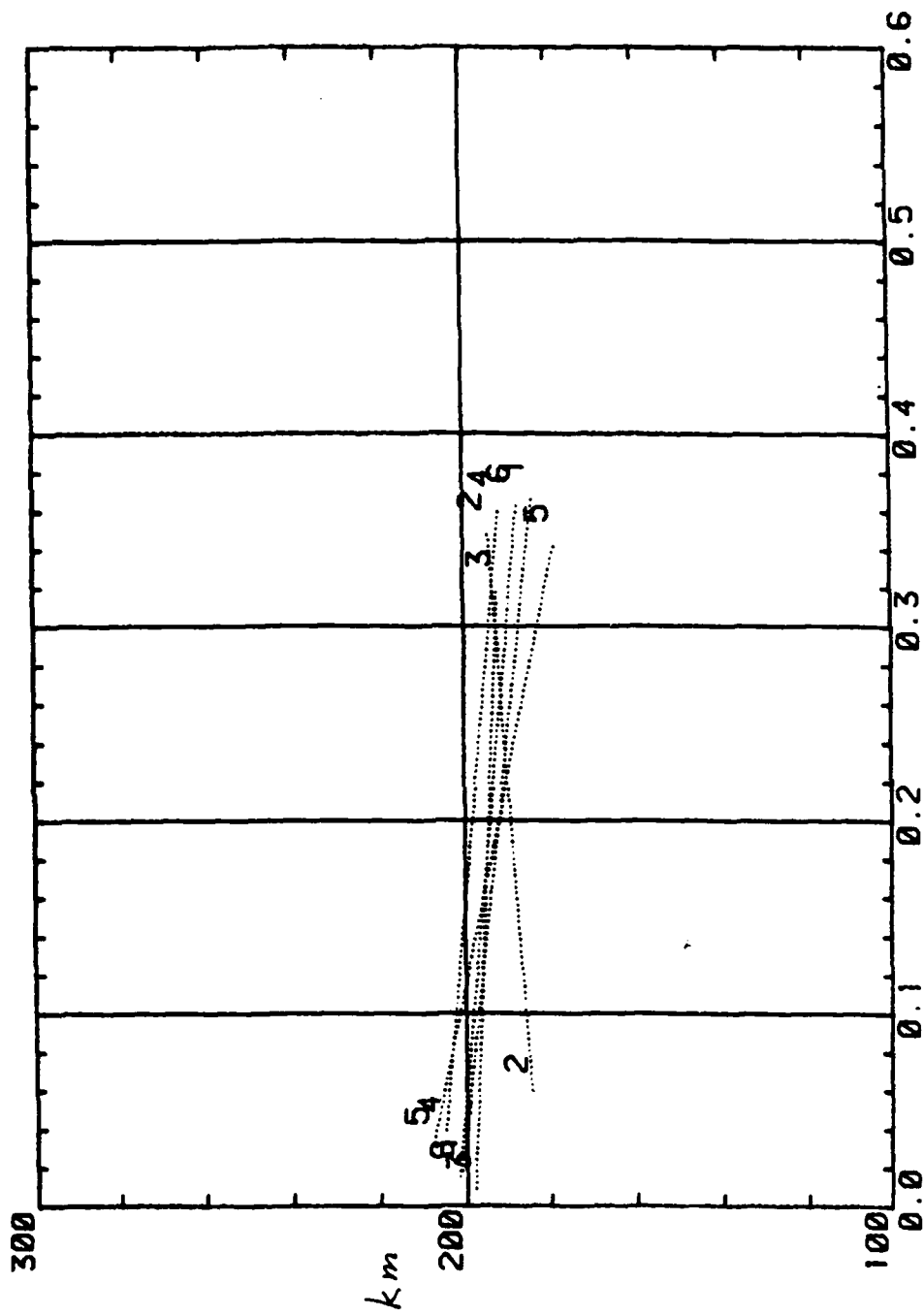
# FBF12 VS. COS(X) L4 Trend Lines



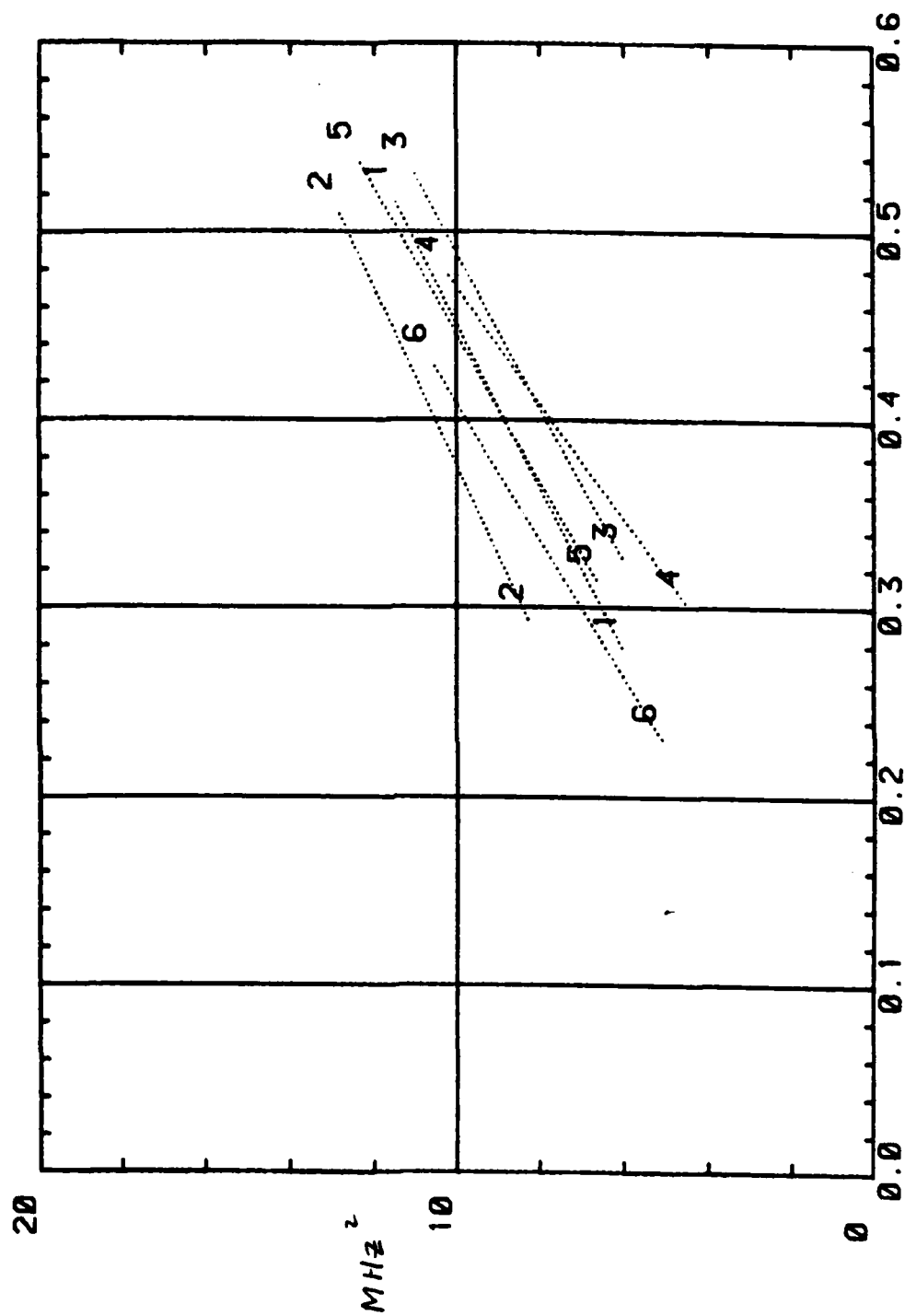
# HBF VS. COS(X) L2 Trend Lines



## 5417 Trend Lines

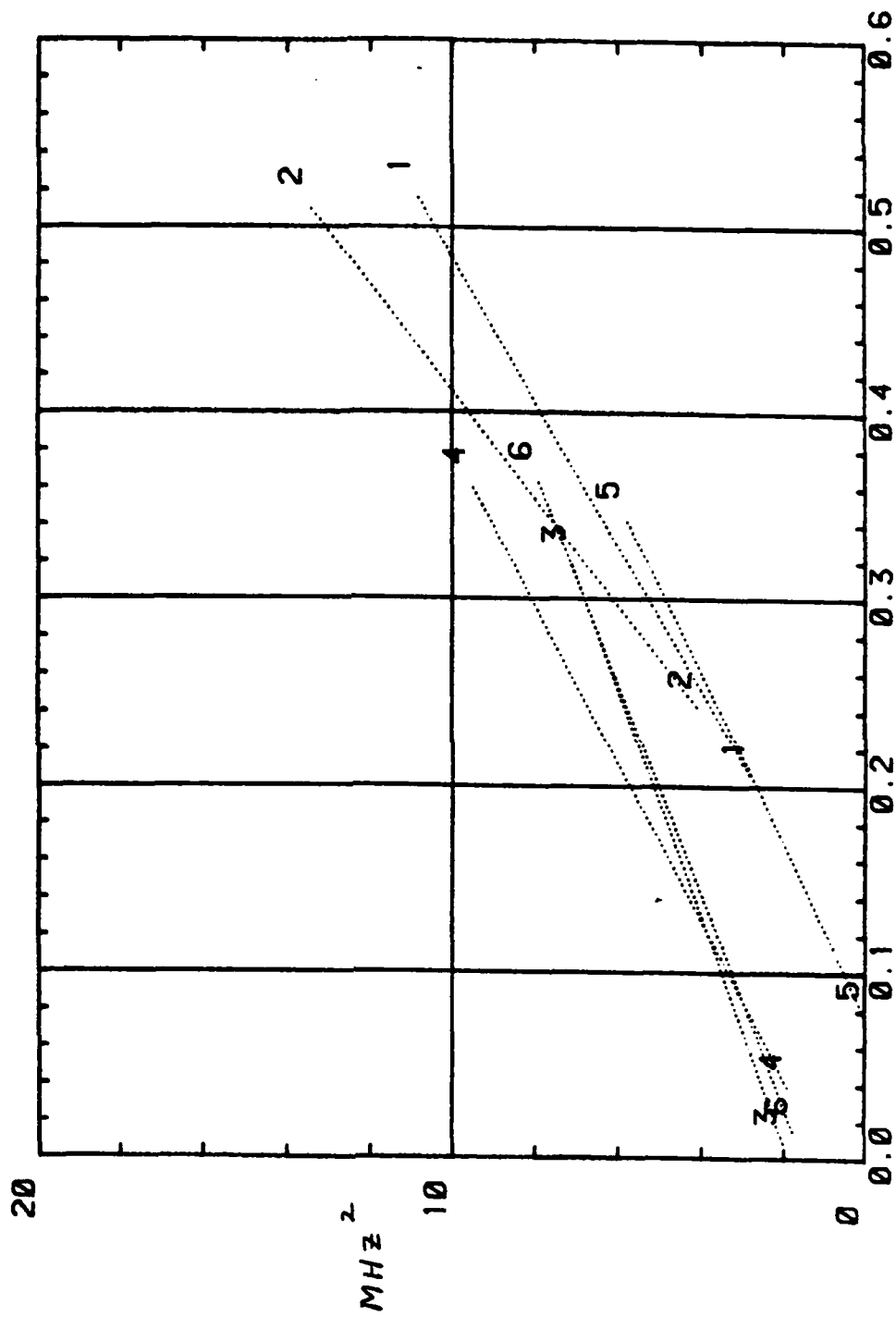


# F0E12 VS. COS(X) L2 Trend Lines





# F0E12 VS. COS(X) L4 Trend Lines



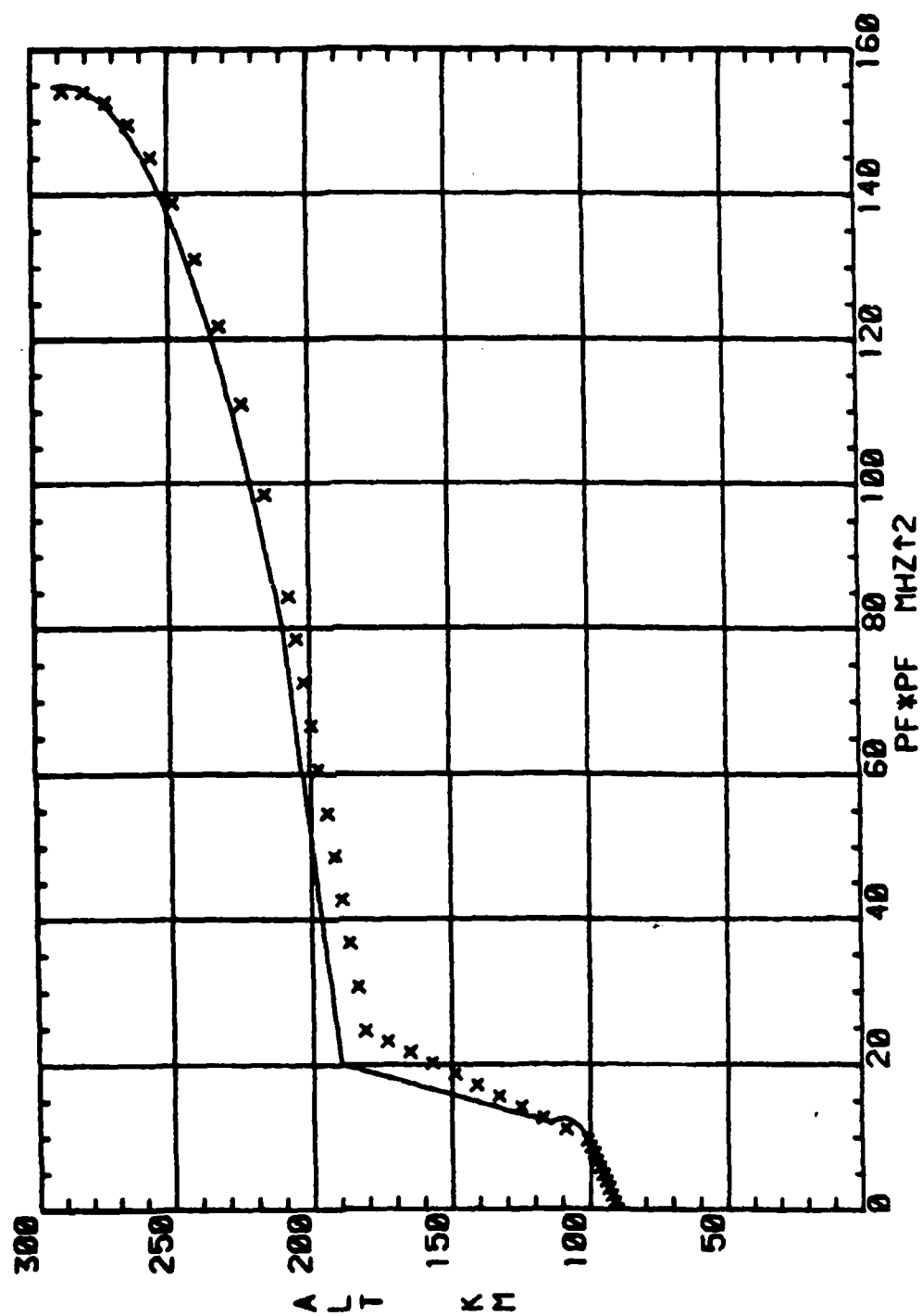
## APPENDIX K

### Comparison of Calculated and Exact Profiles in the SSL-BCT Prototype Calculations

From a nine-parameter idealized profile with a parabolic E layer, one-hop oblique ionograms are calculated for the ranges of the SSL-BCT sounder network (cf. Figure 2). The true height profile calculation procedure is carried out on these ionograms, and the nine-parameter solutions are plotted as X-marks in the ensuing figures. The exact model profile is shown by the solid line curves, for comparison. Section 2C gives a full discussion of the procedure and results.

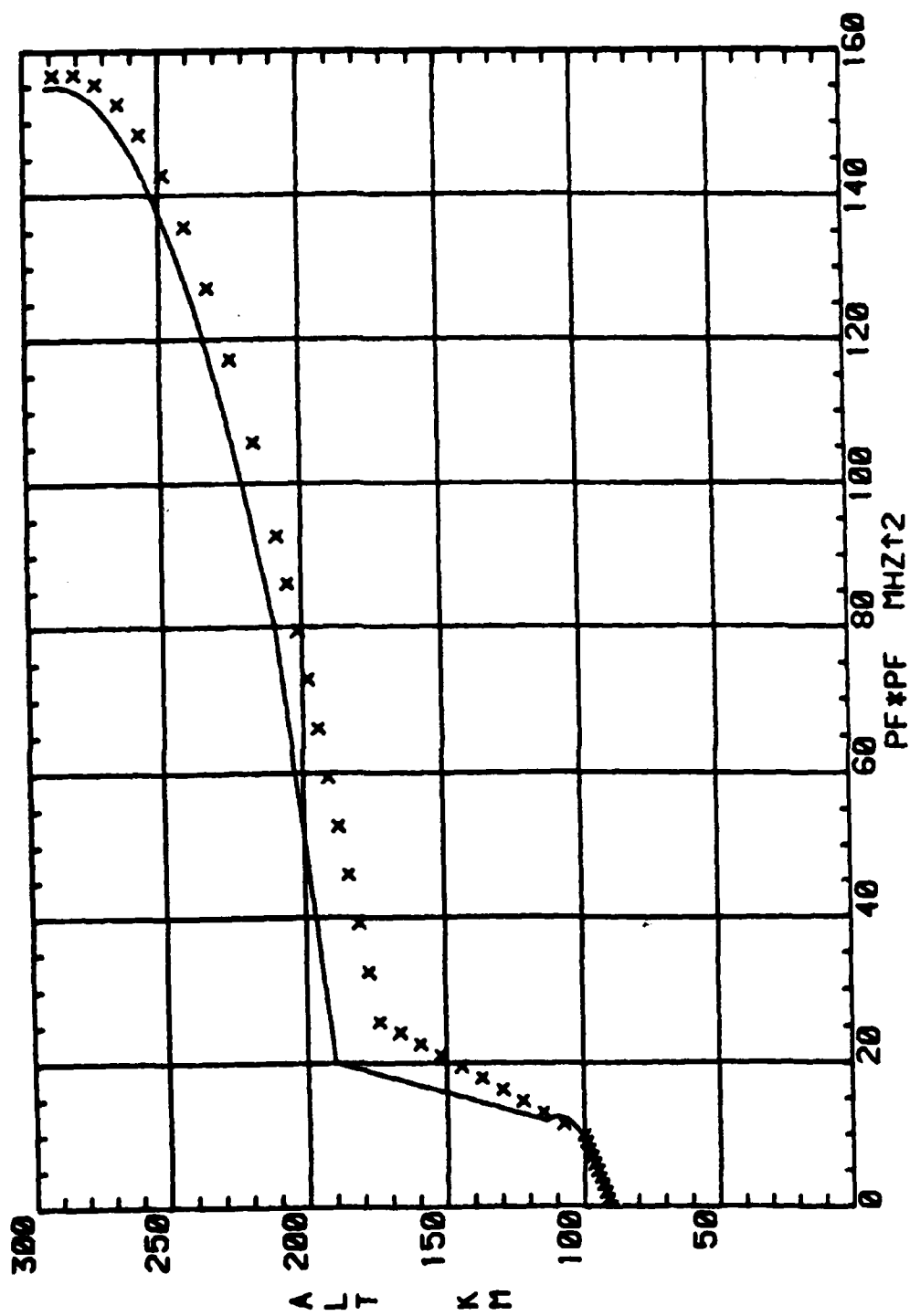
# IONOSPHERIC TRUE HEIGHT PROFILE

No. 1



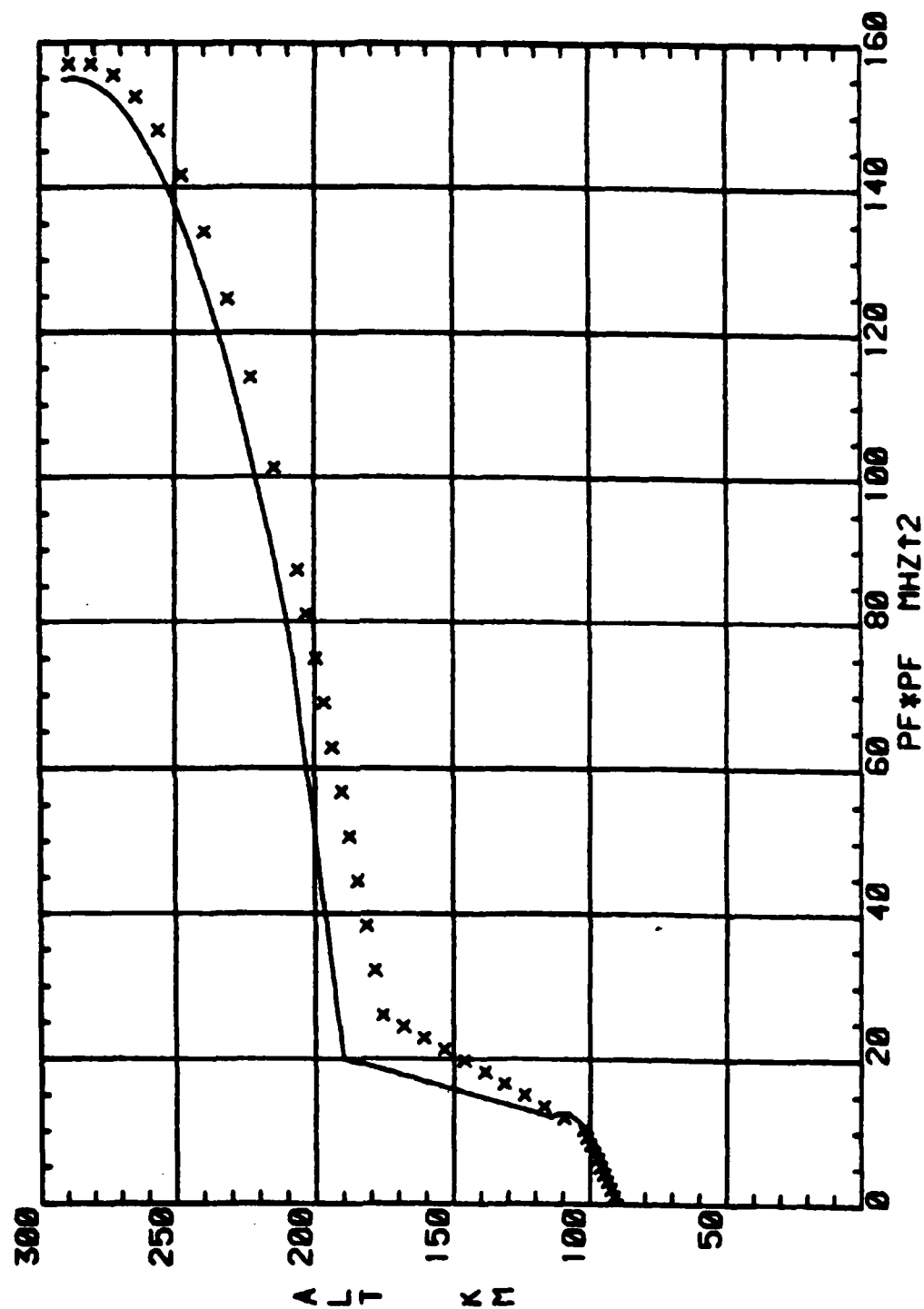
# IONOSPHERIC TRUE HEIGHT PROFILE

No. 2



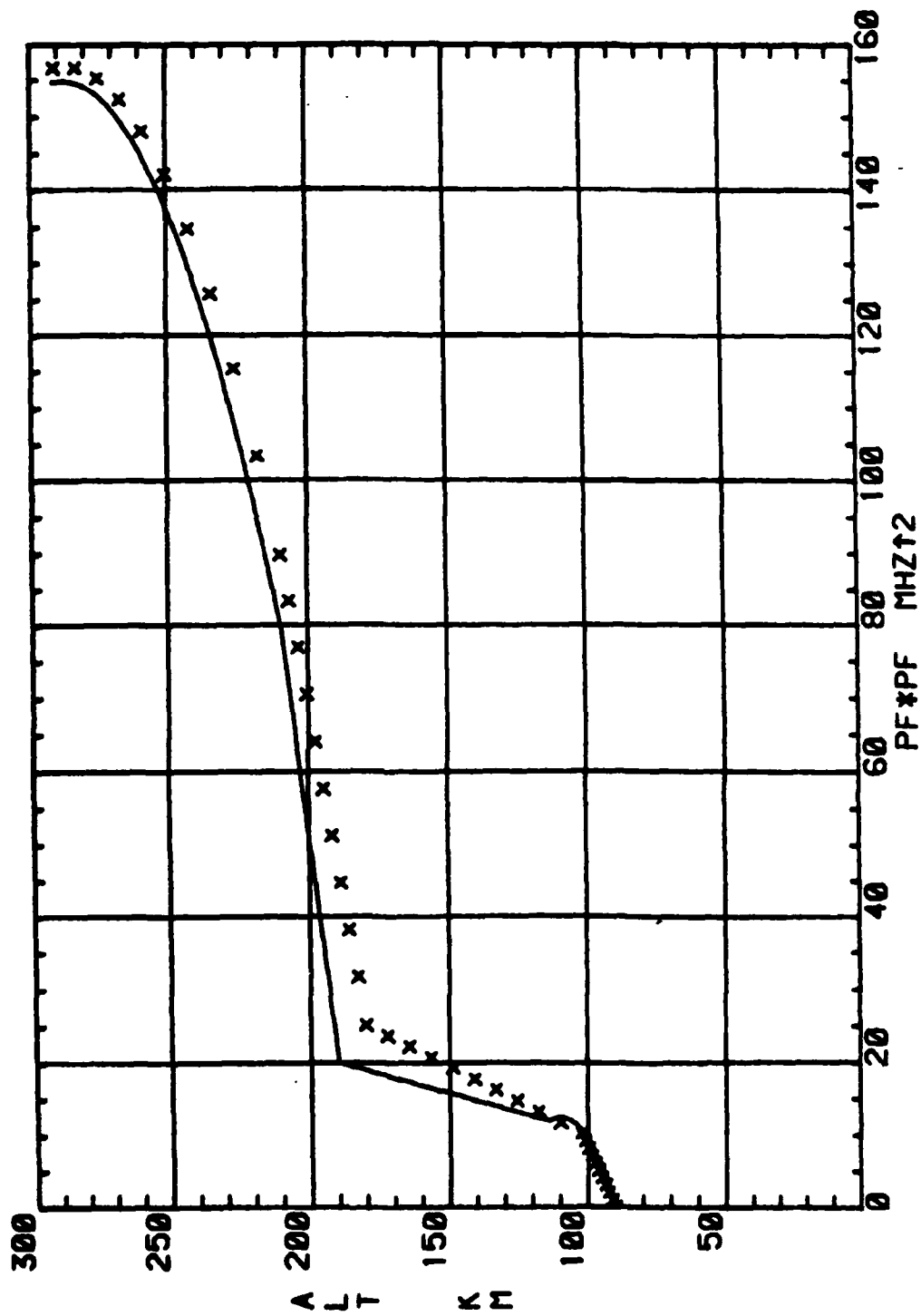
# IONOSPHERIC TRUE HEIGHT PROFILE

No. 3



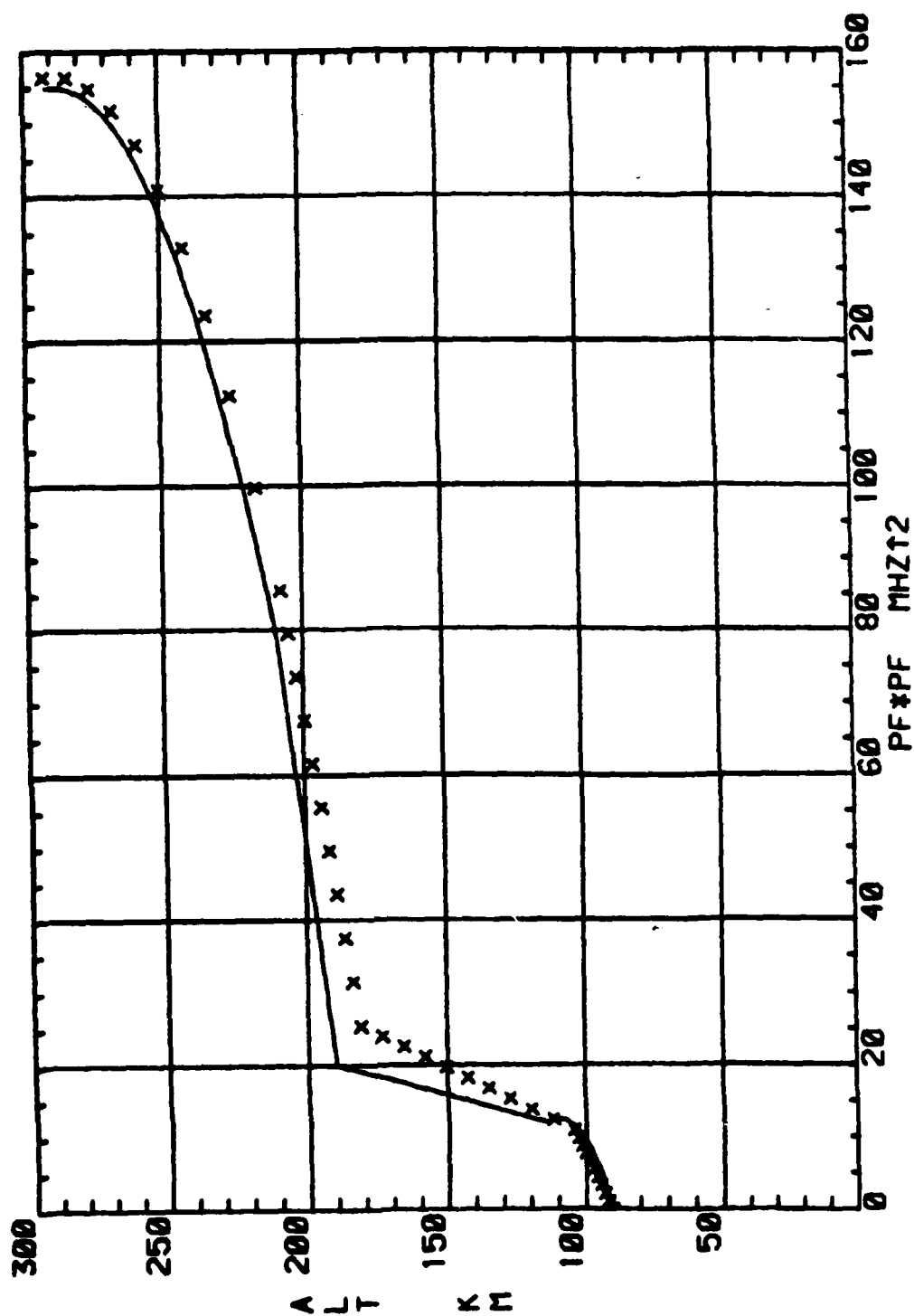
# IONOSPHERIC TRUE HEIGHT PROFILE

No. 4



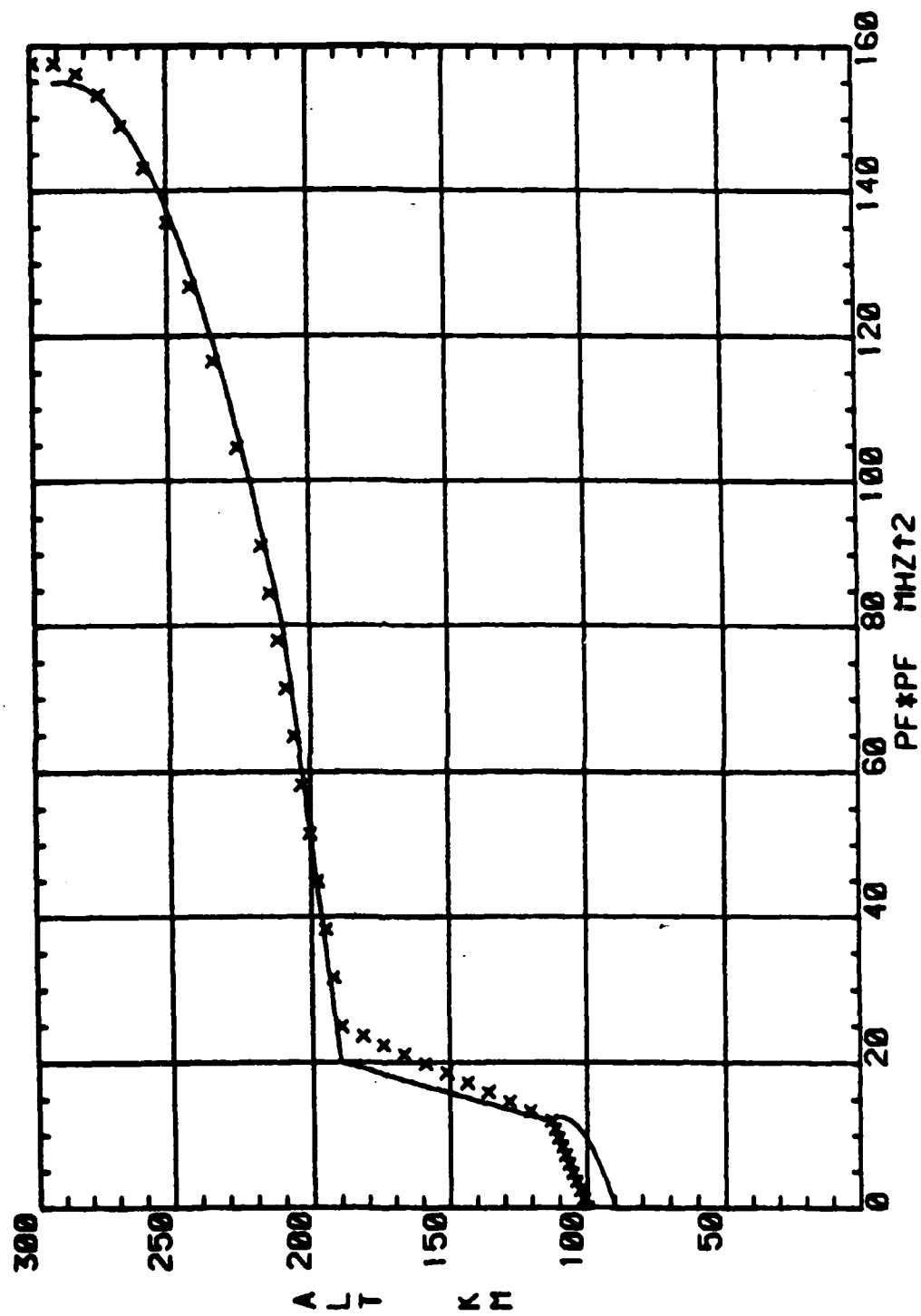
# IONOSPHERIC TRUE HEIGHT PROFILE

No. 5



# IONOSPHERIC TRUE HEIGHT PROFILE

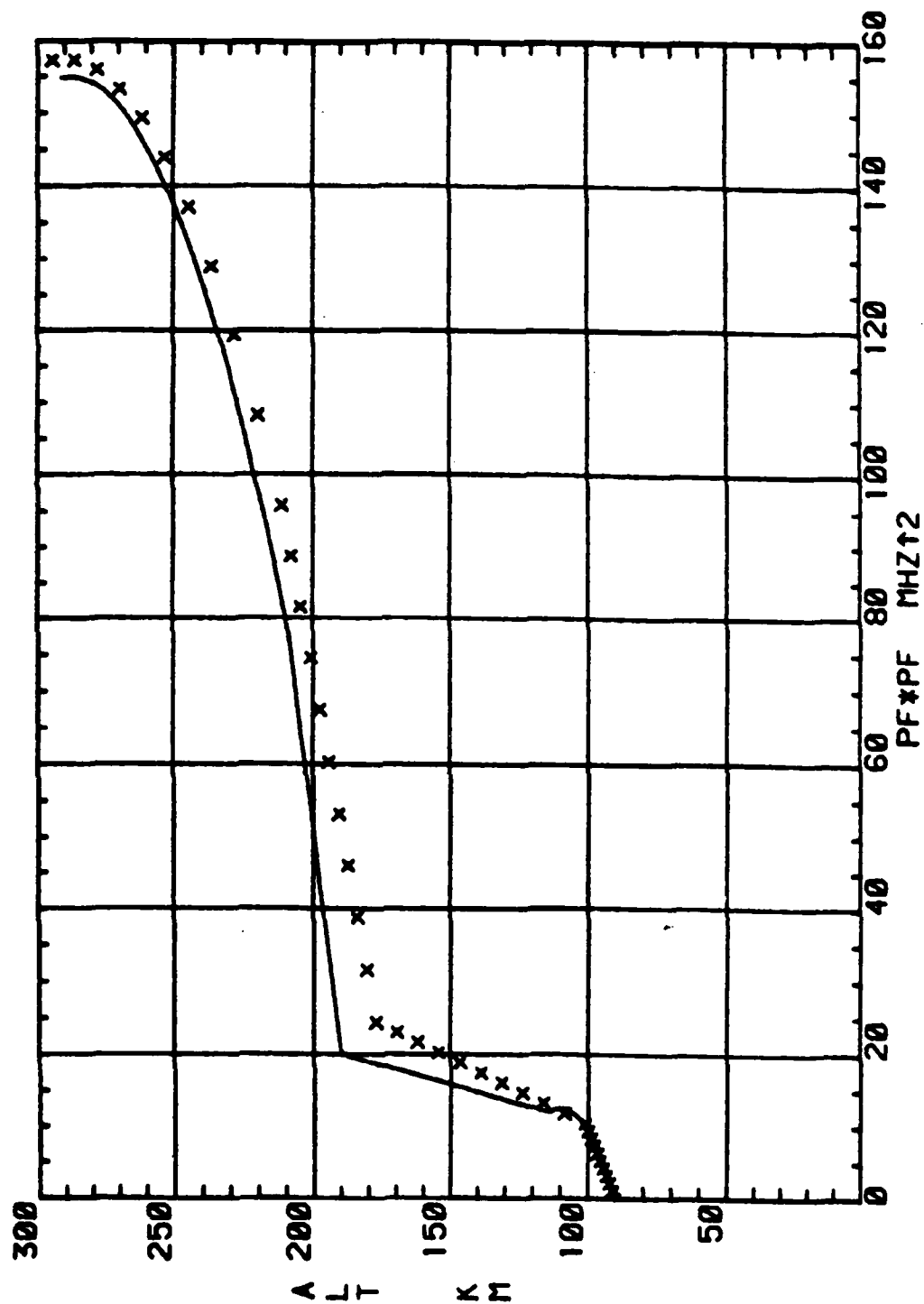
No. 6





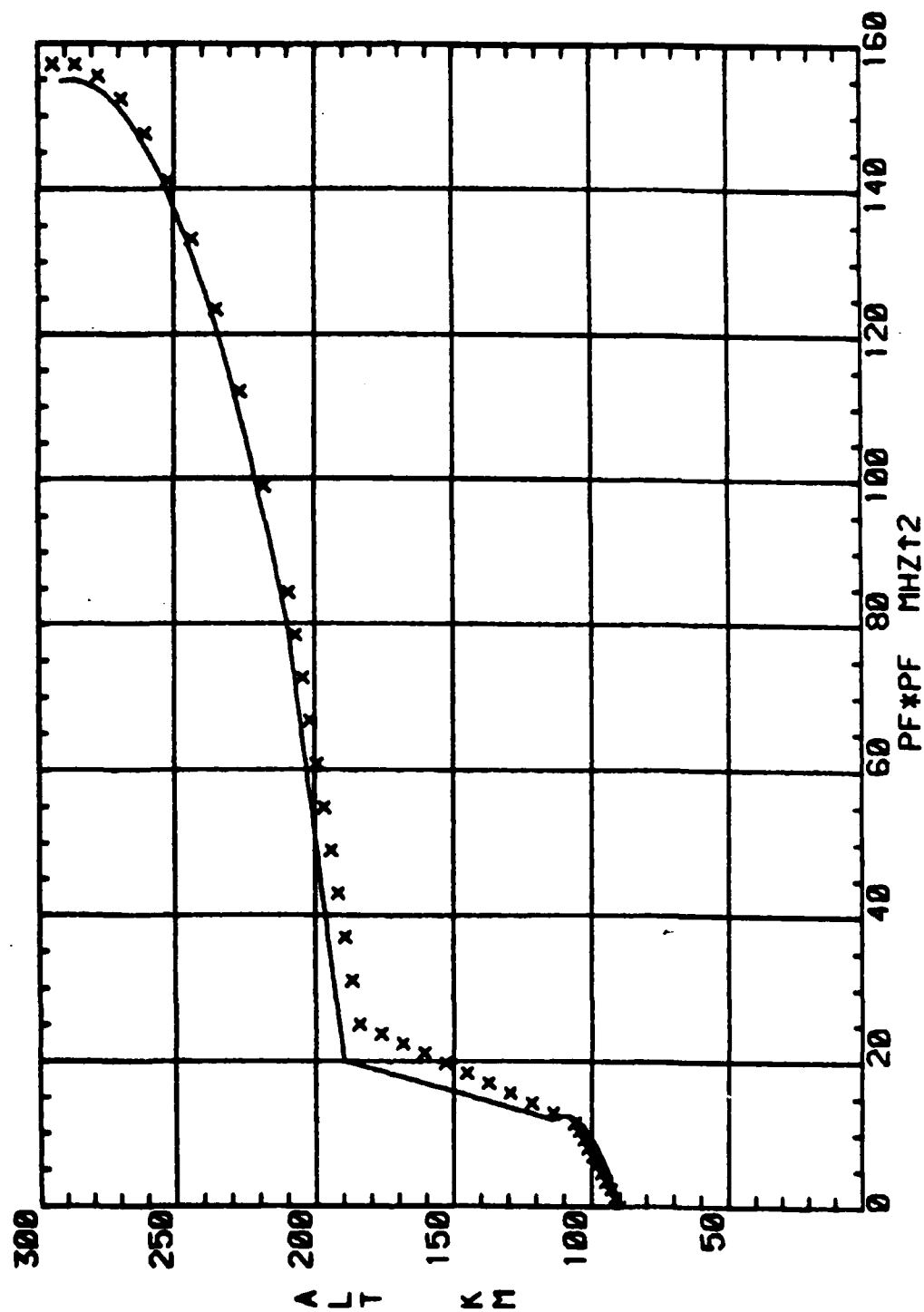
# IONOSPHERIC TRUE HEIGHT PROFILE

No. 7

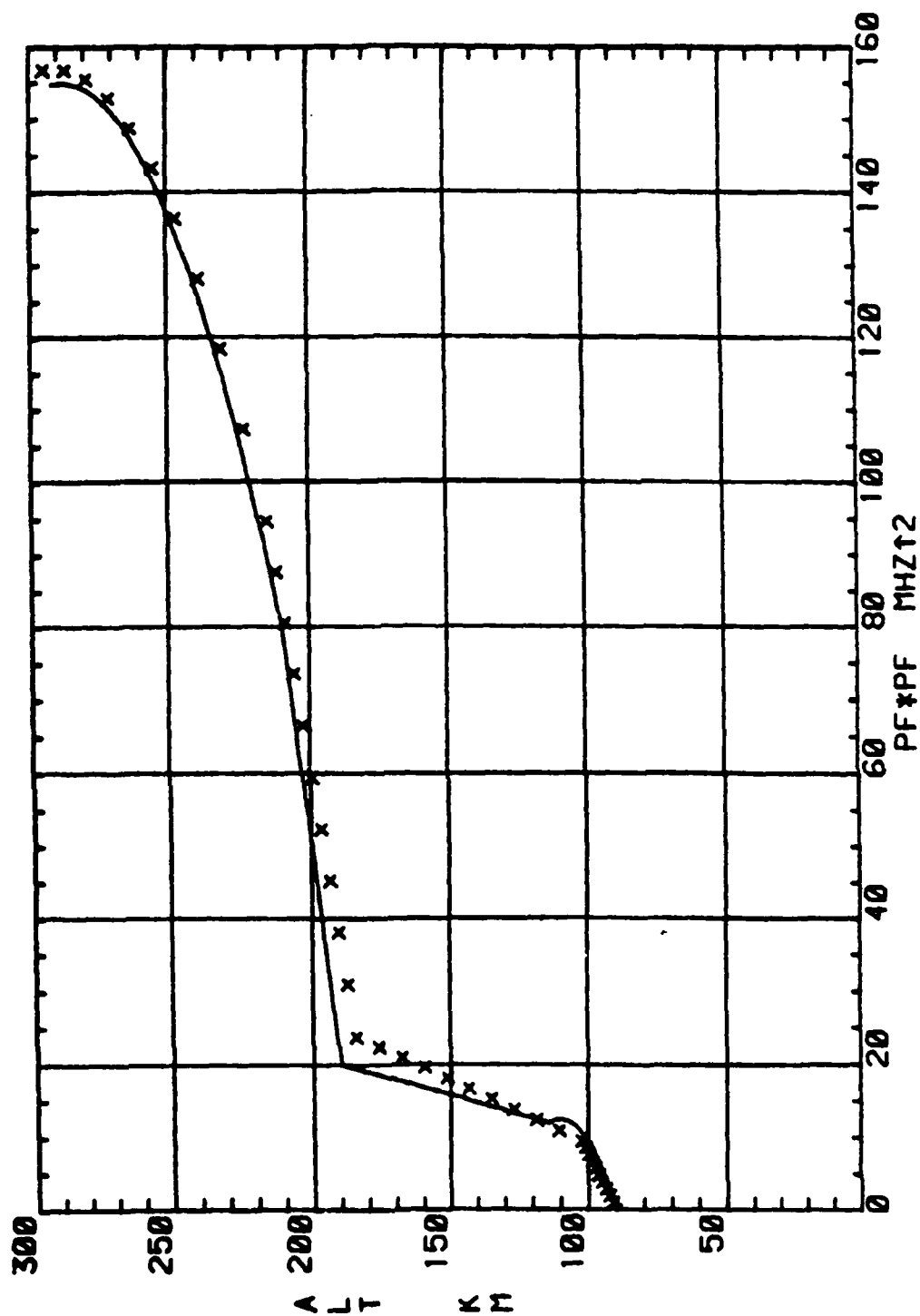


# IONOSPHERIC TRUE HEIGHT PROFILE

No. 8

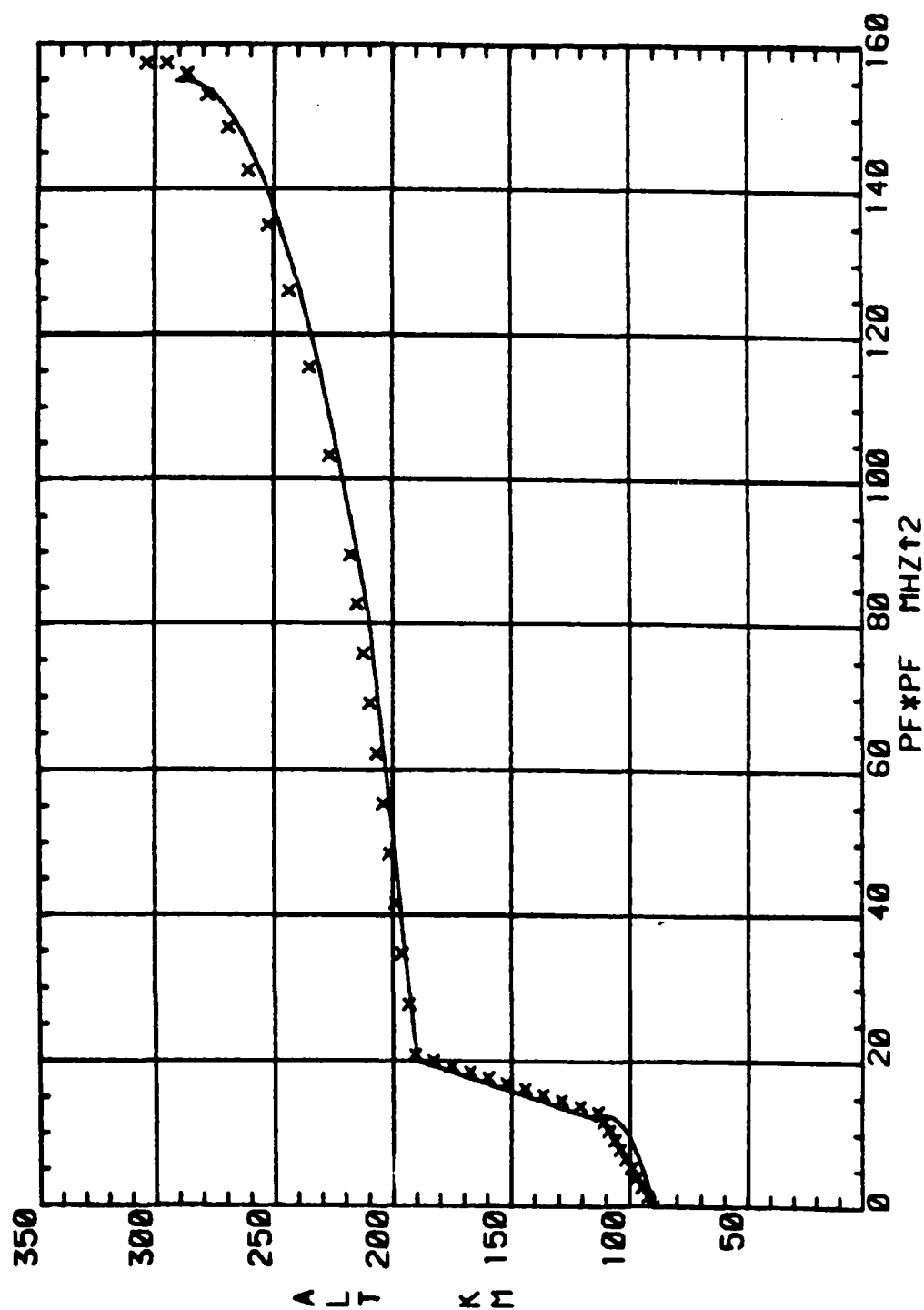


No. 9



# IONOSPHERIC TRUE HEIGHT PROFILE

No. 10



UNCLASSIFIED

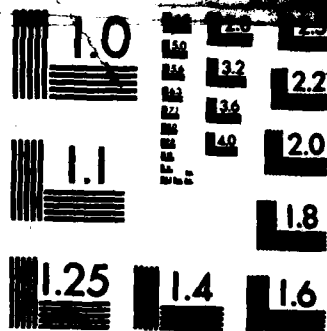
FROM OBLIQUE-INCIDENCE SOUNDERS (OIS) NAVAL RESEARCH LAB  
WASHINGTON DC M H REILLY ET AL. 24 JUN 85 NRL-MR-5586

NI

F/G 20/14

END

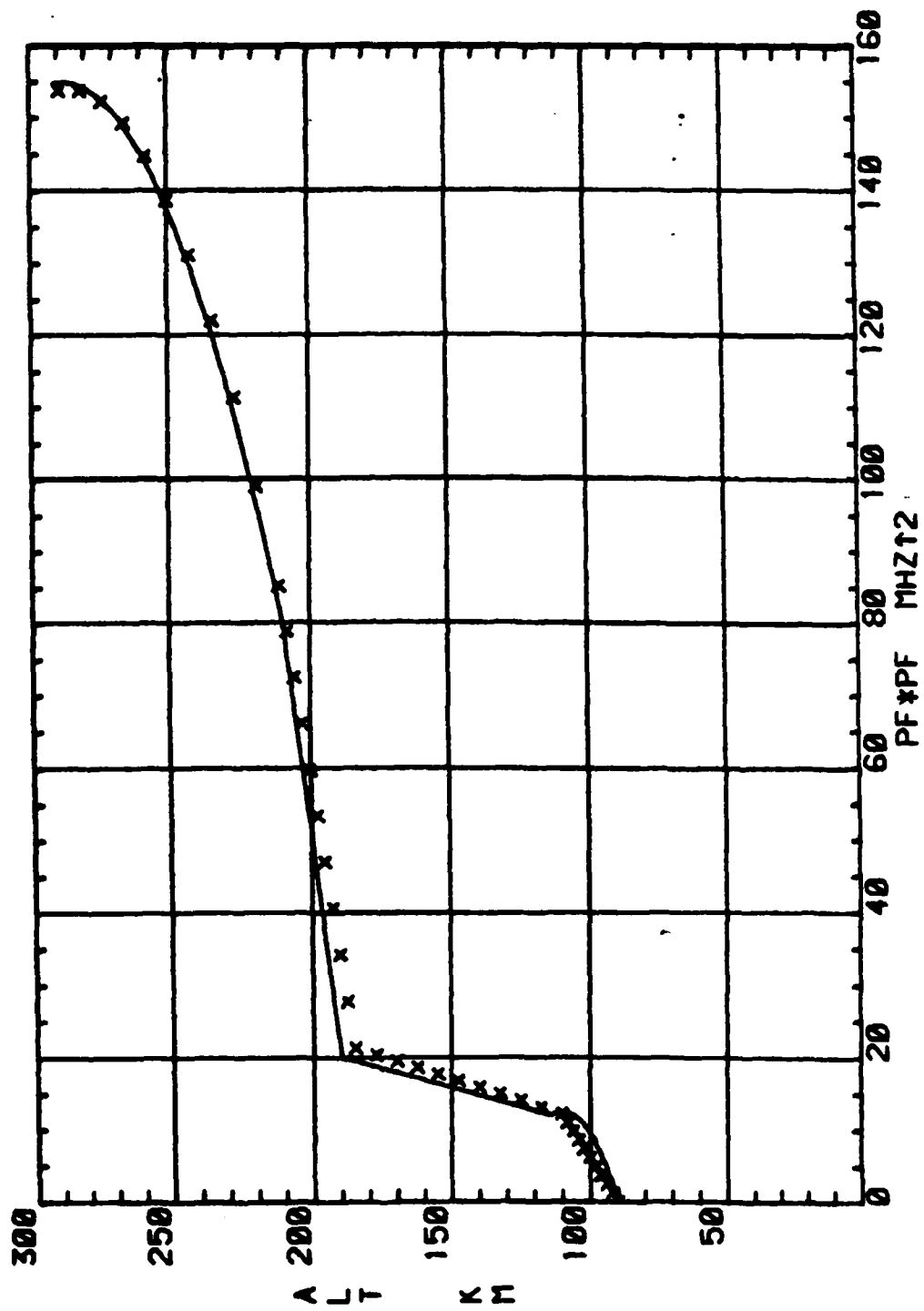
FILED



MICROCOPY RESOLUTION TEST CHART  
NATIONAL BUREAU OF STANDARDS-1963-A

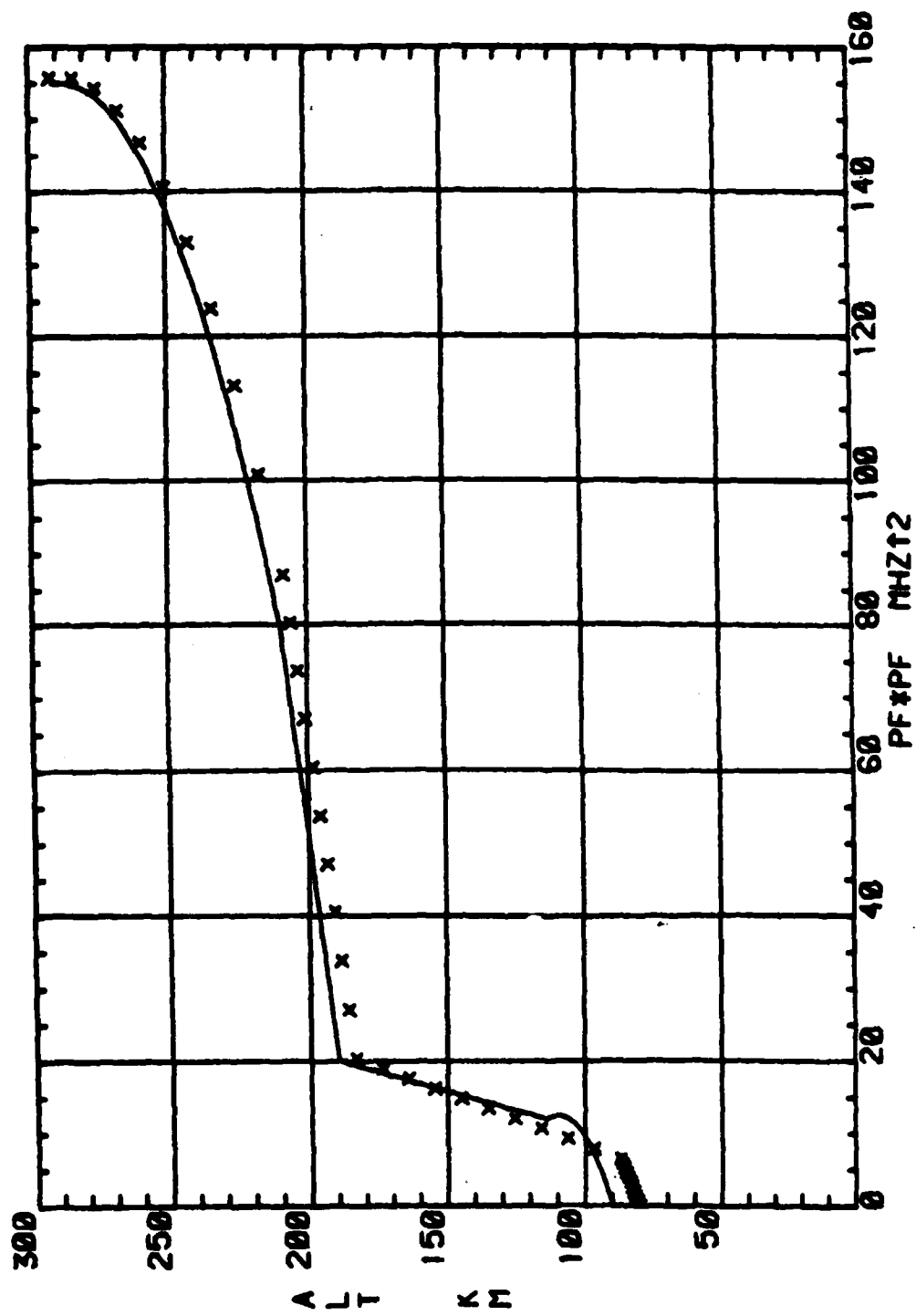
# IONOSPHERIC TRUE HEIGHT PROFILE

No. 11



# IONOSPHERIC TRUE HEIGHT PROFILE

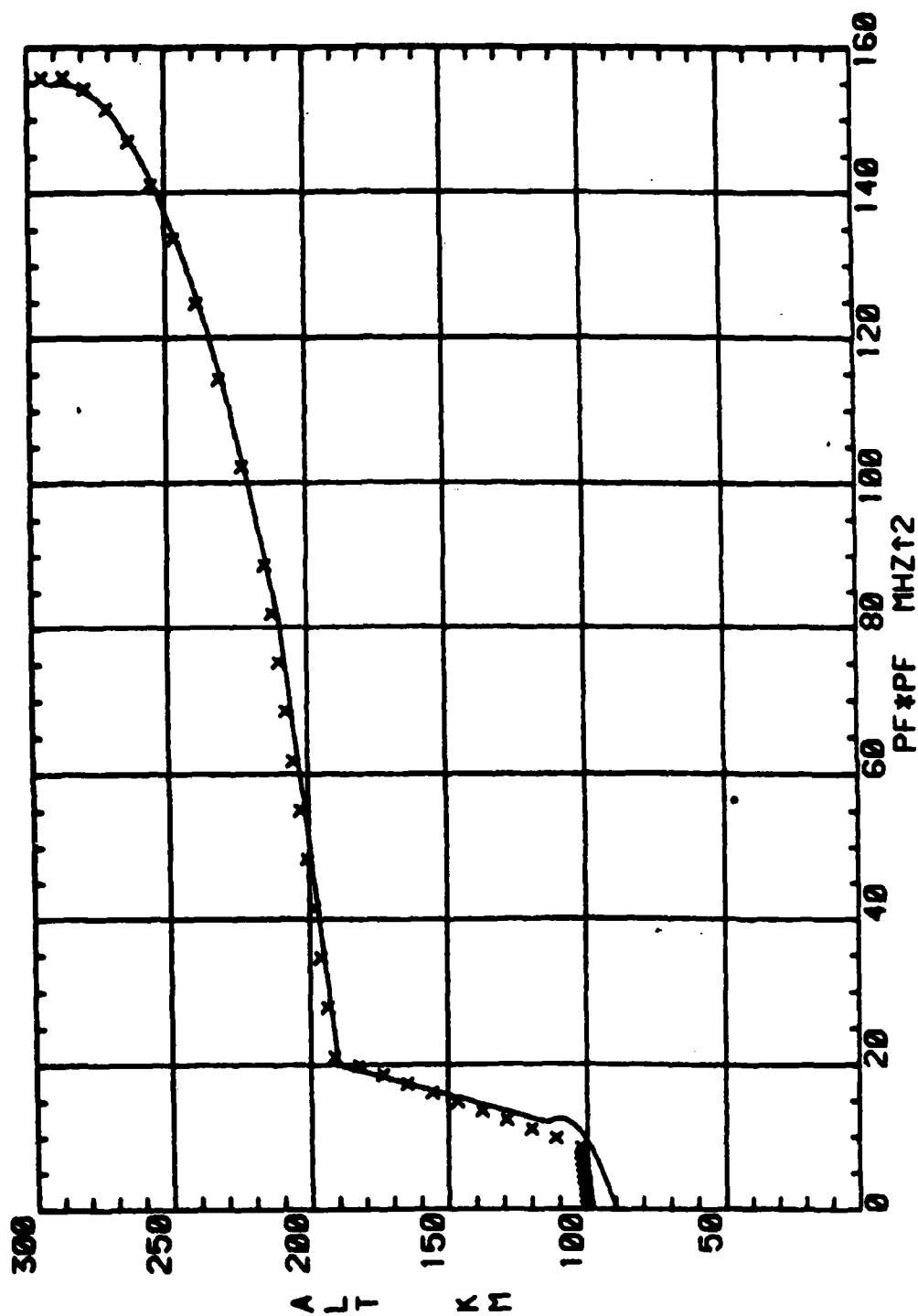
No. 12





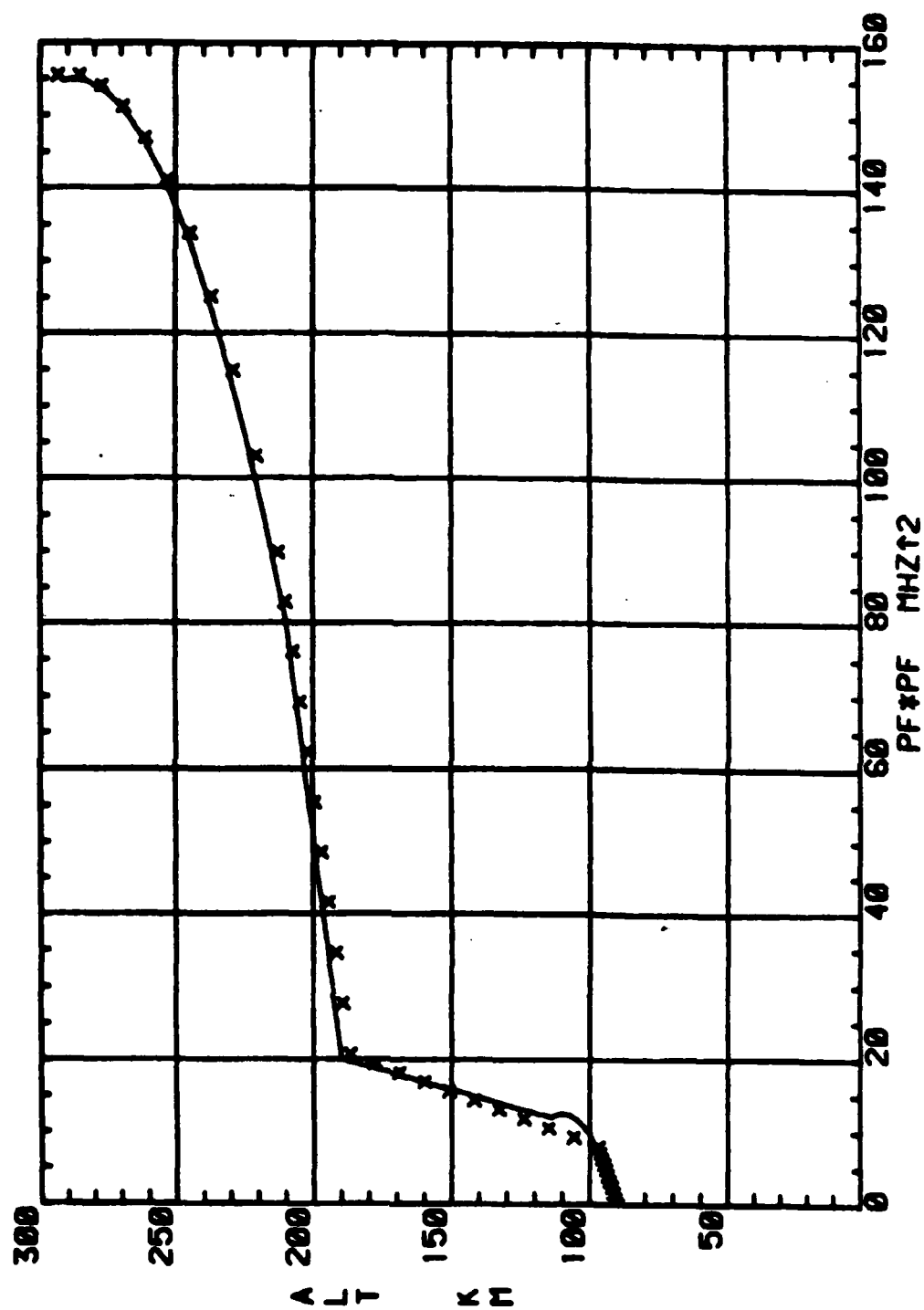
# IONOSPHERIC TRUE HEIGHT PROFILE

No. 13



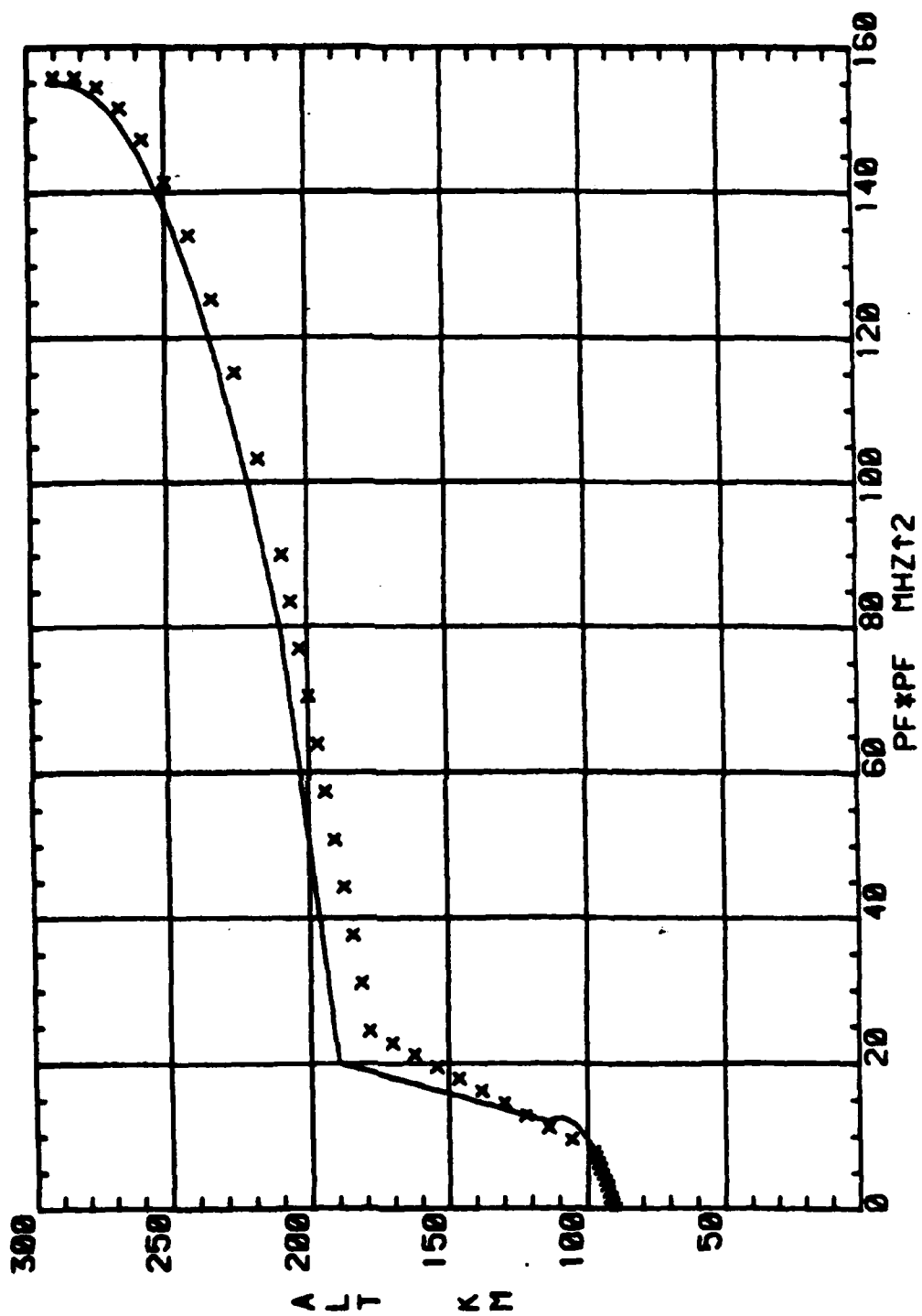
# IONOSPHERIC TRUE HEIGHT PROFILE

No. 14



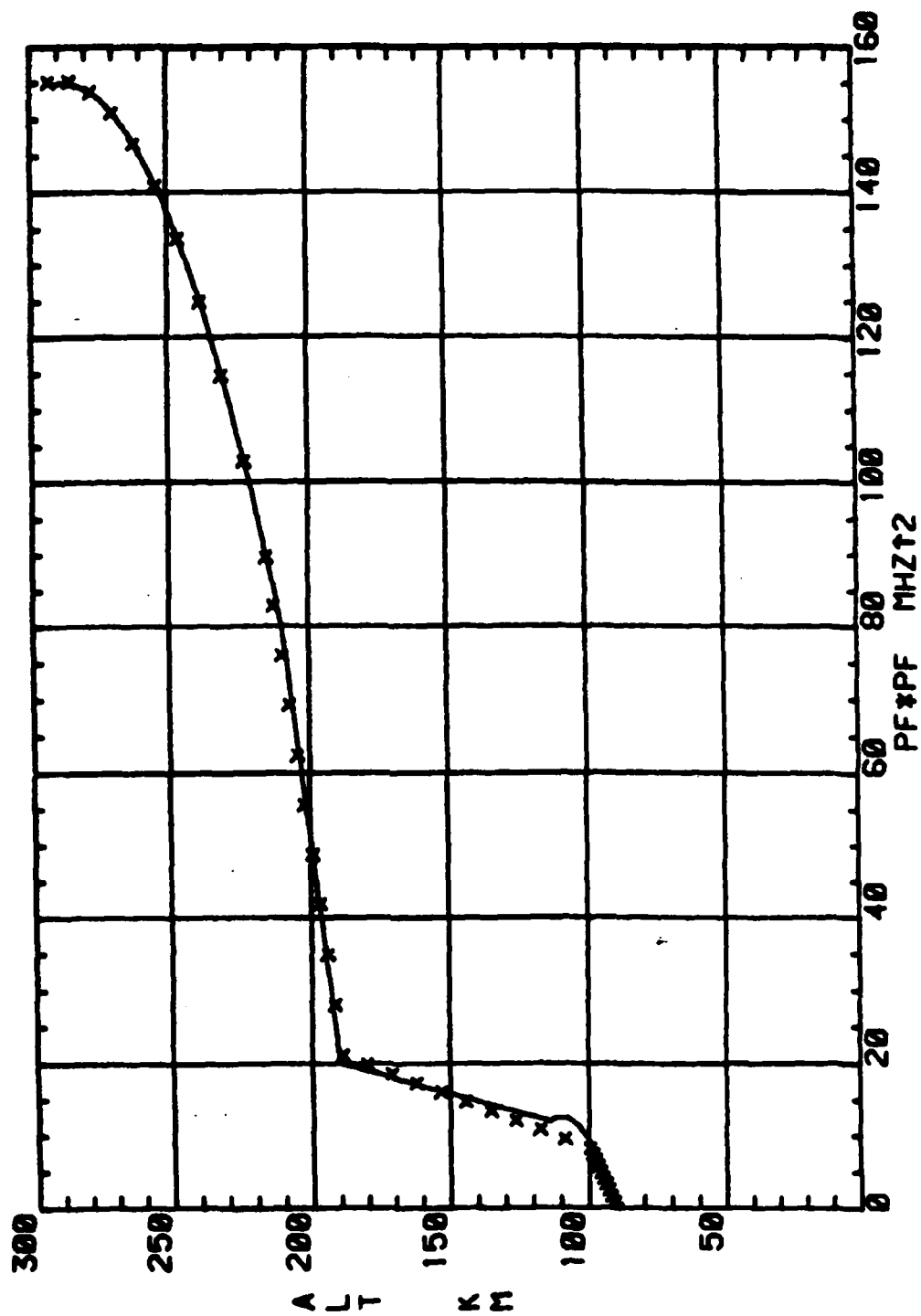
# IONOSPHERIC TRUE HEIGHT PROFILE

No. 15



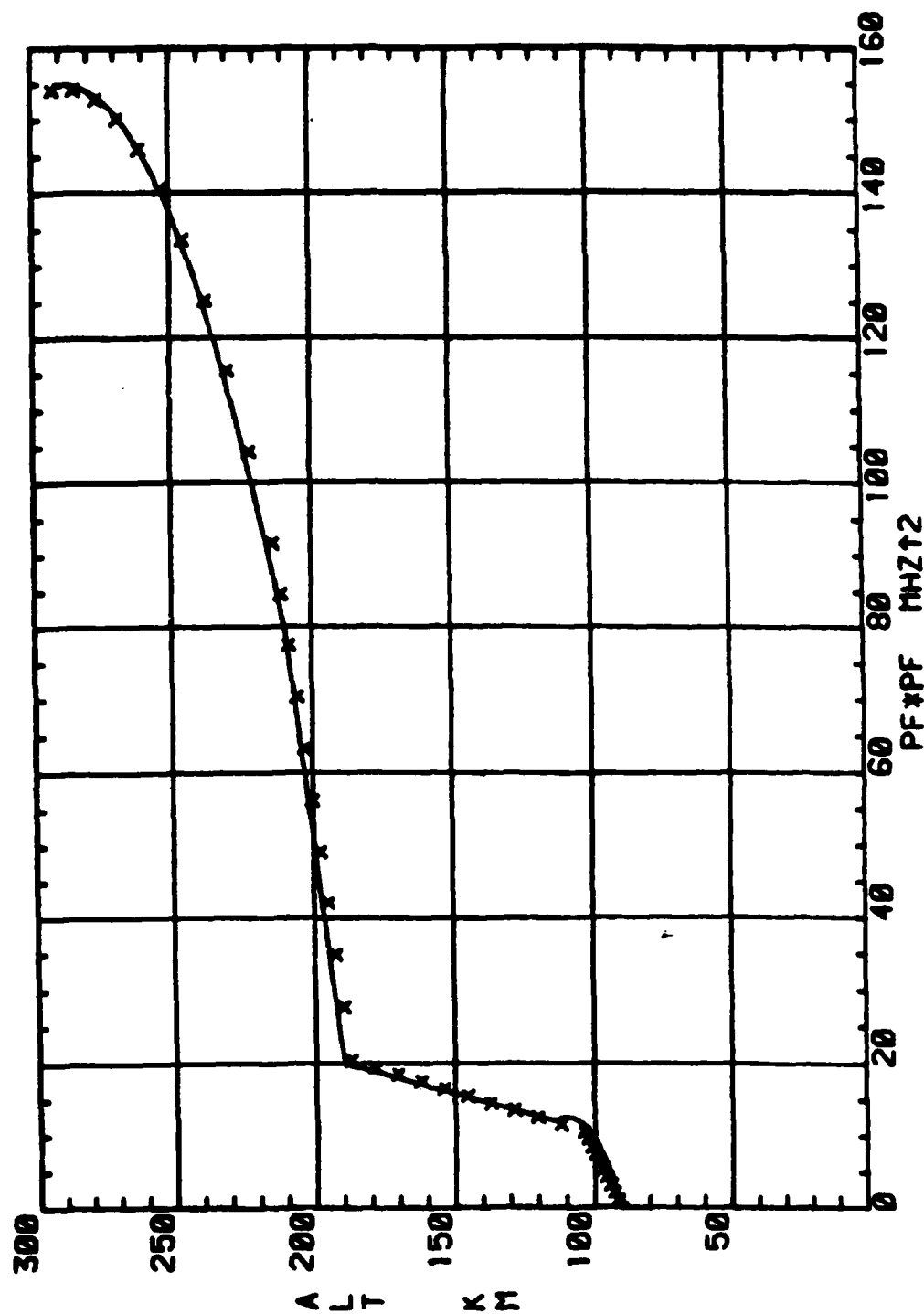
# IONOSPHERIC TRUE HEIGHT PROFILE

No. 16



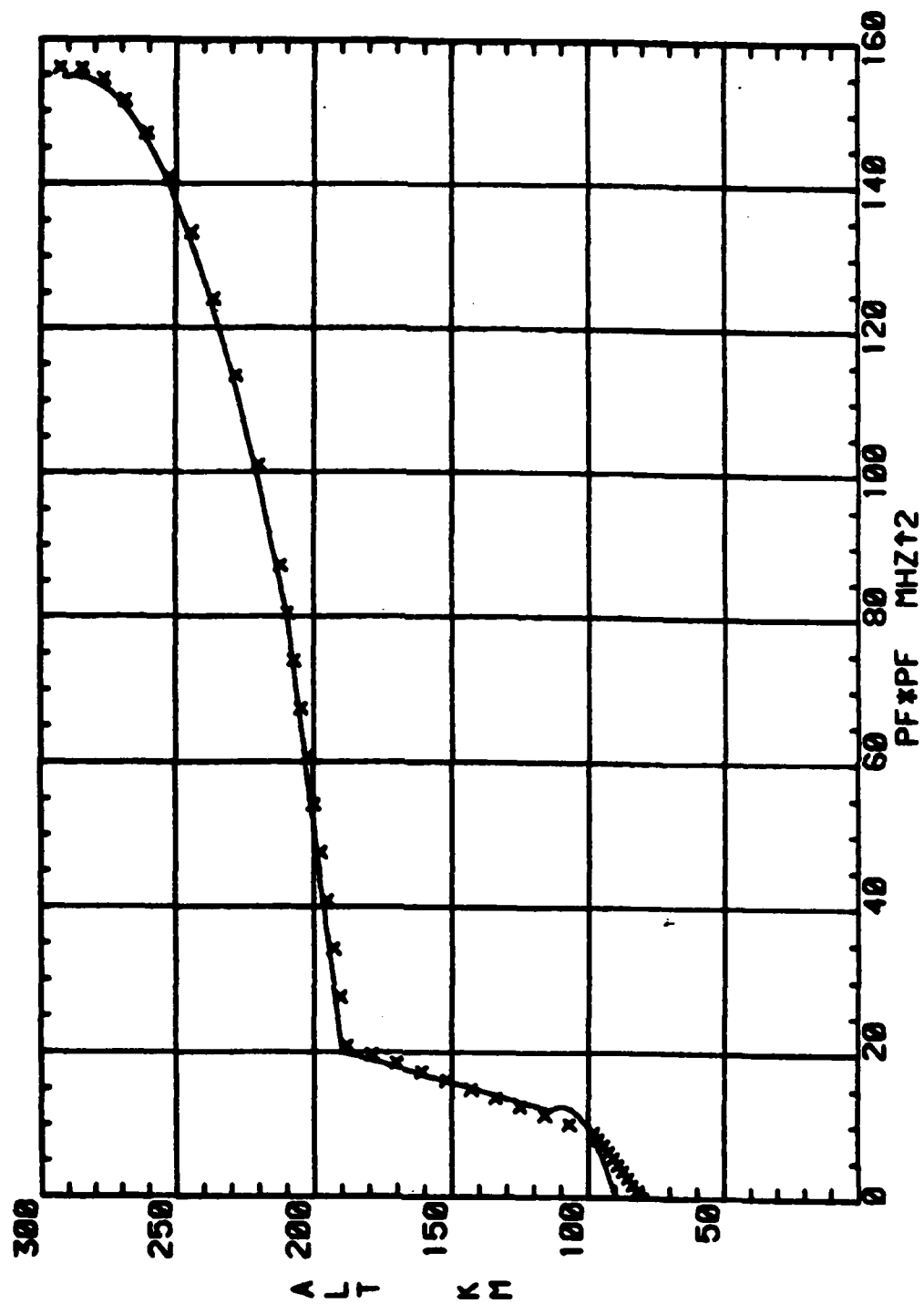
# IONOSPHERIC TRUE HEIGHT PROFILE

No. 18



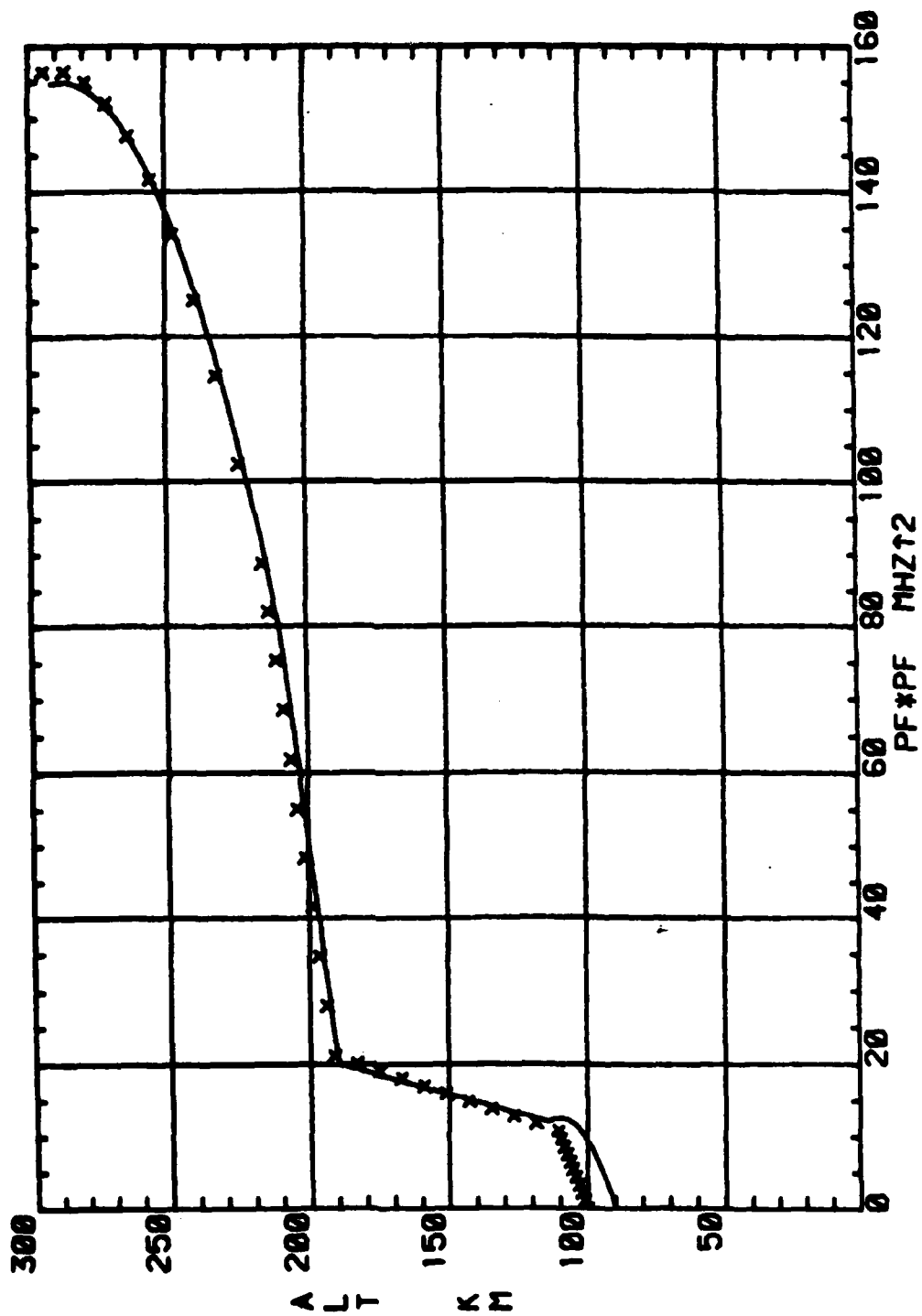
# IONOSPHERIC TRUE HEIGHT PROFILE

06-17



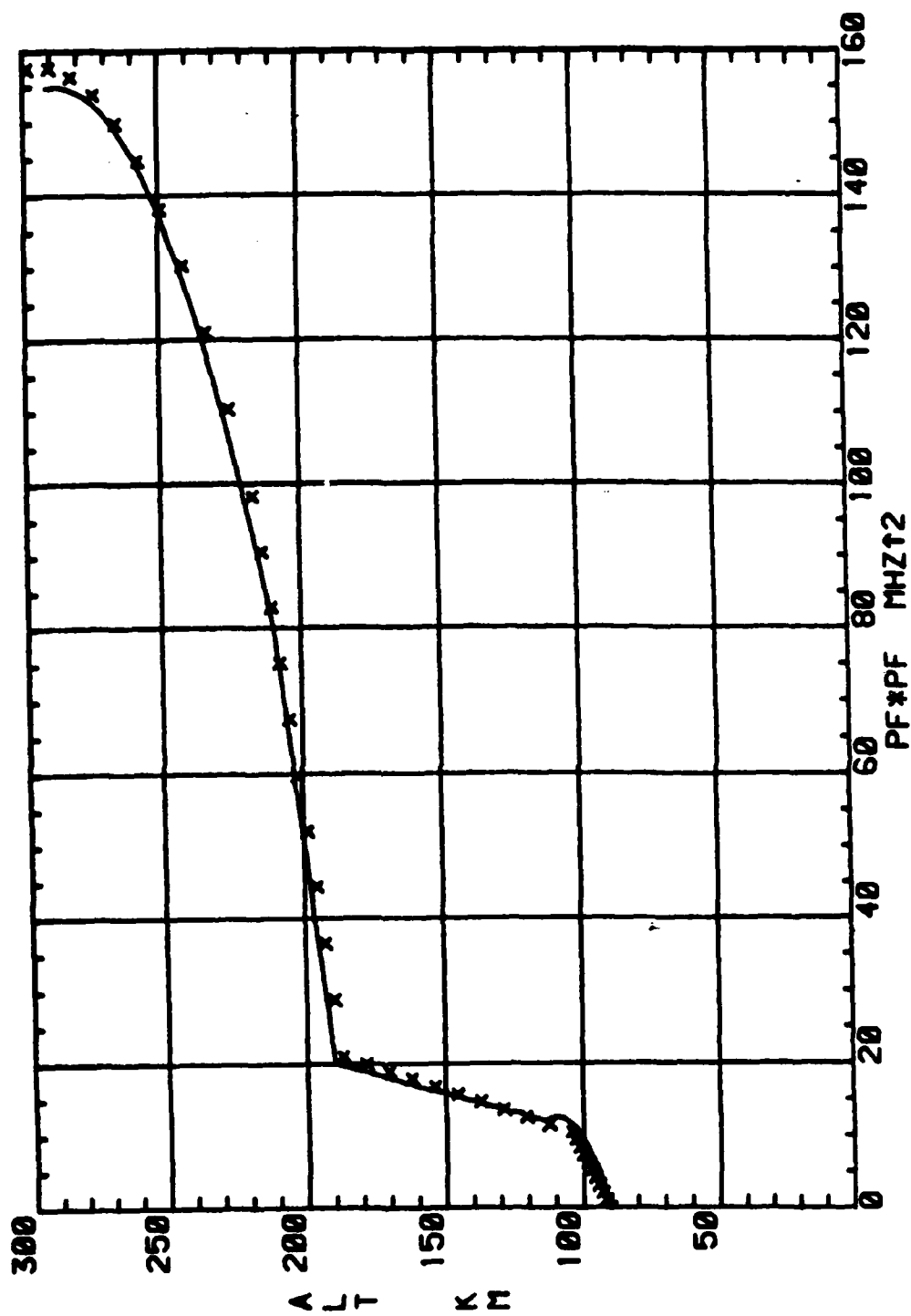
# IONOSPHERIC TRUE HEIGHT PROFILE

No. 20



# IONOSPHERIC TRUE HEIGHT PROFILE

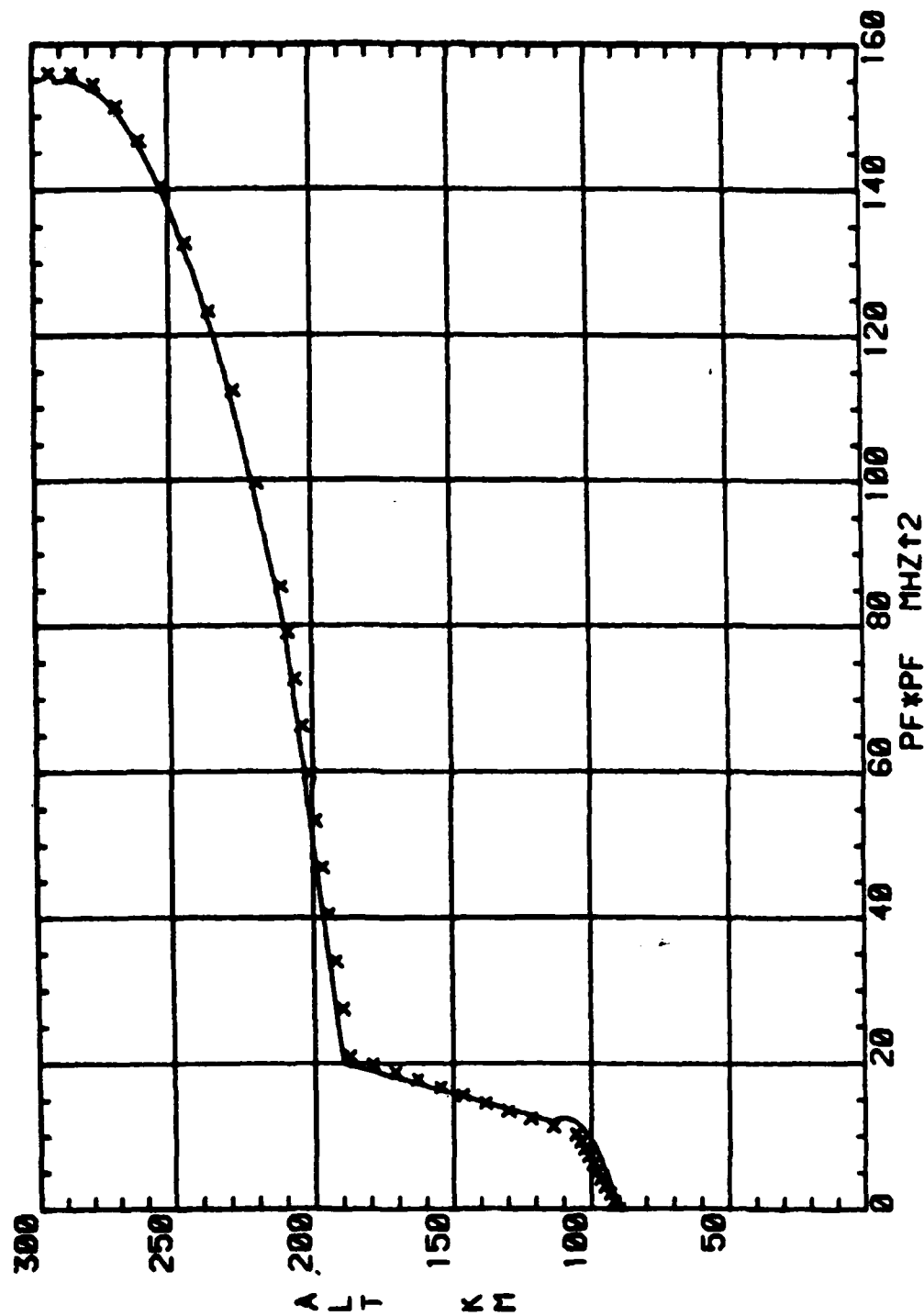
No. 21





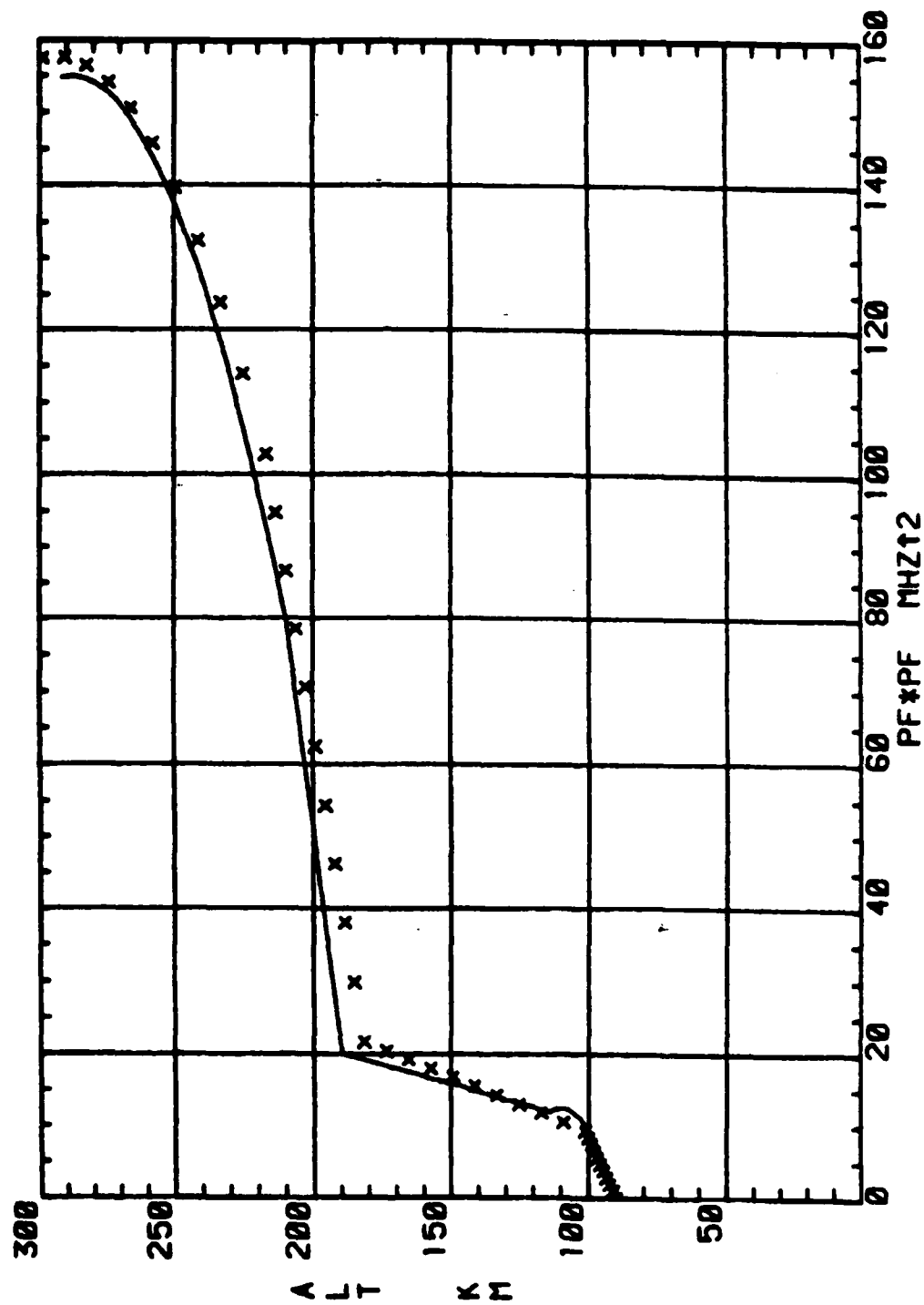
# IONOSPHERIC TRUE HEIGHT PROFILE

No. 22



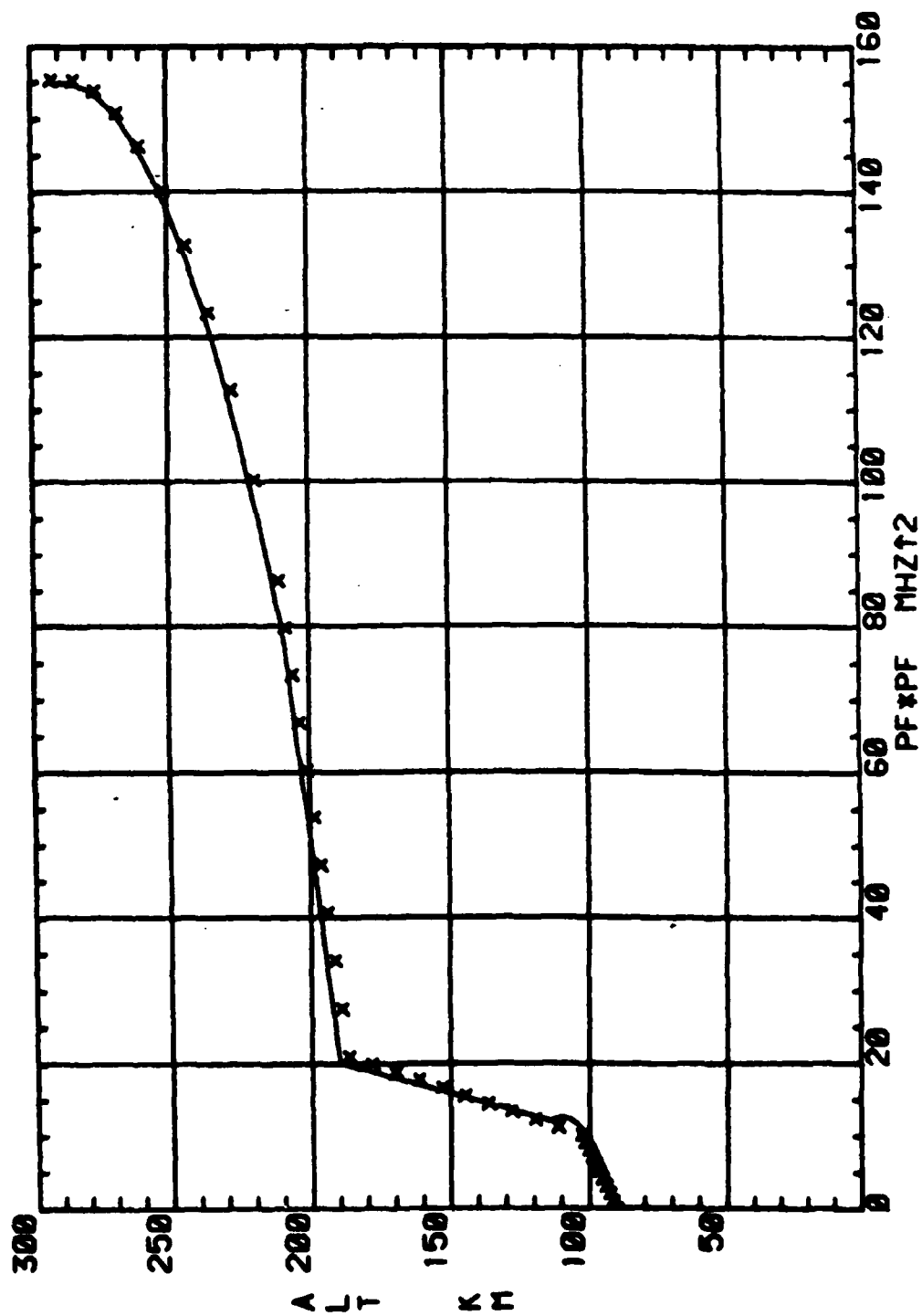
# IONOSPHERIC TRUE HEIGHT PROFILE

No. 23



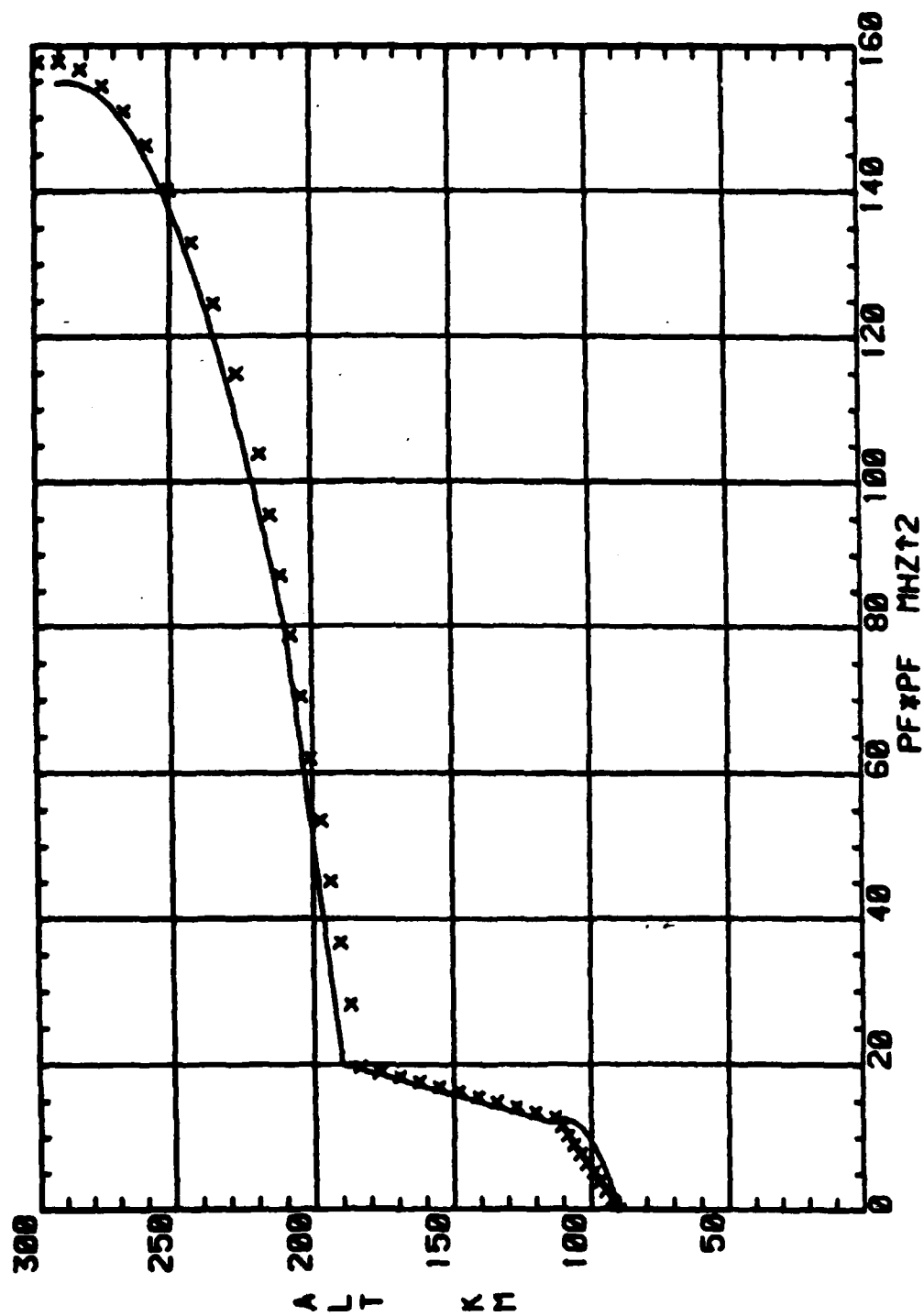
# IONOSPHERIC TRUE HEIGHT PROFILE

No. 24



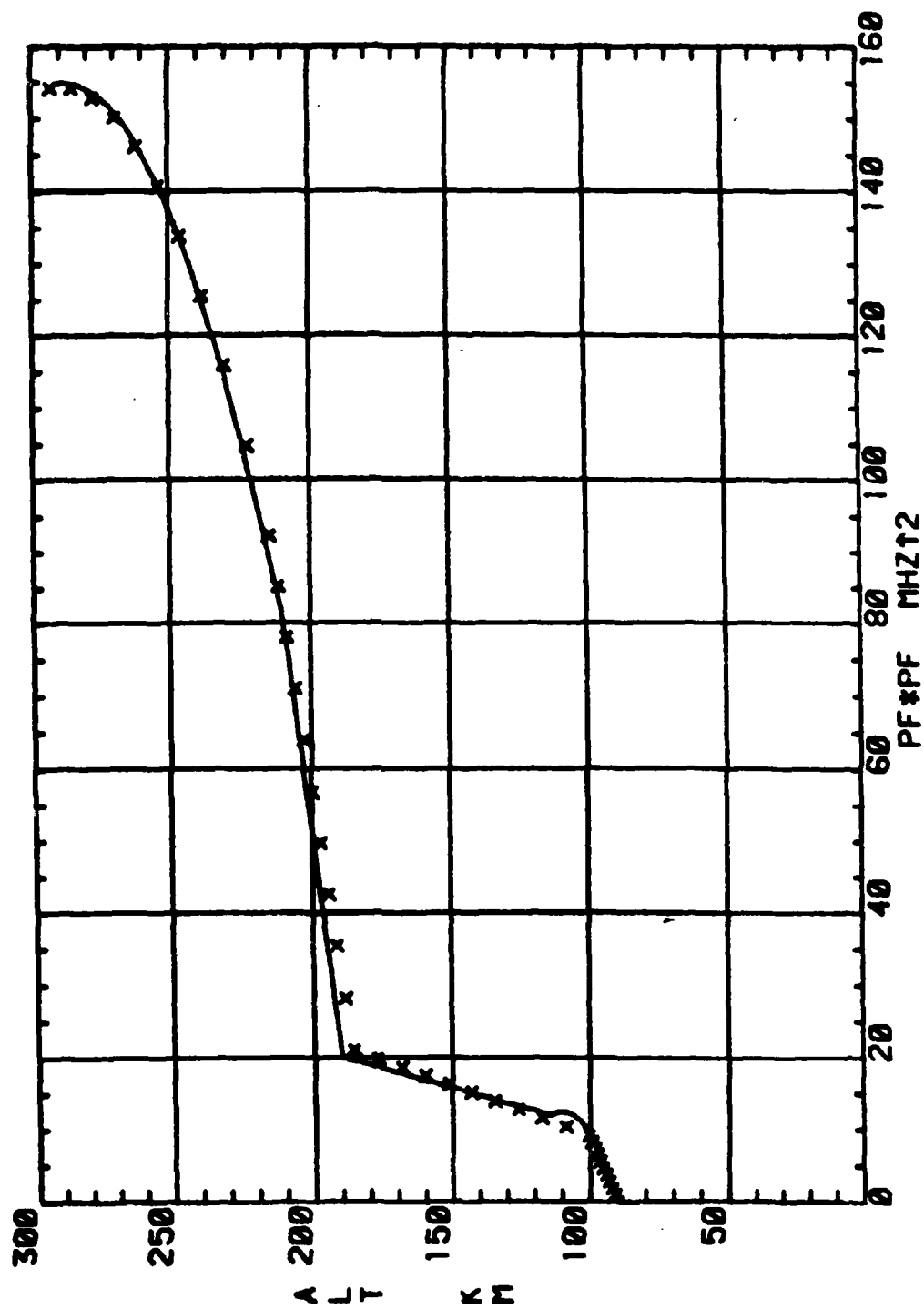
# IONOSPHERIC TRUE HEIGHT PROFILE

No. 25



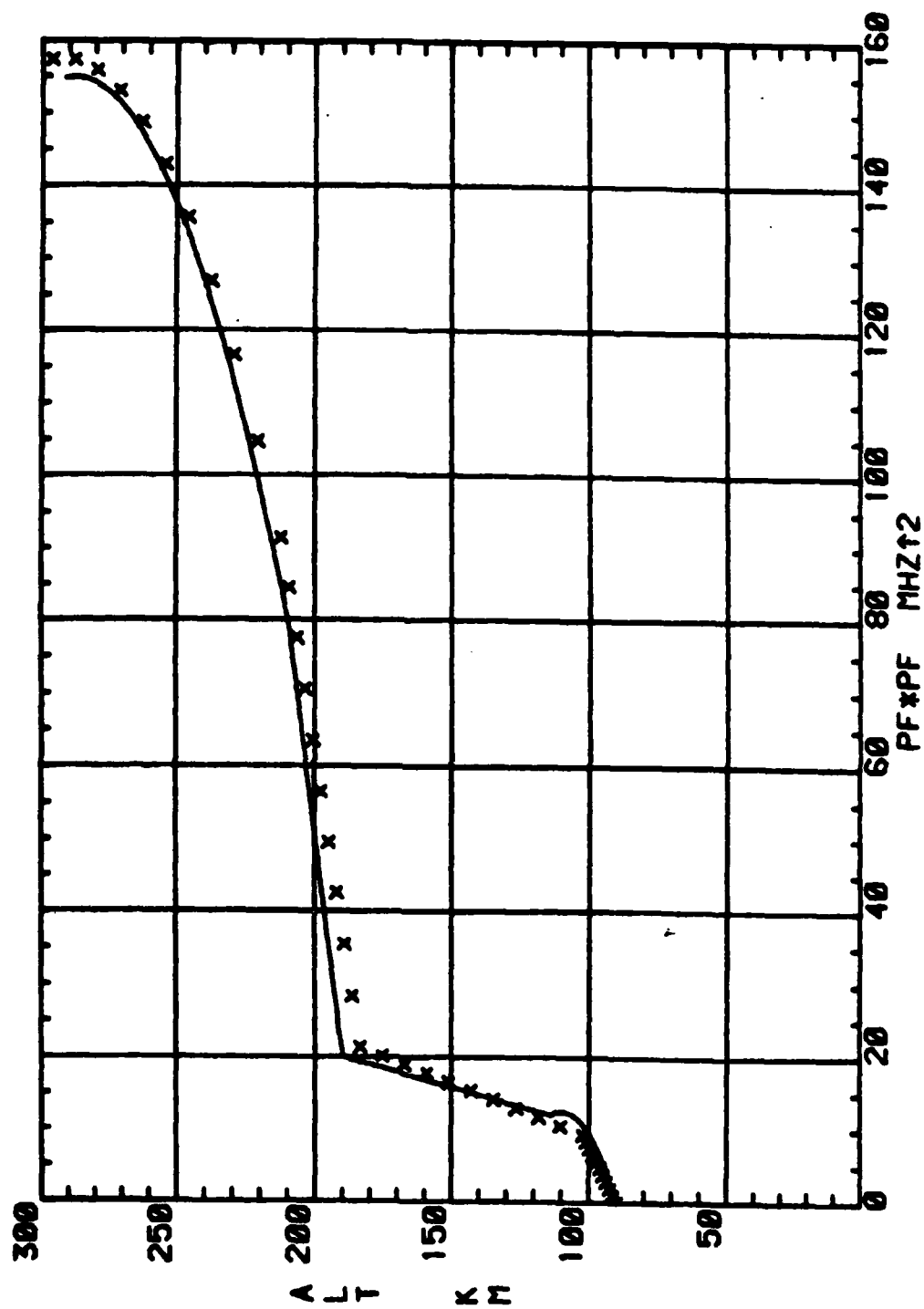
# IONOSPHERIC TRUE HEIGHT PROFILE

No. 26



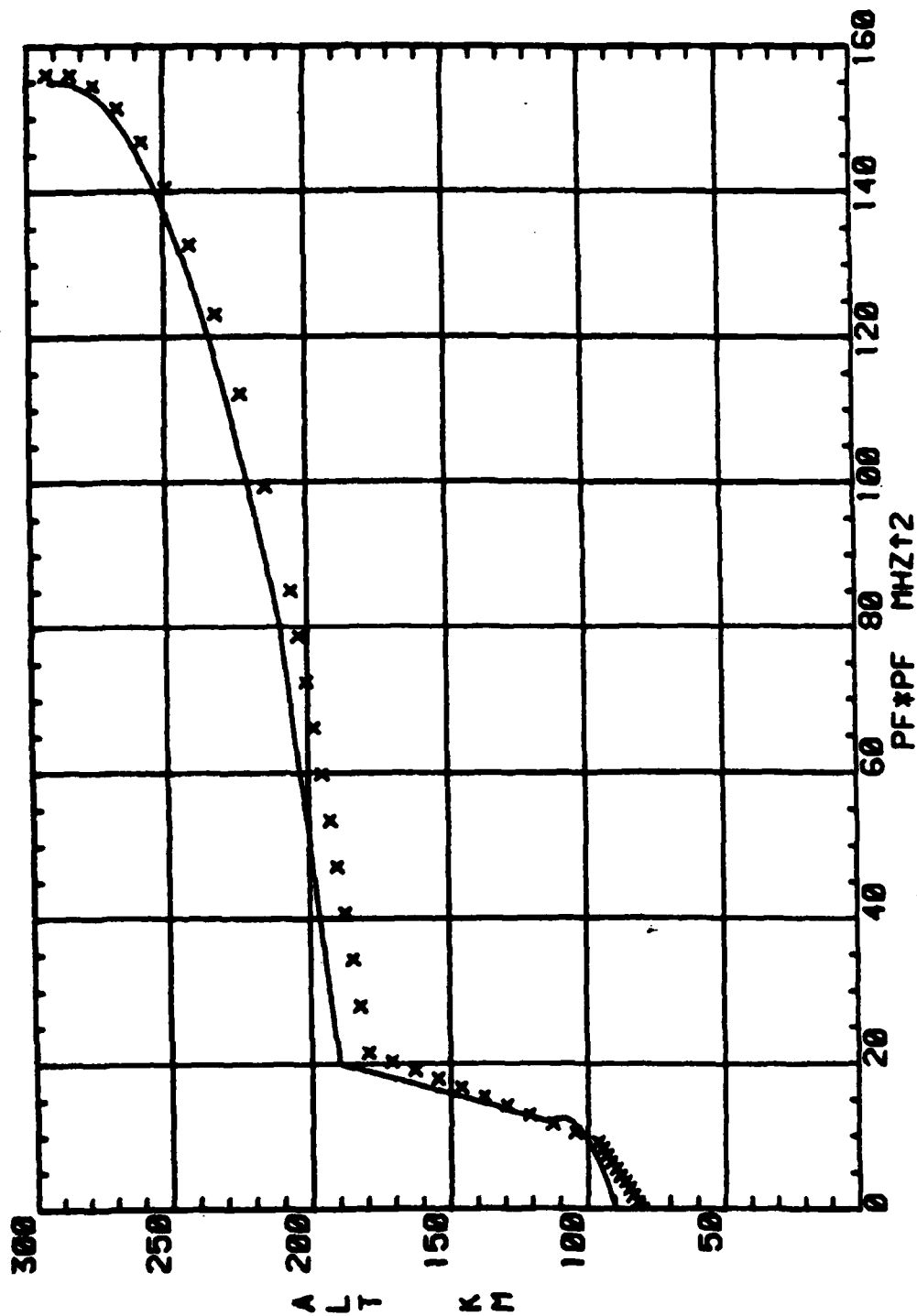
# IONOSPHERIC TRUE HEIGHT PROFILE

No. 2.7



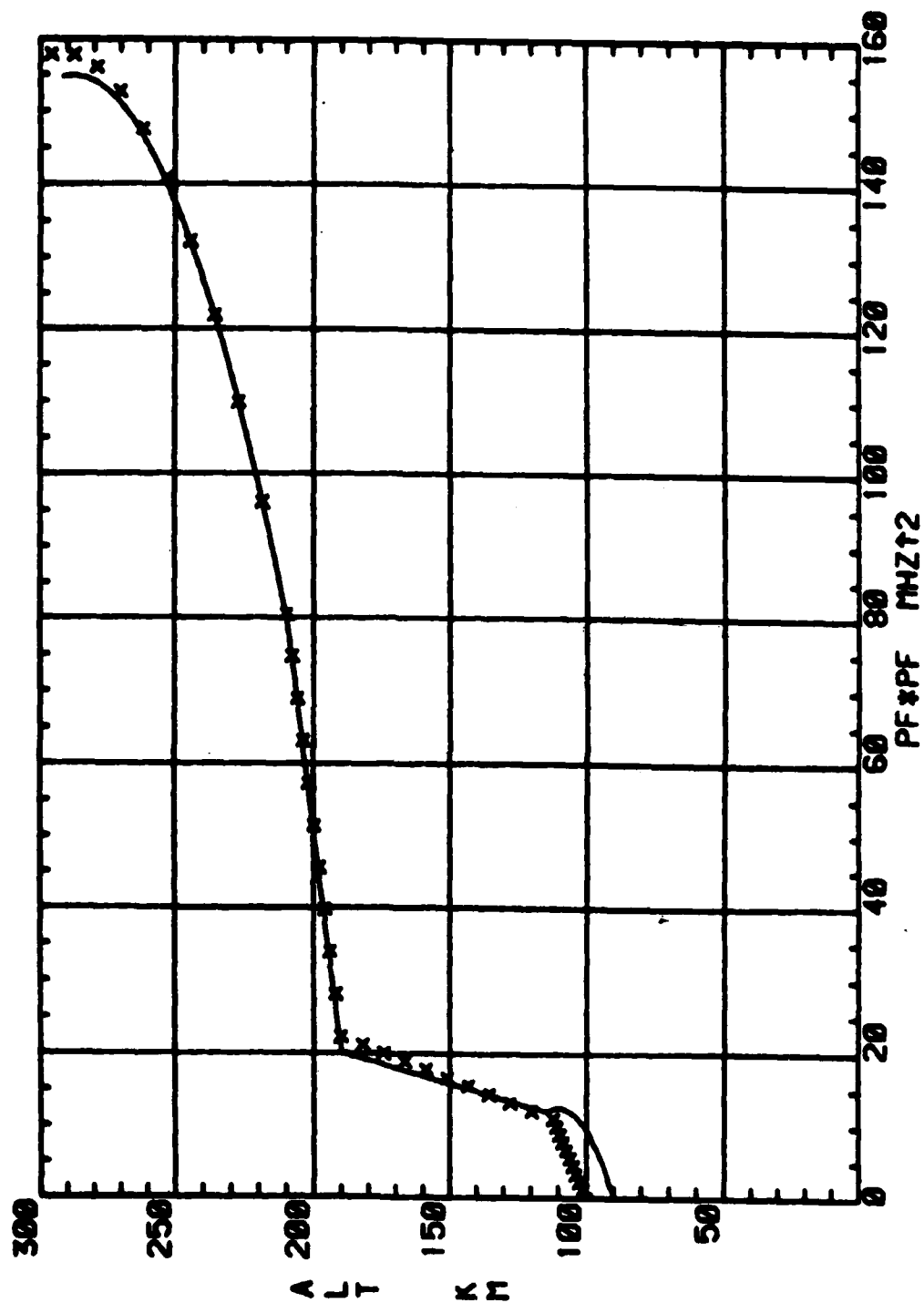
# IONOSPHERIC TRUE HEIGHT PROFILE

No. 28



# IONOSPHERIC TRUE HEIGHT PROFILE

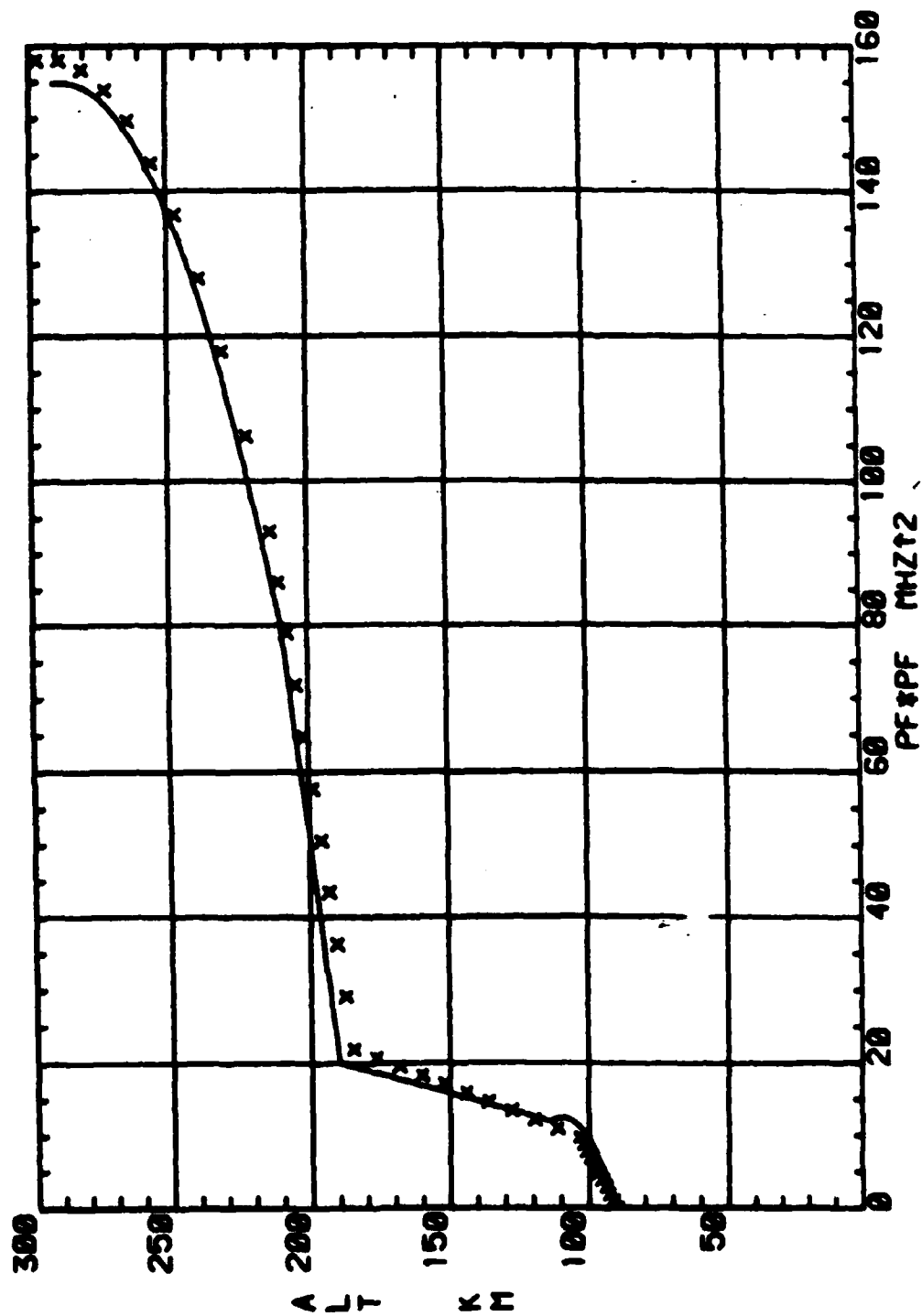
No. 29





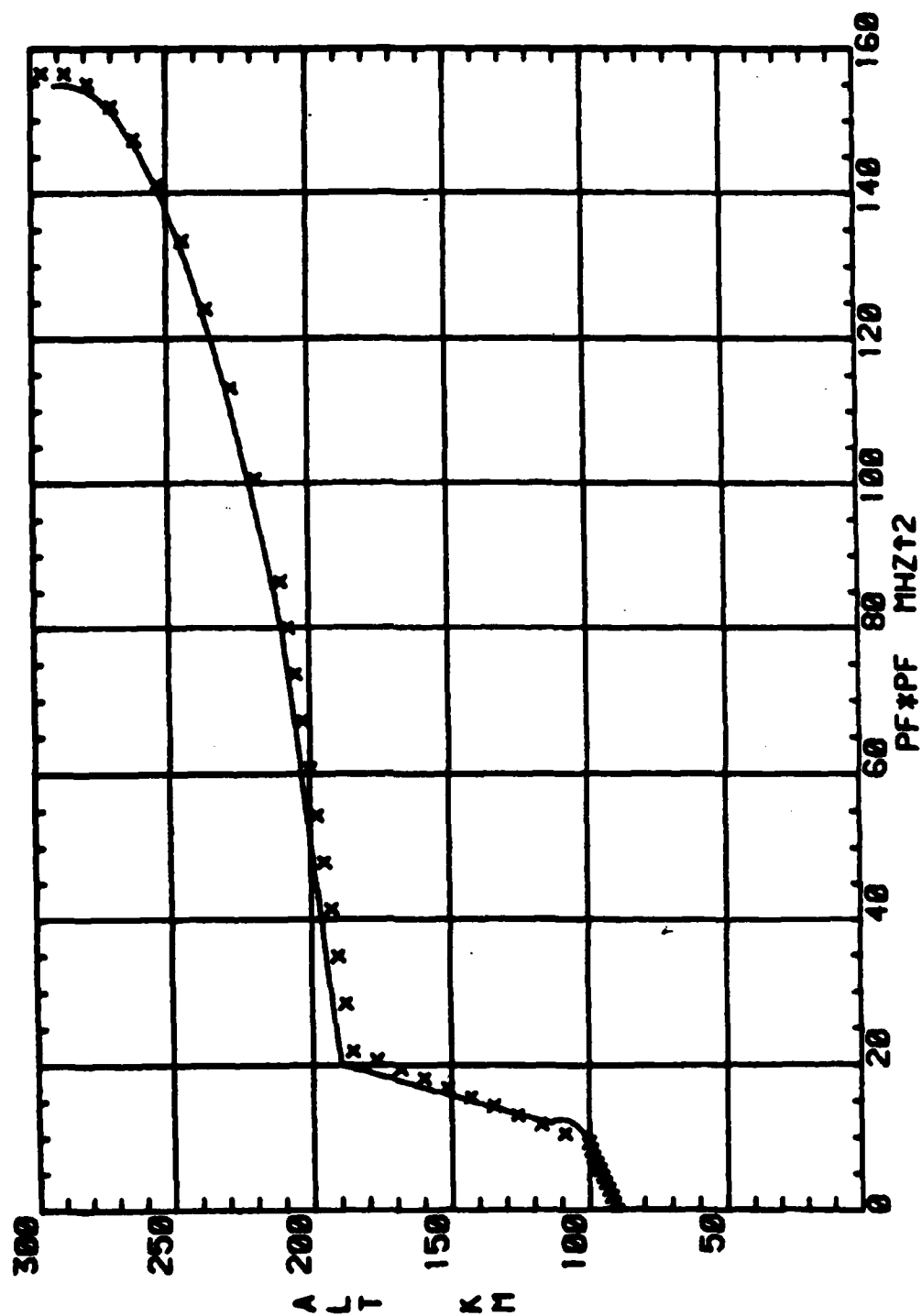
# IONOSPHERIC TRUE HEIGHT PROFILE

No. 30



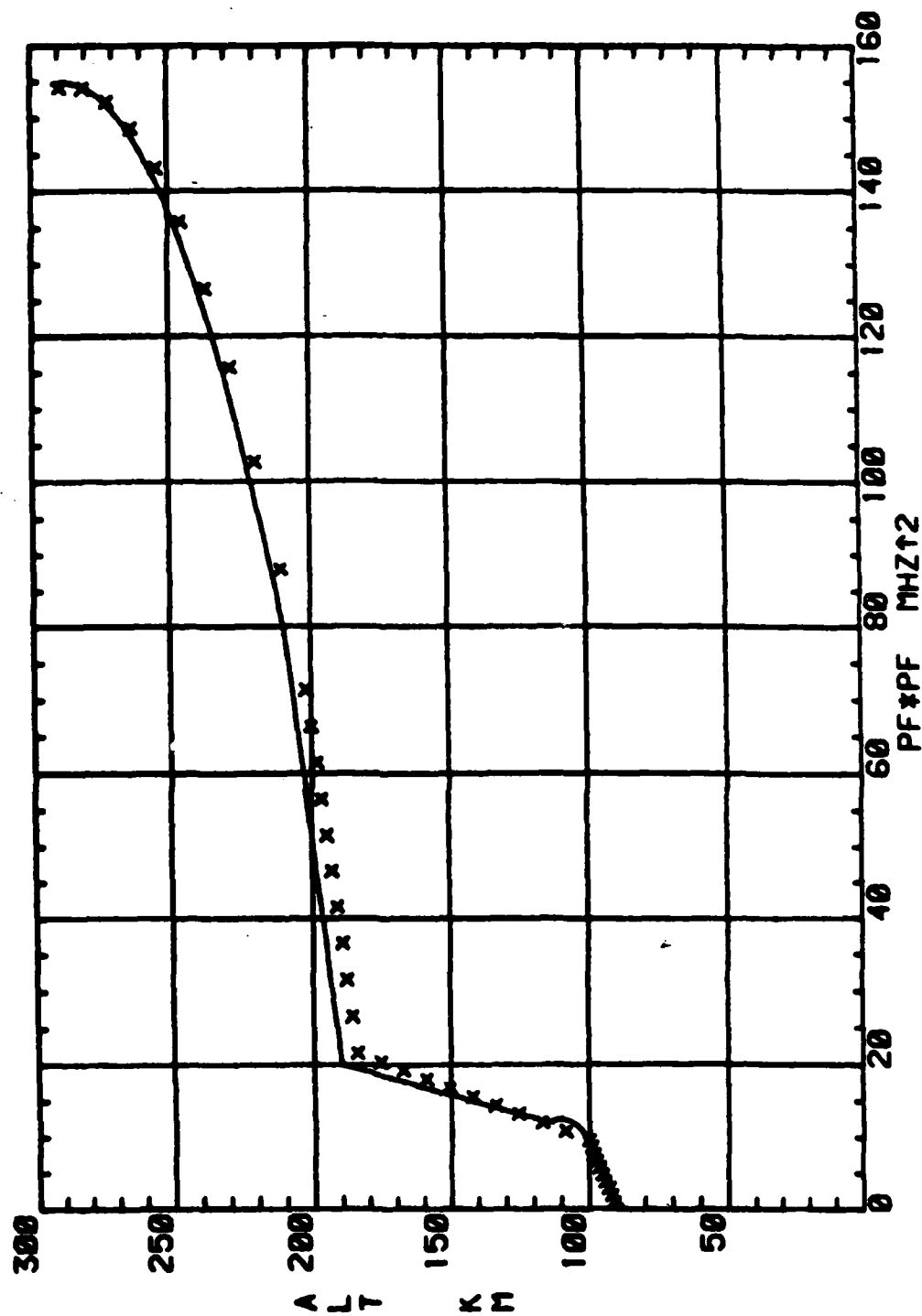
# IONOSPHERIC TRUE HEIGHT PROFILE

No. 31



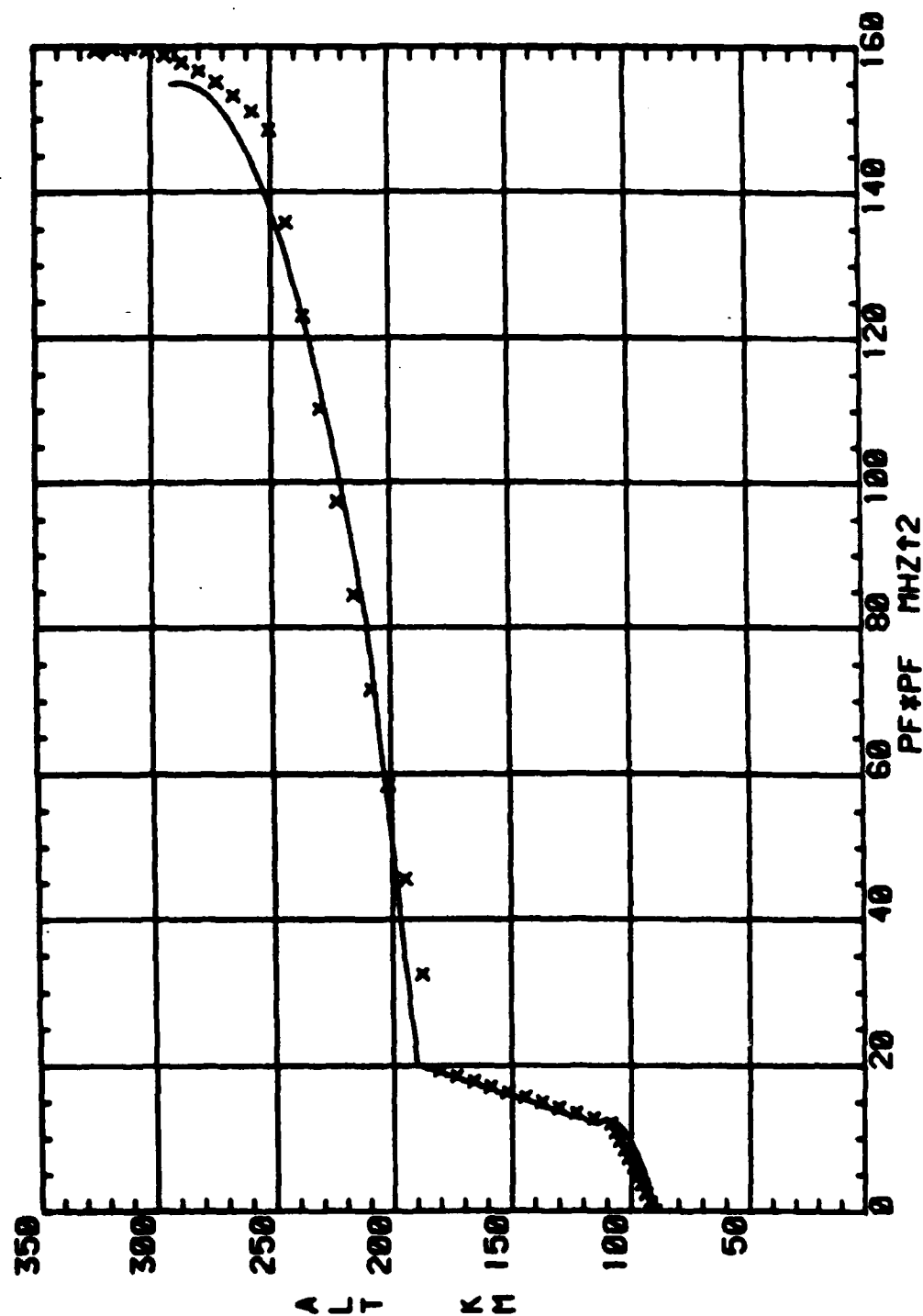
# IONOSPHERIC TRUE HEIGHT PROFILE

NO. 32



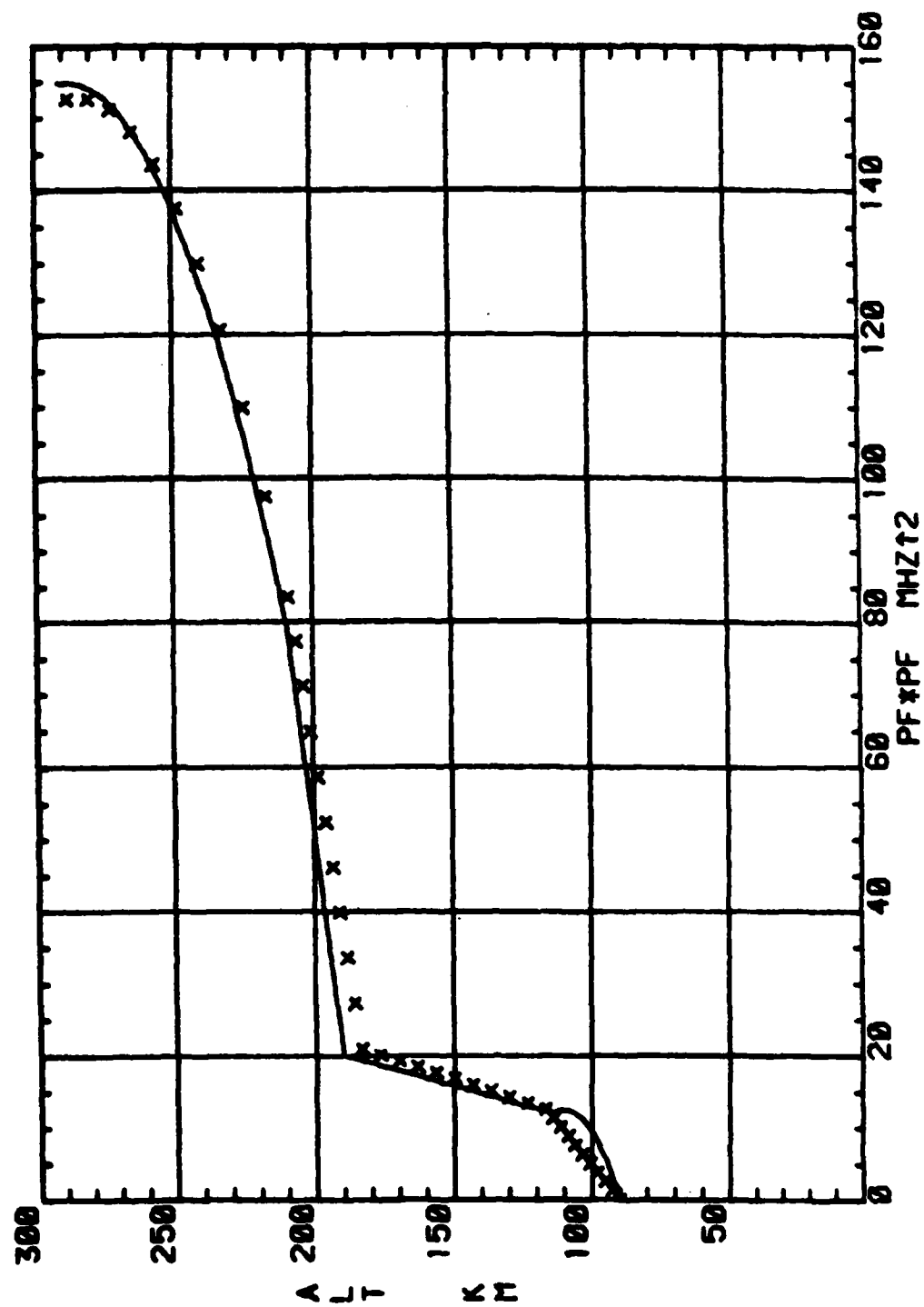
# IONOSPHERIC TRUE HEIGHT PROFILE

No. 33



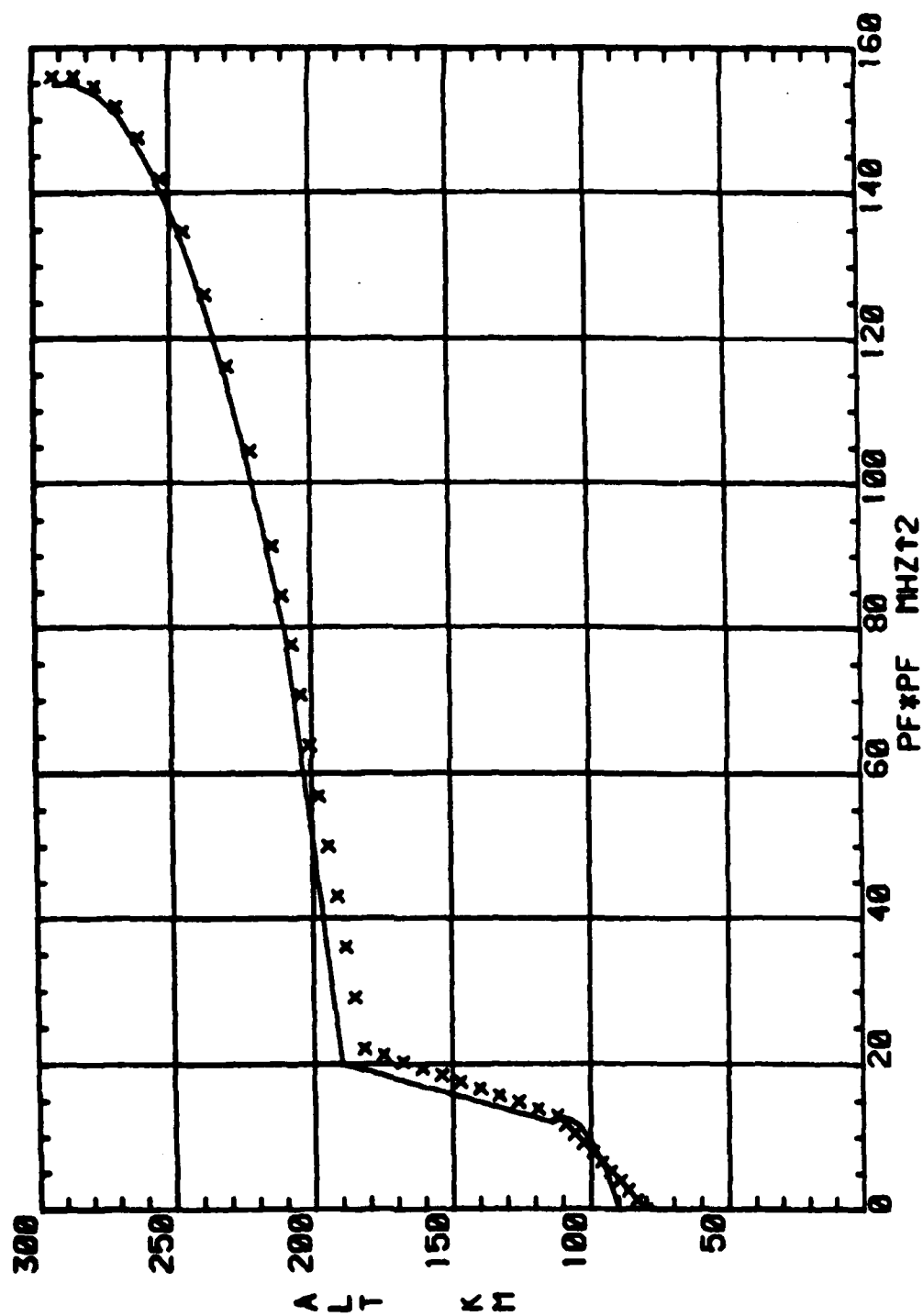
# IONOSPHERIC TRUE HEIGHT PROFILE

No. 34



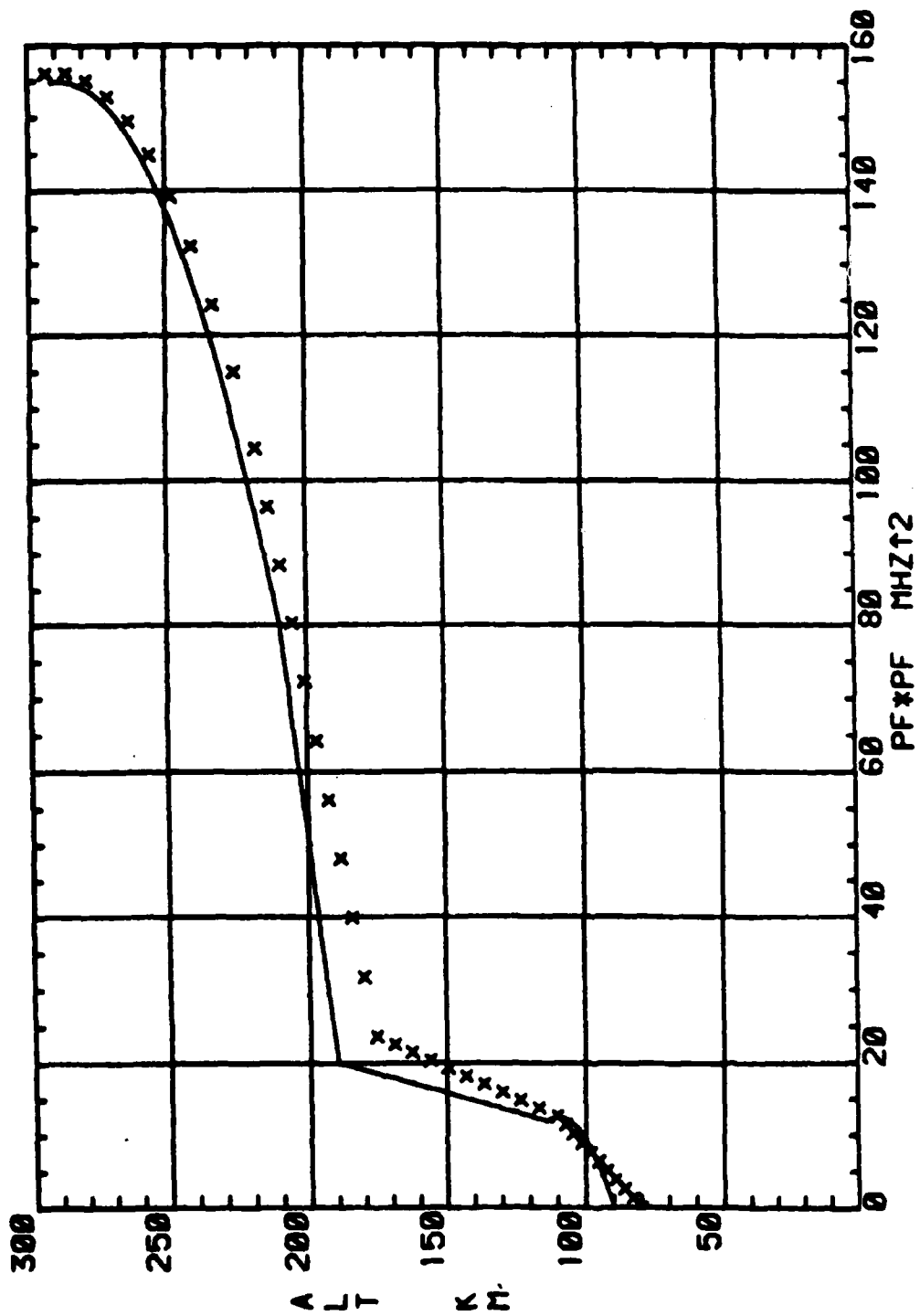
# IONOSPHERIC TRUE HEIGHT PROFILE

No. 35



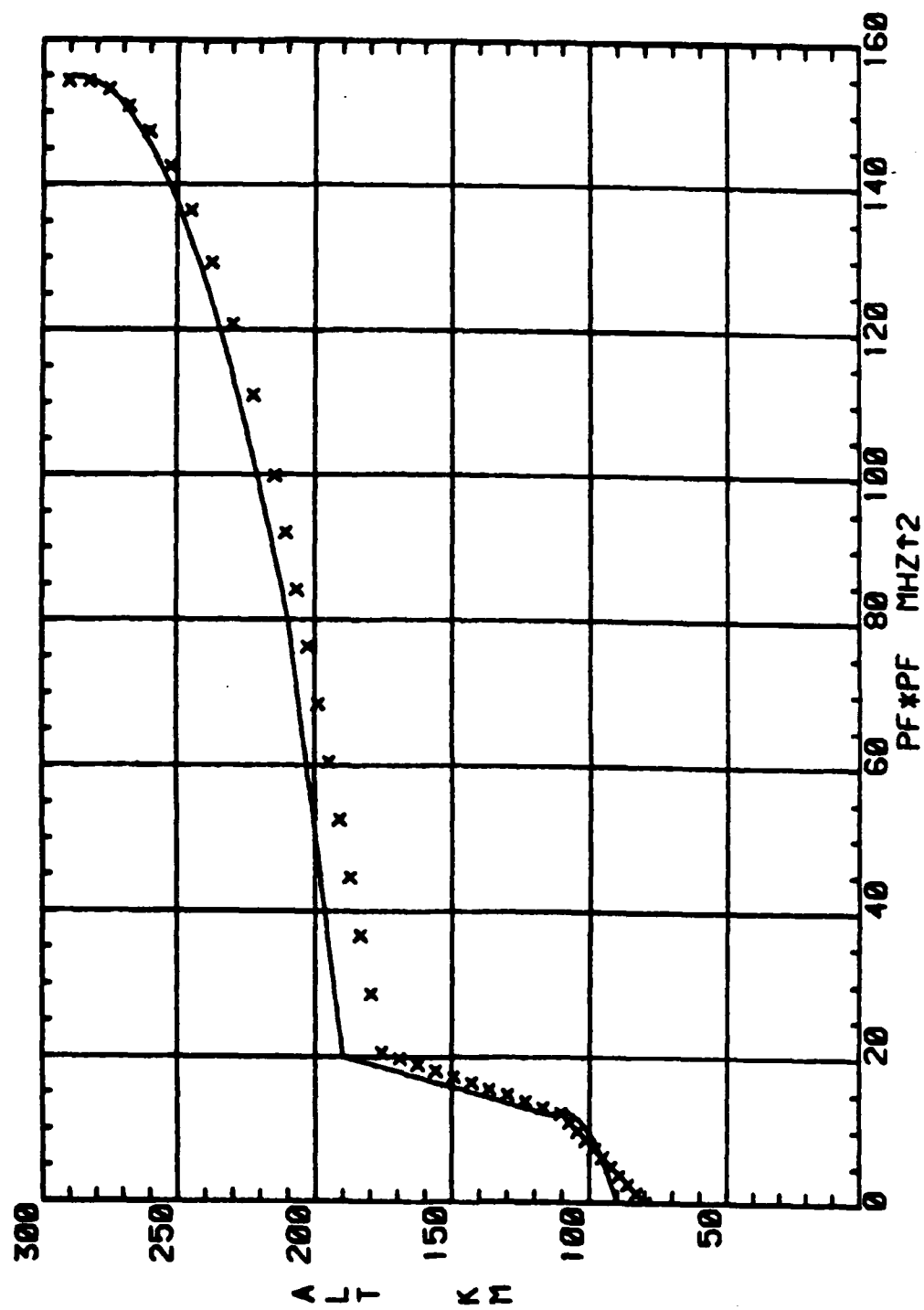
# IONOSPHERIC TRUE HEIGHT PROFILE

No. 36



# IONOSPHERIC TRUE HEIGHT PROFILE

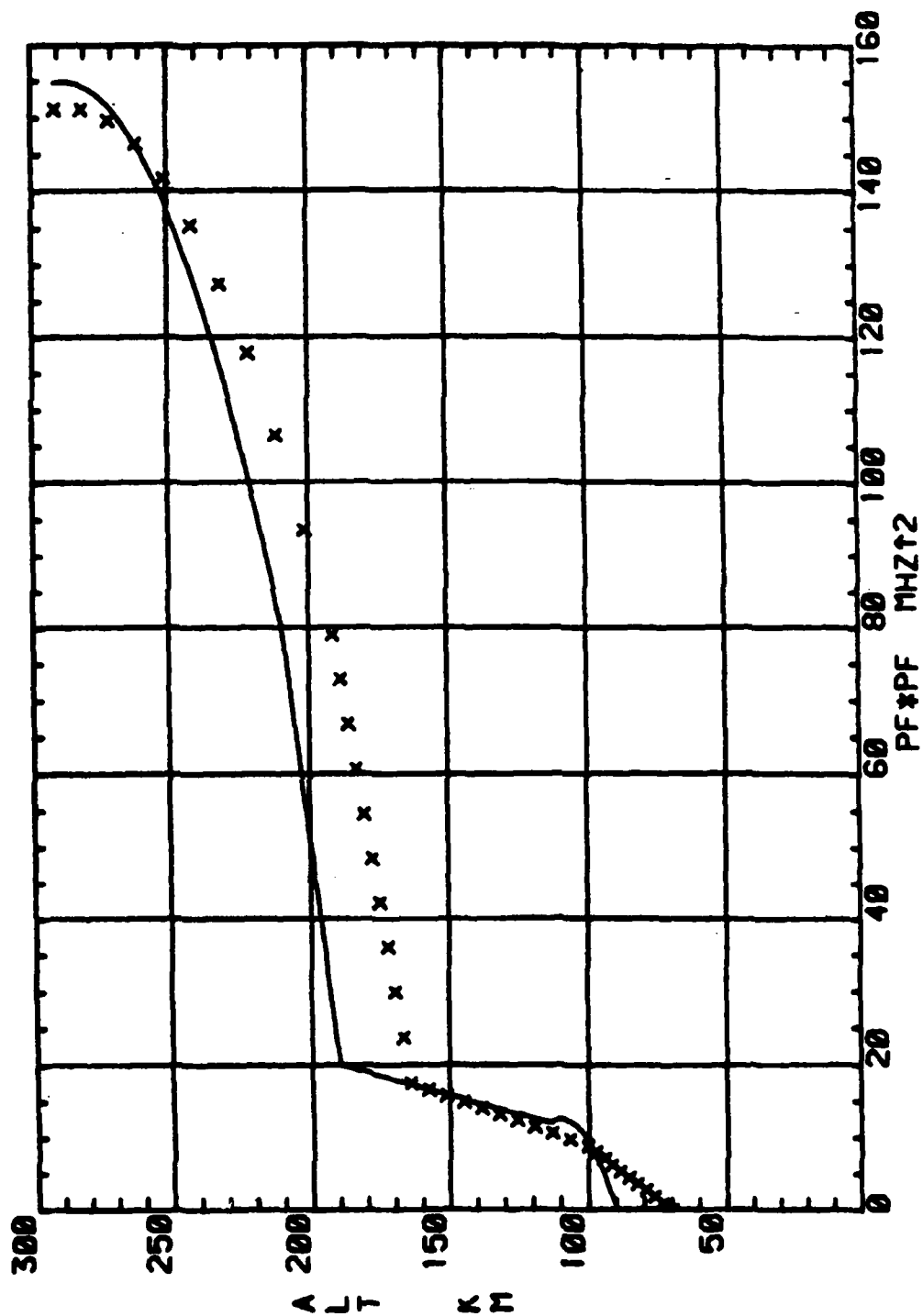
No. 37





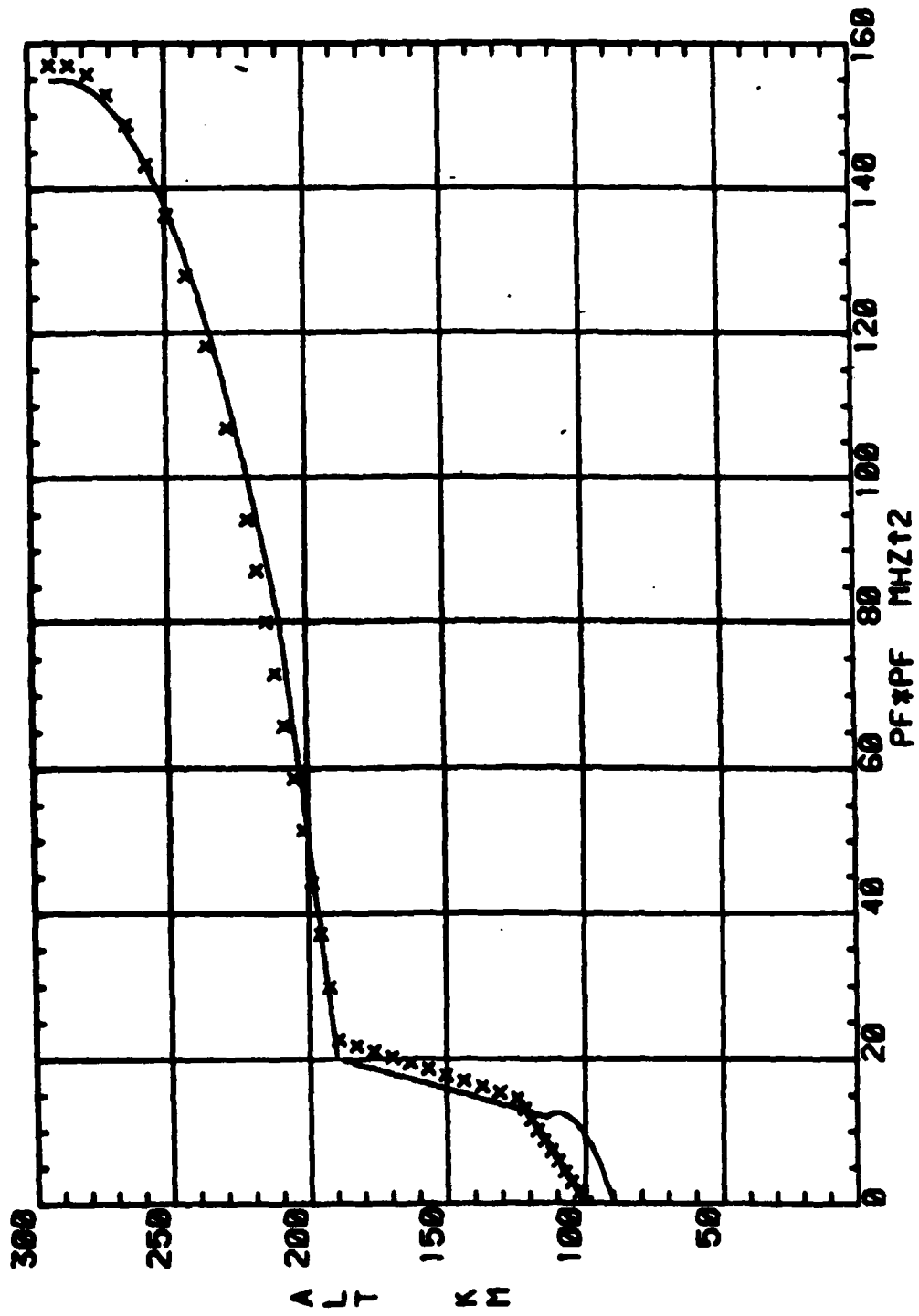
# IONOSPHERIC TRUE HEIGHT PROFILE

No. 38



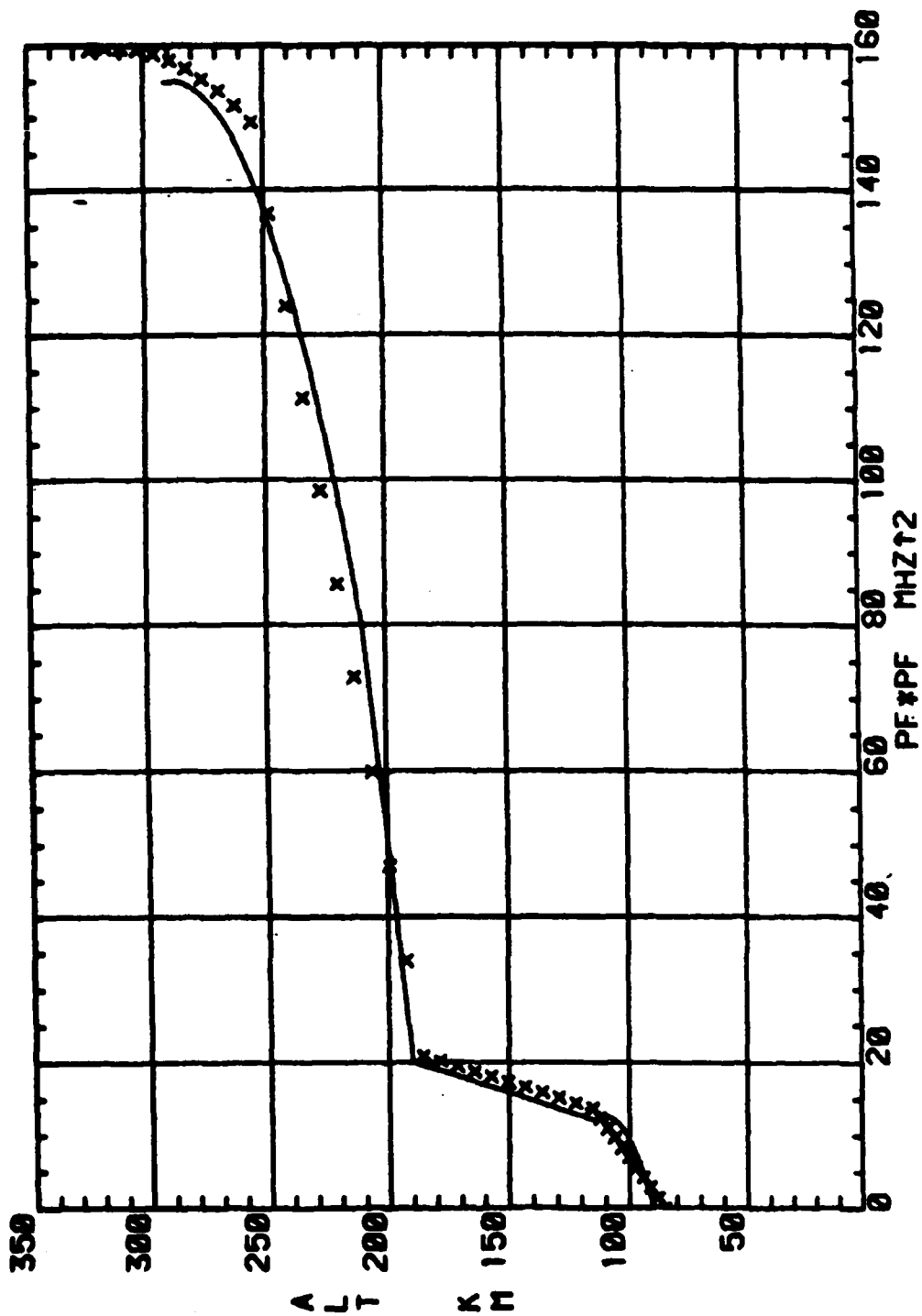
# IONOSPHERIC TRUE HEIGHT PROFILE

No. 39



# IONOSPHERIC TRUE HEIGHT PROFILE

No: 40



**END**

**FILMED**

**9-85**

**DTIC**